COLLEGES SCIENCES
BRETAGNE POUR L'INGENIEUR
LOIRE ET LE NUMERIQUE

IMT Atlantique
Bretagne-Pays de la Loire
École Mines-Télécom

THESE DE DOCTORAT DE

L'ÉCOLE NATIONALE SUPERIEURE
MINES-TELECOM ATLANTIQUE BRETAGNE PAYS DE LA LOIRE –
IMT ATLANTIQUE

ECOLE DOCTORALE N° 648
Sciences pour l'Ingénieur et le Numérique
Spécialité : *Electronique*

Par

Théo DUBASQUE

Flexible conformal antenna array: study of the radiation pattern and matching techniques

Thèse présentée et soutenue à IMT Atlantique, Brest, le 19 Juin 2026
Unité de recherche : Lab-STICC
Thèse N° : 2026IMTA0541

Rapporteurs avant soutenance :

M. Raphaël GILLARD	Professeur, Insa Rennes
Mme Laure HUITEMA	Maitre de conférences HDR, Université de Limoges

Composition du Jury :

Président :	M. Éric KERHERVÉ	Professeur, ENSEIRB-matmeca
Examinateurs :	M. Raphaël GILLARD	Professeur, Insa Rennes
	Mme Laure HUITEMA	Maitre de conférences HDR, Université de Limoges
	M. Benjamin COQUILLAS	Docteur, Thales LAS France
Dir. de thèse :	M. Benjamin POTELON	Professeur, IMT Atlantique
Co-encadrant :	M. Cédric QUENDO	Professeur, Université de Bretagne Occidentale

Invité(s)

M. Koenraad MOUTHAAN,	Associate Professor, National University Singapore
M. Thomas MERLET,	Ingénieur Docteur, Thales

Acknowledgments

I would like to express my sincere gratitude to my thesis director at IMT Atlantique, Professor Benjamin Potelon, for his supervision throughout these years. His guidance, dynamism, and scientific rigor have been of great help to me. I would also like to thank my co-supervisor at UBO, Professor Cédric Quendo, for his support and scientific curiosity. I am also deeply grateful to my supervisors at Thales: Dr. Thomas Merlet for his overall support within the company and his kindness, and Dr. Benjamin Coquillas for his dedicated and always attentive personal guidance. Finally, I would like to thank Professor Koenraad Mouthaan for his warm welcome in Singapore and for all his valuable advice on our joint work.

I am very thankful to my examiners, Associate Professor (HDR) Laure Huitema and Professor Raphaël Gillard, for their corrections, pertinent questions, and valuable advice. In parallel, I would like to thank the chair of the jury, Professor Éric Kerhervé, for his kindness and insightful remarks.

I would like to thank all the interns, technicians, and engineers who enabled me to use the tools necessary for the progress of my work, including Bastien le Seigneur, Bernard Abiven, and Maïna Sinou, and in particular Dr. Annaïg Guennou-Martin for her invaluable help with the use of servers and softwares. In parallel, I would like to thank all the staff of IMT Atlantique and of the SPIN Doctoral School for ensuring its smooth functioning, with special thanks to Delphine Lucas and Marlyse Pracht.

This PhD has given me the opportunity to meet wonderful people, including PhD students, teachers, and engineers. I would like to express my appreciation to Alain, Noam, Vincent, François, Christian, Benjamin, Bryan, Corentin, Yanis, Marin, Clément, Nicholas, Guillaume, Loïc, Andrés, Kevin, and Mufti, and more generally to all the staff of the Lab-STICC. These scientific and human exchanges have been extremely enriching.

Enfin, j’adresse un immense merci à ma famille, et tout particulièrement à mes parents, qui, au-delà de leur amour, m’ont toujours accompagné et soutenu tout au long de mon parcours scolaire, du primaire aux études supérieures. Je remercie également ma sœur pour son soutien constant au fil des années, ainsi que Cécilia Caamano pour m’avoir accompagnée tout au long de cette thèse.

Résumé du manuscrit et des travaux de thèse

L'étude et l'utilisation des antennes flexibles ont connu un essor considérable ces dernières années en raison de leur large éventail d'applications possibles. En effet, la capacité de déformation peut être temporelle, permettant aux antennes d'être montées sur des vêtements ou directement sur la peau avec une adaptation de forme en temps réel, ou continue, comme dans le cas des antennes flexibles intégrées de manière permanente, en se conformant à la structure d'un véhicule, d'un mât ou d'un radôme. Dans le secteur de la défense, cette technologie est particulièrement intéressante pour réaliser des réseaux conformes sur des véhicules afin de faciliter l'intégration du système, et/ou élargir le diagramme de rayonnement du réseau en fonction de l'application.

L'étude détaillée de ces conceptions flexibles peut être abordée sous deux angles principaux : un angle technologique, axé sur les propriétés des matériaux (flexibilité, durabilité, résistance à l'environnement et réalisation industrielle), ainsi qu'un second angle sur la théorie des antennes, qui traite de l'adaptation des réseaux conformes et des impacts de la courbure sur le comportement du diagramme de rayonnement global du réseau. Le second axe d'étude plus théorique est celui qui a été étudié au cours des travaux de thèse.

Les travaux présentés dans cette thèse visent à créer des réseaux de fentes de taille moyenne sur des guides d'ondes intégrés à substrat flexible (SIW) dans les bandes de fréquences X et Ku. Plus précisément, les travaux se concentrent sur la théorie d'adaptation de ces réseaux à fentes, ainsi que sur l'anticipation de l'ouverture du diagramme de rayonnement du réseau pour des rayons de courbure de l'ordre de la longueur d'onde. Cette thèse CIFRE a été réalisée avec le laboratoire commun LATERAL, une collaboration entre Thales LAS et le Lab-STICC. De plus, un échange régulier a été entretenu avec l'université de Singapour NUS.

Contenu général

Le premier chapitre commence par présenter les définitions des grandeurs et paramètres électromagnétiques. Ceux-ci sont ensuite utilisés pour une présentation concise de la théorie des antennes et des réseaux. Ces bases permettent ensuite d'introduire le concept des antennes conformes, leurs avantages et inconvénients, ainsi que la théorie associée, qui diffère de celle des réseaux plans conventionnels. Ensuite, un bref aperçu des différents réseaux d'antennes à fentes, basés soit sur des guides d'ondes rectangulaires (RWG), soit sur des guides d'ondes SIW, est fourni. Enfin, compte tenu des diamètres de fonctionnement spécifiés par l'entreprise, la motivation pour utiliser un réseau SIW flexible est discutée, parallèlement à une revue de l'état de l'art de cette technologie.

Le deuxième chapitre traite de l'amélioration et de la correction directes de la méthode théorique la plus conventionnelle pour concevoir correctement un réseau de fentes de taille moyenne tout en tenant compte des effets de couplage mutuel entre les fentes. Pour y parvenir,

une première étude de la formulation mathématique du comportement individuel des fentes est menée. Une méthode permettant de corriger les paramètres de conception théoriques d'un réseau de fentes grâce à une boucle numérique automatisée entre Python et HFSS est ensuite présentée. Ces deux développements précédents ont ensuite conduit à un algorithme de conception automatisé complet pour de tels réseaux, à partir d'un ensemble de paramètres RF spécifié. Ce travail est illustré par la réalisation de plusieurs prototypes fonctionnant dans les bandes X et Ku.

Le troisième chapitre présente une nouvelle procédure d'adaptation pour les réseaux d'antennes à fentes, particulièrement adaptée aux guides d'ondes très fins (offrant ainsi une grande flexibilité). Le cadre théorique et les aspects algorithmiques de la procédure sont d'abord décrits et validés par la réalisation d'un prototype. La procédure est ensuite appliquée à d'autres études de cas, englobant à la fois des implémentations directement réalisables et des extensions théoriques.

Le quatrième et dernier chapitre se concentre sur l'analyse des variations du diagramme de rayonnement dans le réseau de fentes flexibles pour des rayons de courbure de l'ordre de la longueur d'onde. Cette étude souligne la nécessité d'adapter la théorie classique des réseaux circulaires à notre configuration spécifique, ainsi que l'influence de plusieurs paramètres conventionnels des réseaux sur le diagramme de rayonnement résultant. Enfin, dans le but d'adapter le diagramme de rayonnement du réseau en forme d'arc tout en maintenant les fentes en phase, une étude est présentée sur l'utilisation d'une nouvelle procédure algorithmique qui fournit la pondération d'amplitude requise pour obtenir le diagramme de rayonnement souhaité.

Chapitre 1 – contexte et état de l’art

Le premier chapitre commence par introduire un ensemble de grandeurs et variables utilisées en électromagnétique. Celles-ci sont alors reliées à un ensemble de paramètres permettant de caractériser une antenne en allant de son adaptation en fréquence à son rayonnement. Une présentation des réseaux planaires classiques est réalisée puis confrontée à la difficulté de la théorie des conformes.

Le cahier des charges et les indications donnés par l’entreprise sont ensuite donnés avec la nécessité d’obtenir un réseau conforme, adapté en bande Ku avec de très bonnes caractéristiques. La solution d’utiliser un réseau d’antennes fentes est donc mise en avant avec une définition succincte de ce type d’antenne et leur mise en réseau sur les guides d’ondes classiques.

Les méthodes industrielles classiques permettant la réalisation physique de réseau d’antennes fentes conformes sont d’abord détaillées pour mettre ensuite en avant les intérêts de l’utilisation de SIW flexibles : impression 2D classique, bonne justesse d’impression, low-cost et applicable sur différents supports.

Une présentation succincte de la théorie des matériaux est ensuite apportée en introduisant les différentes variables caractérisant les comportements thermiques, mécaniques,

électriques et chimiques des matériaux. Un état de l'art des matériaux et méthodes de fabrications les plus utilisés sur le domaine d'étude est ensuite apporté. Celui-ci se termine par une justification de la méthode de conception utilisée et des matériaux qui seront utilisés pour la thèse au regard des besoin attendus et des objectifs fixés (travaux de thèse majoritairement portés sur la théorie des réseaux plutôt que leurs méthodes d'usinages).

Partant sur les SIW à fentes flexibles réalisés avec des matériaux comme le polytetrafluorethylene ou les polyimides, un second état de l'art portant sur les meilleurs articles spécifiques à ce sujet ainsi que sur la théorie de dimensionnement des réseaux à fentes la plus proche du sujet est donné. Cet état de l'art spécifique à notre sujet a permis d'identifier les verrous majeurs théoriques qui ont fait l'objet des travaux de thèse :

- La théorie d'adaptation des réseaux fentes sur guide très fins n'est plus adapté
- La théorie des réseaux à conformation cylindrique pour des rayons de l'ordre de la longueur d'onde ne prend pas en compte la déformation du diagramme de rayonnement local de la fente dépendant du rayon de courbure. On observe en effet dans la littérature que ces réseaux sont numériquement optimisés pour un rayon R fixé, donc avec un diagramme de rayonnement individuel constant. Dans le cas où on chercherait à tirer parti de la flexibilité du réseau en le fixant sur une multitude de cylindres de différents rayons, l'approche théorique classique doit être adaptée afin de prendre en compte les variations locales du diagramme de rayonnement unitaire selon R. Ce point est particulièrement intéressant car il permet d'obtenir une approche mathématique valide permettant d'anticiper la déformation globale du diagramme de rayonnement du réseau selon le rayon de courbure.

Le premier verrou fait l'objet des chapitres 2 et 3. Le second celui du chapitre 4.

Chapitre 2 - Modèle théorique amélioré pour les réseaux de fentes fortement couplés : nouvelle équation unitaire par fente et algorithme de correction automatisé

Le second chapitre de la thèse porte sur l'adaptation des réseaux fentes sur guide d'ondes fin. L'approche est assez scolaire : on se base sur la théorie déjà existante, un point particulier y est corrigé afin d'être valide au cas d'étude, puis un algorithme d'automatisation des corrections sur logiciel de simulations électromagnétiques (HFSS) est développé.

Une première partie met en pratique sur logiciel l'observation de l'impact des couplages mutuels entre fentes, externes comme internes, à une même fréquence de travail, pour différentes épaisseurs de RWG. L'adaptation d'une fente dépendant de son offset par rapport au centre x et sa longueur l, l'idée est de venir voir l'importance du décalage de la 'zone of matching' du couple (x, l) lorsque celle-ci est seule, en parallèle à une autre (1 couplage mutuel externe) et en couple avec une autre sur une même ligne (1 couplage mutuel interne). Cet exercice permet de quantifier et visualiser l'impact de la diminution de l'épaisseur du guide sur l'importance de ces 2 types de couplages mutuels, et donc du décalage de la 'zone of matching'

(x, l). La conclusion obtenue est que plus le guide est fin, plus le couplage mutuel externe diminue alors que l'interne augmente.

La prise en compte du couplage mutuel étant absolument nécessaire, la meilleure méthode disponible dans la littérature à ce sujet a été utilisée : l'approche de Elliott. Celle-ci est toujours cité dans la littérature spécifique au sujet de cette thèse. Elle permet de calculer théoriquement les couplages externes comme internes entre toutes les fentes du réseau et ainsi obtenir tous les couples (x, l) de chaque fente. Cette dernière fait souvent appel à la méthode de Stegen qui permet de caractériser l'adaptation en fréquence individuelle d'une fente selon une admittance normalisée équivalent $y_0(x, l)$ dont il propose un processus pour obtenir sa fonction analytique.

A l'aide de l'observation de l'impact des couplages mutuels internes sur le décalage des valeurs (x, l) des fentes pour des SIW très fins, il apparait que l'approche analytique de Stegen n'est plus valide. L'utilisation de fonctions d'interpolation est utilisée dans la littérature. Une nouvelle approche analytique a été trouvée permettant à la fois de rester valide en dehors de la zone de simulation et d'avoir un temps de calcul plus rapide que l'interpolation. Cette approche fait appel aux fonctions Lorentzienne et erreur (erf) dont les coefficients dépendent de l'offset. De très bons résultats ont été obtenus avec cette approche en comparant théorie et simulation.

L'algorithme théorique basé sur l'approche de Elliott est ensuite utilisé permettant ainsi de retourner tous les couples (x, l) de chaque fente. Il apparait que les premiers résultats sur logiciel de simulations électromagnétiques (HFSS) ne sont pas très bons. Un algorithme permettant d'automatiser les corrections sur logiciel a donc été développé. L'idée est de contrôler le logiciel HFSS depuis python permettant ainsi de lancer les simulations, exporter les résultats, mettre en équations les variations de l'adaptation cibles suivant les variables modifiées, en déduire les nouveaux facteurs de correction, et reboucler. On obtient ainsi automatiquement sur logiciel un réseau à fentes MxN adapté à la fréquence attendue.

Les scripts développés sur le point précédent ont ensuite été intégrés dans un algorithme plus général d'automatisation de tout le processus de conception de réseau d'antenne fente. Cela permet ainsi, depuis une IHM, de rentrer l'ensemble des paramètres radiofréquences attendus et d'obtenir automatiquement en sortie le réseau adapté sur le logiciel. Ceci nécessite l'automatisation de la procédure de caractérisation d'une antenne seule (Stegen, Lorentzienne ou interpolation), l'application de l'algorithme de Elliott, l'automatisation des dessins du réseau sur logiciel puis de lancer l'algorithme de la correction automatique. La version actuelle de l'algorithme demande entre 24 et 36 heures pour obtenir le réseau MxN sans toucher au logiciel.

Chapitre 3 – développement d'une nouvelle méthode pour l'adaptation des réseaux sur guide d'ondes très fins.

Au regard de la théorie étudiée et utilisée dans le second chapitre, et des résultats bruts obtenus sur la première simulation avant correction, l'écart avec les résultats attendus met en avant les limites de l'approche théorique de Elliott pourtant considérée comme la meilleure sur le sujet des réseaux à fentes. Ces limites peuvent s'expliquer par la négligence de certains points

lors de la démonstration électromagnétique non négligeable dans le cas de SIW très fins. De plus, l'utilisation de cette méthode est discutable lorsque l'on considère tout le temps nécessaire à sa compression et son développement algorithmique associé par rapport aux mauvais résultats obtenus sur la première simulation.

L'idée a donc été de développer une nouvelle approche où le raisonnement général de Elliott est repris, mais aucune des formules théoriques n'est retenue. Toutes les fonctions théoriques intermédiaires liant les différentes grandeurs ou anticipant les couplages mutuels sont simulées sur logiciel puis mise en équation sur python à partir des résultats empiriques. On obtient ainsi un système matriciel caractérisant l'admittance normalisée équivalente de chaque fente dont la valeur dépend du comportement individuel de la fente et de l'impact du couplage mutuel avec les fentes voisines. Un algorithme récursif de la même logique que celui d'Elliott est alors employé afin d'obtenir les couples (x, l) de chaque fente.

Un processus de différentes étapes de simulations, raisonnement associé et mise en équation est présenté. Celui-ci demande environ une trentaine d'heures de simulations et d' approximations numériques. Une démonstration numérique sur logiciel de simulations électromagnétiques est effectuée avec un guide d'onde d'épaisseur 127 µm, épaisseur jamais employée dans la littérature. Les résultats obtenus pour la première simulation du design dimensionné avec cette nouvelle approche sont bien meilleurs que ceux obtenus avec l'approche de Elliott, tant sur la fréquence de résonnance que sur l'adaptation à cette fréquence donnée. De plus, ce processus reste entièrement applicable dans le cas où un film de protection serait ajouté sur le réseau pour des raisons de protections thermiques et chimiques. Les résultats obtenus restent tout aussi bons.

Cette approche matricielle qui fait appel à un ensemble de fonctions définies au cours du processus de simulations a ensuite été élargi à 2 cas d'études différents. Le premier cas consiste à adapter un réseau à fente pour un mode de propagation TE20. Cela permet ainsi pour un même nombre M de lignes de fentes de retirer (M-1)/2 lignes de vias métalliques et gagner ainsi en flexibilité. De plus, une théorie de dimensionnement de ces types de réseau qui prendrait en compte les couplages mutuels, n'existant pas dans la littérature, la nouvelle approche proposée reste simple à comprendre d'un point de vue théorique et les résultats obtenus en simulations sont tout à fait acceptables. Le second cas d'étude porte sur la prise en compte dans le modèle matriciel du couplage mutuel externe. Cette ouverture a un intérêt lorsque les guides d'ondes sont d'épaisseurs toujours faibles (donc prise en compte du couplage mutuel interne) mais pas suffisamment faibles pour ignorer le couplage mutuel externe. Ce cas d'étude se rapproche donc de la théorie de Elliott. Le processus des étapes de simulations, la mise en équation et le système matriciel associé ont donc été adaptés. Pour simplifier l'étude, seul le couplage mutuel externe avec les 2 fentes voisines dans le plan E (couplage externe le plus fort) a été considéré afin d'alléger les temps de simulations et la taille du système matriciel utilisé ensuite dans l'algorithme de convergence. Les résultats obtenus sont acceptables bien que moins bons que dans le cas des guides d'ondes très fins. L'utilisation de cette nouvelle approche plutôt que celle de Elliott pour ce cas d'étude est alors discutable : la procédure de Elliott demande une compréhension théorique beaucoup plus importante alors que la traduction

algorithmique reste assez simple, alors que cette nouvelle approche est très intuitive d'un point de vue théorique mais demande un développement algorithmique plus important.

Chapitre 4 – étude théorique et expérimentale de l'impact de la courbure sur le diagramme de rayonnement d'un réseau flexible SIW à fente

Comme évoqué précédemment, la littérature de bon niveau sur ce sujet d'étude de réseau SIW à fentes flexible de conformation cylindrique porte sur l'optimisation du diagramme de rayonnement du réseau pour un rayon R donné. Une grande partie de ce chapitre essaie de se démarquer en considérant le rayon R comme une variable, ce qui nécessite alors d'adapter la théorie des réseaux conformes circulaires au cas où le diagramme de rayonnement local d'une fente varie avec le rayon. L'étude se fait pour des courbures convexes comme concaves, dans les 2 plans E et H.

La première étude consiste donc à simuler le diagramme de rayonnement d'une seule fente courbée dans les différents plans d'étude pour différents rayons $R/\lambda_0 < 10$, puis de mettre en équation son diagramme de rayonnement normalisé par la valeur maximale de celle de la fente planaire. On obtient ainsi les variations $h(\theta, R)$ et $e(\theta, R)$ correspondant aux diagrammes de rayonnement normalisés en champs de la fente courbée dans les plan H et E. Celles-ci sont alors mises en équation à l'aide de série de Fourier paire dont les coefficients sont dépendant du rayon R. Les variations de ces coefficients selon R sont approximées par des fonctions exponentielles saturées.

L'idée générale étant de pouvoir anticiper théoriquement les variations du diagramme de rayonnement d'un réseau courbé par rapport au réseau planaire (rayon infini), une relation quadratique entre le diagramme de rayonnement en champ normalisée et le gain réel normalisé mesuré est développée dans ce chapitre. Dans cette relation, un ensemble de paramètres importants du réseau ne pouvant être isolé analytiquement, une étude numérique sur l'impact de la pondération, la distance entre les éléments et la directivité unitaire sur la rapidité d'ouverture du diagramme de rayonnement et perte de directivité associée en fonction du rayon de courbure R est effectué. Cette étude théorique est ensuite appuyée par un ensemble de mesures en salle anéchoïque effectué sur différents réseaux SIW à fentes flexibles 4x8 adaptés à 10 GHz ou 15 GHz avec pour diélectrique le SF280 de 127 µm et le RT/Duroid 5880 de 254 µm. L'ensemble des mesures est comparé aux simulations et résultats théoriques anticipés. L'ensemble montre une bonne concordance.

Enfin, Une approche d'optimisation du diagramme de rayonnement pour un rayon R donné, basée sur le dénombrement, est proposée. Le diagramme et le rayon étant fixés, seules les pondérations d'excitation des fentes en phase sont ajustées. Contrairement aux méthodes génétiques, cette approche se veut simple et rapide à développer tout en donnant des résultats acceptables. Elle repose sur le théorème des étoiles et des bars pour générer et tester toutes les combinaisons discrètes possibles. La difficulté principale est la croissance exponentielle du nombre de combinaisons, nécessitant une vectorisation et une formulation matricielle pour limiter les contraintes mémoire. Un exemple avec un réseau 1×8 courbé (R = 2 cm, ouverture 180°, ripple inférieur à 2 dB) montre un bon accord entre théorie et simulations HFSS.

Table of Contents

Acknowledgments i
Résumé du manuscrit et des travaux de thèse ii
Table of Contents ix
Table of figures and tables xii
General introduction ..... a
Chapter 1 - context and state of the art 1
1.1 Introduction 2
1.2 Radiating elements and associated physical quantities 2
1.3 Antenna characteristics 5
1.3.1 Input parameters 6
1.3.2 External parameters 7
1.4 Linear and planar array antenna 9
1.5 Conformal array antenna 11
1.5.1 Definition and overview 11
1.5.2 Ring array theory 14
1.6 Slotted array antenna 15
1.6.1 Choice of slotted array antenna 15
1.6.2 Rectangular waveguide and substrate integrated waveguide 16
1.6.3 Radiation of a slot and matching on RWG 18
1.6.4 Array configuration 21
1.6.5 Technical realization for a conformal slotted waveguide 24
1.7 Flexible antenna 24
1.7.1 General overview and characteristics 24
1.7.2 Flexible SIW slotted array 28
1.7.3 Current limitations in the synthesis of flexible slotted waveguide arrays 29
1.8 Conclusion 30
Chapter 2 - Improved Theoretical Model for Strongly Coupled Slot Arrays: New Unit-Slot Equation and Automated Correction Algorithm 31
2.1 Introduction 32
2.2 Theoretical method for the matching of a Standing-wave fed slot array 33
2.2.1 Unit slot and associated normalized admittance 33
2.2.2 Observation of the impact of mutual coupling between slots 35

2.2.3 Formulation of Elliott's equations and associated recursive algorithm 38
2.3 New Y/G_0 analytical function 43
2.3.1 Theoretical approach 43
2.3.2 Computational procedure 45
2.3.3 Comparison with Stegen's method 46
2.4 Automated dimensional corrections of slot array antennas in simulation software 48
2.4.1 Objectives of the correction of the design matrix in the simulation software 48
2.4.2 Developed method 49
2.4.3 Example with 1 design 54
2.5 Development of a general algorithm for automatization 58
2.5.1 Objectives 58
2.5.2 General operation 58
2.5.3 Realized designs 60
2.6 Conclusion 64
Chapter 3 - Development of a new method to match thin slotted array 65
3.1 Introduction 66
3.2 Mathematical approximation and associated procedure 67
3.2.1 Software model used 67
3.2.2 Slot's electromagnetic behaviour 68
3.2.3 2 Slots' electromagnetic behaviour 70
3.2.4 Matrix model 72
3.3 Associated algorithm procedure 74
3.3.1 General procedure 74
3.3.2 α and v_0 functions 75
3.3.3 p_{ab} function 78
3.3.4 Recursive algorithm 80
3.3.5 Notes and tips 81
3.4 Extension of the method to other possible case studies 84
3.4.1 consideration of a protective film on the waveguide 84
3.4.2 Application to the TE_{20} mode of propagation 85
3.4.3 Consideration of the external mutual coupling 92
3.5 Application of the method to realize a flexible slotted SIW 101
3.6 Conclusion 102

Chapter 4 - Theoretical and Experimental Investigation of Curvature Effects on SIW Slotted Array Radiation Pattern 104
4.1 Introduction 105
4.2 Study of the radiation pattern formula of conformal array for curved slot with small radii of curvature 106
4.2.1 Study of 1 curved slot radiation pattern 106
4.2.2 Adaptation of the general arced radiation pattern formula 113
4.2.3 Study of the impacts of linear arced array parameters on the opening of the main beam with radii of curvature 121
4.3 Comparison of the last developed theoretical approach with the range of simulations and measurements on the flexible SIWSA designs 124
4.3.1 General protocol for the study 124
4.3.2 Measurements of the matching of the 3 tested designs and their associated gain for different radii of curvature in each plane 127
4.3.3 Comparisons between the results from theoretical approach, simulations and measurements 131
4.4 Optimisation of the radiation pattern of a curved in-phased slotted array with a given radius of curvature based on theory from combinatorics 133
4.4.1 Mathematical approach 133
4.4.2 Numerical test 135
4.5 Conclusion 141
General conclusion and perspectives 143
References 145

Table of figures and tables

Figure 1 : Schematic representation of radiation zones. 4
Figure 2 : Far field radiation vectors in spherical coordinate system. 4
Figure 3 : Circuit representation of the antenna and the source. 5
Figure 4 : Illustration of reflection coefficient and associated bandwidth. 7
Figure 5 : Radiation pattern in Polar and Cartesian representations (linear scale). 8
Figure 6 : Schematic of a M×N and 1×N array with constant spacing between elements. 10
Figure 7 : Conformal canonical Array Antenna for data transmission for LEO satellite of ESA, faceted active array antenna with six dual polarized dipole elements in each facet (Courtesy of Roke Manor Research Ltd., Roke Manor, Romsey, Hampshire, UK.) 12
Figure 8 : Several antennas integrated into the aircraft structure, serving different functions, figure from [6], © 2006 IEEE. 13
Figure 9 : Conformal arrays with (a) radius of curvature of the order of the dimension of the array (b) and with radius of curvature much larger than the dimensions of the array. 13
Figure 10 : Geometry for ring array. 14
Figure 11 : Photographs of (a) a RWG linear slotted array[11], CC-BY, and (b) SIW linear slotted array with schematic vectors of **E** and **H** fields 16
Figure 12 : Geometry of rectangular waveguide (left) and substrate integrated waveguide (right). 17
Figure 13 : Schematic transition from microstrip to SIW line from [20], © 2010 IEEE 18
Figure 14 : Fields planes for the electric dipole and complementary magnetic dipole polarizations. 19
Figure 15: Geometrical model of 1 slot on the RWG. 20
Figure 16 : General behaviour of the slot matching at a given frequency depending on the slot's length 2l and the offset x. 21
Figure 17 : Equivalent electric model for a 1×N slotted waveguide. 22
Figure 18 Schematic of a slotted SIW array showing external (green) and internal (orange) mutual coupling relationships between the slots. 22
Figure 19 : simulated (a) slot's equivalent normalized admittance function y_0 and (b) S_{11} parameter at 15GHz with a RT/Duroid 5880 dielectric of 254µm. 33
Figure 20 : variation of the h functions with γ ratio for different offsets from [27] , © 1952 IEEE 35
Figure 21 : 3 tested configurations to observe the effects of mutual couplings. (a) Single slot. (b) Two identical slots on parallel waveguides. (c) Two identical slots on the same waveguide. 36
Figure 22 different values of couple (x, l) for different thicknesses of the 3 configurations of Figure 21 37
Figure 23 variations in percent of the slot length resonance with mutual coupling for different thicknesses 37
Figure 24 : Geometrical representation of the used variables for MC calculus. 40
Figure 25 : Variations of the g_{mn} function depending on the normalized distance in both planes (a) in the E-plane (b) in the H-plane 41

Figure 26 : Calculus of g_{mn} values for each identical slot of the 8x8 array. 41
Figure 27 : Variations of (a) h_1 and (b) h_2 functions depending on the length ratio γ for different offsets in the case of RT/Duroid 5880, 0.254mm at 15GHz. 43
Figure 28 : Global shifting behaviour of (up) the real and (down) the imaginary parts of the normalized admittance Y/G_0 with the offset x. 44
Figure 29 : Illustration of finding the $l_{res}(x)$ function from the b(l) function of each iteration (step 4). 46
Figure 30 : Finding the coefficients of the Lorentzian function on the (up) real and (down) imaginary parts of the normalized admittance for each offset (step 6). 46
Figure 31 : Deduce the quadratic behaviour of each factor depending on the offset (step 7).. 47
Figure 32 : Comparison of absolute difference between the simulation of normalized conductance, (left) with the Stegen method and (right) with the Lorentzian developed method. 47
Figure 33 : Comparison of absolute difference between the simulation of normalized susceptance, (left) with the Stegen method and (right) with the Lorentzian developed method. 47
Figure 34 : Representation of the convergence zone of the two steps. 49
Figure 35 : (Up) Reflection coefficients Sii and (down) associated normalized admittances for an 8x8 array with f_0 = 15 GHz and h_{rwg} = 254 µm, simulated between 14.5 and 15.5 GHz ... 50
Figure 36 : (Up) y function and (down) its associated derivate of imaginary part for different length simulated between 14.5 and 15.5 GHz..... 51
Figure 37 Real and imaginary parts of the input normalized admittance and associated derivative of the first input waveguide for tested 8x8 array simulated between 14.5 and 15.5 GHz. 52
Figure 38 : Flowchart of the general algorithm of the design correction with Python and HFSS. 53
Figure 39 : Derivative of the real and imaginary parts of the normalized admittance of the second line depending on frequency. 55
Figure 40 : Derivative function of the normalized admittance for different fact_l depending on frequency and (down) associated shift in frequency depending on fact_l. 55
Figure 41 : (Up) Real and imaginary parts of the normalized admittance for different fact_x depending on frequency and (down) associated decreasing of the maximal conductance depending on fact_x. 56
Figure 42 : Validation of the checking of Δf_1 and Δg on y function and new checking of Δf_2 and Γ_{min} on the second loop. 57
Figure 43 : Final S-parameter for each waveguide respecting the fixed conditions on Δf_2 and Γ_{min}. 57
Figure 44 : Flowchart of the general processus of automatization to obtain an adapted slotted array on RWG or SIW. 59
Figure 45 : Realized design of 4x8 SIW slotted array with SF280 in Ku band, (left) top and (right) bottom. 61
Figure 46 : Measured and simulated reflection coefficient vs. frequency for (a) SF280_Ku design, (b) SF280_X design, (c) Ro5880_Ku and (d) Ro4350_X. 62

Figure 47 Measured and simulated reflection coefficient vs. frequency for (a) SF280_Ku design, (b) SF280_X design, with retro simulation with $\varepsilon_r = 3.08$..... 63
Figure 48 : Comparison simulation vs measure for both designs in Ku band: the design SF280 (a1) in E-plane and (a2) H-plane, and Ro5880 (b1) in E-plane and (b2) H-plane. 63
Figure 49 : Screen from HFSS software presenting the lines of integration for the slot voltage V_s and the mode voltage V_{in}. 68
Figure 50 : Variations of (top) normalized admittance y_0 and (bottom) normalized slot voltage v_0 depending on the couple (x, l) values for 1 slot with RT/Duroid 5880 127µm at 15GHz... 69
Figure 51 : Variations of the α function depending on the couple (x, l) values for 1 slot. 70
Figure 52 : Variations of the values of (left) p_{12} and (right) p_{21} depending on (x_1, l_1) values for a fixed couple 72
Figure 53 : Schematic representation of a 1×8 linear array with the representation of the adaptation of v_{14} depending directly of the coefficient factor p(14,13) and p(14,15). 73
Figure 54 Variations of the coefficients of approximations a(x) and b(x) for α function. 75
Figure 55 : Comparison of the HFSS α values and the well-matched approximation with python, plus the comparison with Elliott anticipated theoretical values. 76
Figure 56 : Variations of the sigmoid function's coefficients depending on the offset x to approximate v_0(x,l) function. 77
Figure 57 : Comparison between HFSS results and numerical approximation for the values of v_{10}. 77
Figure 58 : Example of the variations with the offset x of the coefficients of the real part of the approximation function for p_{ab} simulated values. 79
Figure 59 : For a given (x2, l2) couple, comparison of the calculated coefficient p12 values for different couples (x1 ,l1) and its numerical python approximation for real and imaginary parts. 79
Figure 60 : Variations of the reflection coefficient for the 1x10 lossless, lossy and adapted lossy design. 81
Figure 61 : Reflection coefficients for half of the waveguides from the 9 times duplicated 1×10 waveguide previous design and its associated radiation pattern. 82
Figure 62 Array data of p_{ab} function obtain with p_{12} and p_{21} simulation process. 83
Figure 63 : Variations of the reflection coefficient for a 1×8 lossless, lossy and modified lossy design with coat of varnish..... 85
Figure 64 radiation pattern of an 8×8 slotted array coated with varnish..... 85
Figure 65 : From [50], the surface current distribution for TE_{20} mode and the four-slot configuration. 86
Figure 66 : Numeration of 2×N slot array in TE20 mode. 87
Figure 67 : Tested design for TE_{20} study with (a) individual external (b) configuration internal configuration and (c) mutual coupling study 88
Figure 68 : Comparison of the (left) imaginary and (right) real parts of the v_0 function for both the internal and external configurations for the slot couples. 89
Figure 69 : Comparison of the (left) imaginary and (right) real parts of the α function for both the internal and external configurations for the slot couples. 89

Figure 70 : Reflection coefficient of the TE20 mode for a 2×8 slotted waveguide lossless, lossy and lossy with corrections. 90
Figure 71 : Real and imaginary parts of the normalized admittance Y/G_0 of the TE20 mode for a 2×8 slotted waveguide, lossless, lossy and lossy with corrections..... 91
Figure 72 : Reflection coefficient of the 4×8 slotted array in TE20 mode and its associated normalized radiation pattern..... 91
Figure 73 : (left) Geometrical representation of a symmetrical even M×N array and (right) coefficients of mutual coupling p and e in a subsection..... 92
Figure 74 : diagram of the building of the Q matrix 94
Figure 75 3 used designs to analyse the electromagnetic behaviour of (a) the individual slot, (b) the external (c) and the internal mutual coupling..... 96
Figure 76 : Variation of α function depending on (x,l) values for the Ro4003 design and its numerical approximation..... 97
Figure 77 : Variation of v_0 function depending on (x,l) values for the Ro4003 design and its numerical approximation..... 98
Figure 78 : Variations of the p_{12} and p_{21} coefficients depending on (x_1, l_1) for (x_2, l_2) fixed at (-0.3, 3.14) mm. 98
Figure 79 : Variations of the e_{12} and e_{21} coefficients depending on (x_1, l_1) for (x_2, l_2) fixed at (-0.3, 3.14) mm. 99
Figure 80 : Reflection coefficient and normalized admittance for the 2 first waveguides of the 4×8 Ro4003 design of 1.574 mm. 99
Figure 81 : Reflection coefficient for the 2 first waveguides of the corrected 4×8 Ro4003 design of 1.574 mm and its associated radiation pattern in log scale. 100
Figure 82 : Variations of the reflection coefficient and its associated normalized equivalent admittance for the 1×8 lossless, lossy and matched lossy designs. 101
Figure 83 : Final results from HFSS of the reflection coefficient of the 4×8 slotted design and its associated normalized radiation pattern in log scale. 102
Figure 84 : 1 slot curved in H plane (left) and E plane (right) for radius of 2cm in cylindrical convex way. 107
Figure 85 : 1 slot curved in convex (left) and concave (right) for radius of 4cm in H-plane. 107
Figure 86 : Directivity in dB of a curved slot in H-plane for convex (a) and concave (b) curvature. 108
Figure 87 : Variations of the maximal directivity D_{max} and the associated half power beamwidth (HPBW) with radius in convex and concave curvature. 108
Figure 88 Variations of the normalized maximal directivity d_{max} and the associated half power beamwidth (HPBW) with radius in convex curvature in both E- and H-planes. 109
Figure 89 : Normalized field radiation pattern (dB) in H-plane for a SF280 slot curved convexly (a) and concavely (b). 110
Figure 90 : Variations of the coefficients of the even Fourier's series depending on the radius and their quadratic approximations for the approximation of the normalized radiation pattern of 1 slot convexly curved in H plane. 111

Figure 91 : Variations of the coefficients of the even Fourier's series depending on the radius and their saturating exponential function approximations for the normalized radiation pattern of 1 slot convexly curved in H plane. 112
Figure 92 Comparison between simulated normalized radiation pattern of 1 slot convexly curved in H plane and its numerical approximation thanks to an even Fourier's series. 112
Figure 93 : Orientation of the coordinate system on a cylindrically curved SIWSA. 113
Figure 94 : Application of geometrical cosine theorem on 1×N arced array in convex and concave. 114
Figure 95 : Geometrical pattern of arced array in convex as in concave used for the demonstration. 114
Figure 96 : Tested 1×8 designs in flat configuration and curved in H-plane in convex and in concave. 117
Figure 97 : Variations of the maximal directivity and HPBW depending on the ratio R/λ_0 for curvature in H plane in convex and concave. 118
Figure 98 : Normalized directivity $d(R, \theta)$ in convex (a) and concave (b). 119
Figure 99 : Comparison between simulations and theoretical approach of the variation of the normalized maximal directivity d_{max} and HPBW depending on the radius for a 1×8 convexly curved SIWSA. 119
Figure 100 : Comparison between simulations and theoretical approach of the variation of the normalized maximal directivity d_{max} and HPBW depending on the radius for a 1×8 concavely curved SIWSA. 120
Figure 101 : Comparison between simulations and theoretical approach of the normalized radiation pattern for different radii of a 1×8 convexly curved SIWSA. 120
Figure 102 : Comparison between simulations and theoretical approach of the normalized radiation pattern for different radii of a 1×8 curved SIWSA in concave. 121
Figure 103 : Variations of the normalized maximal directivity and half-power beam width depending of the radius for different distances between the slots of a 1×8 array curved in H-plane. 122
Figure 104 : Variations of the maximal normalized directivity and half-power beam width depending of the radius for different tapering excitation of a 1×8 array curved in H-plane.. 123
Figure 105 : Variations of the maximal normalized directivity and half-power beam width depending of the radius individual slot's directivity of a 1×8 array curved in H-plane. 123
Figure 106 : Realized protypes of slotted SIW 4x8 array: SF280 at 15GHz, Ro5880 at 15GHz and SF280 at 10GHz from left to right on a squared grid of 0.5mm. 125
Figure 107 : Photo of the used anechoic chamber and the associated rotating mast. 126
Figure 108 : Some of the 3D printed resin pieces used for measurements. 126
Figure 109 : Example of fixed measured designs for convex curvatures in H-plane (a), E-plane (b) and concave curvature in H-plane (c). 127
Figure 110 : Opening of the normalized radiation pattern in dB for different ratio R/λ_0 in E plane (a) and H plane (b) in convex for the SF280_X design. 128
Figure 111 : Opening of the normalized radiation pattern in dB for different ratio R/λ_0 in E plane (a) and H plane (b) in convex and concave for the SF280_Ku design. 128

Figure 112 : Opening of the normalized radiation pattern in dB for different ratio R/λ_0 in E plane (a) and H plane (b) in convex and concave for the Ro5880_Ku design. 129
Figure 113 : Variations of the HPBW of the 3 designs for different radii of convex curvature in both planes..... 130
Figure 114 : Variations of the normalized maximal gain g_{max} of the 3 designs for different radii of convex curvature in both planes. 130
Figure 115 : Comparison of the normalized maximal gain g_{max} and associated HPBW for different ratios R/λ_0 between measures, simulations and theory for the SF280 design adapted in X band convexly curved in both planes E and H. 132
Figure 116 : Comparison of the normalized maximal gain g_{max} and associated HPBW for different ratios R/λ_0 between measures, simulations and theory for the SF280 design adapted in Ku band convexly curved in both planes E and H. 132
Figure 117 : Comparison of the normalized maximal gain g_{max} and associated HPBW for different ratios R/λ_0 between measures, simulations and theory for the Ro5880 design adapted in Ku band convexly curved in both planes E and H. 132
Figure 118 Design of the 1×8 curved slot array. 136
Figure 119 Comparison of the normalized field radiation pattern for 1 slot placed on the centre of the curved reflector plane (a) and the one's in the locale position of half the slots of the design. 137
Figure 120 Comparison of the normalized radiation patterns from the weighting obtained for the 3 tested sampling intervals. 138
Figure 121 Comparison of the normalized radiation patterns for the 5 best the weighting. .. 139
Figure 122 Normalized radiation pattern in log scale of the 1×8 curved simulated design and the 2 theoretical approaches. 140

Table 1 : summary on few articles close to the subject of flexible SIWSA 29
Table 2 : Physical characteristics of the 3 used dielectrics..... 61
Table 3 : Example of (x, l) couples obtained with this new method for an adaptation at 15GHz of a 1x10 SIWSA with RT/Duroid 5880 of 127µm..... 80
Table 4 : Matching range of couple (x, l) values for different slots configurations. 88
Table 5 : Values of the couples (x, l) for each section of the 2×8 SIWSA in TE20 obtained with python..... 90
Table 6 : Matching zone for the (x, l) couple for the 3 used designs with an external MC study. 97
Table 7 : Deduced couple (x, l) values for the design of a 1×8 array at 15 GHz with Ro5880 of 127µm..... 101
Table 8 : Measured RF characteristics of the 3 tested designs. 128
Table 9 : Distance between the radiating elements for the 3 designs relative to their wavelength of adaptation in both planes E and H. 129
Table 10 Obtained weighting and associated ripple for different sampling intervales. 137
Table 11 Obtained best weighting and associated ripples with consideration of local slot's radiation pattern..... 138

Table 12 Comparison between theoretical expected weighting and the flat and curved HFSS designs. 139

General introduction

The study and use of flexible antennas have grown significantly in recent years due to their wide range of potential applications. Indeed, the ability to deform may be temporary, allowing antennas to be mounted on clothing or directly on the skin with real-time shape adaptation, or continuous, as in the case of flexible antennas conformally integrated onto the structure of a vehicle, a mast, or a radome. In the defence sector, such designs are particularly attractive for achieving conformal arrays on vehicles and/or for widening the array radiation pattern across a broad range of frequency bands, depending on the specific application. Moreover, the detailed investigation of these flexible designs can be approached from two main perspectives: a technological one, focused on material properties (flexibility, durability, environmental resistance, and reproducibility), and an electromagnetic one, addressing the matching of conformal arrays and the impacts of the curvature on the radiation behaviour.

The work presented in this doctoral thesis aims to create medium-sized slot arrays on flexible Substrate Integrated Waveguides (SIW) in the X and Ku bands. More specifically, the work focuses on the matching theory for these designs, where the coupling between radiating elements is very strong, as well as on anticipating the opening of the array's radiation pattern for radii of curvature of the order of the wavelength.

The first chapter begins by introducing the definitions of electromagnetic quantities and parameters. These are subsequently used for a concise presentation of the theory of both single-element and array antennas. This foundation then allows for the introduction of the concept of conformal antennas, their advantages and disadvantages and the associated theory, which differs from that of conventional planar arrays. Then, a brief overview of various slot antenna arrays, based on either Rectangular Waveguide (RWG) or Substrate Integrated Waveguide (SIW), is provided. Finally, in view of the operating conformations specified by the company, the motivation for using a flexible SIW array is discussed, alongside a state-of-the-art review of this technology.

The second chapter addresses a direct improvement and correction of the most conventional theoretical method for properly designing a medium-sized slot array while accounting for mutual coupling effects between slots. To achieve this, an initial investigation into the mathematical formulation of individual slot behaviour is conducted. A method for correcting the theoretical design parameters of a slot array through automated communication between Python and HFSS is then presented. These two preceding developments subsequently lead to a comprehensive automated design algorithm for such arrays given a specified set of RF parameters. This work is demonstrated through the realization of several prototypes operating in the X- and Ku-bands.

The third chapter presents a new matching procedure for slot antenna arrays that is specifically suited to very thin waveguides (thus enabling flexibility). Both the theoretical framework and algorithmic aspects of the procedure are first described and validated through

the realization of a prototype. The procedure is then applied to other case studies, encompassing both directly realizable implementations and theoretical extensions.

The fourth and final chapter focuses on the analysis of radiation pattern variations in the flexible slot array for curvature radii on the order of the wavelength. This study highlights the need to adapt classical circular array theory to our specific configuration, as well as the influence of several conventional array parameters on the resulting radiation pattern. Finally, with the aim of tailoring the radiation pattern of the arc-shaped array while maintaining the slots in phase, a concise investigation is presented on the use of a novel algorithmic procedure that provides the required amplitude weighting to achieve the desired radiation pattern.

Chapter 1 - context and state of the art

1.1 Introduction

The field of the defence has historically driven innovations in communication and radar antenna technologies, many of which have subsequently found applications in the civilian domain. Since the Second World War, one major line of research has focused on the development of conformal antenna arrays. These were initially conceived with the objective of designing radiating elements that conform to the surface of the supporting structure. The primary motivation was to minimize aerodynamic drag and, at the same time, potentially modify or widen the radiation pattern of the antenna.

The present study focuses on the design of conformal antennas and arrays by means of flexible planar solutions, with a particular emphasis on slot-based Substrate Integrated Waveguide (SIW) structures that can accommodate curvature. This chapter is therefore dedicated to substantiating the necessity of the investigations presented in the following sections. It introduces the underlying topology, the theoretical framework and the state of the art, while also highlighting both practical and theoretical limitations in existing approaches, thereby motivating the research undertaken in this work.

To this end, we first provide a brief overview of fundamental concepts in electromagnetic wave propagation. The characteristics of the antenna, followed by the mathematical modelling of its array integration, are then discussed. This is completed by a survey of conformal arrays and their associated body of literature. Subsequently, the theory of slot antenna arrays, selected here as the radiating element for our study, is presented. Then, the choice of employing flexible slot antenna arrays is justified and a review of relevant literature directly related to our research focus is proposed. Finally, several theoretical limitations concerning the matching of slot-based network designs on flexible SIW structures and the anticipation of their radiation patterns under bending conditions are examined.

1.2 Radiating elements and associated physical quantities

Antenna theory is rooted in the broader field of electromagnetism, which concerns the study of phenomena related to the electric field **E** in V/m and the magnetic field **H** in A/m, along with their interactions with matter and electromagnetic waves, as described by Maxwell's Theory published in 1865. Such waves arise from the superposition of time-varying electric and magnetic fields and are typically described by two fundamental parameters: the wavelength λ in meter, which represents the spatial distance between two successive wavefronts at a given moment, and the period T in second, which corresponds to the temporal interval separating two successive wavefronts at a fixed location. These quantities are intrinsically linked through the fundamental relation $c = \lambda/T$, where c denotes the wave propagation velocity in the medium considered ($c_0 = 3\times10^8$ m/s in free space). From this relationship, one can define the frequency $f = 1/T$, expressed in hertz (Hz), which describes the number of oscillations per second, as well as the angular frequency $\omega = 2\pi f = 2\pi/T$, expressed in rad/s. This quantity reflects the angular

rate of variation of the wave and may be interpreted as the number of radians spanned by the signal in one second. By analogy, we define the wave number $k = 2\pi/\lambda$ characterized as the spatial frequency of a wave, indicating the number of oscillations per unit distance.

The radiofrequency spectrum spans from 3 kHz to 300 GHz, with each band associated with specific applications and corresponding antenna types. In the context of this thesis, the focus will be on the Super High Frequency (SHF) band, covering 3 to 30 GHz, with particular emphasis on the X band (8–12 GHz) and Ku band (12–18 GHz), which are widely used for communication systems and radar applications.

The first theoretical contributions to the understanding of electromagnetic wave propagation and generation date back to Hertz's experiments published in 1888, which demonstrated their existence and reflection in the air. A few years later, at the end of the 19th century, Guglielmo Marconi highlighted their potential for wireless communication. However, the technological limitations of the period, notably the power and frequency constraints of oscillators, hindered practical applications. It was not until the 1930s that engineering research made significant progress in both theory and practice, focusing on the study and design of new antennas. During World War II, the rapid development of RADAR technologies (radio detection and ranging) strongly stimulated antenna theory, especially in the field of directional radiation and the introduction of antenna arrays. Today, the wide variety of radiating structures and broad frequency coverage meet to diverse and complex needs. These advances were made possible thanks to numerical simulators based on approximate solutions to Maxwell's equations, enabling computer-aided antenna design.

When an electric charge is accelerated, it produces radiation commonly referred to as an electromagnetic wave. Consequently, a time-varying current can generate such radiation. This physical principle is exploited in antenna theory, which essentially aims to convert an electrical signal into an electromagnetic wave, or vice versa. This process relies on solving Maxwell’s equations, which describe the behaviour of electromagnetic fields and their sources, namely charges and currents. Obtaining the mathematical expressions for the radiated electric (**E**) and magnetic (**H**) fields in free space involves summing the electromagnetic contributions from all local current distributions responsible for the antenna's overall radiation. Although analytical methods exist, the main challenge is to accurately determine the current distribution across the entire antenna structure. Therefore, numerical modelling techniques and software tools are commonly employed today to address these problems.

It is important to note that the electromagnetic field emitted by an antenna is structured into three distinct regions defined by distances from the source as illustrated in Figure 1. The reactive near-field region (or Rayleigh zone), immediately adjacent to the antenna, is dominated by stored reactive fields. Beyond this lies the Fresnel region (or radiating near-field), where the fields begin to form and radiate, and where the angular distribution depends on distance. Finally, the Fraunhofer region (or far-field) corresponds to the area where the radiation pattern stabilizes and becomes independent of distance. It is exclusively in this far-field zone that the wave can be considered planar, and where characteristic antenna measurements such as gain and radiation

patterns are valid. For antennas or antennas arrays whose largest dimension L is greater than or equal to the wavelength, the far-field condition is typically defined by $R >> 2.L^2/\lambda_0$.

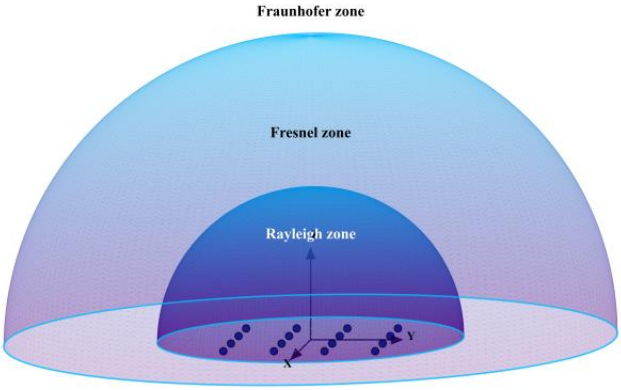

Figure 1 : Schematic representation of radiation zones.

Usually, the spherical coordinate system (r,θ,φ) is used for the general problem on this subject. In the far-field region, the expressions for the electric and magnetic fields indicate that they are mutually perpendicular, in phase, and lie in a plane perpendicular to the radial direction **R** toward the observation point as presented in Figure 2.

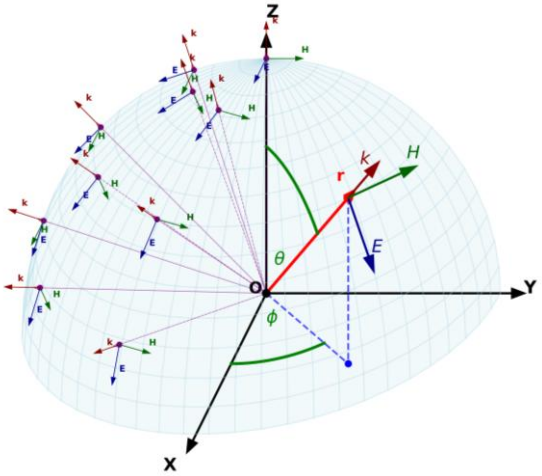

Figure 2 : Far field radiation vectors in spherical coordinate system.

Furthermore, their amplitudes decrease proportionally to 1/r, where r is the distance between the observation point and the antenna. Finally, the ratio Z of the field magnitudes is real and constant:

$$Z = \frac{E}{H} = \eta \tag{1.1}$$

The wave impedance η measured in ohm (Ω) depends on the propagation medium. With the characteristic values in free space, η is given by $\eta_0 = 120\pi$. In addition to the radiated electric and magnetic fields, three other physical quantities are often introduced: the Poynting vector **S**, the radiation intensity U, and the radiated power P_r. In far-field, they can be written as:

$$\boldsymbol{S}(\theta,\varphi) = \frac{1}{2}\boldsymbol{E} \wedge \boldsymbol{H}* \xrightarrow{\textbf{\textit{Far field}}} \frac{1|E|^2}{2\eta}\mathbf{R} = \frac{1}{2}\eta|H|^2\mathbf{R} \tag{1.2}$$

$$U(\theta,\varphi) = Re(\boldsymbol{S})r^2 \circ \boldsymbol{R} \tag{1.3}$$

$$P_r = \oiint U(\theta,\varphi)d\Omega \tag{1.4}$$

$d\Omega = \sin\theta d\theta d\varphi$ corresponds to the solid angle. Different points must be noted:

- the Poynting vector represents the power density flow of the wave by unit of surface expressed in watts per square meter (W/m^2). In the far-field region, it is purely real, decreases proportionally to $1/r^2$, and is directed radially outward, perpendicular to the electromagnetic fields,
- the radiation intensity U quantified in watt by steradians (W/sr) is the power radiated in a given direction per unit of solid angle. It is independent of the distance r,
- the total radiated power P_r in watt (W) from the source is obtained by integrating the radiation intensity U over all angles around the antenna.

1.3 Antenna characteristics

The concepts introduced above are physical quantities that can be studied across several areas of electromagnetics. Within the framework of antenna theory, however, a specific set of parameters must be considered. They may be classified into three categories: input (or matching) parameters of circuit type at the antenna terminals, output parameters related to electromagnetic quantities, and intermediate parameters that link the received fields to circuit-type quantities at the terminals. Given the wide range of parameters used in antenna analysis, we will limit our attention to those that will be applied in the following sections. Intermediate parameters such as the effective aperture or the effective length are not described here. For the upcoming definitions, it is essential to distinguish between three different powers represented in Figure 3:

- the radiated power of the antenna, P_{rad},
- the input power accepted by the antenna at its terminals after impedance matching, P_{in},
- the power delivered by the source, P_0.

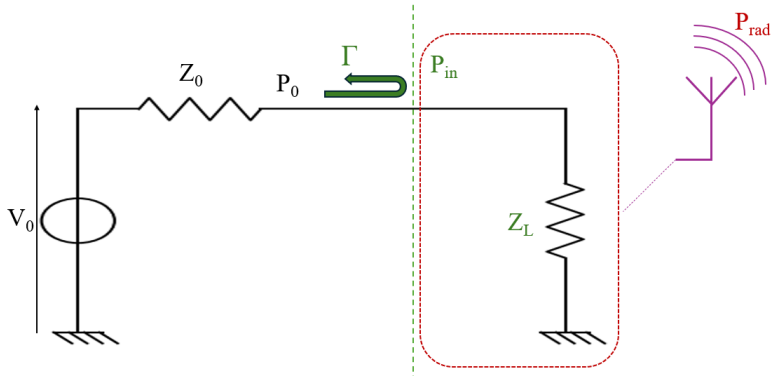

Figure 3 : Circuit representation of the antenna and the source.

1.3.1 Input parameters

- Input impedance Z_{in}

When designing an antenna, a key parameter is the input impedance Z_{in} which varies with frequency. The impedance of an antenna is a complex electrical quantity that characterizes how the antenna "appears" to the connected circuit, relating the voltage and current at the feed point. It is expressed in ohms (Ω) as Z = R+jX. The real part (resistive R) includes the radiation resistance, *i.e. the power actually radiated as electromagnetic wave*, and the ohmic losses due to the dissipation in the antenna materials. The imaginary part (reactive X) reflects the antenna's capacitive or inductive behaviour, i.e., its ability to store energy in the near field. To ensure maximum power transfer between the transmitter and the antenna, the antenna impedance must be matched to that of the transmission line and the source, whose characteristic impedance is commonly denoted Z_0.

- Reflection coefficient Γ

Associated with this impedance is the complex reflection coefficient Γ (also referred to as the S_{11} parameter), which represents the ratio of voltage between the backward and forward waves. It can be expressed as the ratio of the difference and the sum of the antenna input impedance Z_{in} and the characteristic impedance Z_0.

$$\Gamma = \frac{Z_{in} - Z_0}{Z_{in} + Z_0} \tag{1.5}$$

$$\Gamma(dB) = 20log_{10}(|\Gamma|) \tag{1.6}$$

- Bandwidth

The bandwidth characterizes the range of frequencies over which the reflection coefficient remains below a given value, thus enabling the use of the antenna. In the case of a narrowband antenna, as in our study, the relative bandwidth is defined as follows:

$$BW(\%) = \frac{f_2 - f_1}{f_0} \tag{1.7}$$

where f_1 and f_2 are typically taken at the −10 dB threshold as presented in Figure 4.

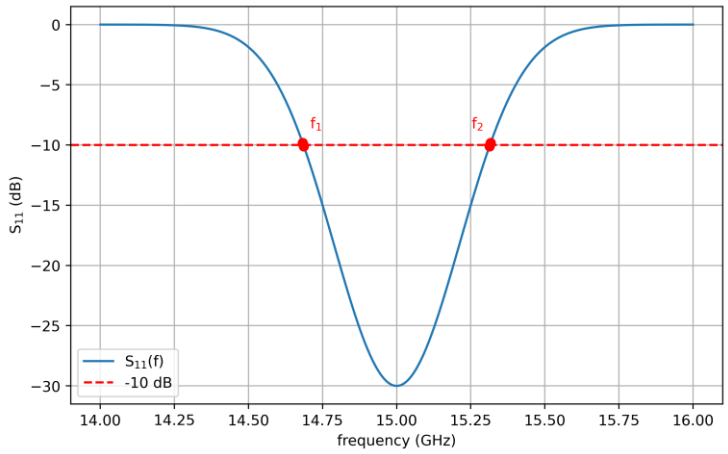

Figure 4 : Illustration of reflection coefficient and associated bandwidth.

The frequency-dependent matching of the antenna is measured using a Vector Network Analyzer (VNA). This instrument provides several specific quantities, such as the reflection coefficient $S_{11}(f)$, along with the associated bandwidth.

1.3.2 External parameters

- **Radiation pattern and radiation intensity**

The radiation pattern is among the most commonly used external parameters. It represents the field or power density radiated by an antenna at a fixed distance (in the far-field region) as a function of the observation angles (θ, φ), with the antenna located at the origin of the coordinate system. This representation is always normalized (typically to its maximum value) and therefore independent of distance. In practice, one considers the normalized magnitude of the electric field **E** (the magnetic field **H** could also be used, since in the far-field, the two are proportional and normalization leads to the same function). This gives the polar radiation pattern:

$$A(\theta,\varphi) = \frac{\left|\left|\boldsymbol{E}(r_0,\theta,\varphi)\right|\right|}{\left|\left|\boldsymbol{E}(r_0,\theta,\varphi)\right|\right|_{ref}} \tag{1.8}$$

Since the power density is proportional to the square of the magnitude of the far-field components, the radiation pattern can also be expressed in normalized form as:

$$P(\theta,\varphi) = A^2(\theta,\varphi) \tag{1.9}$$

The radiation intensity U and the average radiated power can then be expressed as:

$$U(\theta,\varphi) = \boldsymbol{Sr^2}.\boldsymbol{n} = \boldsymbol{U_{max}A^2(\theta,\varphi)} = \boldsymbol{U_{max}P(\theta,\varphi)} \tag{1.10}$$

$$P_r = \oiint_{\Omega} \boldsymbol{U}(\theta,\varphi)\cdot\boldsymbol{d\Omega} = U_{max}\oiint_{\Omega}\boldsymbol{A^2}(\theta,\varphi)\cdot\boldsymbol{d\Omega} = U_{max}\oiint_{\Omega}\boldsymbol{P}(\theta,\varphi)\cdot d\Omega \tag{1.11}$$

In many applications, the radiation of an antenna is of interest only in specific planes, where either the elevation angle θ or the azimuth angle φ varies. The Figure 5 illustrates the

radiation pattern A(θ) of a generic antenna for a given φ, shown in both Cartesian and Polar representations on a linear scale.

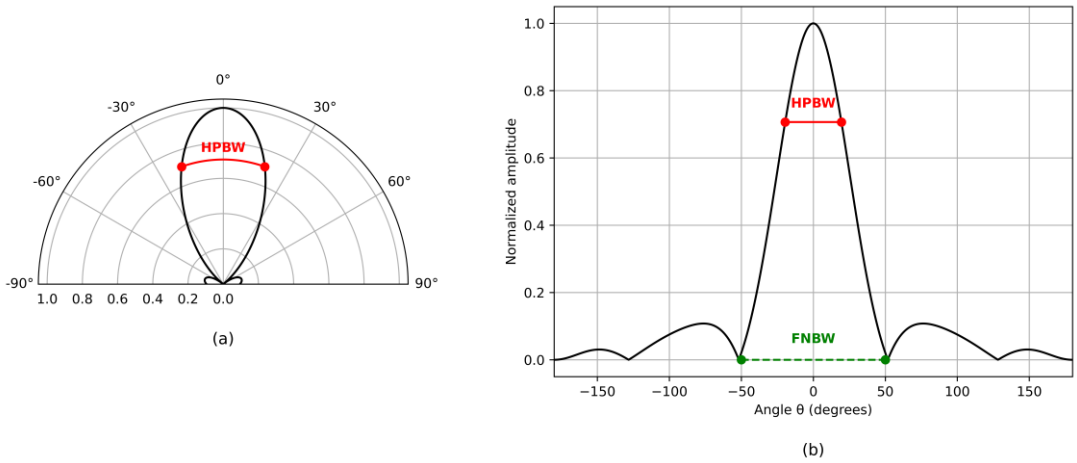

Figure 5 : Radiation pattern in Polar and Cartesian representations (linear scale).

- **Half power beamwidth**

From this radiation pattern, various characteristic points can be determined, such as the side-lobe levels. The half-power beamwidth (HPBW) is defined as the angular width between the points where the radiation power drops to 0.5 in linear scale (–3 dB in log scale), and the first null beamwidth (FNBW) corresponding to the angular separation of the first zero amplitude values.

- **Directivity**

The directivity D(θ,φ) (dimensionless) expresses the antenna's ability to concentrate its radiated power in a given direction. It is defined as the ratio between the radiation intensity U(θ,φ) in the direction (θ,φ) and the theoretical average radiation intensity U_{avg} of an isotropic antenna (omnidirectional antenna):

$$U_{moy} = \frac{P_r}{4\pi} \tag{1.12}$$

$$D(\theta,\varphi) = \frac{U(\theta,\varphi)}{U_{moy}} = \frac{4\pi A^2(\theta,\varphi)}{\Omega_A} \tag{1.13}$$

With Ω_A representing the beam solid angle, in practice the term directivity usually refers to the maximum directivity. It can then be expressed as:

$$D = \frac{4\pi}{\Omega_A} \tag{1.14}$$

Here, Ω_A is considered as the solid angle of an equivalent antenna that uniformly concentrates its radiated power within a cone of opening Ω_A with constant intensity U_{max}. The maximum directivity D_{max} is thus the ratio of two solid angles: that of the total sphere (4π) to that of the antenna beam (Ω_A). It should be noted that the directivity does not depend on the antenna matching. It reflects the antenna's ability to concentrate the power it radiates.

- **Gain and Efficiency**

Another important parameter is the antenna gain for a given couple of angle (θ,φ) G(θ,φ), which reflects the directive capabilities of the antenna relatively to the power supplied at its terminals, P_{in}. The gain therefore accounts for conduction losses and/or dielectric or magnetic losses in certain substrates. This leads to the introduction of the power efficiency, often referred to as the antenna efficiency.

$$G(\theta,\varphi) = \frac{U(\theta,\varphi)}{P_{in}/4\pi} \tag{1.15}$$

$$e = \frac{P_r}{P_{in}} = \frac{G}{D} \tag{1.16}$$

Another parameter is the realized gain G_{re}. This accounts for the antenna's matching to the transmission/reception system through the reflection coefficient.

$$G_{re} = (1 - |\Gamma|^2).G \tag{1.17}$$

This gain, measured in an anechoic chamber, can therefore be related to the directivity by:

$$G_{re} = (1 - |\Gamma|^2).e.D \tag{1.18}$$

- **Polarization**

The final external parameter necessary for the continuation of our study is the polarization. The polarization of an antenna is defined by the type of polarization of the wave it radiates in a given direction in the far field (often referring to the electric field vector **E** along the main axis). Linear polarization occurs when the vector **E** remains in a fixed plane, circular polarization occurs when **E** traces a circle in a plane perpendicular to the direction of propagation, and elliptical polarization occurs when **E** traces an ellipse. Circular and linear polarizations are in fact special cases of elliptical polarization (a flattened ellipse for linear, and a circle for circular). More parameters and theory can be found in reference books on the subject such as [1],[2].

1.4 Linear and planar array antenna

The networking of radiating elements has two main objectives, which may be used simultaneously or independently depending on the study case:

- The improvement of the gain of low-directivity antennas,
- The control of the main lobe direction by adjusting the excitation phase of the elements (widely employed in electronically scanned radar systems).

In this work, linear arrays defined by a constant spacing between elements are considered, with all elements oriented with the same polarization. These elements can be arranged along a single line (1×N array) to enhance directivity in the alignment plane or

distributed over M lines of N elements (M×N array), thereby improving directivity in both planes.

A distinction is made between broadside arrays and end-fire arrays, whose purposes are respectively to produce a main lobe in the plane perpendicular to the array or in the axial plane of the array. The following theoretical discussion of linear arrays is conducted under the assumption of radial radiation (although the approach remains valid for axial radiation).

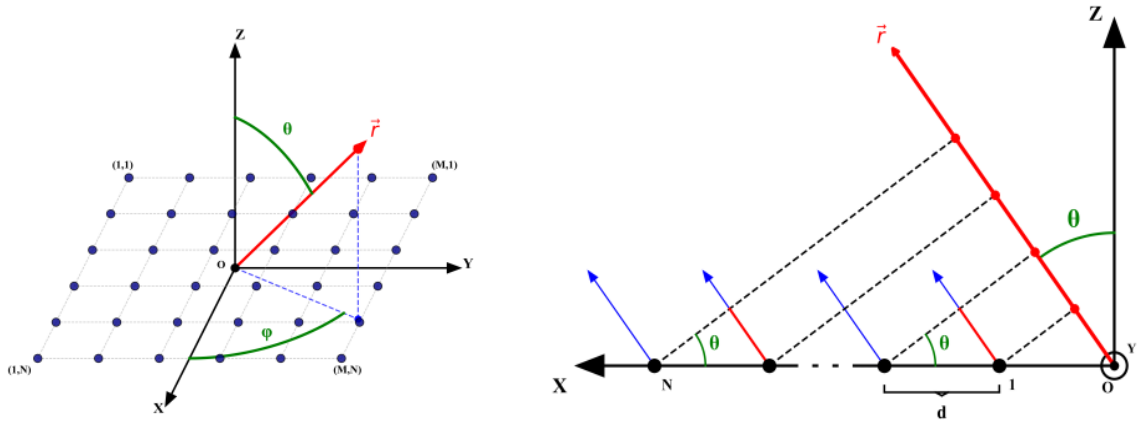

Figure 6 : Schematic of a M×N and 1×N array with constant spacing between elements.

As illustrated in Figure 6, we consider an alignment of N equidistant radiating sources (1×N line), each characterized by its radiation pattern $A_n(\theta,\varphi)$, and excited by a current $I_n e^{j\alpha n}$,where I_n denotes the current amplitude and α_n the phase shift between 2 consecutive elements. In far field, the pointing angle from each element toward the observation point is identical. Consequently, a path difference of d.sinθ is observed, leading to a phase delay of k.d.sinθ + α between elements. Thus, in a given plane, the expression can be written as:

$$A(\theta,\varphi) = \sum_n I_n e^{j.n.\alpha} A_n(\theta,\varphi) e^{j.n.kdsin(\theta)} \qquad (1.19)$$

In the case where all equidistant radiating elements are aligned along a given angle φ (often 0° or 90°) and share the same radiation pattern $A_0(\theta,\varphi)$ with identical polarization, one can write:

$$A(\theta,\varphi) = A_0(\theta,\varphi) \sum_n I_n . e^{j.n.(kdsin(\theta)+\alpha)} = A_0(\theta,\varphi).AF \qquad (1.20)$$

The array factor (AF) solely depends on the phase shift between elements, the weighting applied to each element and the spacing between elements relative to the wavelength d/λ_0. Orienting the main lobe at θ_0 amounts to cancelling the exponential term at this angle, which requires a phase shift between elements of:

$$\alpha = -k.d.sin\theta \qquad (1.21)$$

For a uniform distribution, the resulting array factor corresponds to a sinc function. Since the level of side lobes may sometimes be problematic, different weighting schemes are applied to achieve a trade-off between main lobe beamwidth and side lobe level. The most used weightings are Chebyshev for small arrays and Taylor for larger ones.

It must be noted that for given linear array's characteristics (d, weighting, phase shift), the AF depends only on θ and therefore has no influence on the radiation pattern in the plane perpendicular to the array alignment. Arraying in a single plane improves only directivity within that plane. When improvement is required in both planes, an M×N array is employed, with an adaptation of the radiation function:

$$A(\theta,\varphi) = A_0(\theta,\varphi)\sum_m\sum_n I_{mn}.\, e^{j.m.(kd_x.sin(\theta).cos(\varphi)+\alpha_m)} e^{j.n.(kd_y.sin(\theta).sin(\varphi)+\alpha_n)} = A_0(\theta,\varphi).AF(\theta,\varphi) \quad (1.22)$$

In general, discussions on network factors, weighting, or beam steering can be found in standard reference books on the subject, such as [1], [2], [3].

Furthermore, achieving impedance matching and radiation control in an array requires a thorough consideration of mutual coupling (MC). This phenomenon arises from electromagnetic interactions in the near and intermediate fields between radiating elements. According to the IEEE standard definition [4], mutual coupling has 2 major impacts: it alters the radiation pattern by modifying the actual excitation of each element, and it shifts the input impedance of an individual element when the rest of the array is active, compared to when it is isolated. This phenomenon is extensively studied in the literature and can be found in several reference textbooks, such as previously cited [1], [2], [3].

1.5 Conformal array antenna

1.5.1 Definition and overview

Following the IEEE Standard Definition of Terms for Antennas (IEEE Std 145-1993 [4]), a conformal antenna or array conforms to a surface whose shape is determined by considerations other than electromagnetic ones; for example, aerodynamic or hydrodynamic requirements. From an aerodynamic perspective, the resulting antennas and arrays are often arced, cylindrical, conical, or take on other shapes.

Nevertheless, this definition is often broadened in the literature by considering that non-planar antenna arrays whose primary purpose is to widen the beam coverage (thus for electromagnetic requirements) may also be referred to as conformal antennas. In this sense, in addition to ground-based surveillance radar conformal arrays, circular arrays (often referred to as ring arrays), although implemented in a 2D plane, are also considered as conformal arrays, with their main objective being a full 360° azimuth coverage. Examples are given in Figure 7.



Figure 7 : Conformal canonical Array Antenna for data transmission for LEO satellite of ESA, faceted active array antenna with six dual polarized dipole elements in each facet (Courtesy of Roke Manor Research Ltd., Roke Manor, Romsey, Hampshire, UK.)

As highlighted in the standard reference on the subject by Josefsson and Persson [5], the main objectives of conformal antennas can therefore be summarized as:

- Reducing aerodynamic drag by conforming to the shape of the hosting platform,
- Enabling better system integration, thereby allowing for an increased number and size of arrays within a given surface area,
- Broadening the antenna radiation pattern and steering the main lobe(s) within planes up to 360°,
- Stealth properties, i.e., minimizing the radar cross-section (RCS) of the communication systems of the platform against hostile radar illumination.

A clear representation of the widespread use of conformal antennas is illustrated in Figure 8, showing the large number of such arrays placed on an aircraft structure. The most significant conformations are found in the aircraft nose or tail, whereas the local curvature on the fuselage itself remains minor.

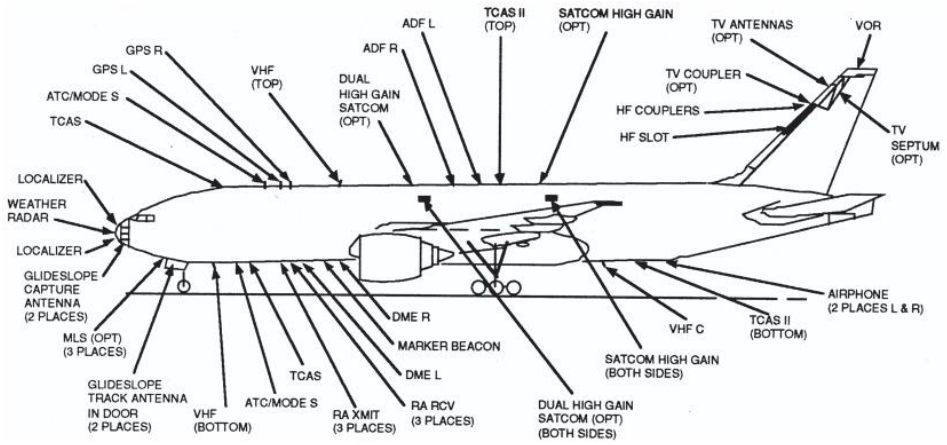

Figure 8 : Several antennas integrated into the aircraft structure, serving different functions, figure from [6], © 2006 IEEE.

Originally developed for military purposes, this technology has subsequently found applications in the civilian domain for various purposes like communications [7], internet of things and health [8].

According to the chapter *"Conformal and Low-Profile Arrays"* [9], conformal arrays can be classified into two categories, each with distinct objectives, designs, and technological challenges:

1. The maximum size of the array L is comparable to the local radius of curvature of the conformal body (Figure 9a), i.e., $L \approx R_1$.
2. The maximum size of the array L is small with respect to the local radius of curvature of the conformal body (Figure 9b), i.e., $L \ll R_2$.

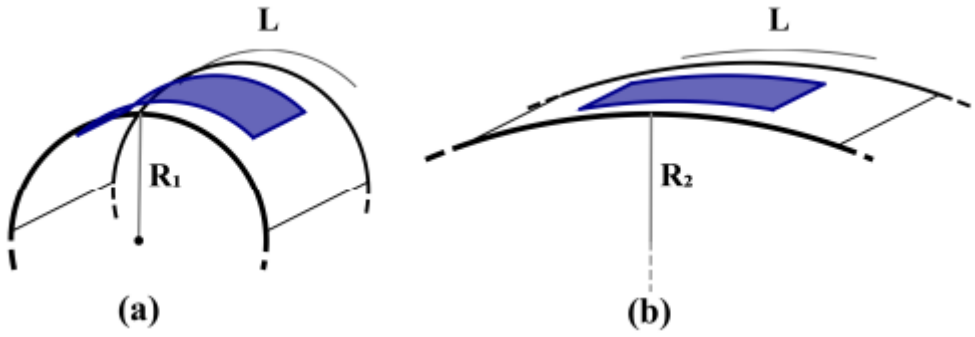

Figure 9 : Conformal arrays with (a) radius of curvature of the order of the dimension of the array (b) and with radius of curvature much larger than the dimensions of the array.

Naturally, the first case involves the most significant difficulties, both in terms of electromagnetic theory and in terms of implementation and mounting. Some of these challenges are highlighted in [10], which focuses mainly on antenna theory issues. Among them:

- The radiating elements are not all oriented in the same direction. From a practical standpoint, this requires individual control of the excitation of each element for proper optimization. From a theoretical perspective, the concept of an array factor is no longer applicable to the total radiation pattern function, as it was for 2D linear arrays.

- As a result, the analysis of the array function becomes much more complex, both in its general form and with respect to beam steering requirements or side lobe level constraints.
- Cross-polarization may differ between elements.
- Mutual coupling between elements, as well as diffraction effects at each element, are far more complex to predict due to the geometric shape of the array, which is sometimes non-uniform between elements (e.g., conical structures).

In addition to these theoretical aspects, further difficulties arise in the physical realization of such arrays, including the feeding of the individual elements.

1.5.2 Ring array theory

A good way to illustrate the impossibility of applying the array factor mathematical concept to conformal arrays is through the example of the ring array.

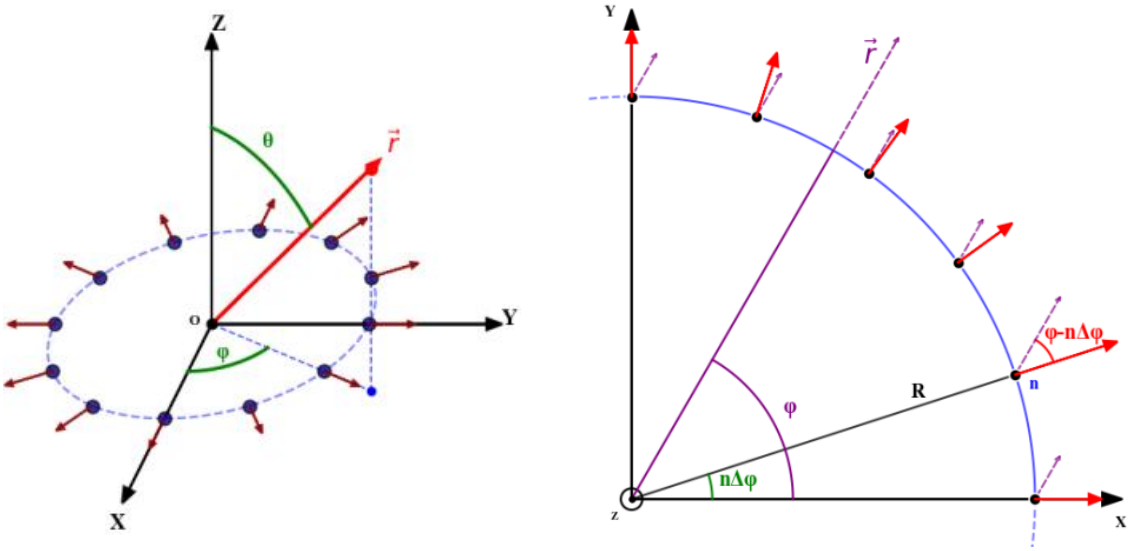

Figure 10 : Geometry for ring array.

In this framework of study as shown in Figure 10, it is assumed that all radiating elements, uniformly placed every Δφ, share the same radiation pattern and are excited by a current $I_n e^{j.\alpha_n}$. It can be observed that the problem in spherical coordinates (R, θ, φ) can be simplified to a circular problem with φ as the variable and θ = π/2 thanks to the geometry of the problem. Furthermore, each element individually points toward an angle φ – nΔφ, with a phase delay of k.R.cos(φ-nΔφ). Hence, we can write:

$$A(\varphi) = \sum_n I_n e^{j.\alpha_n} A_n(\varphi - n\Delta\varphi) e^{j.k.R.cos(\varphi - n\Delta\varphi)} \qquad (1.23)$$

The unit radiation pattern $A_n(\varphi)$ cannot be factored out of the sum to define an array factor unless A_n is uniform in the azimuthal plane (invariant with respect to φ) like theoretical isotropic source or vertical dipole antenna.

It should be noted that this geometrical exercise on ring arrays' radiation pattern can also be applied to curved arrays with elements forming an arc or a circle on the holding structure, although the complexity increases due to diffraction issues of the radiation pattern for each element on the curved surface.

Obtaining an analytical expression for the radiation pattern is thus challenging for specific conformations, and an analytical study is often not feasible. Numerical studies are therefore required to observe the impact of certain parameters, such as element weighting or phase shift, on the resulting radiation pattern. Moreover, the use of simulation software such as CST or HFSS is necessary to obtain valid results. An excellent reference on the study of conformal arrays on various types of supports, as well as the numerical methods associated with their analysis, is a book previously introduced in [5] : *Conformal Array Antenna: Theory and Design*.

1.6 Slotted array antenna

1.6.1 Choice of slotted array antenna

Within the aeronautical domain, onboard electronic systems are required to ensure high electromagnetic performance while simultaneously addressing a set of engineering constraints. These include manufacturing complexity and large-scale reproducibility, ease of integration within the overall system, cost-effectiveness, as well as long-term reliability and aging considerations. Moreover, in the specific case of conformal antenna array requirements, the design must exhibit a low-profile structure and conforms as closely as possible to the intended surface geometry.

Knowing that we want to work in Ku band, waveguide slot arrays represent a natural choice, offering high power handling without risk of electrical breakdown or excessive heating, very low loss at millimetre-wave frequencies leading to superior efficiency and gain, simple implementation for 2D radar apertures compared to reflector-based systems, seamless integration with RF front-ends already employing waveguide components, as well as a low-profile and conformal geometry with the possibility of electronic beam steering through parallel feeding lines. Moreover, these arrays can be covered with a dielectric film, which provides environmental, thermal protection and mechanical robustness without significantly degrading their electromagnetic performance. However, these advantages come at the expense of a relatively narrow operational bandwidth, a greater theoretical sizing difficulty and a fabrication process that is more costly and complex than for arrays such as patches or dipoles.

In the context of antenna engineering, slot waveguide arrays have predominantly employed rectangular waveguides (RWG), a technology that has been in use since World War II, while the concept of substrate integrated waveguides (SIW) has emerged over the past two decades as a planar and more easily integrable alternative. Photos of these both technologies are given in Figure 11. The directions of the **E** and **H** vectors relative to the design are added. Thus, the E-plane corresponds to the field perpendicular to the lines, and the H-plane corresponds to the field parallel to the line.

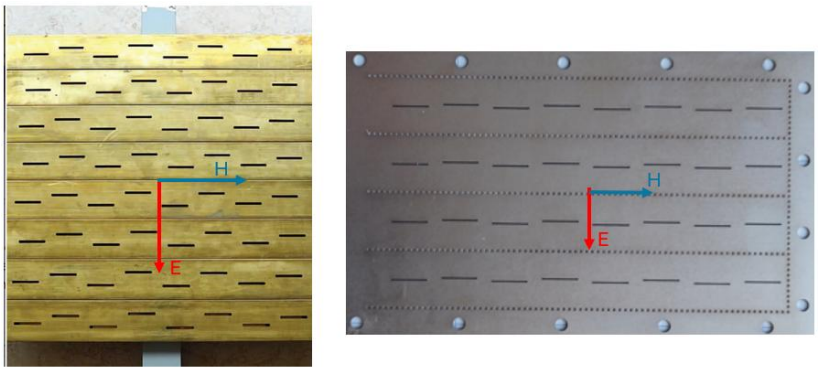

*Figure 11 : Photographs of (a) a RWG linear slotted array[11], CC-BY, and (b) SIW linear slotted array with schematic vectors of **E** and **H** fields .*

To fully understand these arrays, one must first master the fundamental concepts of waveguides, then understand the individual behaviour of a slot, before delving into the adaptation theory of these arrays

1.6.2 Rectangular waveguide and substrate integrated waveguide

A rectangular waveguide (Figure 12.a) is a metallic waveguide with a rectangular cross-section of size (a, b) used to guide electromagnetic waves. Unlike coaxial lines, it cannot support the propagation of the TEM mode, but only transverse electric (TE) or transverse magnetic (TM) modes. It exhibits several advantages, such as very low transmission losses, high power handling capability, and high efficiency in the microwave and millimetre-wave frequency ranges. However, its drawbacks include bulkiness, relatively high weight, and in some cases higher manufacturing cost for large-scale production. In this work, the TE_{m0} modes are considered, corresponding to propagation modes where the electric field remains transverse to the propagation direction, with *m* denoting the number of half-wavelength variations in that plane. The complete electromagnetic demonstrations related to this topic can be found in [13]. For the sake of clarity, we provide here the simplified formulas that will be subsequently employed:

$$\beta_{m0} = \sqrt{k^2 - k_c^2} = \sqrt{k^2 - \left(\frac{m\pi}{a}\right)^2} \tag{1.24}$$

$$\lambda_g = {}^{2\pi}/_{\beta} \tag{1.25}$$

$$f_{cm0} = \frac{k_c}{2\pi\sqrt{\mu\varepsilon}} = \frac{m}{2a\sqrt{\mu\varepsilon}} \tag{1.26}$$

with β as the propagation constant in rad/m, λ_g the guided wavelength in meter, and f_c the cutoff frequency in hertz. Usually, the mode TE_{10} is used for the rectangular waveguide slotted array (RWGSA).

In order to overcome the drawback of bulky rectangular waveguides, a possible solution is to implement slotted waveguide antennas using Substrate-Integrated Waveguide technology

(Figure 12.b). Over the past 25 years, SIW has emerged as a promising alternative, combining several advantages of traditional waveguides with the benefits of planar fabrication processes, including reduced manufacturing cost, ease of integration, thus providing a trade-off between the low-cost and easy integration of microstrip lines and the high electrical performances of conventional rectangular waveguides [14]. Furthermore, SIW structures can be realized on flexible dielectrics with thin conductors, which makes them well-suited for flexible and conformal applications. Its geometrical design is given in Figure 12 with a_{siw} the width of the waveguide, corresponding to the distance between 2 ranges of vias of diameter d and periodically duplicated in z direction with a period p.

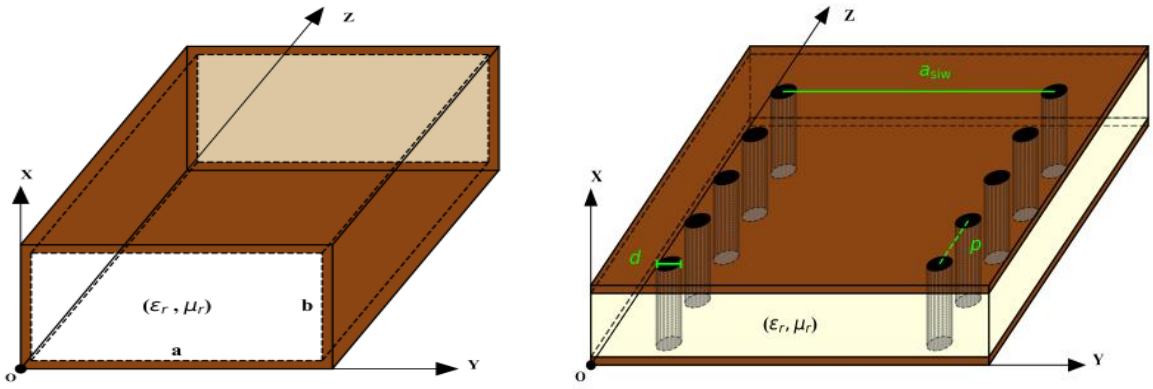

(a) (b)

Figure 12 : Geometry of rectangular waveguide (left) and substrate integrated waveguide (right).

A theoretical electromagnetic study of this type of waveguide can be found in [15]. One of the electromagnetic advantages of SIW is that, provided certain design rules are satisfied, it can be analysed by referring to its equivalent rectangular waveguide (RWG). Several studies have established methods to determine the equivalent width of an RWG that exhibits the same propagation behaviour as the SIW under appropriate design constraints. The most commonly used formula was proposed in [16] :

$$a_{rwg} = a - \frac{d^2}{0.95p} \tag{1.27}$$

with :

$$p > d \tag{1.28}$$

$$0.05 < {}^{p}/_{\lambda_c} < 0.25 \tag{1.29}$$

More complex formulations can be found in the literature, such as in [17] and [18]. In our case study in the X- and Ku-bands, electromagnetic simulations show negligible differences between the designs obtained using the equivalent widths derived from (1.27). Consequently, we restrict our analysis to this simplest expression.

The feeding of M×N rectangular waveguides with slots array (RWGSA) is relatively complex, as the main objective is to excite the TE10 mode within the waveguide. Several approaches exist like feeding from the end of the waveguide, which can be done via another RWG with a 1×M power divider; or using an underlying coaxial probe positioned at a height

allowing to excite the TE10 mode [19]; for SIW implementations, feeding can also be achieved through a microstrip line with a tapered transition into the SIW [20]. Another option is to feed the array from beneath using another slotted waveguide [11], either at its centre or off-centre, depending on the study case.

For the present study, the microstrip feeding line with a tapered transition into the SIW is adopted (Figure 13). The array model is therefore end-fed. For a given dielectric, the microstrip line dimensions can be determined following [13], while the design of the tapered transition can be based on [20].

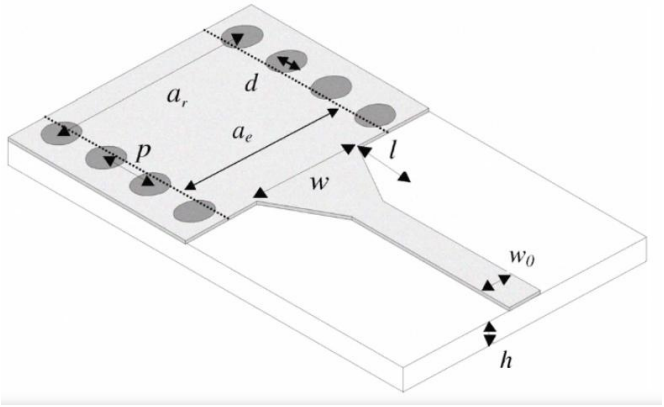

Figure 13 : Schematic transition from microstrip to SIW line from [20], © 2010 IEEE .

1.6.3 Radiation of a slot and matching on RWG

Although the nature of radiation is often described in terms of a current distribution on a conductor, other studies have shown that it can also be produced by a field distribution in apertures in a conductor, such as slots, horns, or patches. In such cases, the equivalence theorem can be employed to approximate the radiation from the aperture using equivalent sources, often referred to as Huygens sources. However, for slot antennas, a much simpler analytical approximation is provided by Booker's method [17], based on Babinet's principle.

The initial theory of radiation from a slot in a conducting plane was formalized by Booker [21], who adapted Babinet's principle from optics to antenna theory. Babinet's principle (1837) states that the amplitudes of light diffracted by an opaque screen with an aperture and those diffracted by a complementary screen formed by the complementary of the first screen, sum to the amplitude of the undisturbed incident wave. This original theorem, however, does not account for electromagnetic polarization effects. Booker's extension rigorously applies the principle to vector electromagnetic fields, taking into account that the orientations of the electric and magnetic fields are interchanged between a dipole antenna and its complementary structure as shown in Figure 14.

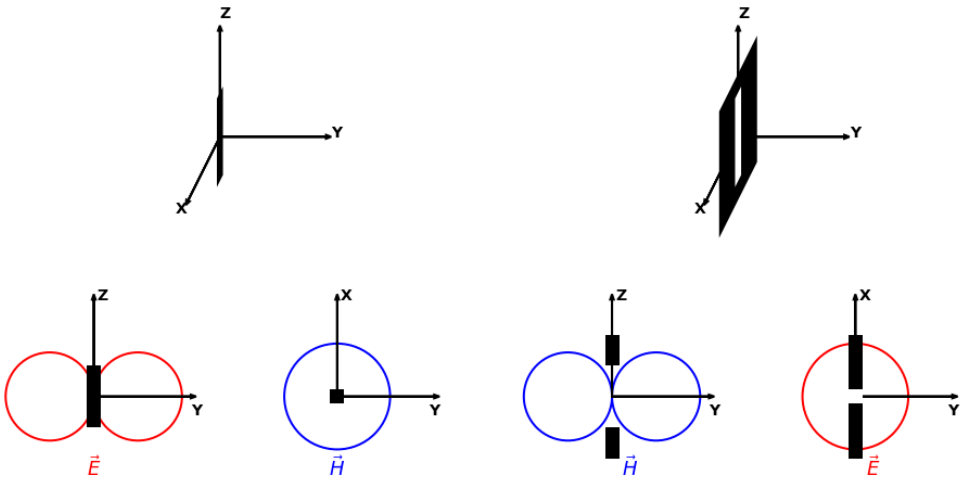

Figure 14 : Fields planes for the electric dipole and complementary magnetic dipole polarizations.

However, Booker's approach assumes a virtual perfect voltage feeding and an infinite reflector plane. In our case of study, the slots are located on the top surface of a rectangular waveguide (RWG). Consequently, two important points should be noted:

- The electric field within the slot arises from the discontinuity created by the slot in the waveguide wall, which interrupts the surface current lines specific to the propagation mode. This interruption leads to an accumulation of charges along the slot edges with a corresponding charge gradient Q. As a result, a time-varying electric field is established inside the slot, oriented perpendicular to the slot, which then behaves as a radiating aperture (often called magnetic dipole).
- The radiation pattern of the slot depends on the size and shape of the reflector surface. For a finite planar case, an early study was conducted in [22], and the demonstration can also be found in [23]. However, for both finite and ideally infinite reflective planes, the magnetic dipole exhibits excellent polarization purity, comparable to that of its complementary electric dipole.

In addition to its general properties in terms of external electromagnetic radiation, it is essential to understand and control the equivalent normalized admittance of the slot antenna and its frequency-dependent matching to the RWG. Proper matching ensures efficient power transfer at the desired operating frequency and minimizes reflections, which is critical for the overall performance of the array. In what follows, we focus on longitudinal rectangular slots that are longitudinal (along the z-axis) with a length of 2l and a width of $w \ll 2l$. In the literature, a length of 2l is typically adopted for mathematical convenience, since it leads to integrals defined over the interval [-l, l]. For a given waveguide and operating frequency, the unit slot can be studied at all the standing-wave maximum corresponding to a distance of $n.\lambda_g/4$ (with n odd) from the short-circuit. For this exercise, it is obviously preferable to simulate short waveguides in order not to waste simulation time. However, placing the slot at $\lambda_g/4$ from the short circuit can sometimes introduce disturbances in the electromagnetic behaviour of the slot. The distance that is classically chosen is therefore $3\lambda_g/4$. The initial study therefore concentrates on matching the slot with respect to its two primary parameters: its offset x from the middle of the waveguide and its length 2l as shown in Figure 15.

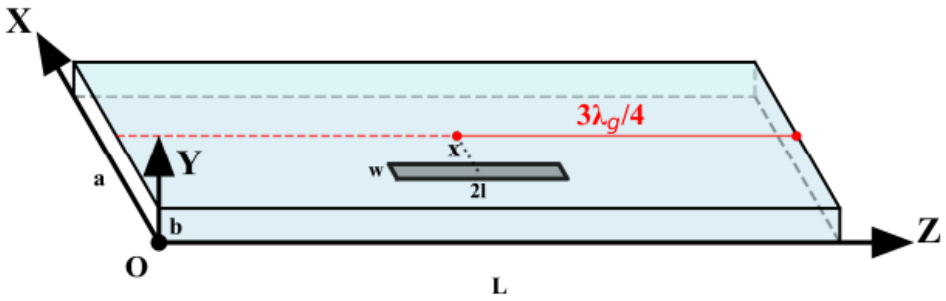

Figure 15: Geometrical model of 1 slot on the RWG.

Both theoretically and practically (through simulation or local measurements), a longitudinal slot is predominantly represented by a normalized admittance Y/G_0. The admittance Y (the inverse of the impedance Z) at a given frequency depends on the slot's geometric properties, specifically its offset x and length 2l, while the conductance G_0 (the inverse of the resistance R_0) corresponds to the characteristic conductance of the transmission line, which is independent of the slot. The normalized admittance can thus be expressed as:

$$Y/G_0\,(x,l) = G/G_0\,(x,l) + j\,B/G_0\,(x,l) \leftrightarrow y(x,l) = g(x,l) + j.b(x,l) \qquad (1.30)$$

Here, the normalisation of the quantities is written in lowercase for the sake of clarity and ease of derivation. The complex value of the normalized slot admittance y(x,l) is composed of a real and imaginary part. g(x,l), the real part of the normalized admittance, represents the conductive component, which is associated with the power actually radiated by the slot. This corresponds to the transfer of energy from the guided mode to free space. In addition, b(x,l) represents the reactive component, corresponding to the energy stored in the near-field (evanescent) regions of the slot, which is exchanged with the guided mode every cycle rather than being radiated into free space. This accounts for the phase shift, which can be either inductive or capacitive depending on the slot geometry. A slot is called a "radiating slot" when its susceptance b = 0. Prior to forming an array with this radiating element, it is essential to know the function y(x,l) of the normalized slot's admittance, which characterizes both its frequency matching and its electromagnetic behaviour (through the values of the normalized conductance g and normalized susceptance b). Around the matching length for a given offset, the general behaviour of the function y(x,l) at a given frequency is illustrated by the curves given in Figure 16.

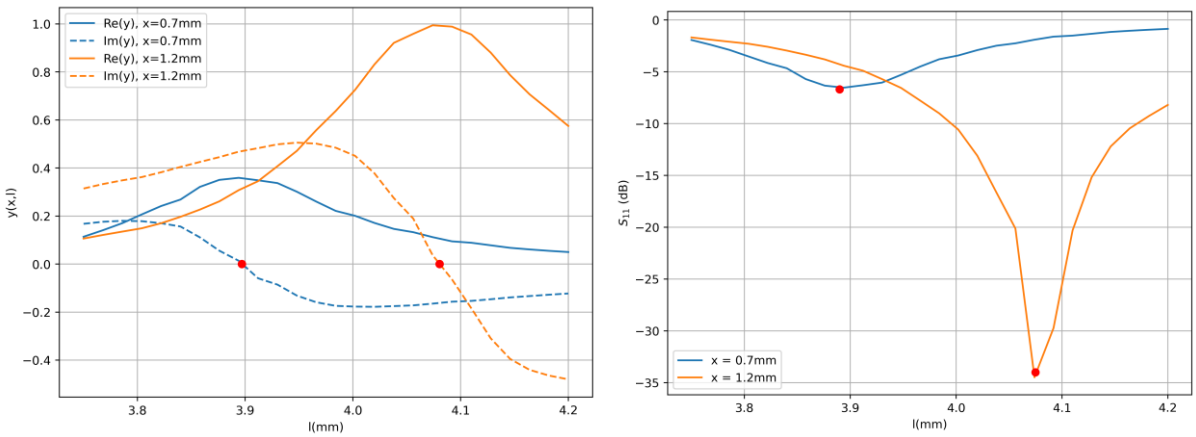

Figure 16 : General behaviour of the slot matching at a given frequency depending on the slot's length 2l and the offset x.

From the waveguide input, at the working frequency, the admittance matching occurs when the normalized admittance is purely real and equal to unity (y = 1 + 0j). Accordingly, the matching can be observed in the reflection coefficient $S_{11}(x,l)$ response at a given frequency f_0, with the minima corresponding to the points where $Im\{y(l_0)\} = 0$. It must be reminded that the knowledge of the functions g and b (real and imaginary part of the normalized admittance) is essential for achieving frequency matching of a single slot or a slot array, as well as for accurately determining its weighting. Different methods exist in the literature, each with distinct domains of validity, associated difficulties, and implementation possibilities. This part will be discussed in the next chapter.

1.6.4 Array configuration

Arraying consists of grouping the radiating slots along a single waveguide (1×N array) and, potentially, placing multiple waveguides in parallel (M×N array). Since a single slot antenna is inherently low-directive, arraying is necessary to achieve higher gain. in our case of RWGSA, the waveguide is terminated at one end by a conductor, referred to as a "short-circuit." By applying guided-wave propagation laws and boundary conditions at the short-circuit, the waveguide maintains its propagation mode by preserving the voltage nodes and antinodes. In the present study, we consider a linear array with a constant spacing between radiating elements d_{e2e}, with the last slot N positioned at $\lambda_g/4$ (or $3\lambda_g/4$) from the short-circuit. Following the chapter [24], two types of RWG slot arrays can thus be distinguished:

- Standing-wave feed (linear array of resonantly spaced longitudinal slots): all slots are spaced by $\lambda_g/2$ with alternating offsets for even and odd slots (i.e., located at successive antinodes and in phase thanks to the sign of the alternative offset). This configuration maximizes radiation in the broadside (zenith) direction.

- Traveling-wave feed (linear array of non-resonantly spaced longitudinal slots): the constant slot spacing differs from $\lambda_g/2$, so the slots are no longer in phase. Consequently, the main beam is steered away from the broadside in the H-plane.

For the remainder of this work, only the standing-wave feed configuration (with slot spacing $d_{e2e} = \lambda_g/2$) will be considered.

As mentioned previously, the unit slot is represented by a normalized admittance $y_0(x,l)$ in parallel as schematically shown in Figure 17. Following circuit theory principles, the end-of-line matching therefore depends simply on the sum of the individual slot admittances.

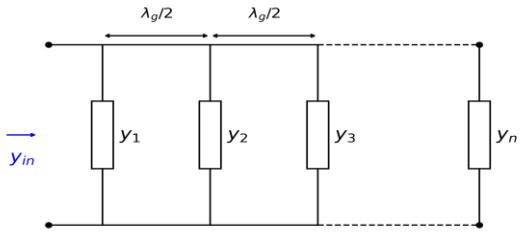

Figure 17 : Equivalent electric model for a 1×N slotted waveguide.

At the desired frequency f_0, each waveguide m must satisfy:

$$y_{in} = \sum_n y_n(x_n, l_n) = 1 + 0.j \qquad (1.31)$$

To array a set of longitudinal slots on a rectangular waveguide, it is necessary to control two major aspects:

- The individual behaviour of each slot according to its offset and length ($y_0(x,l)$)
- The mutual coupling (MC) phenomenon between slots, which perturbs the radiation of each element. As illustrated in Figure 18, one can observe external mutual coupling (MC_{ext}), arising from electromagnetic interactions in the near field, as well as internal mutual coupling (MC_{int}), reflecting slot-to-slot perturbations within the waveguide itself. Consequently, it is often necessary to adjust the dimensions of each slot to compensate for these perturbations and maintain the desired radiation characteristics when a good matching is expected.

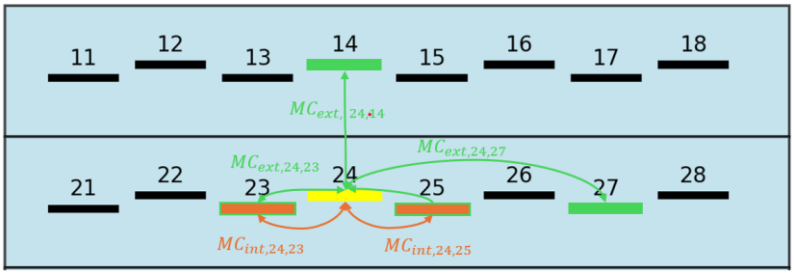

Figure 18 Schematic of a slotted SIW array showing external (green) and internal (orange) mutual coupling relationships between the slots..

The task therefore consists in determining all couples (x_{mn}, l_{mn}) given a normalized admittance y_{mn} pure real and the sum of the y_{mn} values of each waveguide m equal to 1 + 0j. Thus it is necessary to determine the M×N matrix of these couples for each slot in the array in which the values of each couple (x_{mn}, l_{mn}) depend on the values of all the other ones and respect the expected weighting distribution.

To do so, different theoretical methods are possible in the literature. The used one depends on the size of the array (number of slots), the dimensions and electromagnetic

characteristics of the waveguides, the frequency and the rate of RF specifications. At present, the most frequently employed general procedure is to derive from theoretical approximations of various levels of complexity, the coupling matrix (x, l), and subsequently to optimize the array through a full-wave simulation software. Among them, the two most popular are:

- Neglecting of mutual coupling**.** In this case, each slot is assigned the pair (x, l) corresponding solely to its expected weighting y(x, l). The value of y can then be obtained either purely theoretically, following Stevenson's approach [25], or by mathematical approximation based on various simulations (formerly experimental measurements) performed on the slot under study, as in the works of Stegen [26] and [27], Oliner [28], or Khac and Carson [29]. This method is relatively simple from a theoretical standpoint. Moreover, for large array (particularly those with a high number of elements per waveguide N) the equivalent conductance value for each slot, Re(y), becomes very small. This results in a very weak local weighting gradient from one antenna to the next, meaning that the coupling pairs required for perfect matching correspond to very small offsets and nearly identical slot lengths. Therefore, from the coupling matrix (x, l) thus obtained, we generally obtain, in simulation, initial results which, although sometimes shifted from the optimal matching frequency, can be corrected linearly along each waveguide. This approach is also widely used in cases where the matching of the network itself is not the main focus. There are many case studies where the pairs (x, l) are identical for all slots.
- Taking mutual coupling into account. For arrays of more moderate size, achieving proper frequency matching and maintaining the desired amplitude weighting necessarily requires taking into account the mutual coupling between slots. Undoubtedly, the first theoretical works, which remain key references to this day, were proposed by Elliott in [30], [31], and [32]. In [30], the problem is first formulated and expressed mathematically in its initial form, later refined in [31]. The latter introduces three equations that allow the array to be matched for a given amplitude distribution while expressing the normalized admittance of each slot, y_{mn}, as a function not only of its own pair (x_{mn}, l_{mn}) but also of those of all other slots in the array. Reference [32] continues this work by further accounting for the internal mutual coupling that occurs in waveguides with a height smaller than 25% of their width. Once again, this method yields on theoretical demonstrations and the obtained pairs (x_{mn}, l_{mn}) of dimensioning are later adjusted through numerical simulation to ensure matching at the target frequency. This approach requires, in return, a more in-depth electromagnetic study and understanding of the problem and the development of more complex associated algorithms.

In our study case, which concerns a conformal slot array of moderate size implemented in a very thin waveguide, the consideration of mutual coupling is therefore essential. It should be noted that several improvements have been introduced to Elliott's theoretical formulation and design procedure, for example, the inclusion of a dielectric film over the array for thermal protection, as proposed in [33], or even multilayer configurations [34], which modify the formulation of the external mutual coupling (MC_{ext}). Another noteworthy improvement relevant to our study is the adaptation of the derivation presented in [31] to the case of a cylindrically curved RWGSA given in [35].

1.6.5 Technical realization for a conformal slotted waveguide

In the 1940s and 1950s, rectangular waveguides were typically fabricated from conductive metals such as copper, brass, or aluminium, often silver-plated to reduce high-frequency losses. The guides were produced by precision machining or sheet-metal forming, with components assembled through soldering or brazing to ensure tight seams and consistent impedance. Slot arrays were then added by mechanically cutting or punching the apertures at precise locations, followed by fine adjustments through filing or grinding. The final dimensions and positions of the slots were often verified and corrected empirically using RF measurements, as no computer simulations were available at the time.

In the context of slot antenna arrays for onboard radar, beam steering of a 2D array can be achieved electronically through phase control (E-plane) or frequency variation (H-plane), but with limited performance in H-plane. Mechanical steering is therefore often used as an alternative. However, implementing a conformal array addresses the drawbacks of mechanical beam steering. Conformal slot arrays appeared in the middle of the cold war, manufactured using procedures similar to those previously described, but with increased complexity and consequently higher cost.

One of the technical solutions proposed for few years is 3D printing. Several studies on this topic are available in the literature, e.g.,[36]. This method offers the significant advantage of enabling the fabrication of highly specific shapes as a single piece, which can be directly integrated under a radome. Moreover, conventional 3D printing still presents limitations in terms of dimensional accuracy, which can be critical for certain operating frequencies or specific waveguide thicknesses.

Another approach that has emerged in recent years is the use of flexible SIW slot arrays (SIWSA), enabled by thin and flexible dielectric substrates. This method offers excellent ease of fabrication and industrial reproducibility. Furthermore, in the case of cylindrical conformations, the same printed array can be mounted on a variety of different platforms. Within the scope of our research, we have therefore chosen to focus on flexible SIWSA for X- and Ku-band applications with cylindrical conformations.

1.7 Flexible antenna

1.7.1 General overview and characteristics

As observed in the review articles [37], [38], [39], the use of flexible antennas, and more broadly flexible electronics, encompasses a wide range of applications beyond embedded radar systems, including telecommunications, healthcare, the Internet of Things (IoT), and radio-frequency identification (RFID). Front-end electronic devices have very different objectives and operate over a wide range of frequency bands, from several hundred megahertz up to several tens of gigahertz. The most commonly reported flexible radiating elements in the literature are patch antennas, electric or magnetic dipoles, and F-shaped antennas. There is

therefore a considerable technological diversity in terms of the choice of materials and manufacturing techniques.

Flexible materials, both dielectric and conductive, used in these studies are typically characterized by parameters grouped into four main categories of properties: mechanical, chemical, thermal, and engineering. The latter includes aspects such as manufacturability, cost, maintenance, and aging. Many parameters are relevant in these fields. Here, we will focus on the elements most frequently mentioned in technical data sheets and those necessary for an initial comparison between materials.

Electrical characteristics:

- **Relative permittivity ε_r**: measures how much a material reduces the electric field compared to vacuum. It directly affects the propagation characteristics by reducing the wavelength inside the material by a factor of $1/\sqrt{\varepsilon_r}$. It indicates how well the material stores electrical energy in an electric field.
- **Loss tangent tanδ**: measures how much electrical energy is lost as heat in a dielectric material when an alternating electric field is applied.
- **Conductivity σ (S/m):** measures a material's ability to carry electric current.

Mechanical characteristics:

- **Tensile Modulus E_y (N/m²):** measures the stiffness of a material under tension. It is the ratio of stress (force per unit area) to strain (relative deformation) within the material's elastic region. A higher modulus means the material is stiffer and less likely to deform under stress. (also called the Elastic Modulus or Young's Modulus)
- **Ultimate tensile strength – UTS (N/m²):** the maximum stress a material can withstand before breaking or deteriorating when stretched. It represents the peak of the stress–strain curve and defines the material's structural resistance to being pulled apart.
- **Ultimate strain (%):** the maximum relative deformation (elongation) a material reaches before fracturing. It measures the material's ductility, representing the total percentage increase in length at the moment of breakage.

Thermal characteristics:

- **Coefficient of Thermal Expansion – CTE (1/C° or ppm/C°)**: measures how much a material expands or contracts when its temperature changes. It represents the fractional change in length (or volume) per degree of temperature change. A higher CTE means the material expands more with temperature increases.
- **Decomposition Temperature - Td** (°C): the temperature at which a material begins to chemically decompose, meaning its molecular structure breaks down, often resulting in weight loss, gas release, or loss of properties.
- **Specific Heat ($J.kg^{-1}.K^{-1}$):** is the amount of heat energy required to raise the temperature of one unit mass of a substance by one degree.

Chemical characteristics:

- **Moisture Absorption (%):** the measure of how much water a material takes up from its surroundings, usually from humidity or direct contact with water.
- **UV resistance**: measures how well a material retains its properties (color, strength, flexibility) after exposure to ultraviolet light.
- **Chemical Resistance:** indicates a material's ability to withstand exposure to chemicals (acids, bases, solvents) without swelling, dissolving, or losing mechanical strength.

Furthermore, the last 3 cited reviews highlight key concepts related to material theory and associated fabrication methods. From these 3 documents, the following points can be retained:

For materials, a distinction is made between conductors and polymers. In the case of conductive materials, a compromise must be reached between conductivity, flexibility, and adhesion to the dielectric. Various solutions have been proposed, including:

- **Metallic thin films** (such as gold, silver, or copper), which offer excellent electrical conductivity but often require careful engineering to maintain flexibility and adhesion on polymer substrates.
- **Metallic nanomaterials** (such as silver nanowires, carbon nanotubes, or graphene), which can provide both high conductivity and mechanical flexibility, though their uniform deposition and long-term stability may be challenging.
- **Conductive polymers**, which are inherently flexible and compatible with many substrates, but have lower conductivity than metals and may require doping or post-treatment to enhance performance.
- **Hybrid solutions**, where conductive fillers (metal particles, carbon nanotubes, or graphene) are embedded in a polymer matrix, aiming to combine electrical performance with mechanical resilience.

Each of these approaches involves trade-offs between electrical performance, mechanical flexibility, adhesion, and manufacturability, and the choice depends on the specific requirements of the flexible electronic device.

Flexible substrates in electronics can use a wide range of materials beyond traditional polymers. These include thin glass, which combines transparency and dimensional stability with moderate flexibility; natural fibers such as wool or silk, offering biocompatibility and mechanical compliance; rubbers and elastomers, providing high stretchability; and paper, which is lightweight, low-cost, and biodegradable. Each of these materials presents trade-offs in terms of mechanical properties, thermal stability, surface smoothness, and compatibility with conductive layers or fabrication techniques. Among these options, synthetic polymers remain the most widely used and reliable substrates for flexible electronics. Polymers are defined as macromolecules composed of repeating structural units, and their selection is based on a combination of mechanical flexibility, thermal and chemical stability, and suitability for processing. According to [38], the most used types of synthetic polymers include:

- **Polyimides (PI):** Known for its good thermal stability, chemical resistance, and mechanical strength, suitable for high-performance flexible circuits.

- **Polyethylene terephthalate (PET) and polyethylene naphthalate (PEN):** Offer good flexibility, dimensional stability, and ease of processing, widely used in flexible displays and antennas.
- **Polydimethylsiloxane (PDMS):** An elastomeric polymer with high stretchability and biocompatibility, ideal for wearable and stretchable devices. Nevertheless, its thermal properties are limited and it has a bad aging.
- **Liquid crystal polymers (LCP):** Exhibit excellent thermal and chemical stability, low moisture absorption, and good mechanical properties, suitable for high-frequency and high-performance RF applications. Its main disadvantage is its price.
- **Polytetrafluoroethylene (PTFE):** Highly chemically inert and thermally stable, with low dielectric losses, making it suitable for RF and microwave flexible circuits. However, PTFE is mechanically rigid and requires special processing techniques to be used as a flexible substrate.

A direct table of values for the electrical, thermal and mechanical properties between these dielectrics is complex because companies offer many products based on the polymers in question but chemically modified for specific applications. Furthermore, the datasheets are more or less complete scientifically, and the same physical values are sometimes measured under different temperature or frequency conditions, thus limiting direct comparisons.

The selection of a synthetic polymer substrate typically balances flexibility, thermal and chemical stability, adhesion with conductive layers, and compatibility with the intended fabrication processes, making them the preferred choice for most flexible electronics applications. The specific choice of the polymer to be used obviously depends on the thermal and mechanical conditions under which the design will operate, as well as on the trade-off between cost and the expected electrical performance. In addition, it also depends on the chosen radiating element. Indeed, some material ranges sold by industry are so thin (below 120 μm) that certain types of flexible array implementations cannot be realized on them.

Depending on the selected dielectric and conductive materials, different manufacturing techniques can be employed. Each method naturally involves a trade-off between cost, processing speed, and printing accuracy. As presented in [37], the most commonly reported techniques in the literature include inkjet printing, screen printing, 3D printing, chemical etching and SIW based technology.

From materials engineering and flexible electronics perspective, the following questions must be addressed when selecting materials:

- What mechanical stresses will the device undergo? Will it experience regular and varying mechanical deformations, or a constant and fixed deformation? What are the maximum expected deformations, which will determine the required level of elasticity and flexibility?

- What thermal conditions will the device be exposed to? For applications requiring RF performance, the electrical and mechanical properties of the material should remain as stable as possible under variations in temperature or pressure.
- What electrical characteristics are required? For instance, the dielectric loss factor for dielectrics or the conductivity for metals must meet the expected RF performance levels.
- Chemically, will the chosen substrate and conductor exhibit sufficient adhesion? What treatments might be necessary to limit moisture absorption or reactions to UV exposure?
- From an engineering standpoint, which fabrication methods are compatible with the selected materials? Are low-cost production and ease of industrial reproducibility achievable? What is the expected material lifetime or aging behaviour?

1.7.2 Flexible SIW slotted array

Among the many advanced considerations previously discussed regarding the properties of flexible materials and their manufacturing methods, the choice of solution ultimately depends on the specification sheet and on obtaining a favourable RF-performance-to-cost ratio. In our case study, a constant deformation is required in the form of a cylindrical curvature with radii of a few centimetres (on the order of the wavelength). A global deformation is therefore expected, without severe local or repeated deformations. Consequently, the mechanical coefficients that characterize maximum stretchability do not need to be at the upper end of the available range. By contrast, high RF quality is required, implying a low dielectric loss tangent and very high conductor conductivity. The use of synthetic polymers as the dielectric substrate is therefore an obvious choice.

Given that a waveguide slot array was selected as the radiating element, in part because of its good aperture efficiency, a flexible SIW with slot radiators is a natural technical solution. Conceptually this approach is straightforward: use a thin, compliant dielectric layer metallized on both faces, drill and metallize vias to form the waveguide walls, and then etch the radiating slots. The principal industrial challenge lies in achieving the required fabrication accuracy for the slots, which can demand tolerances below 10 µm on very thin substrates (less than 254 µm of thickness).

This use of flexible-slotted SIW structures is widely reported in the literature. Research attention sometimes focuses on materials and industrial fabrication processes such as [40] or [41], the study of conical conformations [42], or the analysis of RF performance for a given cylindrical radius of curvature, because the curvature of a flexible antenna array inevitably affects its radiation pattern as the curvature increases.

We will focus on the latter aspect: a theoretical approach to conformal antenna arrays for a given RF specification. It can be noted that in the literature, most studies on flexible SIW arrays use different kind of PTFE as flexible dielectric, more for its electrical and thermal performance than for its mechanical properties. Furthermore, they are mainly focus on designing arrays for a specific radius and targeted performances. Typical objectives include achieving a flat, fan-shaped main beam in the H-field plane [43] or E-field plane [44], or

optimizing the gain of the main beam for a given radiation angle, as seen in [45] and [46]. In [43], this is achieved by adjusting the number of radiating elements and their amplitude distribution. The optimal parameters are determined by combining a theoretical far-field radiation model with a genetic algorithm optimization and full-wave simulations. In [44], the active element pattern technique is employed alongside an iterative method to compute the excitation ratio between different SIW lines. In [45], an array curved in the H-field plane generates a directive beam by varying the spacing between the slots on each SIW line, thereby controlling the phase distribution. Similarly, in [46], a 1×N array is curved in the H-field plane with the aim of steering the main beam toward a specific angle. This is accomplished by coupling a theoretical far-field radiation model with a convergence algorithm to determine optimal slot spacing and amplitude distribution. A short recap of these four articles and their goals is presented in Table 1.

article	f_0(GHz)	R/λ_0	dielectric, b_{siw}(mm)	goal
[43]	42.2	4.9	RT/duroid 5880 0.508	120° flat-top broad beam in H-plane
[44]	35	2.2	RT/duroid 5880 0.254	flat topped fan beam in E-plane with a 75° 3 dB beamwidth
[45]	25	8.3	RO3003, 0.508	increase directivity by weighting/phase optimization
[46]	28	5.6	RT/duroid 5880 0.254	specific directional beam

Table 1 : summary on few articles close to the subject of flexible SIWSA

In previously cited studies, the objective was to optimize the array for a given curvature radius, a chosen dielectric material (mostly Rogers RT/Duroid 5880 or RO3003), and/or a desired beam shape or steering angle. However, to the author's knowledge, no study has addressed the impact of the curvature radius on the radiation pattern of a curved waveguide slotted antenna array, and especially from the theoretical point of view, considering a wide variety of design parameters.

1.7.3 Current limitations in the synthesis of flexible slotted waveguide arrays

Throughout this PhD work, the emphasis has been placed on the RF theory of conformal antennas rather than on the mechanical properties of flexible materials or the practical aspects of prototype fabrication. As discussed in the previous subsection focused on studies related to our topic, the dielectric substrates employed generally belong to the same material family characterized by good electrical performance and are typically supplied as laminates with electrodeposited copper foil or rolled copper foil on both sides. For more demanding electrical applications, they can also be cladded with a laminated copper foil. Although their mechanical coefficients do not offer the same degree of flexibility as those of highly elastic substrates, the use of a simple and constant curvature (cylindrical or conical) allows the thin polymer class employed to achieve adequate bending of the array. Moreover, these polymers exhibit a wide range of thermal and chemical properties that are particularly advantageous for aerospace applications, often superior to those of materials intended for high and repeated flexing.

Consequently, the topics and challenges addressed in this dissertation concentrate on 2 points:

1) The theoretical matching of SIW slot arrays on flexible thin
2) The radiation pattern of the array for cylindrical conformations with radii on the order of the wavelength ($R/\lambda_0 < 10$)

The first point arises from the fact that the theoretical method, based on Elliott's work, becomes increasingly unsuitable for arrays employing very thin dielectric substrates. Indeed, the internal mutual coupling is so strong that it leads to offset or slot-length values falling outside the nominal matching region of a single slot. Under such conditions, Elliott's correction procedure no longer provides meaningful results. Furthermore, this method does not account for certain parameters, such as slot width or conductor thickness, which can no longer be neglected for substrate thicknesses of 254 µm or even 127 µm (the latter, to the author's knowledge, has not yet been reported in the literature for slotted SIW structures).

The second point arises from an observation in the literature: curved slotted SIW arrays are generally optimized for a specific bending radius and a given set of RF requirements. However, the variations in the radiation pattern of the same array when subjected to different curvature radii are rarely discussed. It would therefore be of particular interest to quantify how the directivity of a single array evolves when mounted on supports of different diameters, and to identify which array parameters can be adjusted to minimize the differences between one curvature and another.

1.8 Conclusion

This first chapter highlights the key points that will be addressed throughout this manuscript. After introducing several fundamental concepts in electromagnetics and antenna radiation, a brief overview of antenna and antenna array theory was presented. The notion of conformal antennas was then defined and discussed to provide a general overview of the topic.

The choice of using slotted arrays as conformal antennas naturally led to a general presentation of such arrays and their associated waveguides. Since the study focuses on linear arrays of resonantly spaced longitudinal slots, a short overview of the main design methods and their limitations was also provided.

As this PhD work is oriented toward flexible electronics, a state-of-the-art review was conducted on this subject, presenting the various use cases and challenges, both in material engineering and RF design, before focusing specifically on flexible slotted SIW structures.

Two major limitations identified concern, on the one hand, the design methodology of such arrays, and on the other, the study of how the field function varies with curvature radius. The following chapters will therefore address these two issues in detail, beginning with a study of the individual behaviour of the slot and its mathematical representations, the limitations of Elliott's model and the need to correct the theoretical results obtained using software.

Chapter 2 -
Improved Theoretical Model for Strongly Coupled Slot Arrays: New Unit-Slot Equation and Automated Correction Algorithm

2.1 Introduction

As part of this doctoral thesis, it was initially decided to follow Elliott's procedure, which enables the theoretical design of an M×N slot array by modelling each slot as a normalized admittance and by explicitly considering the mutual coupling between the radiating elements. This analytical approach leads to a system of equations involving the offset and length pairs (x, l), where the normalized admittance y_{mn} of each slot (m, n) depends on its own pair as well as on all the others due to mutual coupling. A recursive algorithm is therefore employed to iteratively converge toward the required (x, l) values to ensure impedance matching at the operating frequency and the desired excitation weights. As a reminder, the adoption of this method is justified by its high theoretical accuracy and its versatility, allowing its application to various configurations, such as the inclusion of dielectrics other than air within the waveguide, its use in standing-wave as well as traveling-wave arrays, and the possibility of incorporating a dielectric coating on the array surface.

However, Elliott's classical approach begins to show limitations when applied to SIW slot arrays (SIWSA) with flexible or non-standard slot geometries. One of the preliminary steps involves determining the slot's equivalent normalized admittance function $y_0(x, l)$, which characterizes the individual behaviour of an isolated slot element in the absence of other radiators. Since the 1990s, this step has commonly been performed using full-wave electromagnetic simulation tools such as HFSS or CST softwares, which directly provide numerical values of $y_0(x, l)$, from which the function can be approximated. Historically, this mathematical approximation was carried out using the Stegen method [26]; however, its underlying assumptions are no longer valid in the case of thin waveguide structures. Furthermore, the matrix obtained after convergence of Elliott's algorithm often yields theoretical results deviating from expectations, partly due to simplifying assumptions such as lossless models, neglecting conductor thickness, and slot width effects. As a result, a manual correction using simulation software becomes necessary, a process that can be both time-consuming and complex. Finally, the overall procedure consists of the characterization of the slot's equivalent normalized admittance function $y_0(x, l)$, the understanding and implementation of Elliott's recursive algorithm to derive the coupling matrix (x_{mn}, l_{mn}) for each element (m, n) while accounting for mutual coupling and weighting, the computer-aided design of the array using the obtained dimensions, and the subsequent manual fine-tuning. As a result, this process is computationally expensive, prone to human error, and challenging for newcomers to the topic. In the context of thin SIW slot arrays, the analytical modelling of the equivalent normalized admittance of an individual slot $y_0(x, l)$ needs to be revisited. Moreover, Elliott's theoretical design method provides the slots offset–length pairs (x, l) for the array. However, when these values are tested in full-wave simulations, the results are inaccurate. Therefore, the development of a software-based correction algorithm constitutes a valuable tool.

This chapter is therefore divided into four sections. The first provides an overview of the classical theory used for the design of slotted arrays when mutual coupling must be considered. The second focuses on a new analytical method for approximating the slot's

equivalent normalized admittance function $y_0(x, l)$. The third section addresses the automation of the correction of the design matrix initially obtained with Elliott's procedure using a convergence algorithm that employs python language and HFSS simulations in parallel. Finally, the last section presents a general algorithm for automating the entire procedure, from the input of the expected RF parameters to the sizing of the final matched array in software.

2.2 Theoretical method for the matching of a Standing-wave fed slot array

2.2.1 Unit slot and associated normalized admittance

One of the fundamental points to understand the design of slot arrays is the behaviour of its normalized admittance function y_0 and representing matching at a given frequency f_0. For 1 individual slot, the normalized admittance y_0 and the coefficient of reflection have the relationship Γ given by (2.1):

$$y_0 = \frac{1 - \Gamma}{1 + \Gamma} \tag{2.1}$$

An easy way to understand its behaviour is to observe the relationship between both the real and the imaginary parts of $y_0(x, l)$ (a) and the reflection coefficient (b) as shown in Figure 19.

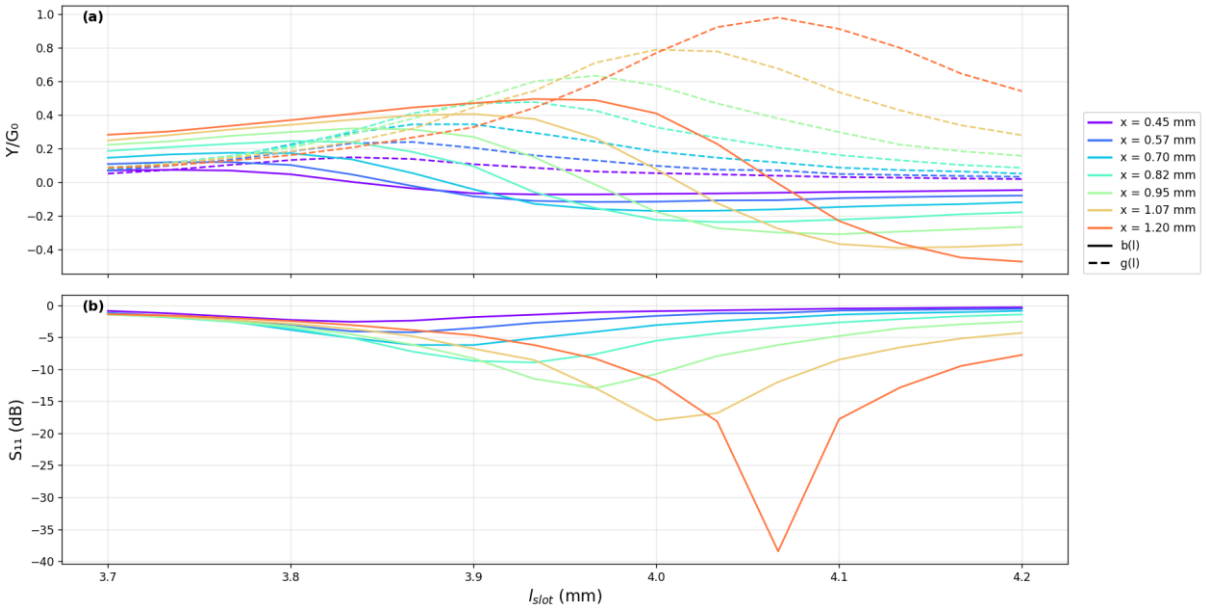

Figure 19 : simulated (a) slot's equivalent normalized admittance function y_0 and (b) S_{11} parameter at 15GHz with a RT/Duroid 5880 dielectric of 254µm.

$g(x, l)$ is the real part of the equivalent normalized admittance and represents the radiated power while $b(x, l)$ is the imaginary part and represents the stored energy causing a phase shift. At a given frequency, the slot is considered radiating when the susceptance b is null. Furthermore, the sign of the susceptance b indicates whether the slot is too long or too short to reach resonance ($b = 0$). Adjusting the offset x allows for tuning of the conductance g to achieve

a local maximum corresponding to the desired weighting. Finally, it can be observed that the local minimum of the reflection coefficient corresponds to the point where the susceptance is zero (resonance). The value of this minimum approaches -∞ on a logarithmic scale as the value of the conductance g approaches 1.

For the design of the array, it is therefore necessary to have a numerical function that takes the pair slot/length (x, l) as an input and returns the most accurate real and imaginary parts of the normalized admittance y. Historically, $y_0(x, l)$ was obtained in two ways. The first, theoretically more complex, consisted in approximating the behaviour of the equivalent normalized admittance $y_0(x, l)$ using methods such as the Method of Moments [29]. The second, simpler but specific to the case under study, relied on measurement tables. Indeed, electromagnetic simulation software only appeared in the early 1990s; before that, the approach involved taking the waveguide under study and creating a set of slots with varying offsets and lengths to obtain a table of $y_0(x, l)$ values at the operating frequency. This table was then either used numerically via interpolation functions (rarely, since computers in these years had very limited computing power) or approximated analytically using Stegen's method [26].

The latter approach remains particularly interesting today, as the measurement procedure can be fully implemented using electromagnetic simulation software. Mathematically, this corresponds to expressing the normalized admittance y_0 as the product of two functions:

$$y_0(x, l) = g_{res}(x).h(\gamma) = g_{res}(x)\big(h_1(\gamma) + jh_2(\gamma)\big) \quad (2.2)$$

$$\gamma = l/l_{res}(x) \quad (2.3)$$

$$h_1(\gamma) = g(x, \gamma)/g_{res}(x) \quad (2.4)$$

$$h_2(\gamma) = b(x, \gamma)/g_{res}(x) \quad (2.5)$$

To avoid confusion in notation the ratio between the slot length l and the expected resonance length l_{res} for a given offset x, which was historically called y, is here defined as γ. The renaming is done to avoid any confusion with the normalized admittance. $l_{res}(x)$ denotes the resonance length at the given offset x (giving a null susceptance).

The function $g_{res}(x)$ therefore represents the resonance conductance of a slot at a given offset x and its associated resonance length l_{res}. The functions $h_1(\gamma)$ and $h_2(\gamma)$ correspond respectively, for a given offset x, to the ratios of the conductance and susceptance obtained for a given l relative to the resonance conductance at that offset. In the original article of Stegen [26], the figures 3 and 5 show that the functions of the resonance conductance $g_{res}(x)$ and resonance length $l_{res}(x)$, both depending only on the offset x, exhibit a quadratic behaviour with respect to the offset. Another one from the article given in [26] illustrates the behaviours of the ratios h_1 and h_2 as functions of γ, which follow more complex exponential forms as shown in Figure 20. They are supposed to represent the pattern behaviour of the conductance and the susceptance of the slot depending on the slot length l observed in Figure 19 (a), normalized by the resonance conductance $g_{res}(x)$ of the used offset x. Therefore, for each offset x, the h_1

function is supposed to be maximal for $l = l_{res}$ ($\gamma = 1$), given $h_1(\gamma = 1) = 1$, and the h_2 function null, as observed in Figure 20.

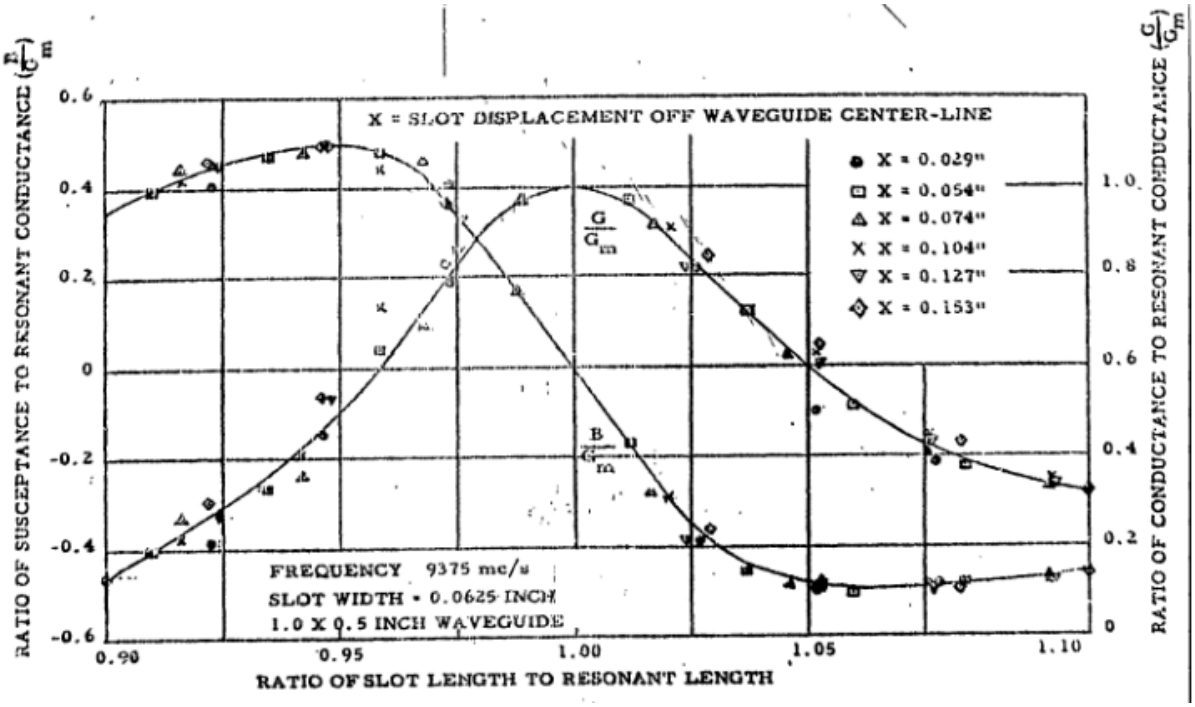

Figure 20 : variation of the h functions with γ ratio for different offsets from [27] , © 1952 IEEE

In the classical literature of the XXth century, the waveguides were thick enough to consider a weak impact of the mutual coupling (exclusively considered as external mutual coupling at this time), leading to a small difference in values between the values (x, l) of the slot without mutual coupling and with mutual coupling (4 – 5 % max). Therefore, the equation of functions h_1 and h_2 was done around $\gamma = 1$, allowing to simplify the problem with polynomial functions. The behaviour of these two functions above was not a need.

In addition to Stegen's mathematical approach, it is now possible, with a minimal knowledge of Python or MATLAB, to use scientific libraries to interpolate the entire set of values obtained for (x, l) and thereby provide a numerical function of the normalized admittance $y_0(x, l)$. However, it should be noted that these functions are typically implemented as numerical objects and are computationally more expensive to use, which may complicate their use in a more general, potentially iterative, code. Furthermore, a major risk of this approach arises when the numerical function $y_0(x, l)$ is used for offsets or lengths outside the original convergence range, as significant errors may occur.

2.2.2 Observation of the impact of mutual coupling between slots

The previous subsection highlighted the individual behaviour of a single slot and the numerical representation of the normalized admittance function y_0. However, as stated in Elliott's papers, proper design of a medium-sized array requires accounting for external mutual coupling (MC_{ext}), and even internal mutual coupling (MC_{int}) when the waveguide is thin.

To clearly illustrate the impact of these mutual couplings, a comparison was performed on the matching of a single slot, two slots on two parallel waveguides, and two slots within the same waveguide, for several different waveguide thicknesses. The study was performed using a RT/Duroid 5880 ($\varepsilon_r = 2.2$) which is the most commonly employed dielectric substrate in the literature on flexible SIW slot arrays. This exercise is done for different thicknesses going from the minimum to the maximum thicknesses available from the manufacturer, 127 µm and 1.578 mm. The models of the three simulated are shown in Figure 21, all having the same thickness and simulated at 15GHz.

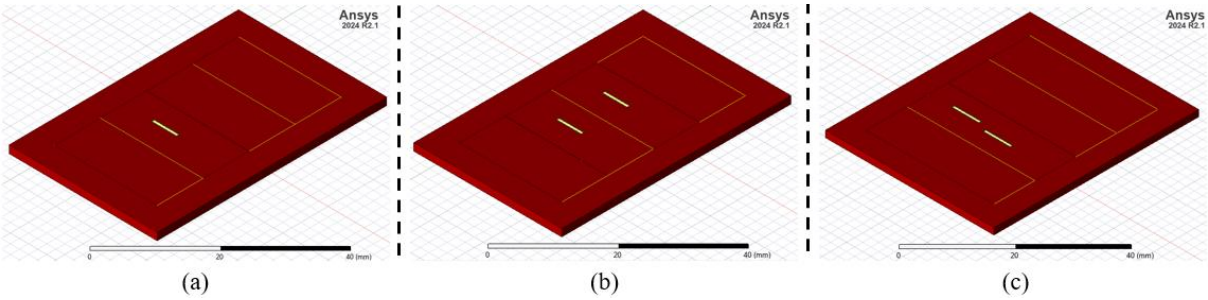

Figure 21 : 3 tested configurations to observe the effects of mutual couplings. (a) Single slot. (b) Two identical slots on parallel waveguides. (c) Two identical slots on the same waveguide.

For the single-slot case (Figure 21 a), the pairs (x, l) corresponding to the normalized admittance $y_{in} = 1 + 0j$ and $0.5 + 0j$ were recorded.

For the two slots on parallel waveguides (Figure 21 b), which are subject to external mutual coupling (MC_{ext}) in the E-plane, the pair (x, l) yielding $y_{in} = 1 + 0j$ was identified and compared with the corresponding pair from the configuration giving the same value. This approach directly shows the impact of the external mutual coupling (MC_{ext}) in a way that if it were not present, the pairs (x, l) would have been the same. Consequently, to remain tuned to the operating frequency, stronger mutual coupling results in a larger shift of identical parameter pairs (x, l) in the two-slot configuration (design b) compared with the single-slot configuration (design a).

For the two slots on the same waveguide (Figure 21 c), which are additionally affected by internal mutual coupling (MC_{int}), the pair (x, l) giving $y_{in} = 1 + 0j$ was recorded and compared with the pair from configuration (a) corresponding to $y_{in} = 0.5 + 0j$. Indeed, without mutual coupling, the equal (x, l) pairs of the two slots in the same waveguide of the configuration (c) simply correspond to the one of the individual slot from the configuration (a) giving the half of the normalized admittance in a way that for 2 slots $y_{in} = 0.5 + 0.5 = 1$. Therefore, as previously, the greater the shift between $(x, l)_{a_0.5}$ and $(x, l)_c$, the greater the mutual coupling. The values obtained from simulations are given in Figure 22 and Figure 23.

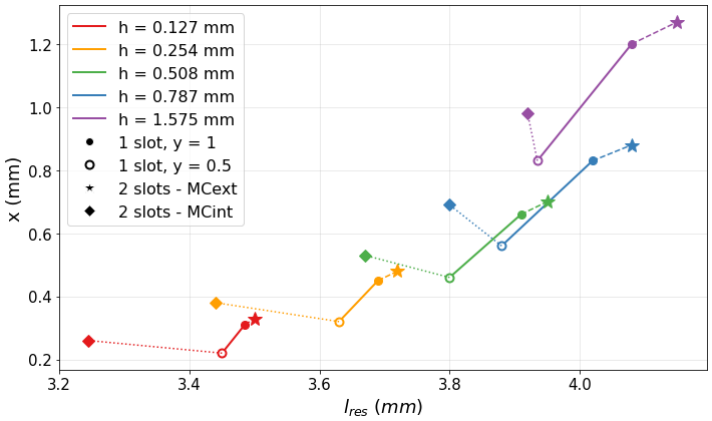

Figure 22 different values of couple (x, l) for different thicknesses of the 3 configurations of Figure 21

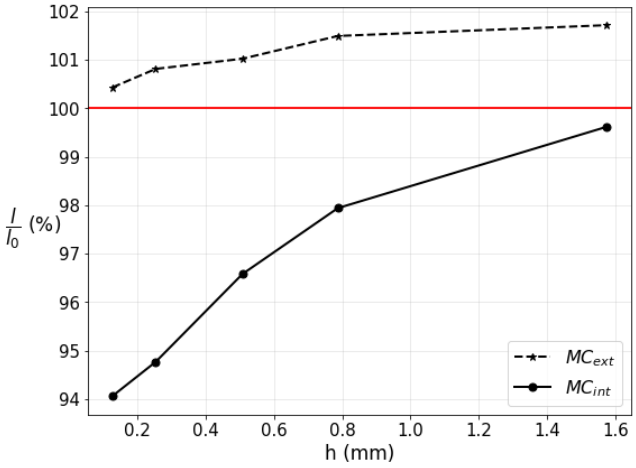

Figure 23 variations in percent of the slot length resonance with mutual coupling for different thicknesses

Different points can be observed:

- For a single slot (design a), keeping adapted to a normalized admittance with a decreasing substrate thickness h requires to decrease the values (x, l).
- The value of the shift of the equivalent individual normalized admittance from y = 1 to 0.5 is significantly lower for the small substrate thicknesses. Consequently, machining errors of the same absolute magnitude will have a much greater impact for thinner substrates than for thicker ones.
- In the case of an external mutual coupling (MC_{ext}) in the E-plane (design b), the (x, l) pairs required to maintain the normalized admittance y = 1 are slightly higher than the reference pair of values (x, l) of the individual slot (design a). However, when the waveguide thickness h decreases, the relative increase in slot offset x compared to the single-slot case becomes slightly larger, while the relative increase in slot length becomes smaller. It can therefore be concluded that, both in absolute and relative terms, the two slots on the thinnest substrate show fewer effects of MC_{ext} than those on the thickest substrate.
- In the case of an internal mutual coupling (MC_{int}) tested here with the design c, as the waveguide thickness h decreases, the percentage increase in slot offset relative to the single-slot case (design a) fitted to y = 0.5 does not follow a clear trend, with an average

increase in offset of about +20%. However, the reduction in the resonance length is much more pronounced as it can be observed in Figure 23.

This series of simulations on the three designs representing the matching of a single slot, two slots with external mutual coupling (MC_{ext}), and two slots with internal mutual coupling (MC_{int}), has shown the increasing influence of MC_{int} as the substrate becomes increasingly thin. This effect shifts the final matching region of the lengths of the pair (x, l) away from that of the unit slot (the value of the offset x staying in the initial zone). It is therefore evident that accounting for these mutual coupling effects in the design procedure is essential.

An interesting point on this last remark is that in the literature, we can see that even if the h_1 and h_2 functions presented in Figure 20 have a particular behaviour for $\gamma \in [0.9, 1.1]$, the mathematical approximation is done only close to 1. It is justified by the fact that the used RWG stays thick enough in a way that the MC_{int} is not too strong and then the final zone of (x, l) adaptation is close to the elementary one. It can be observed in an example given in one of the chapter of a book of Elliott [46], p.412, where γ is taken between 0.95 and 1.05, allowing to approximate the functions h_1 and h_2 with quadratic and linear functions respectively.

In the case under study with a thin waveguide leading to a strong MC, an array consisting of N slots by waveguide has N - 2 slots undergoing at least 2 internal mutual couplings (with the 2 closest neighbours). Following the results observed in Figure 23 showing the impact of only one MC_{int} relation between 2 slots where the shift for the thinnest RWG is around 6%, it can be deduced than the slots undergoing 2 internal mutual coupling will have a shift even more important, thus leading to a shift for γ above 10%. Then, a stronger analytical approach than just using polynomial functions with Stegen approach is necessary.

2.2.3 Formulation of Elliott's equations and associated recursive algorithm

As stated in the first part, Elliott's work is often cited as the theoretical reference on this topic. Among most notable publications from the 1980s, [31] and [32] formulate the effect of the mutual coupling on slot admittance. Although it is not necessary to go into detail about all of Elliott's work on this subject, a brief overview of the general approach and the equalities to be used is given in this section. The complete electromagnetic demonstrations are complex, but the overall initial and final logics remain relatively simple.

The first demonstrations establish the relationship between the normalized admittance y_n (called Y_n^a/G_0 in the article) of a slot n and the voltage at the centre of the slot (slot voltage V_n^s), normalized by the voltage V_n corresponding to the mode voltage presented in the antinode of the TE_{10} mode in the waveguide. The slot voltage V_n^s is a complex quantity whose magnitude and phase depend on the pair (x_n, l_n).

$$\frac{Y_n^a}{G_0} = K_1 f_n \frac{V_n^s}{V_n} \tag{2.6}$$

$$K_1 = \frac{1}{j(a/\lambda)}\sqrt{\frac{2(k/k_0)}{\eta G_0(\beta_{10}/k)(ka)(kb)}} \quad (2.7)$$

$$f_n = \frac{\left(\frac{\pi}{2kl_n}\right)\cos(\beta_{10}l_n)}{\left(\frac{\pi}{2kl_n}\right)^2 - \left(\frac{\beta_{10}}{k}\right)^2}\sin\left(\frac{\pi x_n}{a}\right) \quad (2.8)$$

The sub 'a' in Y_n^a means 'active' for the consideration of the impact of the mutual coupling. It appears a linear relation between the slot's equivalent normalized admittance and the normalized slot voltage throughout the product $K_1.f_n$. K_1 depends only on the frequency and waveguide characteristics like width a or the thickness b, but f_n depends also on the couple (x, l). This last point is particularly important. It reflects the fact that the ratio of two normalized admittances y_n and y_m does not directly correspond to the ratio of the slot voltages (and therefore to the expected field distribution). Indeed, the linearity relation exposed in (2.6) also depends on the pairs (x_n, l_n), and (x_m, l_m) because of the function f_n. The matching problem that satisfies the expected weighting is therefore more complex.

Another very important point is the definition of the slot voltage V_n^s which depends on the slot n alone and the external and internal mutual coupling with all the other slots. We then have:

$$V_n^s = V_{n,1}^s + V_{n,2}^s + V_{n,3}^s + V_{n,4}^s \quad (2.9)$$

$V^s_{n,1}$ and $V^s_{n,2}$ only depend respectively on the slot dimensions and the forward and backward wave in the RWG, $V^s_{n,3}$ takes into account the external mutual coupling with all the other slots, $V^s_{n,4}$ corresponds to the internal mutual coupling with the 2 closest slots on the same waveguide.

The demonstration of $V^s_{n,3}$ is presented in [31], based on the reciprocity theorem. The resulting expression is:

$$V_{n,3}^s = -j(\beta_{10}/k)(k_0b)(a/\lambda)^3\frac{1}{f_n^2}\frac{\frac{Y}{G_0}(x_n,l_n)}{2+\frac{Y}{G_0}(x_n,l_n)}\cdot\sum_{m=1}^{N'}V_m^s.g_{mn}(x_m,l_m,x_n,l_n) \quad (2.10)$$

with

$$g_{mn} = \int_{-k_0l_m}^{k_0l_m}\cos\left(\frac{z'_m}{4l_m/\boldsymbol{\lambda}_0}\right)\left\{\frac{1}{(4l_n/\boldsymbol{\lambda}_0)}\left[\frac{e^{-jk_0R_1}}{k_0R_1}+\frac{e^{-jk_0R_2}}{k_0R_2}\right]\right.$$
$$\left.+\left[1-\frac{1}{(4l_n/\boldsymbol{\lambda}_0)^2}\right]\int_{-k_0l_n}^{k_0l_n}\cos\left(\frac{z'_n}{4l_n/\boldsymbol{\lambda}_0}\right)\frac{e^{-jk_0R}}{k_0R}dz'_n\right\}dz'_m \quad (2.11)$$

Following the coordinate system in Figure 24 where R, R1, R2 are defined, dz corresponds to the distance between the slots n and m in the waveguide direction (H-plane) and

dx is the distance perpendicular to the waveguide (E-plane) between the slots. This function g_{mn} given in [31] should not be confused with the variable g representing the conductance of a slot. Furthermore, it is interesting to note that the slot voltage due to the external mutual coupling $V^s_{n,3}$ is proportional to the thickness b. This is consistent with the observations obtained in 2.2.2 on the impact of mutual couplings depending on the waveguide thickness.

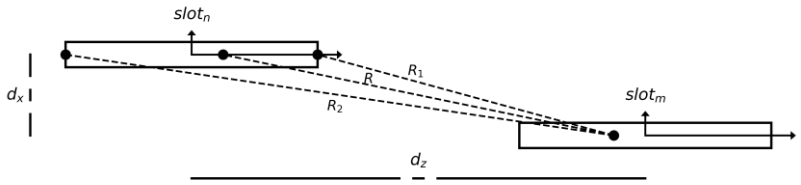

Figure 24 : Geometrical representation of the used variables for MC calculus.

For the internal mutual coupling, the derivation is given in [32], based on the higher-order TE_{20} mode with the reflection coefficient γ_{20}, and yields:

$$V^s_{n,4} = -j\frac{(\beta/k)}{(\gamma_{20}/k)}e^{-(\gamma_{20}/k)(kd)}\left[\frac{h_n}{f_n^2}\cdot\frac{\frac{Y}{G_0}(x_n,l_n)}{2+\frac{Y}{G_0}(x_n,l_n)}\right]\cdot[h_{n-1}V^s_{n-1}+h_{n+1}V^s_{n+1}] \qquad (2.12)$$

with

$$h_n(x,l) = 2\frac{(\lambda/4l)\cosh\left(\frac{\gamma_{20}}{k}kl\right)}{(\gamma_{20}/k)^2+(\lambda/4l)}\cos\left(\frac{2\pi x}{a}\right) \qquad (2.13)$$

All these derivations make it possible to express the slot voltage V_n^s as a function of both the behaviour of the isolated slot and the influence of its neighbouring elements. It is interesting to note that:

- The internal mutual coupling between adjacent slots, represented by $V^s_{n,4}$, always has the same sign (both real and imaginary); only its magnitude varies. Thus, the first and last slots experience a single MC_{int}, whereas the others are affected by two neighbouring slots (n-1 and n+1).
- The external mutual coupling introduced by $V^s_{n,3}$ is more complex, as it accounts for the influence of all the other antennas in the array.

A numerical example for the external mutual coupling MC_{ext} is provided for an 8×8 array operating at 15 GHz on a Ro5880 substrate with a thickness of 1575 µm. The spacing between adjacent slots is dx = 1 cm and dz = 0.9 cm in the E- and H-planes, respectively. A preliminary numerical study of the external mutual coupling between a slot n and a slot m through g_{mn} function given in (2.. 11) is presented in Figure 25. It shows that, for a given antenna element in the M×N array matrix, both the sign and magnitude of the coupling function g_{mn} between two slots vary with the distances dx and dz normalized with respect to the free-space wavelength λ_0.

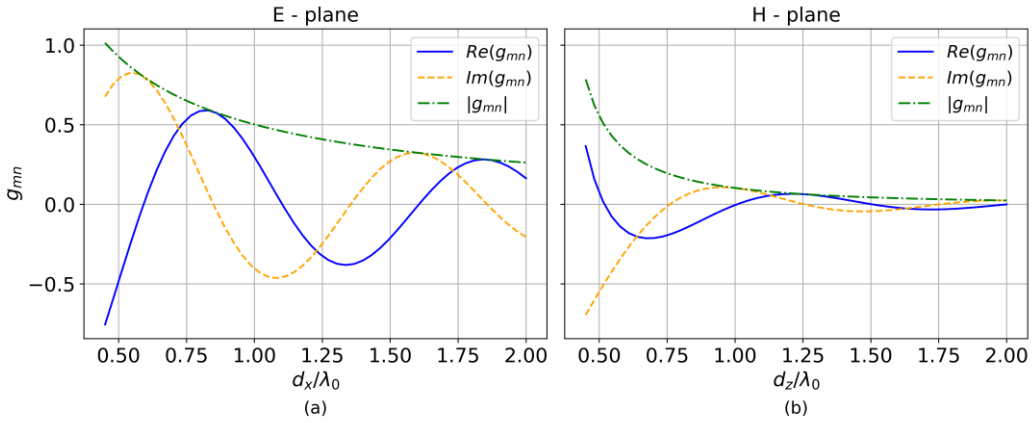

Figure 25 : Variations of the g_{mn} function depending on the normalized distance in both planes (a) in the E-plane (b) in the H-plane

It is observed that the magnitude of the coupling function g_{mn} decreases proportionally to 1/R, with a higher amplitude in the E-plane (between rows, Figure 25 a) than in the H-plane (along the same row, Figure 25 b). The real and imaginary parts are phase-shifted and change sign with distance. As a result, different slots in the array experience either capacitive or inductive mutual coupling depending on their relative positions (dx, dz). It must be noted that this function g_{mn} does not take into account the weighting on the array. The weighting is after multiply to g_{mn} in the sum as presented in (2.10). In the same way, the coupling function g_{mn} values can be tested for a 8×8 array with identical (x_{mn}, l_{mn}) pairs for each element as shown in Figure 26.

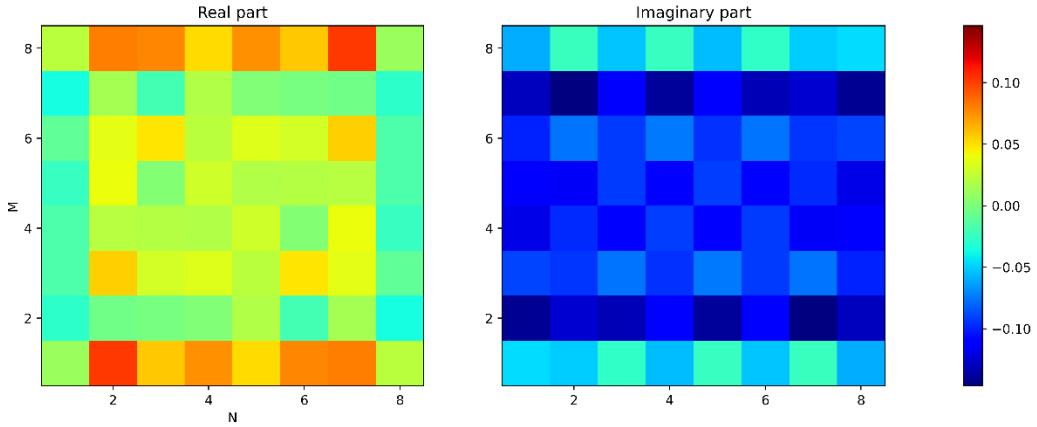

Figure 26 : Calculus of g_{mn} values for each identical slot of the 8x8 array.

It can thus be observed in Figure 26 that even though all slots share the same (x_{mn}, l_{mn}) pair and would radiate the same field in a lossless uncoupled medium, the impact of mutual coupling can vary significantly from one slot to another depending on its position within the array. Furthermore, it is worth noting that the function g_{mn} is defined using distances normalized by the free-space wavelength λ_0, whereas dx and dz depend, among other factors, on the substrate's relative permittivity. Consequently, for a given antenna element (mn), the indices of the neighbouring slots with which the strongest mutual couplings occur may differ from one array configuration to another. Finally, a central symmetry can be observed. Intuitively, one might think that there is double axial symmetry in planes E and H, but this is refuted by the

presence of offsets. Indeed, this leads to local distance dx and dz values that do not meet the criteria for axial symmetry but rather central symmetry.

The construction of the algorithm to obtain the (x, l) pairs for each slot is briefly described in [31]. The main idea is based on 3 design equations. The main goal of the last cited article is to reformulate the "first design equation" (2.6) into the form of the "second design equation" (2.14):

$$\frac{Y_{mn}^{a}}{G_0}(x_{mn}, l_{mn}) = \frac{2f_n^2}{\frac{2f_n^2}{Y/G_0} + MC} \tag{2.14}$$

with :

$$\begin{aligned} \mathrm{MC} &= \mathrm{M}C_{ext} + \mathrm{M}C_{int} \\ &= \mathrm{j}\frac{\beta_{10}}{k}(k_0 b)\left(\frac{a}{\lambda}\right)^3 \sum_{m=1}^{MN'} V_m^s g_{mn}(x_m, l_m, x_n, l_n) \\ &+ j\frac{(\beta/\mathrm{k})}{(\gamma_{20}/\mathrm{k})}\, \mathrm{e}^{-(\gamma_{20}/\mathrm{k})(\mathrm{kd})}\, [h_{n-1}V_{n-1}^s + h_{n+1}V_{n+1}^s] \end{aligned} \tag{2.15}$$

We can observe that even if the normalized admittance takes 2 variables (x_{mn}, l_{mn}), the result depends also on the mutual coupling MC considering the wanted full matrix of all the couple (x, l) and the expected weighting in both planes. Therefore, an iterative method must be used. Finally, as described in (1.6.4), the "third design equation" (2.16) corresponds simply to the matching of the waveguide m.

$$\sum_n y_n^a = \ specified\ constant \tag{2.16}$$

Usually, the sum must be a pure real for a full resonance, and the real part must be equal to the unity, or a fraction of unity if all the waveguides are fed by another single waveguide.

The global logic of the algorithm is presented in more detail in [24] as well as in Elliott's book [46]. To obtain the array design matrix, it is first necessary to have a numerical function $y_0(x, l)$ representing the equivalent normalized admittance of the slot at the wanted frequency without mutual coupling as observed in 2.2.1 (the Stegen method is used in these references). This function is then employed to generate an initial matrix of (x, l) pairs that does not account for mutual coupling. An iterative procedure is subsequently launched in which, for each slot, the mutual coupling is calculated based on the design matrix from the previous iteration. Then, using the first and the second design equations, the (x_{mn}, l_{mn}) pair satisfying $\mathrm{im}(y(x_{mn}, l_{mn})) = 0$ and (2.17) corresponding to the desired weighting is found for each slot. This point may require a second internal iteration in order to validate, in parallel, the attainment of a torque that allows both resonance and compliance with the weighting. Then, the validity of the third equation is verified for each row. Convergence is usually rapid, with five or six general iterations being sufficient.

$$\frac{Y_n^a/G_0}{Y_p^a/G_0} = \frac{f_n}{f_p} \cdot \frac{V_n^s}{V_p^s} \cdot \frac{V_p}{V_n} \qquad (2.17)$$

It must be noted that this theorical procedure based on electromagnetic demonstrations can reveal its limitations in the case of very thin waveguides, as the strong internal mutual coupling leads to final matching regions that significantly reduce the slot lengths compared to an isolated slot. It is therefore necessary that the equivalent normalized admittance function of the slot at the wanted frequency without mutual coupling $y_0(x, l)$ remains valid and that the underlying theoretical assumptions remain applicable. Moreover, as can be seen from the equations in this section, both the slot width and the copper thickness are neglected, as they are assumed to be negligible compared with all the other dimensions.

2.3 New Y/G$_0$ analytical function

2.3.1 Theoretical approach

In the study of flexible SIWSA in the X and Ku bands, the (x, l) couple of the slot exhibits matching regions that can differ significantly from the single-slot matching region, depending on the waveguide thickness h because of the internal mutual coupling. Therefore, the mathematical approach to describe the equivalent normalized admittance function of the unitary slot $y_0(x, l)$ needs to remain right even when the difference in variables' values becomes significant. The Stegen method, which only considers the average of the normalized conductances/admittances relative to the resonance conductance at the given offset (function h_1 and h_2), can lead to significant errors when the slot length deviates from the isolated-slot resonance length as it is the case for strong internal mutual coupling MC_{int}.

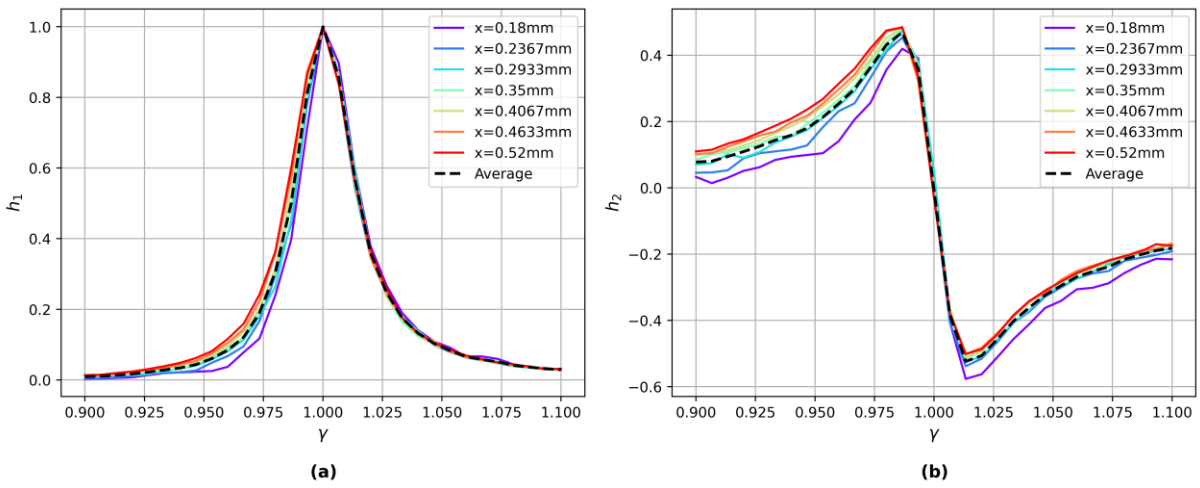

Figure 27 : Variations of (a) h_1 and (b) h_2 functions depending on the length ratio γ for different offsets in the case of RT/Duroid 5880, 0.254mm at 15GHz.

As a reminder, the variable γ used in Stegen's procedure seen in 2.2.1 corresponds to the ratio between the half slot length l and its resonance length l_{res} at a given offset x. As shown in Figure 27 , the absolute error approaches 10% for γ close to 0.97 for real part h_1 (a) and γ = 0.9

for imaginary part h_2 (b) (the case when MC_{int} is strong). Using the average like in Stegen is no longer valid in the final matching region.

As previously mentioned, the use of scientific libraries for interpolation functions provides a solution to this problem. However, its implementation in code is more complex, it is valid only within the initial simulation region, and it exhibits strong divergence effects beyond that range. Moreover, it leaves us analytically "blind" to the behaviour of the function across different (x, l) regions.

Developing a new analytical formula would allow for greater accuracy than the Stegen approach while remaining valid outside the simulation region. Referring to Figure 19, one can observe, for both the real and imaginary parts of the normalized admittance y, a shift in the pattern that broadens with increasing offset, while remaining centred around the resonance length, as also observed in Figure 28.

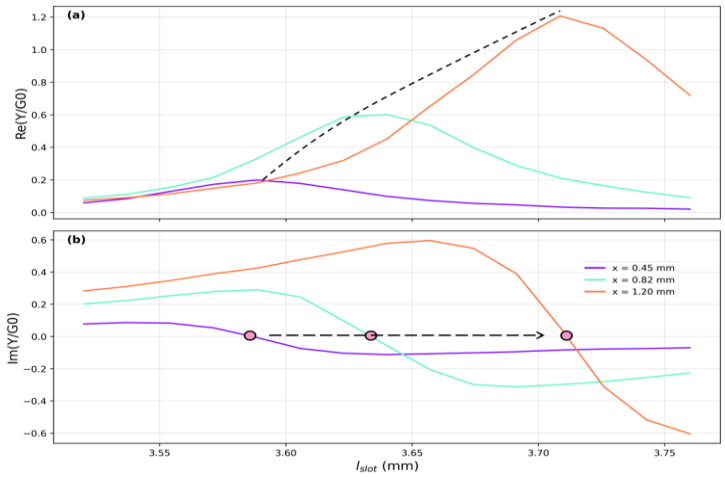

Figure 28 : Global shifting behaviour of (up) the real and (down) the imaginary parts of the normalized admittance Y/G_0 with the offset x.

For a given offset x, the conductance g(l) is quite naturally viewed as a Lorentzian function, whereas the susceptance b(l), which is somehow more complex, can be viewed as the product of a Lorentzian function with the negative error function (erf), both centred on the resonance length for the given offset. It is therefore sufficient to use these functions for the real and imaginary parts with a delay ($l-l_{res}(x)$), whose width coefficients depend on the offset x.

The formulas given below correspond to those which best suited various design cases (different frequencies and dielectrics):

$$g(x,l) = \frac{A}{1+\left(k_0(l-l_{res})\right)^2} + B \tag{2.18}$$

$$b(x,l) = \frac{-A'.erf\left(k_2(l-l_{res})\right)}{1+\left(k_1(l-l_{res})\right)^2} \tag{2.19}$$

It can be observed that although the functions are symmetric around the resonance length (where length ratio $\gamma = 1$), this is not the case when approaching the length ratio $\gamma = 0.9$ or 1.1. It is therefore necessary to distinguish between the parts $\gamma < 1$ and $\gamma > 1$, thus doubling

the number of coefficients. However, the usefulness of this work on this exercise is justified because the values of γ become less than 0.9 due to the strong internal MC. Only the coefficients of the functions for $\gamma < 1$ can therefore be used in the general iterative algorithm, which simplifies the problem. The distinction between the coefficients for $\gamma < 1$ and $y > \gamma$ is simply useful in the general demonstration of this new analytical approach.

It can also be noted that the y-interceptor value (B value in (2.18)) in the conductance function expression is very small or even negligible when working with standard SIW thicknesses ($10^{-4} – 10^{-5}$) in Ku-band. Its usefulness becomes more apparent at lower frequencies (X-band) with greater waveguide thickness.

2.3.2 Computational procedure

The numerical procedure begins with a set of simulations similar to those used in the Stegen procedure. Once all simulation results are exported in a readable format, the coefficients calculations are performed and stored in a file for later use in a more general array design algorithm. The procedure consists of the following steps:

1. (HFSS) Prepare the design for simulation using the target waveguide and a single slot.
2. (HFSS) Identify the simulation range covering the regions around $y(x, l) = 1 + 0j$ and $y(x, l) = 0.1 + 0j$ with python thanks to the HFSS simulations.
3. (HFSS) Run simulations with the determined range of offsets and slot lengths, then export the results.
4. (python) Determine the resonance lengths for each offset by locating l_{res} where $b(l_{res}) = 0$, and deduce the function $l_{res}(x)$ as shown in Figure 29
5. (HFSS) For each pair $(x, l_{res}(x))$, vary l so that the ratio of slot's length $\gamma \in [0.9–1.1]$, then export the results
6. (python) Determine the coefficients of the functions for each offset that best fit the simulation data as presented in Figure 30. It should be noted that, numerically, Python's *curve_fit* or *fsolve* functions tend to achieve a better linear convergence for the coefficients k_1 and k_2 when they are expressed as $1/k_1$ and $1/k_2$, respectively.
7. (python) Find the coefficients of the quadratic functions $A(x)$, $k_0(x)$, etc as shown in Figure 31
8. Save these calculated coefficients in the computer

It then becomes possible to develop a numerical function $y_0(x, l, SavedCoef)$ that best approximates the simulated values. Figure 30 illustrates the last procedure done for RT/Duroid Ro5880 of 254um at 15GHz.

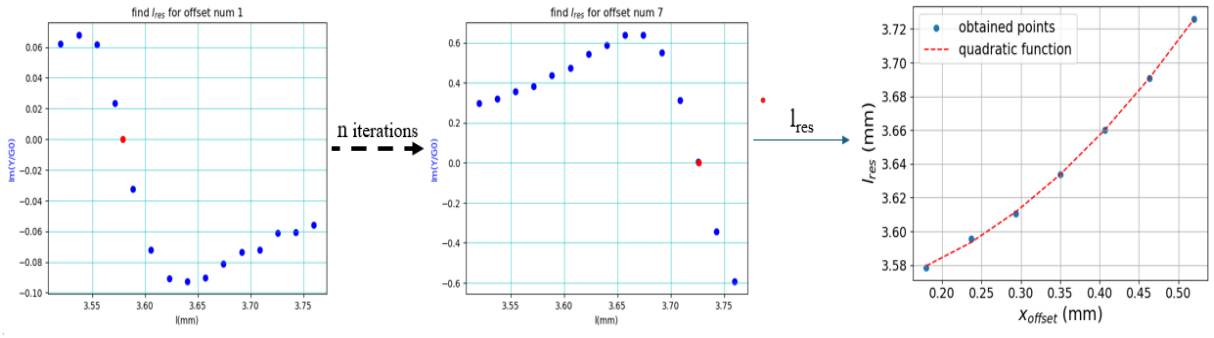

Figure 29 : Illustration of finding the $l_{res}(x)$ function from the b(l) function of each iteration (step 4).

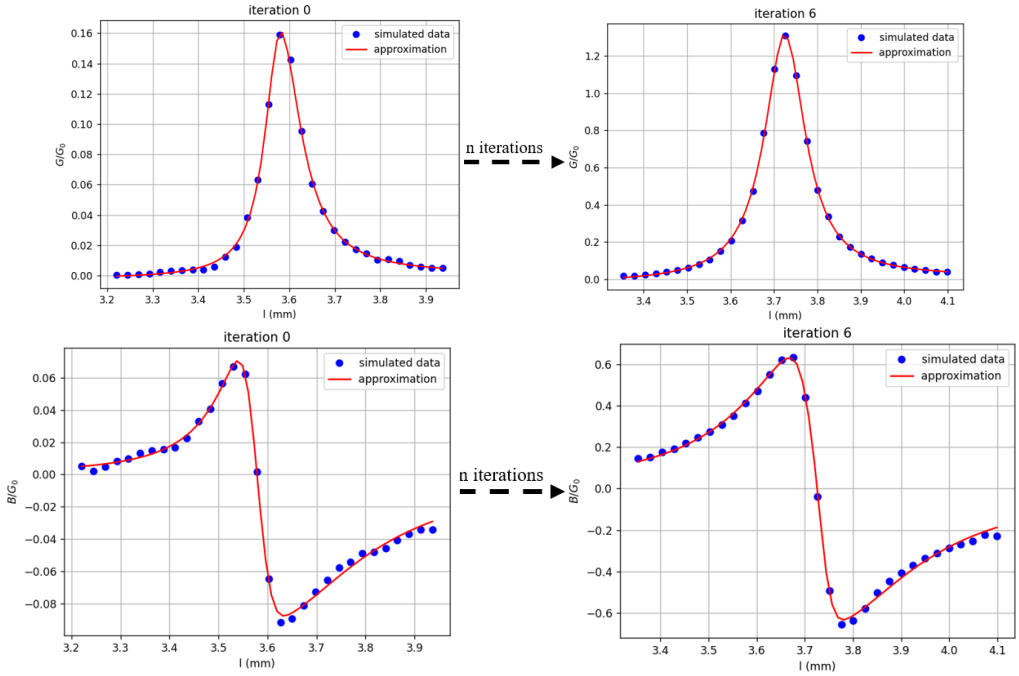

Figure 30 : Finding the coefficients of the Lorentzian function on the (up) real and (down) imaginary parts of the normalized admittance for each offset (step 6).

2.3.3 Comparison with Stegen's method

It is then interesting to compare the results of this method with those obtained using Stegen's approach. To do so, the values of the unitary slot's equivalent normalized admittance $y_0(x, l)$ are simulated over a wide range of offset x and length l ([0.4–1.2] mm with 8 iterations and [3.4–4.5] mm with 21 iterations). The absolute differences in the real and imaginary parts are then compared with the numerical functions $y_0(x, l, SavedCoef)$ obtained from the two methods as presented in Figure 32 and Figure 33.

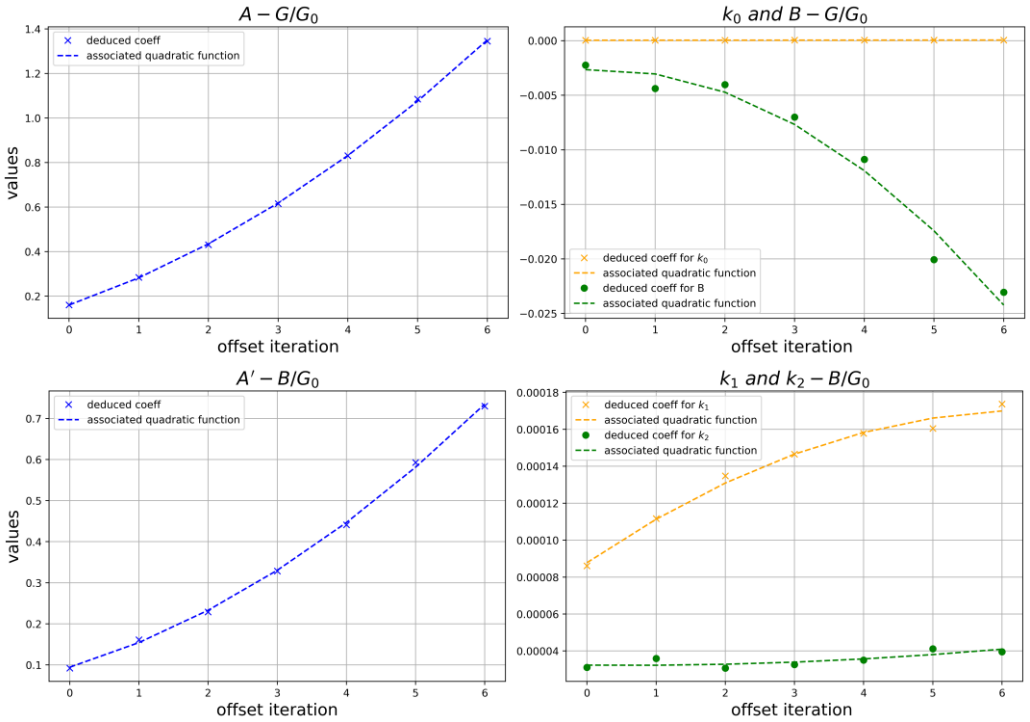

Figure 31 : Deduce the quadratic behaviour of each factor depending on the offset (step 7).

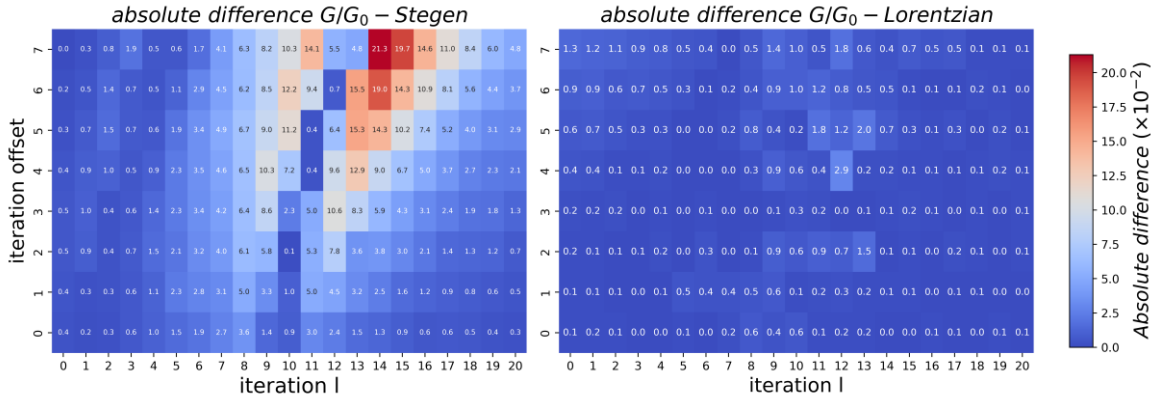

Figure 32 : Comparison of absolute difference between the simulation of normalized conductance, (left) with the Stegen method and (right) with the Lorentzian developed method.

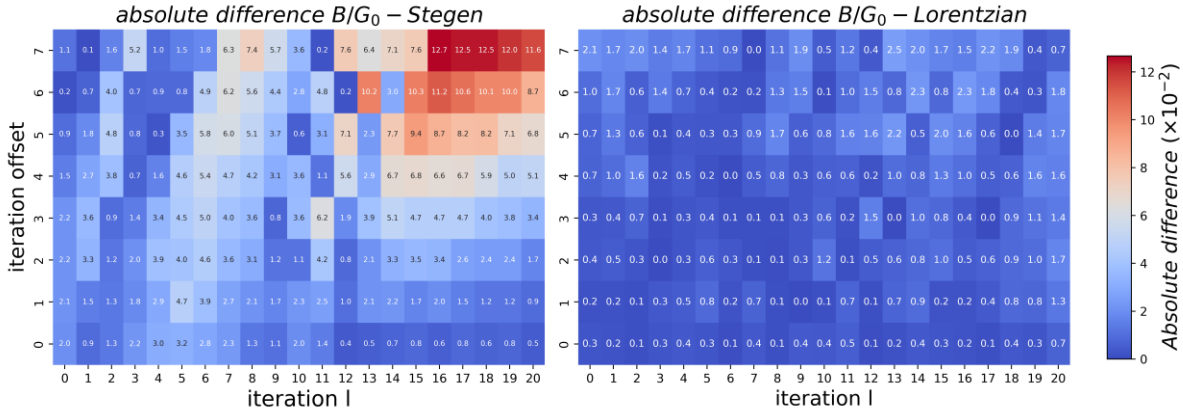

Figure 33 : Comparison of absolute difference between the simulation of normalized susceptance, (left) with the Stegen method and (right) with the Lorentzian developed method.

It is observed that, in general, the Lorentzian approach is more accurate than the Stegen's approach. Nevertheless, although this method always maintains an analytical approach to the problem and eliminates concerns about divergence issues for any chosen pair (x, l), the algorithmic development itself for the procedure, including the calculation of the coefficients and their final implementation, is more complex than with the Stegen's approach, thus requiring a longer development time.

2.4 Automated dimensional corrections of slot array antennas in simulation software

2.4.1 Objectives of the correction of the design matrix in the simulation software

Once the sizing matrix has been obtained using the Elliott's procedure, the network is modelled in an electromagnetic simulation software such as HFSS or CST, and an initial simulation is performed. It is evident that the matching of each waveguide does not occur exactly at the desired frequency, since the numerical sizing values are derived from theoretical formulas that neglect losses and consider certain parameters, such as conductor thickness or slot width, as negligible. It is observed that the deviation between the simulated results and the expected values becomes more significant as the thickness of the waveguide h decreases.

The primary objective is therefore to obtain the best reflection coefficient for each waveguide m at the desired frequency f_0 by bringing the behaviour of the equivalent normalized admittance function y(x, l) seen in Figure 19 a to f_0. This term of 'behaviour' will be used many times in the following to talk about these specific curves of the normalized admittance function y around the resonance. It is important to note that at this level, a slot-by-slot correction is impossible from both a total simulation time and convergence algorithm standpoint. As a reminder, modifying a pair (x_{mn}, l_{mn}) impacts the matching of the slot (m, n) but also the coupling with all the other slots. Consequently, the work is done with correction factors on the offsets and lengths of each waveguide m, named fact_x_m and fact_l_m.

Ultimately, the matching of the array of m waveguides is performed from the analysis of the reflection coefficient S_{mm} and input normalized admittance Y_{mm}/G_0 parameters on each excitation waveport as a function of the correction factors on the slots' offset and length, fact_x_m and fact_l_m. It can be noted that software such as HFSS or CST would theoretically allow for the use of optimization tools to obtain the fact_x_m/fact_l_m values for each waveguide yielding $Y_{mm}/G_0 = 1+0j$ and $|S_{mm}| = 0$ ($-\infty$ in log scale). However, the number of solutions increases exponentially with the number of waveguides m, making the software algorithms ineffective for this problem, not to mention the simulation times and the expected accuracy within 10^{-3} for the correction factors of each waveguide m. Moreover, these algorithms operate at the central matching frequency where the expected behaviour of the normalized admittance y(x, l) is often too much frequency-shifted in the first iterations, causing operation on the inverse behaviour at the given frequency.

Consequently, a convergence algorithm must be developed based on the general rules of the Lorentzian pattern behaviour of the normalized admittance function y studied previously:

- Increasing or decreasing the correction factor on the length fact_l allows shifting the initial pattern toward low frequency or high frequency respectively.
- Increasing or decreasing the correction factor on the offset fact_x allows increasing or decreasing the Re(y) part (conductance).

However, several difficulty points arise:

- Adjusting the offset to vary the conductance g also introduces a frequency shift of the pattern.
- Varying the length for a frequency shift directly impacts the conductance g and susceptance b values at a given offset x.
- It is essential to properly identify the behaviour of the Lorentzian pattern in the frequency sweep simulated from the beginning to avoid working on another part of the curve that would follow different laws.

2.4.2 Developed method

The method presented here proved to be the most stable and provided the best results throughout this work. It consists of an iterative feedback loop between Python and HFSS, in which the design is simulated, the results are exported and analysed, the correction factors on length and offset are then adjusted in the software, and the process is repeated until convergence.

As presented in Figure 34, the convergence is achieved in two main steps. In the first step, the idea is to bring the Lorentzian pattern into a frequency range Δf_1 around f_0 by focusing on the normalized admittance $Y/G_0(f)$ results in which the normalized conductance g(f) must be around 1 (Δg). In the second step, the idea is to converge toward a frequency range Δf_2 (smaller than Δf_1) by focusing only on the reflection coefficient $\Gamma_{mm}(f)$ (expressed as S-parameter in HFSS), whose minimum point must be below a threshold value Γ_{min}.

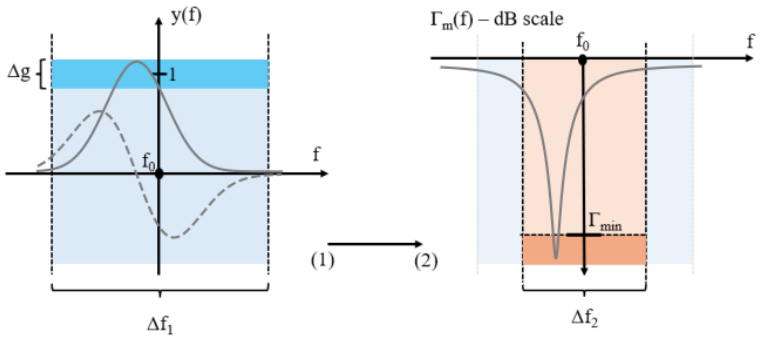

Figure 34 : Representation of the convergence zone of the two steps.

The reason for focusing on the reflection parameter Γ_{mm} more than the normalized admittance y_m at the end is due to the fact that working on the correction factors fact_x_m and

fact_l_m does not correct the possible linear mismatches within the line itself, partly due to losses. This implies a potential little shift between the real and imaginary parts of the normalized admittance function $y_m(x,l)$, with sometimes the centre of the imaginary part behaviour (local maximum derivative) below the abscissa around f_0, sometimes flattened, or even with multiple im(y) = 0 points around f_0. Knowing that in the second step, the research normalized admittance behaviour is already around the wanted frequency f_0, the solution to refer to the minimum point of the reflection coefficient is chosen.

A crucial step is to numerically locate the target behaviour of normalized admittance function y (Lorentzian – Lorentzian.Erf) on which the convergence is based. This exercise is more difficult for thin substrates because the simulation results obtained with theoretical dimensioning are becoming less and less accurate. Some difficulties on this point can be observed in the Figure 35 corresponding to the first simulation of an 8×8 array theoretically dimensioned for f_0 = 15 GHz, h_{rwg} = 254 µm and ε_r = 2.2. Considering the symmetry of the network in the E-plane, only the M/2 waveguides are initially studied to facilitate the analysis (thus the study is performed on 4 waveports rather than 8).

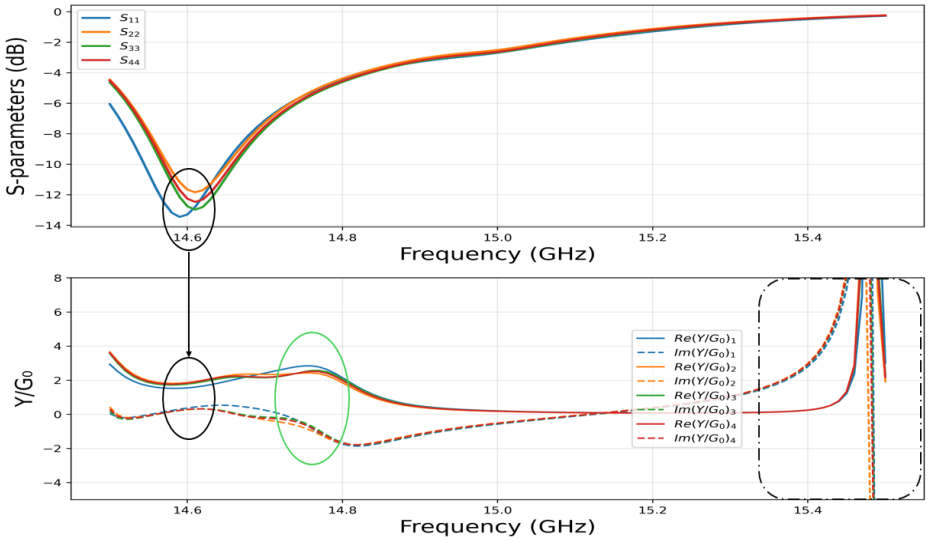

Figure 35 : (Up) Reflection coefficients Sii and (down) associated normalized admittances for an 8x8 array with f_0 = 15 GHz and h_{rwg} = 254 µm, simulated between 14.5 and 15.5 GHz

It can be observed that the expected behaviour of the normalized conductance g (local maximum) and susceptance b (decreasing trend) occurs around 14.75 GHz within the green ellipse. However, this does not correspond to the local minimum of the S-parameter at 14.6 GHz, where the normalized conductance reaches a local minimum around 1 and the normalized susceptance increases while crossing zero. Therefore, identifying the target behaviour of the normalized admittance y(x, l) based on the local minimum of the reflection coefficient is not feasible during the first iterations. Furthermore, around 15.5 GHz, a significant divergence of the y function can be observed, with values reaching up to ±40. Consequently, locating the target behaviour of the normalized admittance function y by searching for the maximum value of the normalized conductance g(f) cannot be applied either. The adopted solution is to use the derivative of normalized admittance function y(x, l). The behaviour of the derivate can be well observed in the Figure 36. Mathematically, the target behaviour is

identified using the derivative where the local maximum of the conductance corresponds to a zero for the derivative, and the decrease of the susceptance by a local minimum of the derivative.

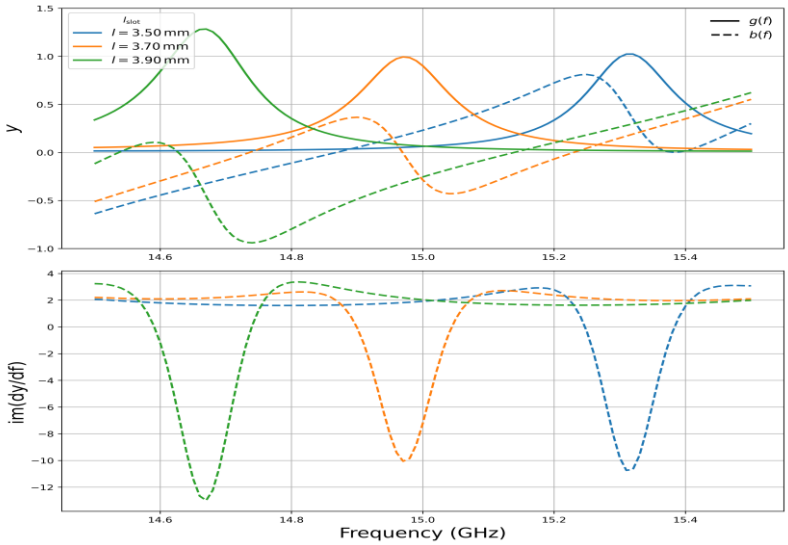

Figure 36 : (Up) y function and (down) its associated derivate of imaginary part for different length simulated between 14.5 and 15.5 GHz

Furthermore, an important interest in using this approach is that it allows the target behaviour of the normalized susceptance b to be located, even though it is not centred around the x-axis, and even does not necessarily pass through the x-axis (i.e. im(y) = 0 is invalid) as it can be the case at the first iteration as it can be observed in Figure 35 where the target behaviour zone (green ellipse, around 14.75 GHz) has a normalized susceptance b that is under the x-axis for some waveguides. Nonetheless, its derivative will have a local minimum reflecting the decrease in the target behaviour. This can be highlighted in Figure 37 by observing the frequency variation curves of the normalized admittance of one of the waveguides and its derivative.

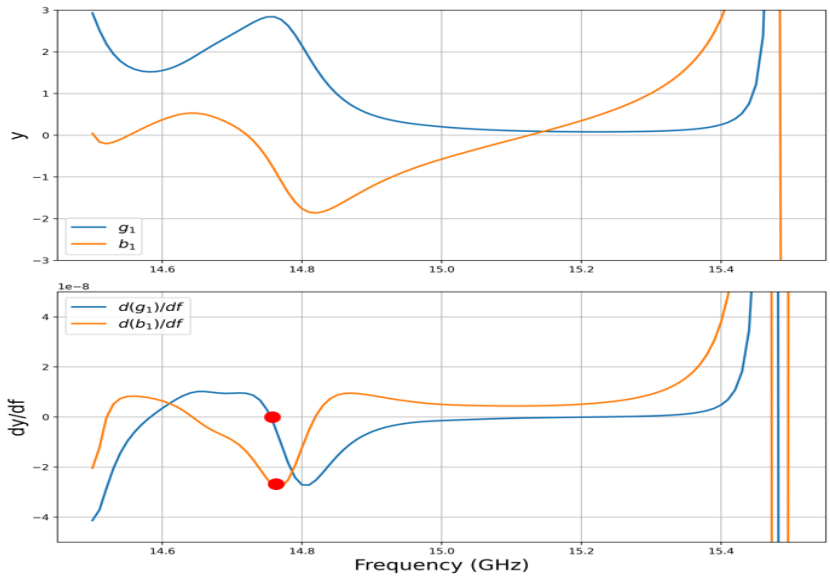

Figure 37 Real and imaginary parts of the input normalized admittance and associated derivative of the first input waveguide for tested 8x8 array simulated between 14.5 and 15.5 GHz.

It should be noted that this approach is also valid at frequencies where the normalized admittance function y(x, l) diverges. Therefore, in addition to using y'(x, l), a threshold value on the normalized conductance g(x, l) is added, ensuring that we stay on the target behaviour and not in the divergence zones.

As previously stated, the process is initiated with the design drawn in HFSS from Elliott's theoretical matrix, then the final convergence occurs when all waveguides have a reflection coefficient below a threshold Γ_{min} and within a frequency range Δf_2 around the matching frequency f_0. The general logic can be observed in the flowchart in Figure 38. Although the entire process is controlled from Python, the light green dashed rectangles correspond to 100% Python steps while the light blue ones correspond to simulation and HFSS control steps managed from Python.

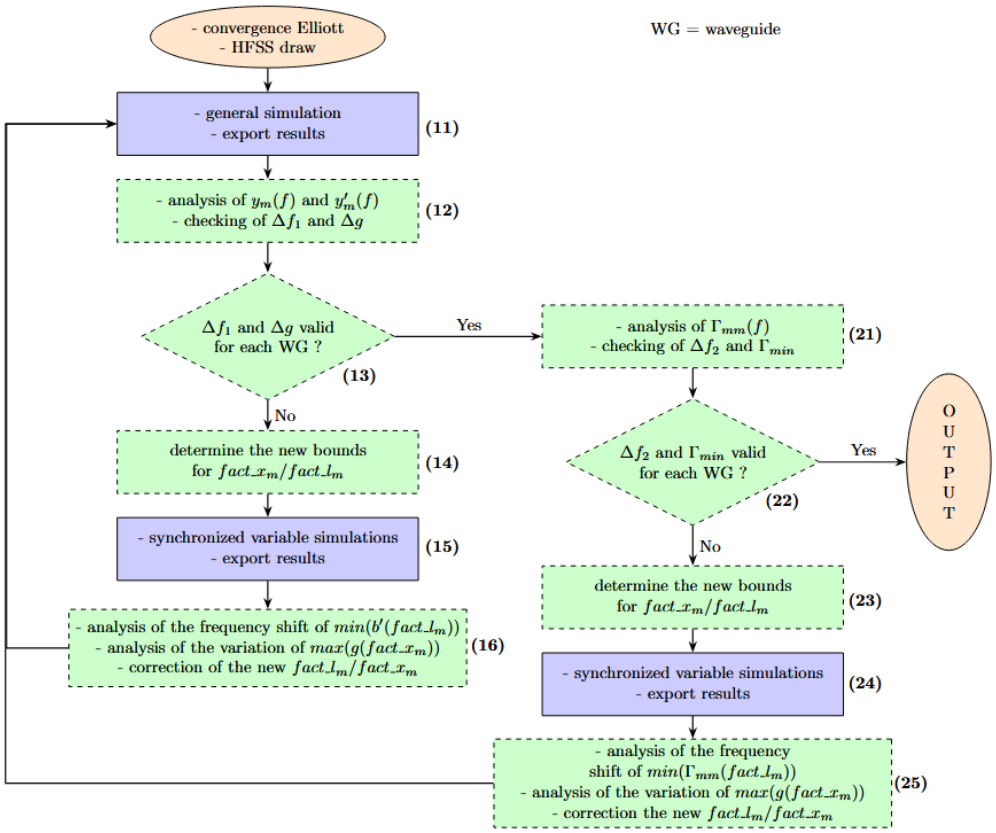

Figure 38 : Flowchart of the general algorithm of the design correction with Python and HFSS.

Some details can be added for each stage. They can be named as (1n) for the first loop and (2n) for the second one. Concerning the first loop:

(11) The design is simulated and the results exported to a given file.

(12) For each waveguide m, the target behaviour is located using the method described above, based on the normalized admittance function y(f) and its derivative y'(f). It can then be validated whether the target behaviour of $y_m(f)$ is within the desired first frequency range Δf_1 and whether the conductance is around 1 with Δg (Figure 34).

(13) It is checked whether all waveguides meet the True condition for Δf_1 and Δg. If False, loop 1 (14) is continued with the aim of running 'parametric' simulations. Otherwise, loop 2 (21) is entered.

(14) The objective of this step is to prepare the variation ranges of the correction factors on slots' length and offset of each waveguide, $fact_x_m$ or $fact_l_m$ values, for the next simulations. For each iteration of loop 1, a waveguide m will vary only one of the two factors $fact_x_m$ or $fact_l_m$. Usually, $fact_x_m$ is varied if the normalized conductance g(f) is outside the Δg zone, and $fact_l_m$ if the pattern is outside the Δf_1 zone. In the case where both must be corrected, they are alternated from one iteration to the next, starting with $fact_l_m$. In addition, to improve convergence, the min/max bounds of the correction factor variations must be retained in order to adapt to the results and bounds from the previous iteration.

(15) Synchronised parametric simulations are run where one of the two correction factors for each waveguide varies at the same time. The results are then exported.

(16) The analysis of the results then consists in obtaining the coefficients of the quadratic function representing the frequency shift according to the correction factor on the length $fact_l_m$, or the variation in conductance according to the correction factor of the offset $fact_x_m$. These coefficients are then used to find the new correction factor that brings the pattern closer to f_0 or returns the conductance to around 1. The correction factors are then implemented in HFSS before starting a new iteration.

Once the first loop is finished, the second one begins:

(21) The first actual step in loop 2, similar to (12), consists in validating line by line whether the minimum value of the reflection coefficient is within a Δf_2 range with a value of reflection coefficient below Γ_{min}.

(22) It is checked whether all waveguides meet the True condition for Δf_2 and Γ_{min}. If False, loop 2 (23) is continued with the aim of running 'parametric' simulations. Otherwise, the convergence algorithm is exited with the expected results.

(23) This stage has a same principle as (14). Note that if the reflection coefficient Γ_{min} condition is not valid, we refer to the values of the normalized conductance g(f) which have a local maximum in the area.

(24) Synchronised parametric simulations are run where one of the two correction factors for each waveguide varies at the same time. The results are then exported.

(25) Using the same model than (16), the frequency shift of the minimum point of the reflection coefficient or the variation in conductance is observed and evaluated numerically. These equations enable to obtain the new correction factors, which are updated in the HFSS design.

It is important to note that the following iteration takes us back to step (11) rather than a new independent general simulation on loop 2, because it may occur that the results of the first iteration of loop 2 lead to general simulation values that cause the expected behaviour of the normalized admittance y_m to deviate by one or two waveguides beyond $\Delta f_1/\Delta g$, even if the reflection coefficient Γ_m remains within acceptable bounds. Thus, the initial steps of loop 1 is started again (which could equally well be independent within loop 2) in order to verify the condition on $\Delta f_1/\Delta g$ before examining $\Delta f_2/\ \Gamma_{min}$.

In the various use cases in the thesis, the algorithm converges between 4 and 7 iterations, often with 2 to 3 iterations on the first loop.

2.4.3 Example with 1 design

A demonstration of design matching is performed using the same design as in Figure 35: 8x8 array at 15 GHz with a symmetrical distribution in the E and H planes, RT\Duroid 5880 ($\varepsilon_r = 2.2$, $\tan\delta = 0.9*10^{-3}$) with $h_{rwg} = 254$ µm. The following parameters are fixed:

- $\Delta f_1 = \pm 25$ MHz, $\Delta g = \pm 0.08$, $\Delta f_2 = \pm 5$ MHz and $\Gamma_{min} = -30$ dB

- Initial parametric step of 0.5% on $fact_l_m$ and 4.5% on $fact_x_m$

- **First iteration**

(11)-(12)-(13) As shown in Figure 35, the target model coming from the design drawn with theoretical formulas is around 14.75 GHz and not 14.6 GHz (min(S_{mm})). The method described above is then used to locate it using the normalized admittance y function and its derivative y'.

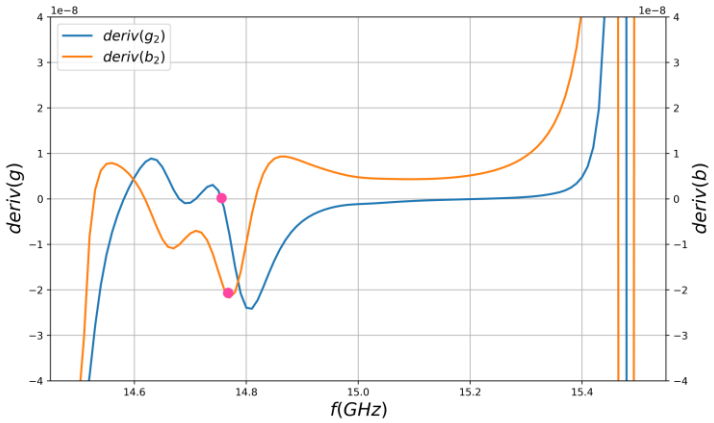

Figure 39 : Derivative of the real and imaginary parts of the normalized admittance of the second line depending on frequency.

Identifying the target behaviour is complex in the first iteration. It can be observed in Figure 39 that two frequencies correspond to g'(f) = 0 and b'(f) = local minimum. However, as both are 0.2 GHz lower than f_0, the boolean checking is False for Δf_1, leading to (14).
(14)-(15) All of the waveguides must be corrected. Knowing that the pattern is below f_0 for all the waveguides, the correction factors on the slots' length fact_l_m must decrease for each waveguide. The parametric step on the initial fact_l is used. The parametric simulations are then launched and the results exported.

(16) The results obtained show the frequency alignment of the pattern as a function of the slots' length correction factor fact_l_m as can be observed for the second waveguide in Figure 40.

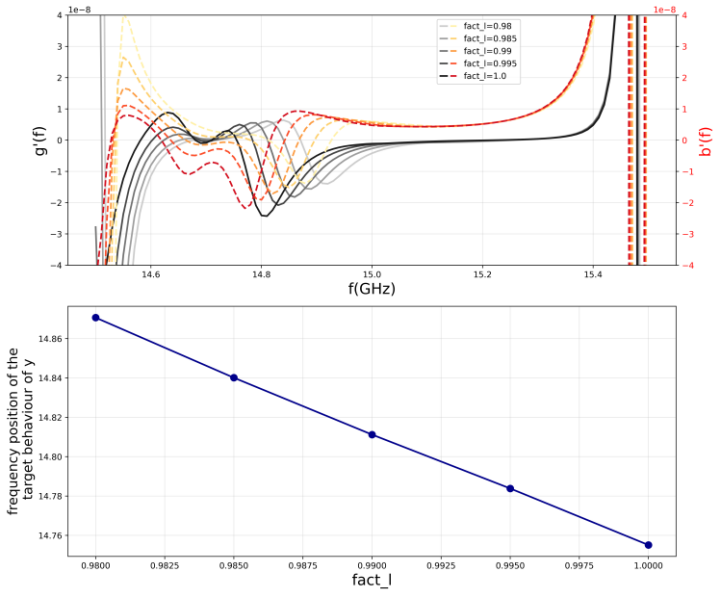

Figure 40 : Derivative function of the normalized admittance for different fact_l depending on frequency and (down) associated shift in frequency depending on fact_l.

This work is done for each waveguide, thus obtaining the correction factors for the four waveguides, which are then implemented in HFSS.

- **Second iteration**

A new iteration of loop 1 is launched, starting with the initial simulation of the design. It can be observed that the desired behaviour of the normalized admittance y(f) is centred around f_0 (as can be seen in Figure 41 for fact_x = 1), but the set still does not meet the conditions Δf_1 and Δg to move on to the second loop. A second series of simulations in which the slots' offset correction factor $fact_x_m$ decreases is then launched, and the exported results are used to obtain the function $max(g(f, fact_x_m))$.

The importance of the decreasing of the maximum conductance thanks to the decreasing of $fact_x_m$ can be observed as well as the little shift in frequency undergone because of the procedure. As before, the best correction factor on the slots' offset $fact_x_m$ for each waveguide is calculated and updated in the software.

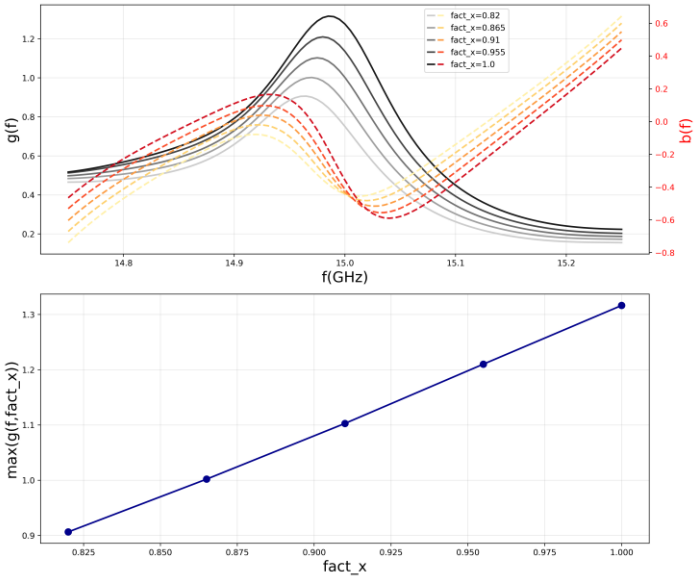

Figure 41 : (Up) Real and imaginary parts of the normalized admittance for different fact_x depending on frequency and (down) associated decreasing of the maximal conductance depending on fact_x.

- **Still 2 iterations are necessary before the checking of iteration 5:**

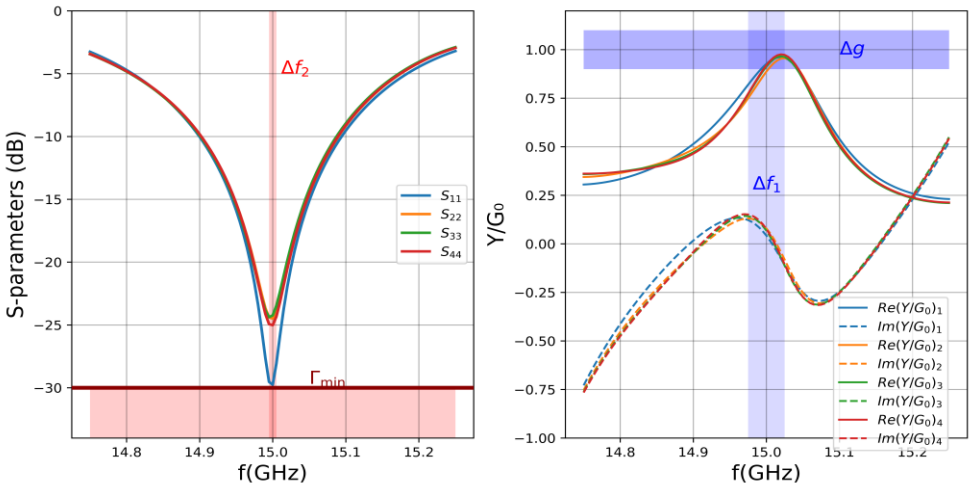

Figure 42 : Validation of the checking of Δf_1 and Δg on y function and new checking of Δf_2 and Γ_{min} on the second loop.

It can be observed in Figure 42 that the checking for Δf_1 and Δg on the normalized admittance function y can be validated. Nevertheless, the conditions for Δf_2 and Γ_{min} are not validated. The reflection coefficients for each waveguide are already around f_0. To lower the minimum value below Γ_{min}, we test different fact_x_m coefficients. it finally ends up with:

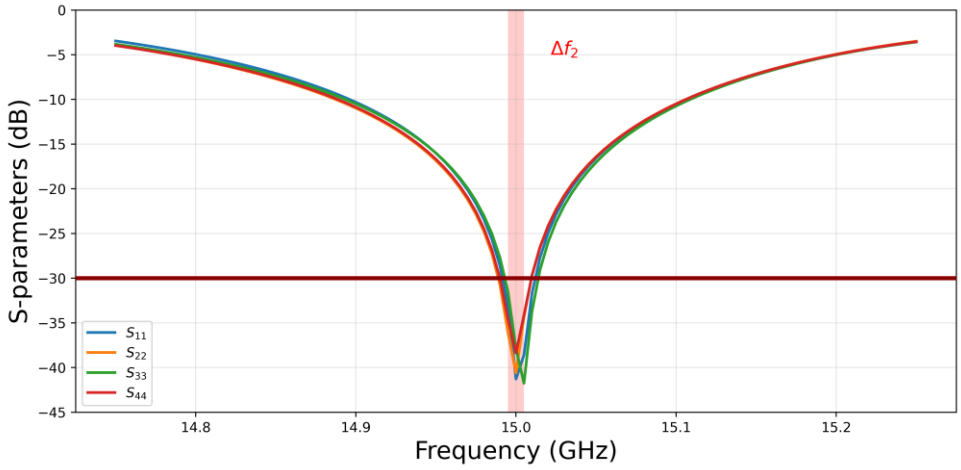

Figure 43 : Final S-parameter for each waveguide respecting the fixed conditions on Δf_2 and Γ_{min}.

Six iterations were therefore necessary to converge to the network at f_0 for our 8x8 network. The values of the correction factors are around 0.95 for the slots' length (fact_l_m) for all the waveguides and between 0.85 and 0.92 for the slots' offset (fact_x_m).

The nominal simulation using a multicore simulation server takes about 30 minutes and the 5-variable parameter simulation 1 hour 20 minutes. The total time required was therefore just under 8 hours between the initial design based on Elliott's theoretical sizing and the final adaptation on the software.

2.5 Development of a general algorithm for automatization

2.5.1 Objectives

As previously stated, the design procedure of slot arrays based on Elliott's theory is scientifically complex. The algorithms require a certain amount of development time, as does the drawing of the design using software tools, and the subsequent correction and adaptation process can also be intricate.

This procedure requires, beforehand, a solid theoretical background to properly understand Elliott's method (although not all theoretical demonstrations are directly useful), as well as proficiency in programming languages such as MATLAB or Python in order to characterize or use the equivalent slot's normalized admittance function $y_0(x, l)$ and to implement the recursive algorithm that generates the matrix of slot pairs (x_{mn}, l_{mn}) while taking into account the RF parameters. Additionally, a good command of HFSS or CST software is required for the design and the necessary corrections.

For this doctoral work, since the goal was to design multiple SIW slotted array for different frequencies, dielectric materials, or array sizes, it was decided to develop a set of algorithms, accessible through a graphical user interface, in order to fully automate the entire design procedure from start to finish. Thus, the objective of the tool is to take several essential RF data inputs and to output the corresponding design at the desired frequency directly into the electromagnetic simulation software (HFSS), without requiring any human intervention.

Several useful features have also been implemented to enhance the understanding of the topic, such as the visualization of various plots that provide better insight into the unitary behaviour of the slot (function y_0), the ability to simulate the designed structure both with and without considering internal and external mutual coupling, and the display of the convergence of Elliott's matrix correction algorithm at each iteration of the loops described in section 2.4.3. Furthermore, the tool allows for adaptation for both rectangular waveguide and substrate integrated waveguide configurations.

2.5.2 General operation

As discussed previously, certain Python scripts are used to control HFSS simulations, display the expected results, export them, or modify specific dimensional parameters. Another type of Python script, not employed in the correction algorithm, involves the use of drawing commands. This functionality makes it possible to generate large array structures within a few minutes. Thus, these drawing scripts, together with the simulation control scripts, enable full automation of the conventional procedure required to obtain the M×N array design within the software environment. This procedure is illustrated in the flowchart shown in Figure 44.

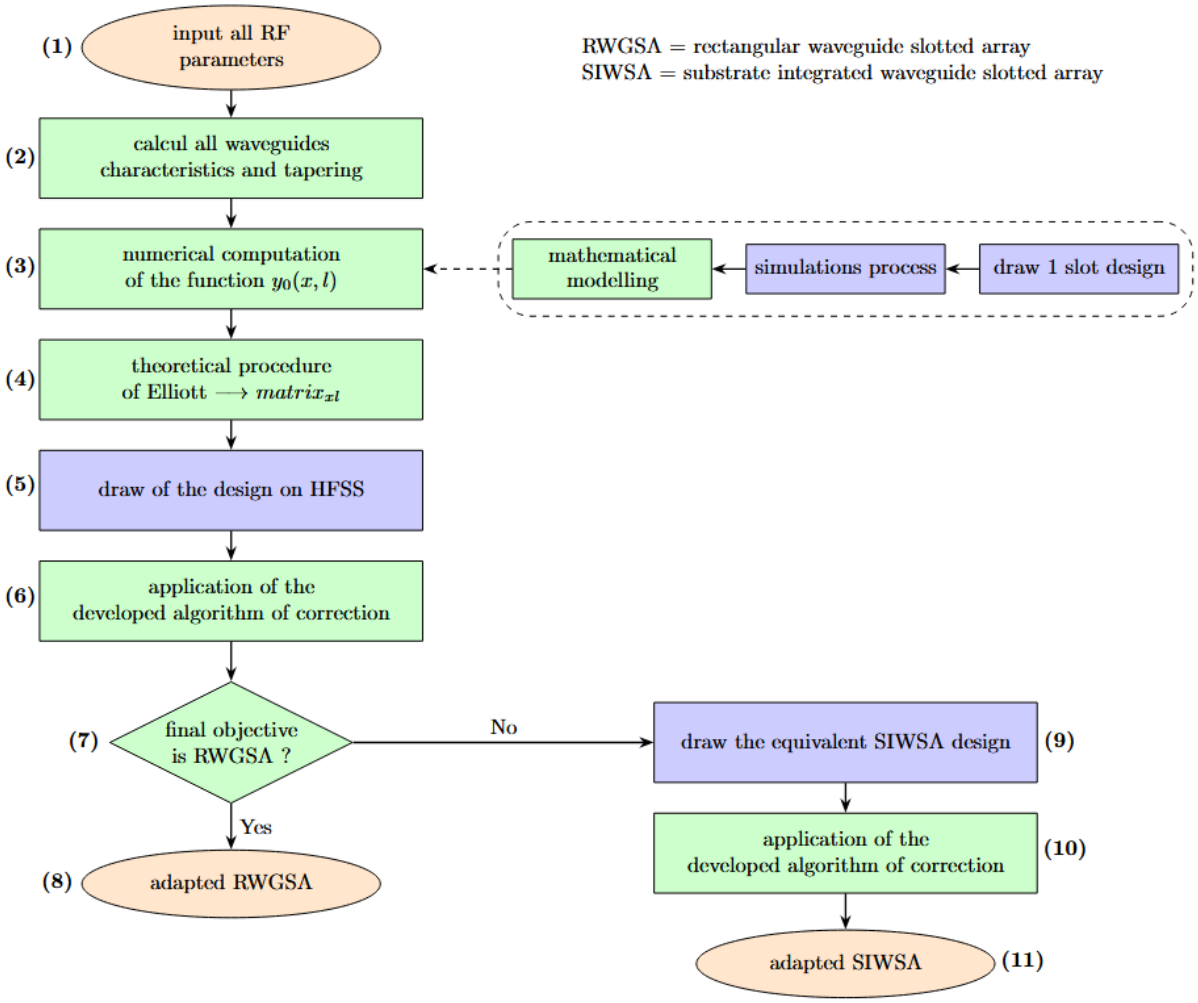

Figure 44 : Flowchart of the general processus of automatization to obtain an adapted slotted array on RWG or SIW.

Like on the last flowchart, some details can be added for each stage:

(1) Input all RF parameters consists in giving the frequency of work f_0, the number of waveguides M and elements by waveguide N, the wished tapering, and the characteristics of the waveguides: RWG or SIW, cut off frequency f_{c10}, dielectric and conductor properties, distance between waveguides and if SIW is selected, the size of the vias and their period.

(2) From all the input RF parameters, all the theoretical calculations for waveguide dimensions and pondering are done.

(3) The crucial step of obtaining the coefficients of the numerical function y_0(x,l,SavedCoef) representing the equivalent normalized admittance is broken down into several sub-steps. The first consists in automatically creating the design with the RWG and a single slot on HFSS. Following one of the three selected methods (Stegen, Lorentzian, interpolation), the series of simulations with potential intermediate analyses (Stegen and Lorentzian, Figure 29) is launched and the results are exported. The mathematical analysis specific to the selected method is performed on the obtained results and the associated coefficients are saved. This step takes approximately 30min with the interpolation method and around 1 hour for the methods of Stegen or Lorentzian.

(4) Elliott's theory and its associated algorithmic procedure discussed in 2.2.3 are used to obtain the sizing matrix of the slot coupling pairs (x_{mn}, l_{mn}) of the array.

(5) a design is created and generated with all the theoretical calculated values for the waveguides and the slot array.

(6) The developed iterative algorithm presented in 2.4 is applied with the aim of generating the corresponding RWG slotted array design adapted for implementation in HFSS.

(7) If the aim was to obtain the slotted array in a RWG, the procedure finishes with (8). Otherwise, it continues with the SIW procedure. The reason why the adaptation is first carried out on the RWG slotted array, even though the final goal is to obtain an SIW slotted array, is that the electromagnetic behaviour of the SIW can be approximated by its equivalent RWG structure, and the simulation time is significantly shorter in the case of the RWG slotted array than for the SIW slotted array. Indeed, the presence of vias in the SIW requires a finer mesh in simulations and introduces slight local perturbations of the TE_{10} mode, resulting in significantly longer computation times compared to the RWG slotted array. Thus, since several iterations are required in the correction algorithm, it is more efficient to perform them on the RWG slotted array rather than on the SIW slotted array.

(9) Like in (5), the SIW slotted array is drawn with the corrected matrix of the slot coupling pairs (x_{mn}, l_{mn}) obtained from (6)

(10) During the transition from RWG slotted array to SIW slotted array, a slight frequency shift of a few tens of MHz is often observed. The same correction algorithm is then applied to the SIW slotted array, with typically only one or two iterations being sufficient.

(11) We then obtain the wanted SIW slotted array adapted at f_0 on HFSS

The automatization of all this procedure allows to obtain a M×N slotted array for a given waveguide best meeting the given RF specifications in less than 24 hours. This tool, which has not previously been reported in the literature, proved to be extremely useful for this thesis, as it enabled the rapid generation of a large number of HFSS-compatible designs for multiple operating frequencies and dielectric materials. More generally, a user without prior experience in electromagnetic simulation software or slotted antenna array design can, within one day, achieve an array that meets the targeted RF characteristics. An interesting extension of this algorithmic approach would be to subsequently correct the slotted array on a slot-by-slot basis.

2.5.3 Realized designs

Using this presented design flow, a set of designs were dimensioned on HFSS for two frequencies (10 and 15 GHz), respectively in bands X and Ku, an uniform distribution in E-plane and a distribution of Chebyshev in H-plane allowing to fix the level of the side lobe (SLL) of the array factor of the radiation pattern at -23dB and 3 dielectrics (SF280, RT/Duroid 5880, Ro4350). The SF280 [47] is a Modified Polyimide (MPI) composite with flexible copper clad laminate (FCCL) produced by Taiwanese company Shengyi Technology Co.. RO4350 [48] and RT/Duroid 5880 [49] are both produced by the American company Rogers Corporation but with

different chemical properties : RT/duroid 5880 is PTFE with glass reinforcement and RO4350B a ceramic-filled glass/epoxy composite.Table 5 helps to compare the 3 used dielectrics:

	SF280	RT/Duroid 5880	RO4350
ε_r – tanδ(10^{-3})	2.92 – 3.1	2.2 – 0.9	3.66 – 3.7
used thickness (µm)	127	254	254
moisture absorption	0.4%	0.02%	0.06%
C.T.E for (x,y,z) in ppm/°C	-	(34,48,237)	(10,12,32)
Tensile Modulus for (x,y) in MPa	-	1070, 860	16800, 14200

Table 2 : Physical characteristics of the 3 used dielectrics

Unfortunately, there is little common basis for comparison between the datasheets of the three dielectric materials. The SF280 datasheet is notably lacking in mechanical specifications. After direct comparison, it appears that the SF280 is the most flexible (by far) allowing to curve a SIW slotted array (SIWSA) for a radius of 1cm, following by the Ro5880 and finally the RO4350B allowing to curve a SIWSA for a radius of maximum 8cm.

The application of the general automatized procedure for the 2 Rogers dielectrics converged without problem, but difficulties were encountered for the 127 µm thick SF280. Indeed, because of the thinness, the very strong internal mutual coupling MC_{int} leads to final slot length in a region where the unit slot (without MC) doesn't radiate ($l_{slot_final} < 0.9l_{res}(x)$) leading to difficulties to converge during the Elliott's procedure and also to converge during the developed algorithm of correction on HFSS.

The final SIWSA designs matched on HFSS are fed by a 1×4 power divider in the opposite side of the slot array as we can see in Figure 45 in order to minimize the interaction between the feeding network and the radiating structure.

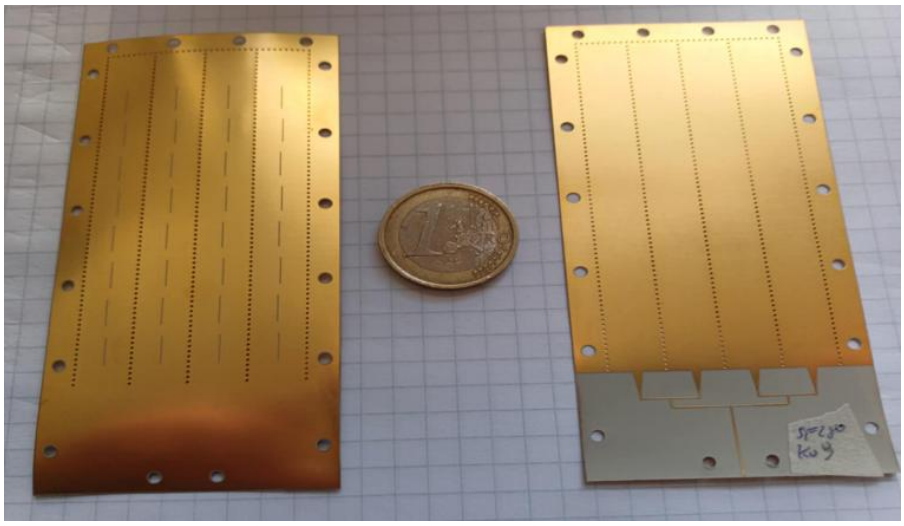

Figure 45 : Realized design of 4x8 SIW slotted array with SF280 in Ku band, (left) top and (right) bottom.

Some tested designs in flat configuration are given in the following. The reflection coefficients given in Figure 46 are measured thanks to a vector network analyser (VNA).

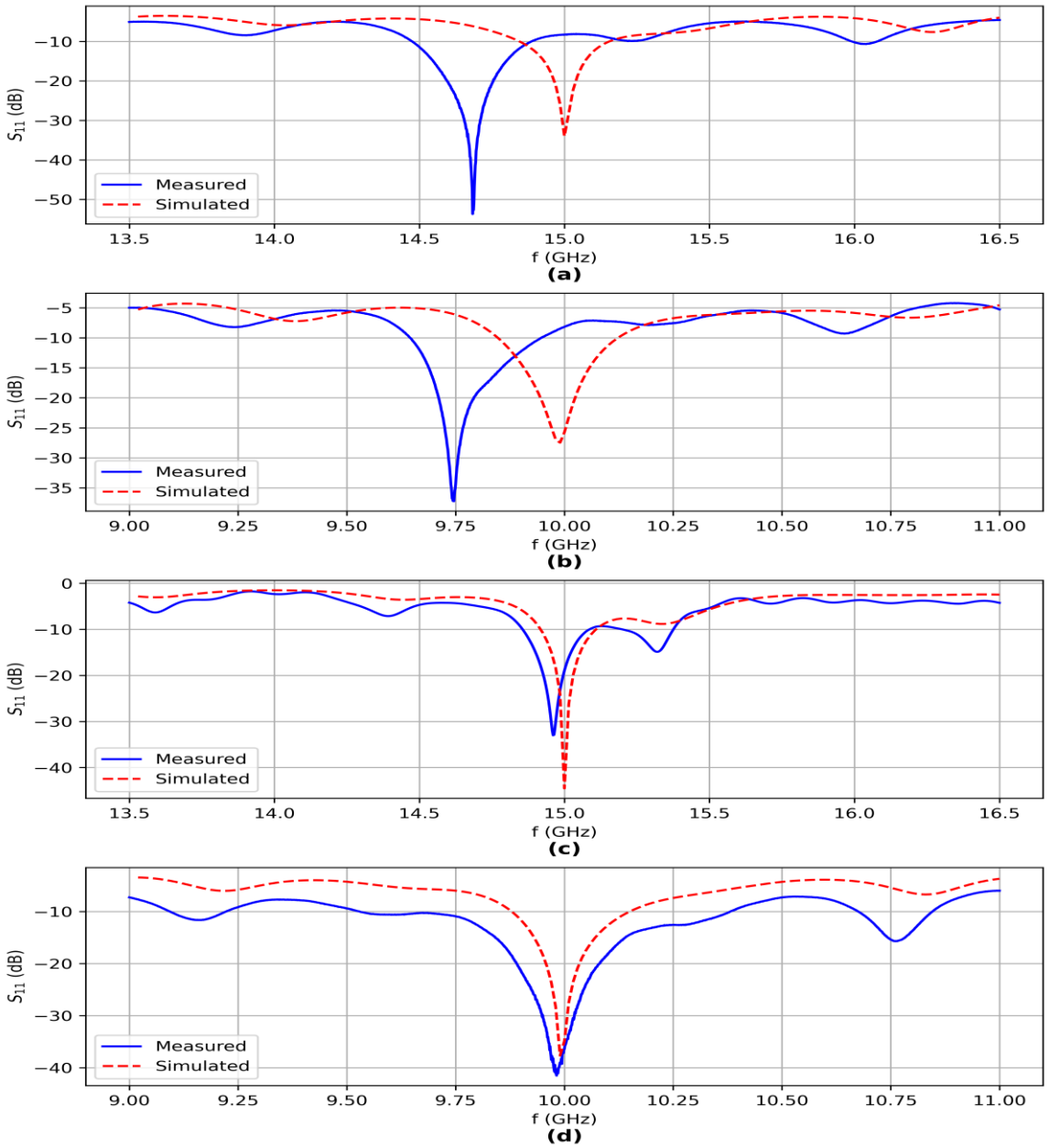

Figure 46 : Measured and simulated reflection coefficient vs. frequency for (a) SF280_Ku design, (b) SF280_X design, (c) Ro5880_Ku and (d) Ro4350_X.

As it can be seen in Figure 46, the 2 Rogers dielectric (c) (d) are well matched at the wanted frequency contrary to the SF280 designs (a) (b) with a shift of 0.25 - 0.30 GHz in frequency. This is probably due to a shift in the relative dielectric permittivity of the material, which exhibits a slight discrepancy with the value provided in the datasheet (2.82). The retro-simulations performed using a relative dielectric permittivity of $\varepsilon_r = 3.08$ produce results in good agreement with the measurements for X and Ku designs as observed in Figure 47, suggesting that the discrepancy is related to the real value of the dielectric permittivity analyses.

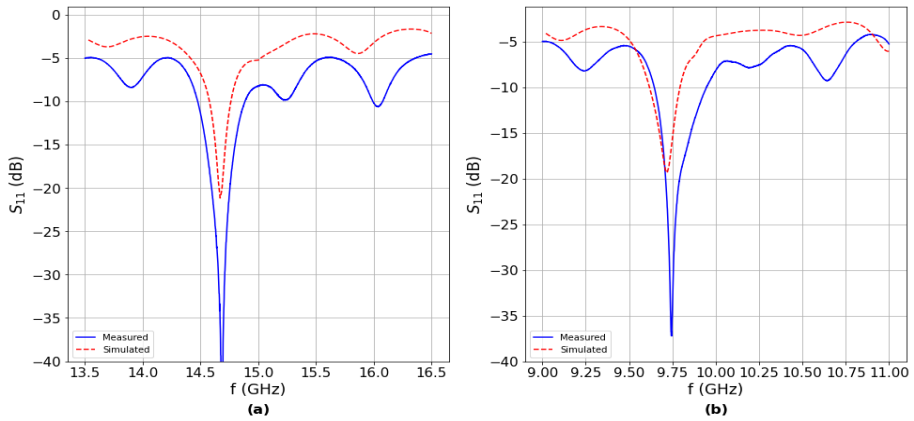

Figure 47 Measured and simulated reflection coefficient vs. frequency for (a) SF280_Ku design, (b) SF280_X design, with retro simulation with $\varepsilon_r = 3.08$

In the same way, the gain in both planes E and H are measured in anechoic chamber. More details on the measurement process are given in chapter 4.3. Measures are compared to simulation for the designs. An example is given in the following figures:

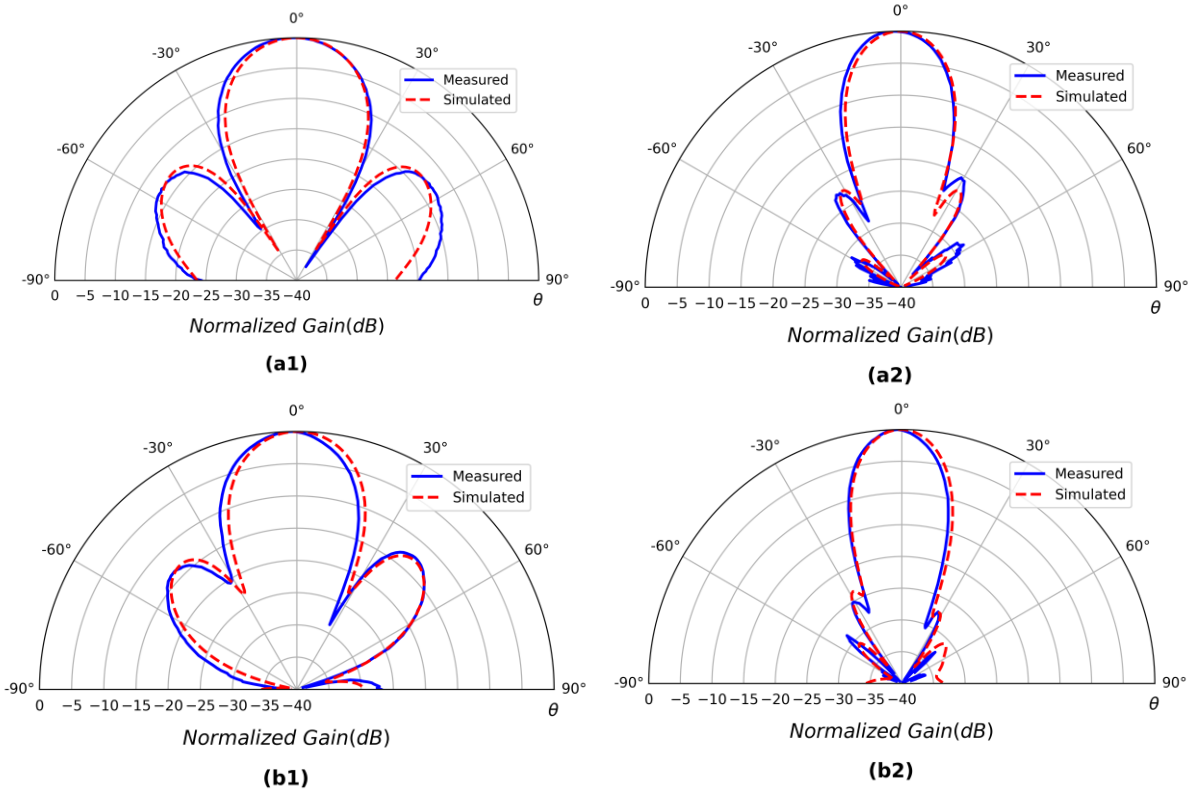

Figure 48 : Comparison simulation vs measure for both designs in Ku band: the design SF280 (a1) in E-plane and (a2) H-plane, and Ro5880 (b1) in E-plane and (b2) H-plane.

It can be observed that the simulated and measured results match well in both planes. Nonetheless, an asymmetry in the H-plane can be observed for both designs. Different reasons can explain it. Firstly, the reflector plane itself is asymmetrical due to the 1×4 power divider. Furthermore, the correction algorithm used to bring the circuit matching for each waveguide back to the correct frequency does not correct the 1×N network locally for a given waveguide. As a result, slight asymmetry is often present in each waveguide due to losses but also to the electromagnetic impact of the short circuit on the last slot. It is then difficult to find perfect

symmetry and wanted tapering. The two Ku-band designs presented here will be used in Chapter 4 on conformation studies due to their flexibility properties.

2.6 Conclusion

This second chapter first provided an overview of standing wave feed slot array matching and the importance of considering the mutual couplings. Elliott's theoretical procedure, often taken as a reference, was then briefly presented. In our case study where mutual couplings (MC) are very strong, the final values of the pairs (x_{mn}, l_{mn}) can be far from the initial values and thus from the behaviour of the function y_0 representing the normalized admittance of a single slot without MC.

Since Elliott's method for designing these arrays requires a numerical approximation function of y_0 beforehand, a new analytical method based on Lorentzian functions and providing more accurate results than the reference method was developed. Subsequently, knowing that a significant discrepancy exists in the SIW slotted array (SIWSA) framework (undergoing strong intern mutual coupling) between the theoretical design results obtained with Elliott's procedure and the corrected design in simulation software, an algorithm for automating the correction in software through recursive dialogue between Python and HFSS is presented. Along the same waveguides, a set of more general algorithms controlled from a graphical user interface (GUI) is presented with the objective of automating the entire design procedure from start to finish, including software-based matching, for a given set of specifications. This incorporates the work on the convergence algorithm previously cited as well as the work on the slot's equivalent normalized admittance function y_0. Finally, a brief presentation of various designs realized with this tool is provided.

It should be noted that the work carried out in this chapter was highly valuable for a thorough electromagnetic understanding of SIW slotted array (SIWSA) through in-depth theoretical study and the development of associated computational codes and tools. These are particularly effective for most dielectric thicknesses used in SIW slotted array fabrication (flexible or otherwise).

However, difficulties were encountered when using very thin substrates such as 254 µm and especially 127 µm. Indeed, for these thicknesses, the internal mutual coupling is so strong that Elliott's procedure becomes too approximate, as can be seen from the convergence difficulties for theoretical dimensioning and the significant deviation from the target results in the first simulation. This phenomenon becomes increasingly significant as the thickness of the dielectric decreases and its relative permittivity ε_r increases. A new matching procedure for such thin flexible arrays should be implemented.

Chapter 3 - Development of a new method to match thin slotted array

3.1 Introduction

To investigate flexible SIW slotted array (SIWSA) structures with the aim of achieving bending radii of only a few centimetres, the stiffness of the dielectric materials commonly used for optimal electromagnetic performances (such as Rogers's dielectrics reported in the literature) necessitates the use of thin samples across each range. As previously discussed, the slot's equivalent admittance matching of very thin linear slot arrays is strongly affected by internal mutual coupling (MC_{int}), which complicates the analysis. As observed in section 2.2.2, a shift of approximately 6% in the resonant length was observed by simulations when comparing 1-slot design to 2-slots design, each subject to a single MC_{int}, for a rectangular waveguide (RWG) of 127 µm. In the case of a 1×N linear array configuration, each slot experiencing two MC_{int} would undergo an overall reduction of about 12% in resonant length. This leads to offset and length pairs (x, l) for which the unitary slot is not matched at all. The use of the Stegen's procedure, presented in section 2.2.1, which examines the slot behaviour for variations of ±10% (or even ±5% in most references, such as Elliott's work [46]), becomes less meaningful in this context. Moreover, for thin waveguides, the normalized conductance g and susceptance b values already tend to approach zero when the slot length equals $0.9 \cdot l_{res}(x)$. The mutual coupling itself is responsible for the adaptation.

Furthermore, the Elliott's procedure used in the previous chapter presents significant limitations for these study cases. The unitary slot's equivalent normalized admittance function y_0 obtained from full-wave simulations tends to zero in the final matching region, making the process entirely dependent on theoretical electromagnetic demonstrations. In addition, both the theoretical and algorithmic work related to external mutual coupling (MC_{ext}) becomes almost irrelevant (as observed in section 2.2.2, since MC_{ext} decreases linearly with thickness (2.10)). The determination of the normalized active admittance values for each slot therefore relies exclusively on fully theoretical formulas, namely (2.7), (2.8), and (2.15), which moreover neglects certain non-negligible parameters at such small thicknesses, such as the slot width or the conductor thickness.

In summary, applying this method requires substantial theoretical understanding as well as several days of algorithmic development, while its final validity range remains debatable and the results obtained are far from the final software-corrected values. It would thus be of interest to identify a new method specifically adapted to this study case and ideally theoretically simpler and more intuitive, easier to implement, and capable of producing preliminary simulation results much closer to the expected outcomes.

The approach that was followed consisted in retaining a single theoretical formula from Elliott (2.6) in link with (2.9), and in determining all the functions of its variables/coefficients entirely from simulation software. To accomplish this, the software tools that perform the local electromagnetic calculations on the simulated structure are used to obtain the voltage across the slot V_{slot} as well as that of the propagation mode in the waveguide V_n. This makes it possible to obtain, for the given waveguide, the normalized slot voltage v_s found in (2.6) as well as the ratio between the normalized admittance y and the normalized slot voltage v_s, corresponding to the product of (2.7) and (2.8). This exercise can be performed for one slot as well as for several, thus enabling the behaviour of the normalized voltage alone v_0 and the slot-to-slot mutual coupling factors to be observed. Consequently, the new method is to mathematically refine the V_{slot} voltage by using the software tools and simulations to obtain its numerical function rather than theoretical formulas.

This chapter therefore presents several points of interest. First, from a purely theoretical perspective, the approach leading to the derivation of the matrix system used for the matching of a linear in phase slotted array is introduced. The associated algorithmic procedure is therefore described in a second time. Then, several extension cases of the developed method are examined, such as its application to the matching of a linear slot array operating in the TE_{20} mode, as well as the consideration of external mutual coupling effects for thicker waveguides. Finally, as in the previous chapter, a concise presentation of the designs obtained using this new method will be provided.

3.2 Mathematical approximation and associated procedure

3.2.1 Software model used

In the previous chapter, the final equations used for the slot's equivalent normalized admittance y and the mutual couplings involved the concept of slot voltage V_{slot} across the bounds of the magnetic dipole only when considering the field distribution in the calculation of mutual couplings. The actual notion of the superposition theorem applied to the slot voltage V_{slot}, as demonstrated in [31] and [32], is therefore overlooked when employing the final equations of Elliott's method.

The main idea behind this new method is to refine the slot's voltage V_{slot}, but using the software tools directly to obtain its value at the desired frequency f_0 rather than theoretical formulas. Indeed, on a simulation software such as HFSS, certain calculations such as the integration of an electric field $\vec{E}$(V/m) along an oriented segment $\overrightarrow{dl}$ (m) are possible at the working frequency, giving the complex voltage drop, in volts:

$$V = \int_l \vec{E} \cdot \overrightarrow{dl} \tag{3.1}$$

This tool is used on different segments that can be placed in the middle of each slot or on all maxima of the TE_{10} propagation mode (including the excitation port). For a lossless model, it can be observed that the voltage V_{mode} at the centre of each antinode n of the TE_{10} mode (from the waveport to $\lambda_g/4$ of the short circuit) is equal in amplitude and opposite in sign for two consecutive segments. When slots are added, the measurement of V_{mode} voltages becomes extremely disturbed by the slot above. Indeed, with the fineness of the guide, the offset of the slots is very small and sometimes less than $W_{slot}/2$, which leads to a local very strong electromagnetic disturbances returned to the waveguide, especially at the location where the measuring segment for V_{mode} is situated. This produces aberrant results. These significant errors obtained using software are nevertheless avoidable in the sense that, according to Stevenson and Elliott's theory: "when all the slots are in a common waveguide and resonantly spaced ($\lambda_g/2$), the mode voltage V_{mode} is common to all slots except for an alternation in sign". Thus, the voltage measured on the waveport excitation, undisturbed by the radiation from each slot, corresponds to the value of the voltage V_{mode} that is supposed to be common to all slots on the same waveguide. Note that the waveport must also be located at an antinode of the propagation mode, like the slots. V_{mode} can therefore be renamed V_{in} for more simplicity.

Finally, working on a 1×N waveguide, the HFSS design can be prepared such that a segment is present in the middle of each slot giving the local voltage in the slot plus the voltage on the waveport, providing the general mode voltage V_{in}. An example is given in Figure 49.

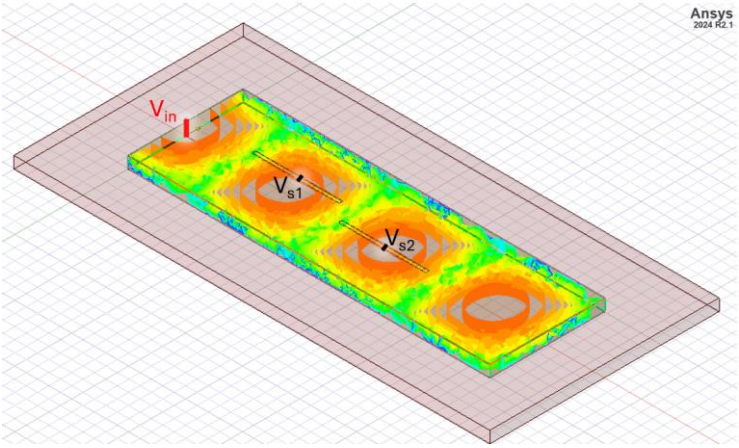

Figure 49 : Screen from HFSS software presenting the lines of integration for the slot voltage V_s and the mode voltage V_{in}.

In the Figure 49, the 2 black lines correspond to the 2 segments giving the voltage in the slots 1 and 2 (V_{s1} and V_{s2}), while the purple one on the wave port (top left corner) gives the mode voltage. Next, knowing that we will initially be working with 1×N waveguide, N slot voltages are simulated/calculated and the associated a single mode voltage V_{in}. Therefore, we will use the numbering V_1, V_2,...V_n for the voltage of the N slots. Talking about normalized slot voltages v_n simply corresponds to the ratio between the slot voltage and the propagation mode voltage V_n/V_{in}. A distinction must therefore be made between the numbering used for this chapter and the original numbering given in [31] and [32]. It must be kept in mind that all the analysis and simulations are performed at the working frequency f_0.

3.2.2 Slot's electromagnetic behaviour

Based on the software design model presented above, which allows the voltage in the slot and the propagation mode voltage in the guide to be obtained at the working frequency f_0, the relationship between the equivalent normalized admittance of the slot y_n and its normalized slot's voltage v_n can be studied. This relationship corresponds to Elliott's first equation (2.6). Summarising his analysis [30]: 'the mode voltage and slot voltage are in phase quadrature if y is pure real'.

To test our software model, the 127µm RT/Duroid 5880 design matched at 15GHz is used with 1 slot in the rectangular waveguide (RWG). Figure 50 presents a comparison of simulated values of the slot's equivalent normalized admittance $y_0(x, l)$ and the normalized slot's voltage $v_0(x, l)$ for 1 slot (without mutual coupling).

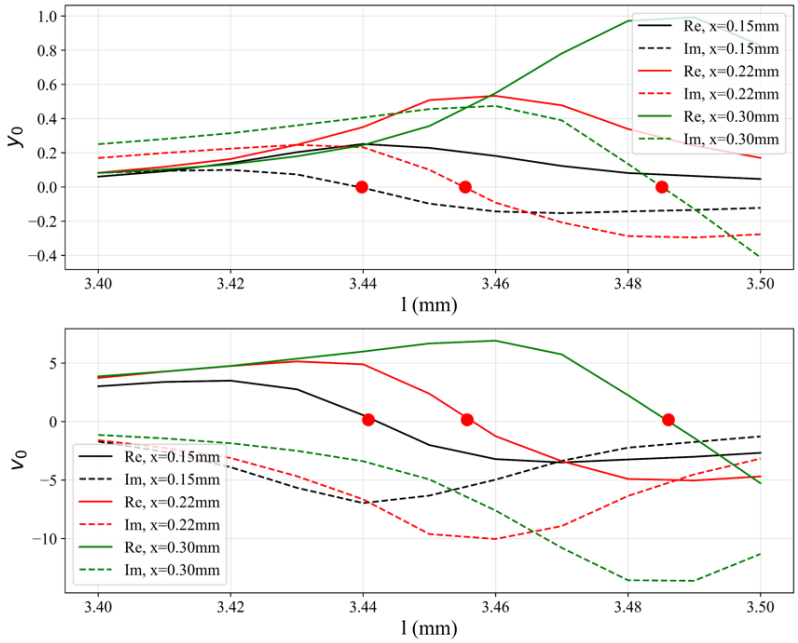

Figure 50 : Variations of (top) normalized admittance y_0 and (bottom) normalized slot voltage v_0 depending on the couple (x, l) values for 1 slot with RT/Duroid 5880 127µm at 15GHz.

From Figure 50, the logic of the (complex) relationship between the normalized admittance y_0 reflecting the resonance of the slot and its normalized slot voltage v_0 is clearly observable: the slot resonates when real and imaginary parts of $y_0(x, l)$ are max and null respectively, which correspond to a zero and a minimum value for $v_0(x, l)$. The real and imaginary behaviour are inversed, as mathematically anticipated with the definition of $K_1.f(x, l)$ in (2.7) and (2.8) supposed imaginary pure. It must be noted that the sign of $v_0(x, l)$ on the simulated sign depends on the chosen sign for the offset x and also the direction of the drawn vector $\overrightarrow{dl}$ on which the electric field $\vec{E}$ is integrated. Therefore, a fixed direction must be chosen when drawing the design.

The rest of the reasoning will therefore be based on the Elliott's first equation, rewritten with the indices more appropriate to our model:

$$\frac{Y_n}{G_0} = K_1.f(x_n, l_n)\frac{V_n}{V_{in}} \Leftrightarrow y_n = \alpha(x_n, l_n).v_n \qquad (3.2)$$

For a 1-slot design, at the working frequency f_0, the function $y_0(x, l)$ can be obtained as before, to which are added the normalized slot voltage $v_0(x, l)$ and the ratio between these last two renamed $\alpha(x, l)$. For the same range of simulations that for the last tested design, α has the following behaviour:

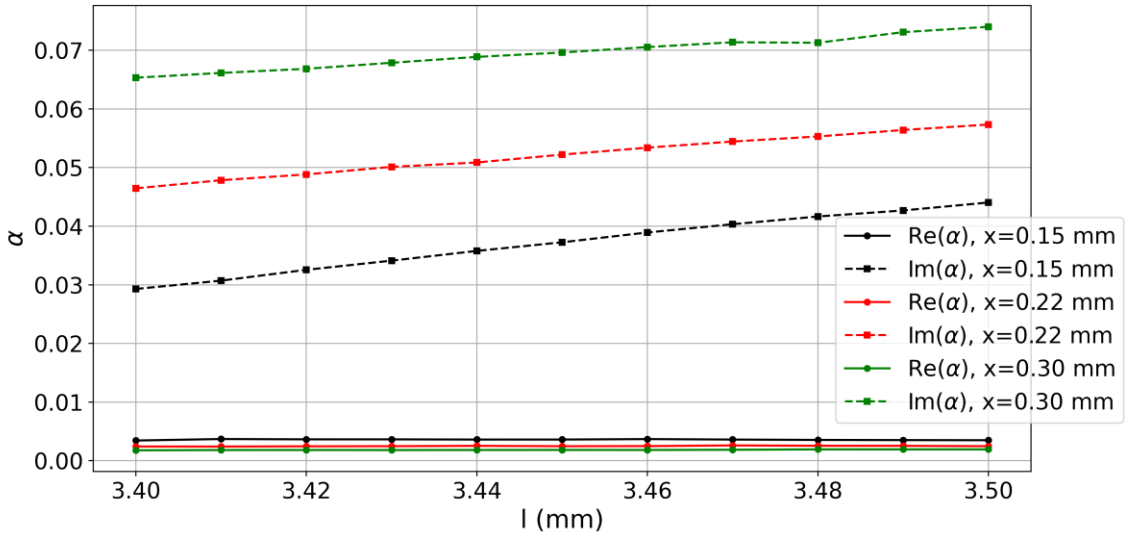

Figure 51 : Variations of the α function depending on the couple (x, l) values for 1 slot.

The direction of the segment on the slot is chosen in a way that the imaginary part is positive. α is supposed to be imaginary pure. Nonetheless, simulations' results give also a real part. The real values here can be attributed to the simulation noise and also the fact that the slot disturbs the TE_{10} initial propagating mode leading to a perturbation on the real guided wavelength λ_g value and then the expected phase quadrature is not fully respected. Regarding the imaginary part, a simple affine function behaviour can be observed.

3.2.3 2 Slots' electromagnetic behaviour

While the previous design allowed the behaviour of a single slot to be studied, the design with two slots on the same line allows the mutual coupling (MC) factor between slots to be studied based on the slots' voltages V_1 and V_2 obtained by simulation at the working frequency. It should be noted here that the impact comes obviously from the internal mutual coupling but also represents the strongest external mutual coupling that can be found in the H plane (Figure 25).

Considering that for a given mode voltage V_{in} the slot voltage V_i of slot i corresponds to the own voltage of the elementary slot V_{i0}, plus part of the voltage of neighbouring slot j, called p_{ij}, we can then write the following system:

$$\begin{cases} V_1 = V_{10} + p_{12}V_2 \\ V_2 = V_{20} + p_{21}V_1 \end{cases} \quad (3.3)$$

Although things are written differently, we remain within the framework of equation (1) from [32] given in (2.9), considering the voltage in the slot as the sum of the voltage specific to the slot and that comes from the external and internal mutual couplings. The major difference is that here, we consider the mutual coupling with only the nearest neighbour. The main difficulty here is to obtain the value of V_{n0} corresponding to the slot own voltage for the given value of the propagating mode voltage V_{in}. To do this, we return to the initial equation $y = \alpha.v$. For the individual slot:

$$y_{10}(\mathrm{x},\mathrm{l}) = \alpha(x,l).\frac{V_{10}(x,l)}{V_{in}} = \alpha(x,l).v_{10}(x,l) \tag{3.4}$$

Knowing that for a given couple (x, l), the ratio $y_{10}(\mathrm{x},\mathrm{l})/\alpha(x,l) = C^{te}$, we can conclude that the ratio $\frac{V_{10}(x,l)}{V_{in}} = v_{10}(x,l) = C^{te}$. It means that for a given value of V_{in} in a given design (simulation):

$$V_{10}(\mathrm{x},\mathrm{l}) = \frac{y_{10}(\mathrm{x},\mathrm{l})}{\alpha_{10}(\mathrm{x},\mathrm{l})}.V_{in_{simulation}} = v_{10}.V_{in_{simulation}} \tag{3.5}$$

Consequently, the last system can be rewritten with:

$$\begin{cases} V_1 = v_{10}.V_{in_{simu}} + p_{12}V_2 \\ V_2 = v_{20}.V_{in_{simu}} + p_{21}V_1 \end{cases} \tag{3.6}$$

And by normalizing the results by the simulated input voltage V_{in} of the design:

$$\begin{cases} V_1/V_{in_simu} = \dfrac{v_{10}.V_{in_{simu}}}{V_{in_{simu}}} + p_{12}\, V_2/V_{in_{simu}} \\ V_2/V_{in_simu} = \dfrac{v_{20}.V_{in_{simu}}}{V_{in_{simu}}} + p_{21}\, V_1/V_{in_{simu}} \end{cases} \tag{3.7}$$

giving:

$$\begin{cases} v_1 = v_{10} + p_{12}v_2 \\ v_2 = v_{20} + p_{21}v_1 \end{cases} \tag{3.8}$$

We can then work with normalized quantities and use the normalized function v_{10} deduced from 1-slot design even if the V_{in} values are different from one design to another. We can then deduce p_{ij}:

$$\begin{cases} p_{12} = \dfrac{v_1 - v_{10}}{v_2} \\ p_{21} = \dfrac{v_2 - v_{20}}{v_1} \end{cases} \tag{3.9}$$

Thus, by exporting the results of the 1-slot design (including v_{10}) and the results of the 2-slots design (v_1 and v_2), we can calculate the complex factors p_{12} and p_{21}. An example of the behaviour of the function $p_{ab}(x_a, l_a, x_b, l_b)$ is shown in Figure 52 in the adaptation zone of the same dielectric for 2 slots. Here, the pair (x_1, l_1) varies within the adaptation zone of 2 slots with a fixed pair (x_2, l_2).

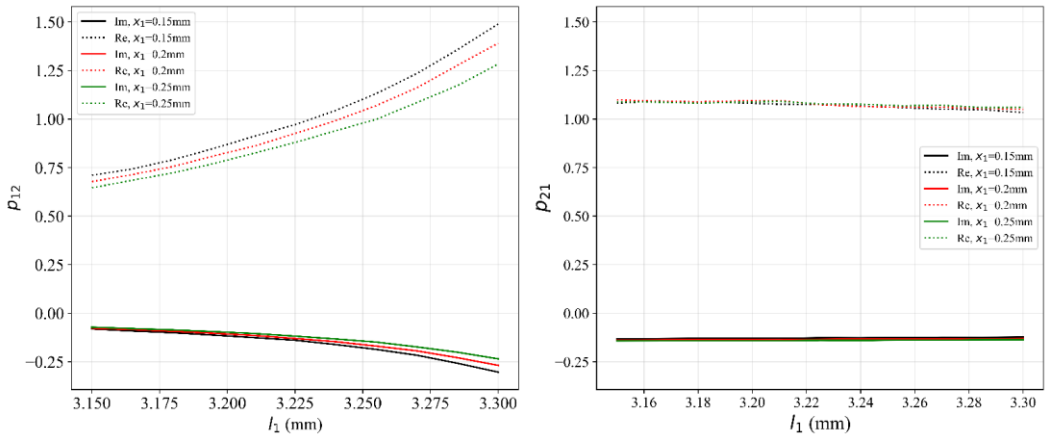

Figure 52 : Variations of the values of (left) p_{12} and (right) p_{21} depending on (x_1, l_1) values for a fixed couple (x_2, l_2) = (-0.2, 3.25) mm.

Important points of observation can be done:

- p_{12} represents the impact of fixed slot 2 on slot 1 when varying (x_1, l_1). This varies significantly when varying the parameters (x_1, l_1), thus directly affecting the matching of slot 1.

- p_{21} represents locally the impact on the fixed slot 2, the work on the matching of the neighbouring slot 1. The variations in x_1 as in l_1 are very small.

It is important here not to get confused with the indices, and to view this work as the study of the function $p_{ab}(x_a, l_a, x_b, l_b)$ when varying the first pair (x_a, l_a), which corresponds here to the study of p_{12}, or the second pair (x_b, l_b), which corresponds here to the work on p_{21}. It can therefore be concluded that the coefficient p_{ab}, which reflects the impact of slot b on slot a, varies significantly when working on slot a itself, whereas it varies only slightly when the adaptation work is done on the neighbouring slot b.

At first glance, based on the reciprocity theorem and the properties of the impedance matrix Z, one would expect $p_{12} = p_{21}$, just as $Z_{12} = Z_{21}$. However, V_{10} does not represent the self-voltage of an isolated slot in the absence of mutual coupling. Rather, it corresponds to the own voltage of the considered slot for a given propagation-mode voltage V_{in}, which itself is affected by mutual coupling. Consequently, p_{12} and p_{21} are generally different, and their values depend on the considered pairs (x_1, l_1) and(x_2, l_2).

3.2.4 Matrix model

For a more general study of a 1×N linear array, it can be observed that each slot has 2 neighbours except the ones in the extremity (1 and N). It can be schematised on Figure 53.

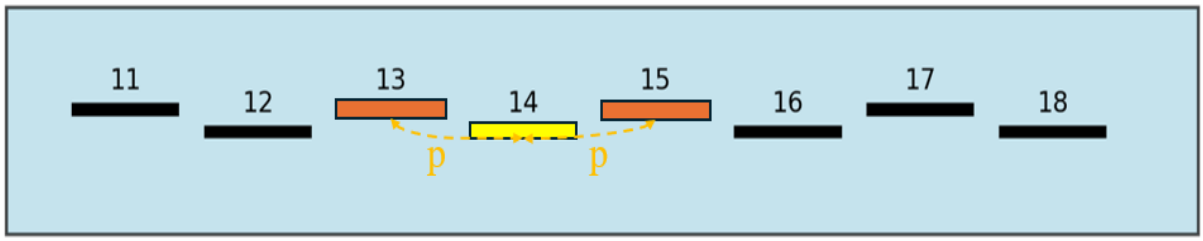

Figure 53 : Schematic representation of a 1×8 linear array with the representation of the adaptation of v_{14} depending directly of the coefficient factor p(14,13) and p(14,15).

Consequently, the full system can be written as follows:

$$\begin{cases} v_1 = v_{10} + p_{12}v_2 \\ v_2 = v_{20} + p_{21}v_1 + p_{23}v_3 \\ v_3 = v_{30} + p_{32}v_2 + p_{34}v_4 \\ \vdots \\ v_N = v_{N0} + p_{N.N-1}v_{N-1} \end{cases} \quad (3.10)$$

It can be observed in each line that the slot voltage without mutual coupling v_{n0} appears only once. The system can be rewritten as follows:

$$\begin{cases} v_{10} = v_1 - p_{12}v_2 \\ v_{20} = v_2 - p_{21}v_1 - p_{23}v_3 \\ v_{30} = v_3 - p_{32}v_2 - p_{34}v_4 \\ \vdots \\ v_{N0} = v_N - p_{N.N-1}v_{N-1} \end{cases} \quad (3.11)$$

It is now simpler to reason by matrix system:

$$\begin{pmatrix} v_{10} \\ v_{20} \\ v_{30} \\ . \\ . \\ . \\ v_{N0} \end{pmatrix} = \begin{pmatrix} 1 & -p_{12} & 0 & 0 & . & . & 0 \\ -p_{21} & 1 & -p_{23} & 0 & . & . & 0 \\ 0 & -p_{32} & 1 & -p_{34} & . & . & 0 \\ . & . & . & . & . & . & . \\ . & . & . & . & . & . & . \\ . & . & . & . & . & . & . \\ 0 & 0 & 0 & 0 & . & -p_{N(N-1)} & 1 \end{pmatrix} \begin{pmatrix} v_1 \\ v_2 \\ v_3 \\ . \\ . \\ . \\ v_N \end{pmatrix} \Leftrightarrow v_0 = p.v \quad (3.12)$$

With respectively v_0, p and v the names of the corresponding matrices in (3.12). p is the matrix of passage considering the mutual coupling with the closest neighbour for each slot. Without mutual coupling, we would have a unitary diagonal matrix. It is interesting to reverse the equality:

$$v = p^{-1}v_0 \Leftrightarrow \begin{pmatrix} v_1 \\ v_2 \\ v_3 \\ . \\ . \\ . \\ v_N \end{pmatrix} = \begin{pmatrix} 1 & -p_{12} & 0 & 0 & . & . & 0 \\ -p_{21} & 1 & -p_{23} & 0 & . & . & 0 \\ 0 & -p_{32} & 1 & -p_{34} & . & . & 0 \\ . & . & . & . & . & . & . \\ . & . & . & . & . & . & . \\ . & . & . & . & . & . & . \\ 0 & 0 & 0 & 0 & . & -p_{N(N-1)} & 1 \end{pmatrix}^{-1} \begin{pmatrix} v_{10} \\ v_{20} \\ v_{30} \\ . \\ . \\ . \\ v_{N0} \end{pmatrix} \quad (3.13)$$

The initial relation (3.2) $y_i = \alpha_i . v_i$ can then be used giving:

$$\begin{pmatrix} y_1 \\ y_2 \\ y_3 \\ . \\ . \\ . \\ y_N \end{pmatrix} = \begin{pmatrix} \alpha_1 v_1 \\ \alpha_2 v_2 \\ \alpha_3 v_3 \\ . \\ . \\ . \\ \alpha_N v_N \end{pmatrix} = \begin{pmatrix} \alpha_1 & . & . & . & . & . & . \\ . & \alpha_2 & . & . & . & . & . \\ . & . & \alpha_3 & . & . & . & . \\ . & . & . & . & . & . & . \\ . & . & . & . & . & . & . \\ . & . & . & . & . & . & . \\ . & . & . & . & . & . & \alpha_N \end{pmatrix} \begin{pmatrix} v_1 \\ v_2 \\ v_3 \\ . \\ . \\ . \\ v_N \end{pmatrix} \Leftrightarrow y = \alpha v \qquad (3.14)$$

Consequently, knowing the functions $\alpha(x_n, l_n)$, $v_0(x_n, l_n)$ and $p_{ab}(x_a, l_a, x_b, l_b)$, the values of each slots' equivalent normalized admittance y_n can be calculated. A convergence algorithm can be developed with this matrix model to adapt a 1×N slotted waveguide considering the mutual coupling between each slots' neighbour.

3.3 Associated algorithm procedure

3.3.1 General procedure

The general process and work to obtain the final matrix of couple (x, l) for each slot is quite simple:

1) from the RF specifications, dimension the waveguide and draw it on HFSS with a first design with 1 slot and the second one with 2 slots
2) find the matching zone for 1 slot corresponding to the range of (x, l) pairs yielding a purely real normalized admittance y, with the normalized conductance g ranging from 0.1 to 1
3) find the matching zone for 2 slots as in (2) and note the shift on (x, l) from 1-slot design to 2-slots design (like in Figure 22 and Figure 23)
4) knowing N-2 slots undergo 2 mutual coupling (MC) and 2 undergo 1 MC, an estimation of the final matching zone can be deduced from (2) and (3) results
5) for 1-slot design, a parametric simulation on (x, l) is applied in the selected zone of simulation from (4) to obtain the functions $v_0(x, l)$ and $\alpha(x, l)$
6) for 2-slots design, a heavy parametric simulation on $(x_1, l_1).(x_2, l_2)$ is applied in the aim to obtain the $p_{ab}(x_a, l_a, x_b, l_b)$ function
7) with python, the matrix model is built, and a recursive algorithm is used to obtain all the couple (x_n, l_n) for the wanted normalized admittance distribution

As it was observed in the previous chapter, the most difficult thing in this problem is to have the desired behaviour of the normalized admittance function close to the expected frequency. Once it is done, applying a work on the correction factor is then easier. It can be observed that passing from a design without losses (perfect electric conductor and $\tan\delta = 0$) to a lossy waveguide simply reduces the conductance and flattens the susceptance behaviour but the shift in frequency is low. Looking at the great number of simulations necessary to obtain the p_{ab} function, it is easier to stay with a lossless waveguide to save time until the first design simulation and convert it in lossy waveguide to apply the correction factor method.

Another important point is the numerical translation for the α, v_0 and p_{ab} functions. By default, all the approximations can be done with interpolation functions from scientific libraries.

Nonetheless, as highlighted in the previous chapter, important problems of divergence occur when the used variables are out of the initial range of simulations. Furthermore, the interpolated functions are heavier and limit the possibilities for iterative algorithm of solving. Then, the three following points talking about the digital translation of these functions put forward an analytical solution staying valid out of the initial range of simulations. The ones presented are the one giving the best results during the PhD works, even if other one can be possible.

The numerical curve examples in the following section will still be with a RT/Duroid 127µm dielectric at 15GHz. Knowing that for one mutual coupling undergone, the shift for resonant length is around 6% and the offset must be increased, the final chosen range for simulations allowing to obtain α, v_0 and p_{ab} functions is x ∈ [0.1 – 0.25] mm and l ∈ [3.0 – 3.25] mm.

3.3.2 α and v_0 functions

With the 1-slot design, a set of simulations at the working frequency f_0 are applied in the selected range of values for (x, l). Thanks to the fields calculator, we can export v_0 and α values (directly calculated on the software as y_{in}/v_0).

- **Alpha function**

The alpha function α, making the relation between the slot's equivalent normalized admittance y and its slot voltage v_s, is the simplest one to approximate analytically as it can be observed in Figure 51. The affine function can be used:

$$\alpha(x,l) = a(x).(l - l_{min}) + b(x) \tag{3.15}$$

with l_{min} the minimal value of l_{slot} previously simulated. It can be done without this shift but doing this, b(x) simply corresponds to the offset on the y-axis of simulations result and then the shallow slope coefficient a(x) is better identified. Following this, a(x) and b(x) follow quadratic function behaviour as shown in Figure 54.

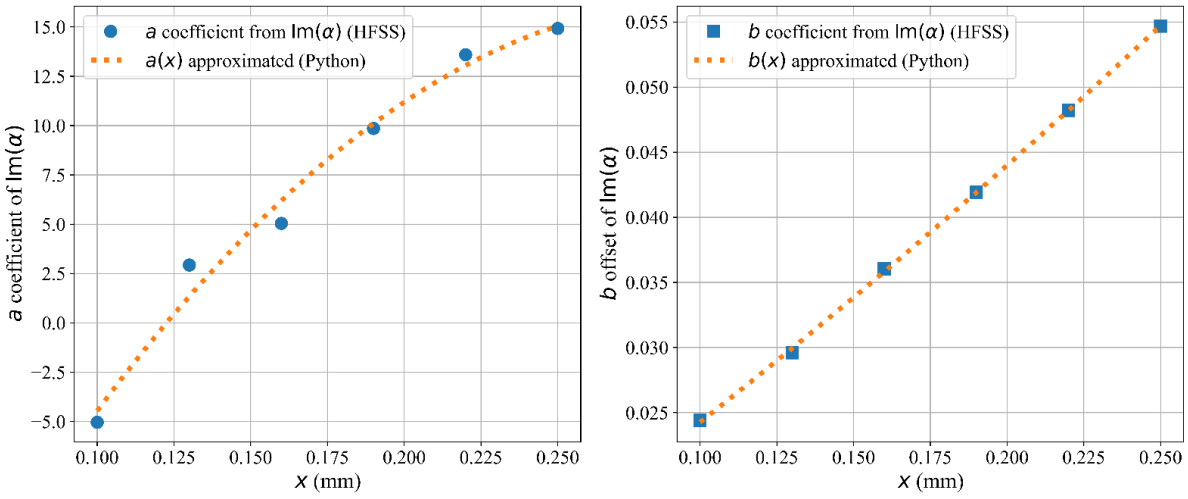

Figure 54 Variations of the coefficients of approximations a(x) and b(x) for α function.

By saving the coefficients of the quadratic functions used to approximate a(x) and b(x), a numerical function α(x, l, SavedCoef) is obtained, allowing to approximate the result of simulations. Furthermore, this function is the only one which can directly be compared with the Elliott theoretical approach corresponding to the product $K_1.f(x,l)$ given in (2.7) and (2.8). The Figure 55 shows the good approximation between the obtained α function and the HFSS simulations' values as well as the comparison between the theoretical Elliott values from the equivalent α function and the simulated values.

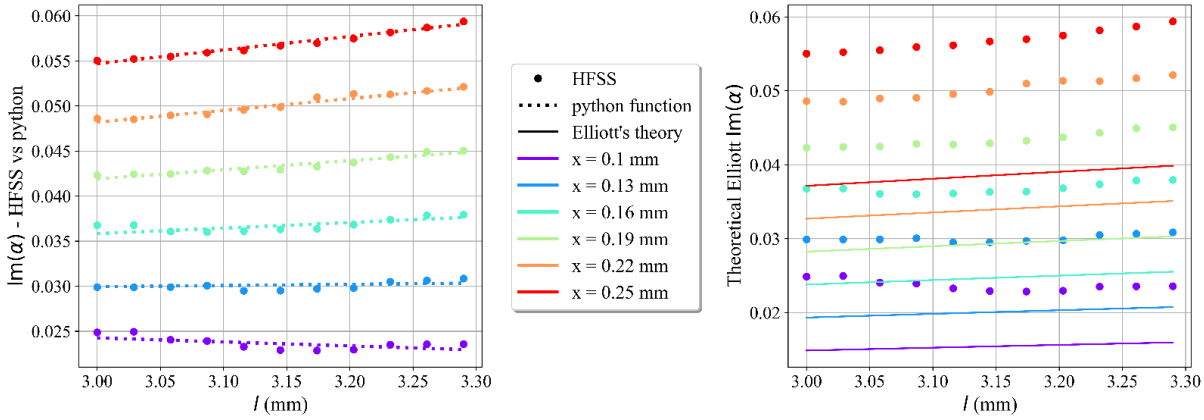

Figure 55 : Comparison of the HFSS α values and the well-matched approximation with python, plus the comparison with Elliott anticipated theoretical values.

It can observed that the numerical function α(x, l, SavedCoef) is consistent with the simulated values whereas the theoretical approach of Elliott presents an import error. Knowing that α is the relationship between the slot's normalized admittance and its associated normalized slot's voltage, the relative error is more important than the absolute error. Here, until 30% of relative error can be observed, which is tremendous when trying to adapt the network. As previously highlight, this error is probably due to the ignorance of slot width (more important that the waveguide thickness here) or the thickness of the conductor (16% of the waveguide thickness here).

- **v_0 function**

The normalized slot's voltage obtained without mutual coupling v_0 can be approached with a sigmoid function:

$$v_0(x,l) = \frac{L(x)}{1 + e^{-k(x).(l-l_0(x))}} + C(x) \qquad (3.16)$$

Like for the α function, the coefficients L, k, l_0 and C are function of x. They are computed and their variations are approximated by quadratic function.

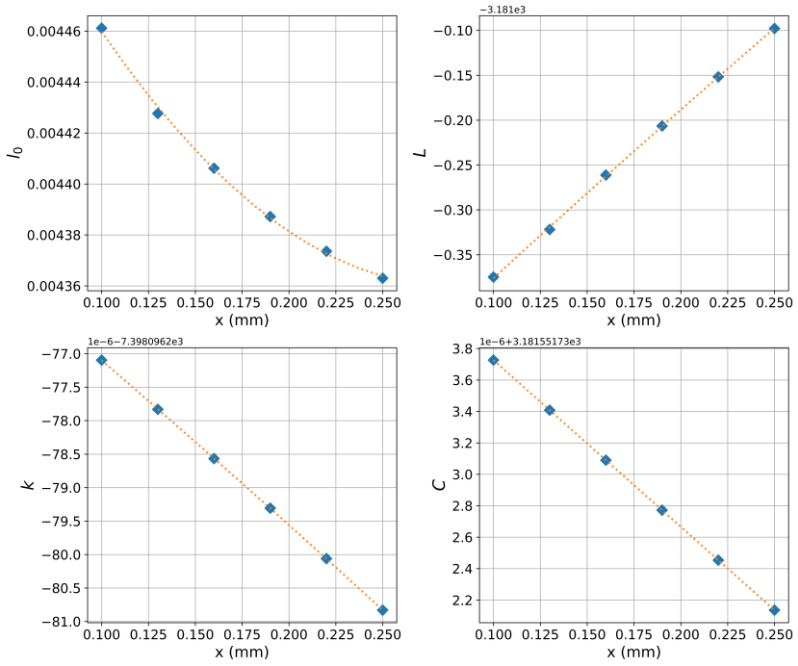

Figure 56 : Variations of the sigmoid function's coefficients depending on the offset x to approximate $v_0(x,l)$ function.

It is important to distinguish 2 points: l_0 and L coefficients follow well the wanted quadratic behaviour, whereas k and C coefficients are mainly constant. Indeed, it must be noted for the 2 subgraphs of the second line that the y-axis has a scale of 1e-6 and values of offset around ±1e3. Consequently, even if visually it appears to follow an affine function behaviour, these values can be considered as constant.

The coefficients of the polynomial functions following the variations of the coefficients l_0, L, k and C depending on the offset x can then be saved and used for the numerical approximation of the function v_0(x, l, SavedCoef). A comparison between HFSS simulation values and this analytical approach is given in Figure 57.

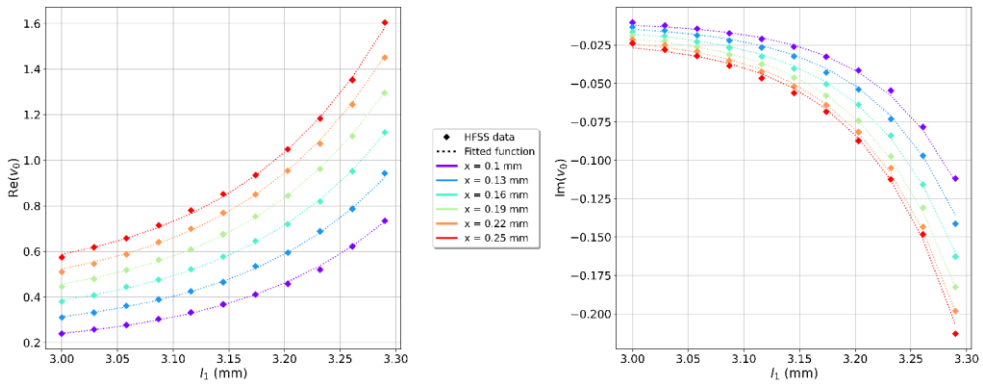

Figure 57 : Comparison between HFSS results and numerical approximation for the values of v_{10}.

There is excellent matching between the simulation results and the approximation function selected.

Finally, for both functions α(x, l) and v_0(x, l), the found coefficients fitting the simulations with analytic expressions are saved in a csv files allowing then to have the

numerical functions α(x, l, SavedCoef) and v_0(x, l, SavedCoef') which stayed valid above the range of simulations (while the internal mutual coupling stays predominant).

3.3.3 p_{ab} function

Like previously, the aim is to obtain a function $p_{ab}(x_a, l_a, x_b, l_b)$ from a set of simulations in order to translate the coupling between two slots. This point is particularly difficult because there are 4 variables. The simplest and most basic method is to run a whole set of parameters varying the pairs (x_a, l_a) and (x_b, l_b) over the same ranges of values, calculate p_{ab} for each iteration and analyse mathematically the results after.

The first problem lies in the simulations. Even if the global idea is quite simple and direct, it must be noted that apply it on the range of (x, l) values with 6 samples for x and 12 for l, it leads to a parametric simulation on (x_a, l_a) of 72 simulations for a given (x_b, l_b) couple, then $72^2 = 5184$ simulations. Furthermore, in addition to being time-consuming, the fields being saved for each simulation and calculations performed on these results, computing servers may not be powerful enough and cause the machine to crash. However, this simple method has been chosen. Tips for improving the total simulation time using a different approach are given in 3.3.5. However, the issue of limited computing power on servers must be considered. To overcome this problem, an HFSS script algorithm automates the simulations. This allows to simulate the voltage in the slot v_s over the expected range of values (x_a, l_a) for a single pair (x_b, l_b), obtain and export the results in the ROM, delete them on the software, and start again with a new pair (x_b, l_b).

The second problem then lies in converting the simulation results into equations that take the four variables into account. To do so, a first try to obtain an analytical expression of p_{ab}(xa,la) for a fixed (x2, l2) is done. For the different tested designs, it appears that the exponential function gives the best result with:

$$p(x,l) = a(x).e^{b(x).(l-l_{min})} + c(x) \qquad (3.17)$$

with a(x), b(x), c(x) functions of first order and l_{min} the minimal used length value for the range of simulations. Then, the same logic that with function v_0 is applied. An example is given in Figure 58.

The quadratic function behaviour of the example for the coefficients a, b and c for the real part of p_{12} function is well identified. The same work is done for the imaginary part and then the polynomial coefficients of the a, b and c variations with the offset can be saved to finally obtain the numerical function $p_{ab}(x_a, l_a,$ SavedCoef) valuable for a given (x_b, l_b) couple. An example of use is given in the Figure 59.

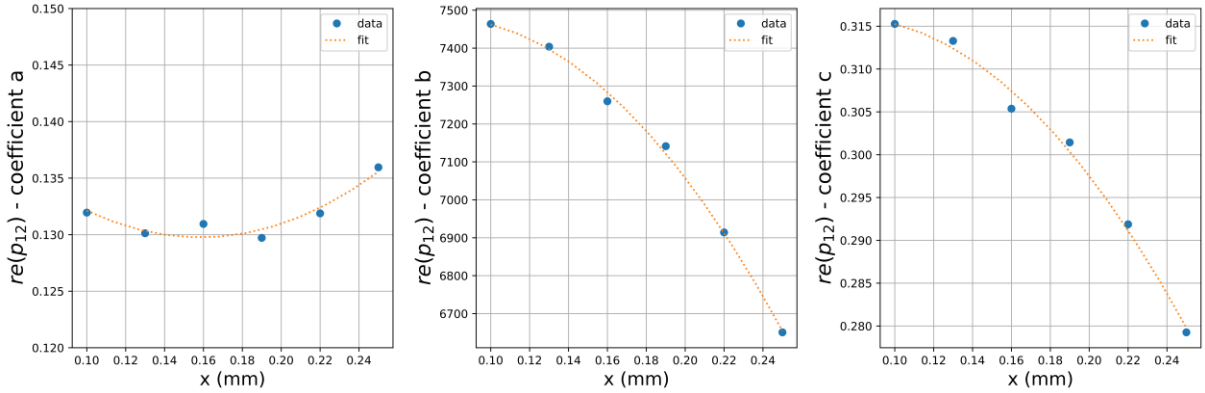

Figure 58 : Example of the variations with the offset x of the coefficients of the real part of the approximation function for p_{ab} simulated values.

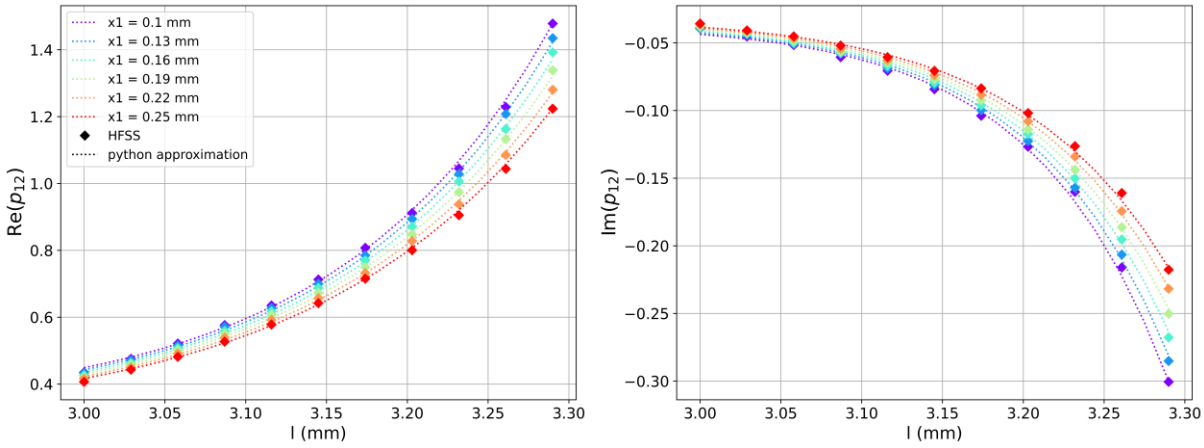

Figure 59 : For a given (x2, l2) couple, comparison of the calculated coefficient p12 values for different couples (x1 ,l1) and its numerical python approximation for real and imaginary parts.

Once again, an excellent agreement between the simulation results and the chosen approximation function can be observed.

Nevertheless, this procedure is valid only for a given couple (x_b, l_b). The consideration of variations in the second couple (x_b, l_b) must be incorporated into the final function. Nonetheless, putting into equations the variations of p_{ab} function being already complex only for one couple of (x_b, l_b), a direct work on the variations of the polynomial functions of the coefficient a, b, c depending on the variations of (x_b, l_b) is too much complex and shows few satisfactory results.

The idea that has been adopted is therefore to use a numerical dictionary in which the keys cor respond to all the simulated pairs (x_b, l_b). The value assigned to each key corresponds to the saved coefficient allowing to fit the p_{ab} function with the variation of (x_a, l_a) for the fixed couple (x_b, l_b), the key itself. Finally, the numerical function p_{ab}(x_a, l_a, x_b, l_b, Dictionnary) starts to find the two keys closest to x_b and the two keys closest to l_b, apply the function p_{ab}(x_a, l_a, SavedCoeff) to the four keys surrounding (x_b, l_b) and finally return the value of the bilinear interpolation in x and l of the second pair.

3.3.4 Recursive algorithm

- **Global approach**

The 3 last developed numerical functions α, v_0 and p_{ab} are directly used to build the matrix system given in (3.14). This system allows us to obtain the equivalent normalized admittance y_n for each slot n and the associated normalized slot's voltage v_n. A recursive algorithm must be used to obtain all the couples (x_n, l_n).

The global rules are the same than for Elliott's approach:

- each slot's normalized admittance y_n must be pure real and their sum equal to 1
- the ratio between 2 normalized admittance is equal to the ratio of their respective slot's voltages v_n times the respective α_n values

To do so, 2 nested loops are used with the global one calculating the matrix of mutual coupling p with the global couples (x, l) values of the last iteration, and the little loop searching for all the new slot couple (x_n, l_n) based on the previous calculated matrix of mutual coupling p. Convergence occurs fairly quickly in less than 10 iterations.

- **Example**

The latest figures were obtained at 15 GHz using RT/Duroid 5880 with a thickness of 127 µm. As an example, a 1×10 array is also designed with the same parameters, following a Chebyshev amplitude distribution with a sidelobe level (SLL) of -23 dB. After using the presented procedure, the following values are obtained thanks to the convergence algorithm:

slot number	1 - 10	2 - 9	3 - 8	4 - 7	5 - 6
l(mm)	3.252	2.950	3.111	3.063	3.093
x(mm)	0.906	0.896	1.095	1.310	1.300

Table 3 : Example of (x, l) couples obtained with this new method for an adaptation at 15GHz of a 1x10 SIWSA with RT/Duroid 5880 of 127µm.

The 1x10 array is first tested on lossless waveguide, then lossy waveguide and corrected as observed in Figure 60. The first match for the design without losses has a frequency adaptation very close to the expected one, add the losses causes a loss in the reflection coefficient and a shift in frequency but a little correction on slots' length and offset allows to obtain an excellent reflection coefficient at the wanted frequency.

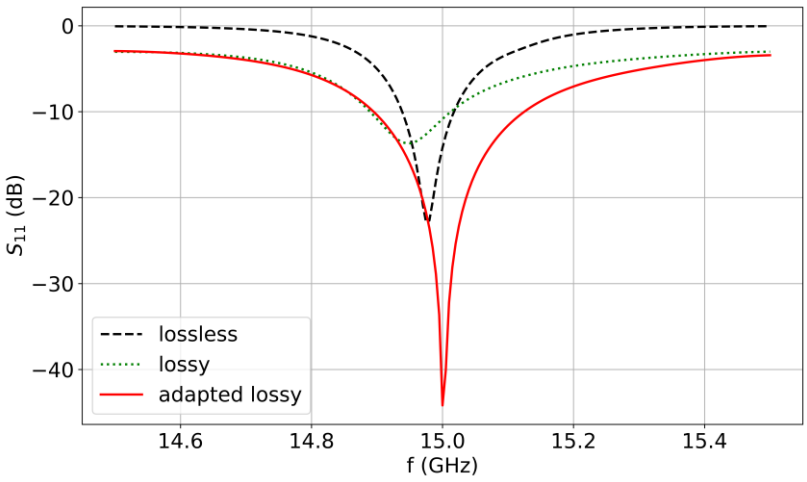

Figure 60 : Variations of the reflection coefficient for the 1x10 lossless, lossy and adapted lossy design.

Looking at this first example, it can be advanced that for this case of study, the developed method is far more precise than the use of the Elliott's theoretical approach: a 127µm SIW slotted array was designed at 15GHz with a first matching test at least than 0.14% of relative error with an initial theoretical approach that is very easy to understand.

3.3.5 Notes and tips

- **Approximation functions**

In the presented processus, an effort has been made to keep these approximation α, v_{10} and p_{ab} functions as analytical as possible. This therefore requires greater upstream algorithmic development complexity, as well as their use in the final matrix model. The primary objective is to be able to provide search limits on the final convergence algorithm potentially beyond the initial simulation boundaries. Furthermore, the associated numerical functions have a higher execution speed than functions created with 2D interpolation, which improves the probability of convergence when using numerical solvers from the SciPy library.

Nevertheless, in case of difficulties to analytically approximate these functions, or lack of time to develop the associated numerical function f(x, l, SavedCoef), the 2D interpolations solution stays powerful and easier to implement.

- **Upstream simulation time**

The main disadvantage of this approach is the necessary time of simulation specific to each case of study (frequency and waveguide's characteristics). To give an idea, with the university's servers, allowing the multi-core and distributed simulations, finding the matching zone takes around 1 hour, studying the individual slot around 30 minutes and the set of simulations for p_{ab} function between 24 and 36 hours depending on the sampling. Even if all can be automated, the range of simulations and the sampling must be defined wisely to avoid unnecessary simulation time and resources.

- **application to an M×N array**

Concerning the possibilities of the presented method, an interesting point is the possibility to duplicate the waveguide. The strong intern mutual coupling being the masterpiece allowing the validity of this design method, it is possible to duplicate M times the matched waveguide 1×N and add the wished tapering on the M waveguides without disturbing the adaptation of the waveguides. It can be observed by continuing with the last example of the 1x10 slotted waveguide which is duplicated 10 times and a tapering of Chebyshev for side lobe level at -23dB is applied between the waveports:

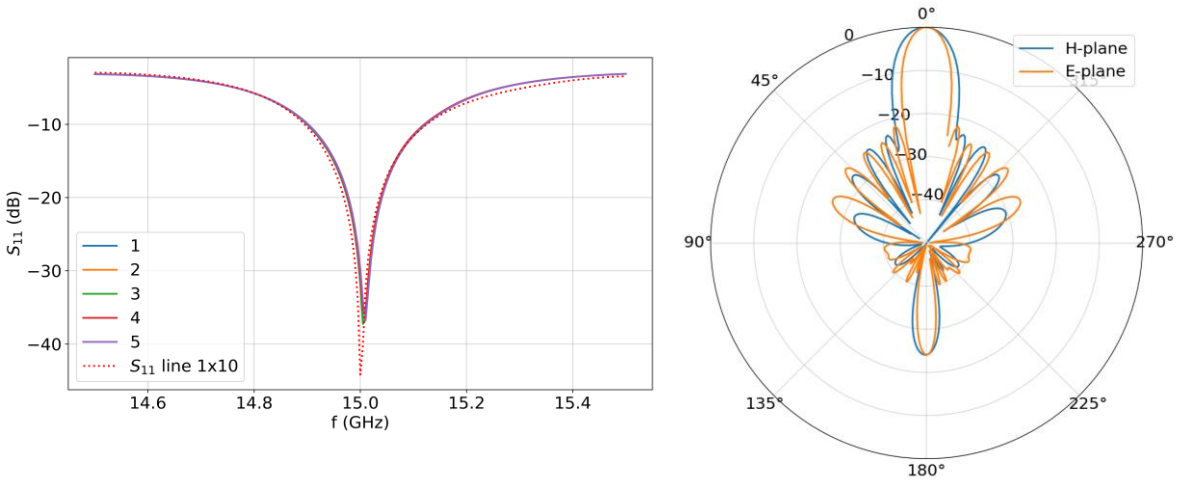

Figure 61 : Reflection coefficients for half of the waveguides from the 9 times duplicated 1×10 waveguide previous design and its associated radiation pattern.

It can be observed that the direct impact of the waveguide duplication on the reflection coefficients is very low passing from 1x10 design to 10x10. Furthermore, the global radiation pattern of the 10x10 array is in adequation with the expected expectations.

Consequently, the versatility of the developed method is important: based on a set of simulations for a 1-slot and 2-slots model, the calculation of the associated functions and the constructed matrix model, a M×N network can be adapted with only minor software corrections.

- **Improvement of the simulation method to obtain p_{ab} function**

In the simulation procedure used to obtain the function p_{ab}, for a pair (x_b, l_b), the presented procedure uses only the results of $p_{12}(x_1, l_1)$ for a given (x_2, l_2) couple (a = 1 and b =2), leading to a total number of simulations of N^2 with N being the number of couple parameters. However, if the behaviour of $p_{21}(x_1, l_1)$ is also studied for a fixed (x_2, l_2) with a = 2 and b = 1. This would also give the values of $p_{ab}(x_b, l_b)$ for fixed (x_a, l_a). Reasoning in terms of an N×N matrix as presented in Figure 62, the first iteration would require a parameter of N simulations, the second N-1, the third N-2, etc. Ultimately, it would be necessary to perform sum(N)=N(N+1)/2 total simulations rather than N^2. This would result in significant time savings. However, the difficulty of algorithmic automation for modifying the simulated parameter at each iteration and processing the results downstream is more complex.

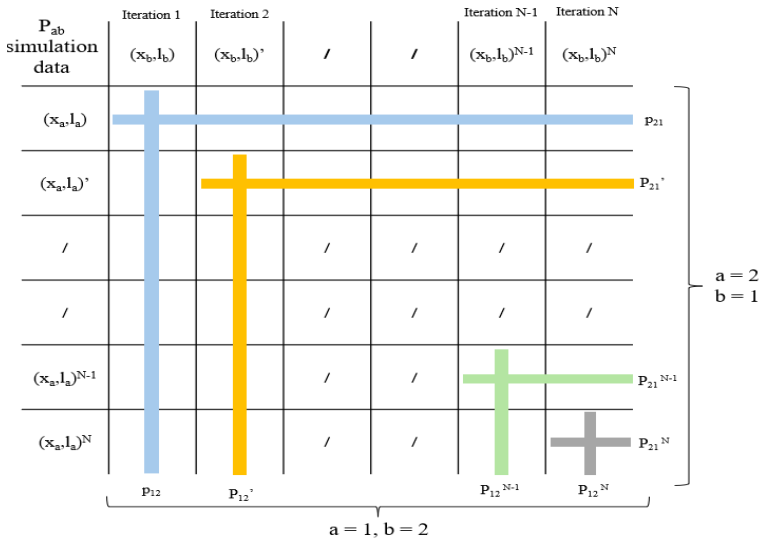

Figure 62 Array data of p_{ab} function obtain with p_{12} and p_{21} simulation process.

In line with the same idea of optimising total simulation time, observing that the variations $p_{ab}(x_a, l_a)$ for a given (x_a, l_a) follow a classical exponential function, the sampling can be reduced. The final results obtained remain perfectly acceptable, although less favourable. A compromise can therefore be made between the total simulation time required to prepare the dimensioning tool and the deviation from the RF values expected on the software during the first simulation.

- **Improvement of the convergence algorithm**

To facilitate convergence of the algorithm giving the pairs (x, l) for each antenna, the expected 1×N network is often symmetrical. The problem can therefore be reduced to square or column matrices of size N/2, thus facilitating numerical calculations. The matrix p can therefore be rewritten as:

$$p = \begin{pmatrix} 1 & -p_{12} & 0 & 0 & . & . & 0 \\ -p_{21} & 1 & -p_{23} & 0 & . & . & 0 \\ 0 & -p_{32} & 1 & -p_{34} & . & . & 0 \\ . & . & . & . & . & . & . \\ . & . & . & . & . & . & . \\ . & . & . & . & . & . & -p_{\left(\frac{N}{2}-1\right)\frac{N}{2}} \\ 0 & 0 & 0 & 0 & . & -p_{\frac{NN-1}{2\ 2}} & 1-p_{\frac{NN+1}{2\ 2}} \end{pmatrix} \quad (3.18)$$

Note that the values of $v_{N/2}$ and $v_{N/2+1}$ are assumed to be identical due to the symmetry, hence the final value in the matrix is $1\text{-}p_{NN+1}$. The expected sum of slot's equivalent normalized admittance y_n values is therefore 0.5+0j.

Still with a view to improve convergence on the matrix model, it can be observed that the numerical function p_{ab}, which is called a large number of times for each iteration, requires each time to find the four closest keys (x_b, l_b) corresponding to neighbouring slots in order to

first apply the function $p_ab_x_bl_b(x_a, l_a, Coeff)$ to the 4 keys and then perform a binomial interpolation on these values in order to return the complex p_{ab} value. However, it should be noted that for sufficient initial sampling, the differences in values obtained on the four keys and the final interpolation are very small. Therefore, when the number N of elements by waveguide is important, it can be interesting to start the convergence algorithm by referring only to 1 closest key (x_b, l_b) in the first iterations and pass to the binomial interpolation to affine the results in the last iterations.

- **Initial improvement of the simulated design**

It can be observed that adding slots on the waveguide slowly increases the value of the guided wavelength λ_g (less than 1%). Knowing this, few simulations for the design with 1, 2 and N slots can be quickly done to obtain the correction factor on λ_g of few thousandths to optimize the results.

3.4 Extension of the method to other possible case studies

For the time being, the developed method was presented for the TE_{10} mode of propagation in a classical rectangular waveguide (or SIW). During this PhD some extensions of this method were investigated. The three main ones are presented here, namely the possibility to add a film on the top of the waveguide, the application in TE_{20} mode and the adaptation of the process to consider the external mutual coupling.

3.4.1 consideration of a protective film on the waveguide

Although a protective film is often necessary in aeronautical applications, this film disturbs the equivalent admittance values of the unit slot, as well as both internal and external mutual coupling. As it was previously mentioned, adding this option on the theoretical method of Elliott adds an important layer of complexity, which is once again purely theoretical [33], [34]. The entire presented process stays valid and can directly be used when a protective film or varnish is added to the network. Using this new protocol directly considers the real electromagnetic behaviour of the waves for a given film and does not require any changes to its procedure.

An example is given Figure 63 where an 1×8 slotted array is matched at 15 GHz using a RT/Duroid 5880 of 127 µm thickness with a coat of varnish of 30 µm of thickness, $\varepsilon_r = 5.4$, $\tan\delta = 0.02$.

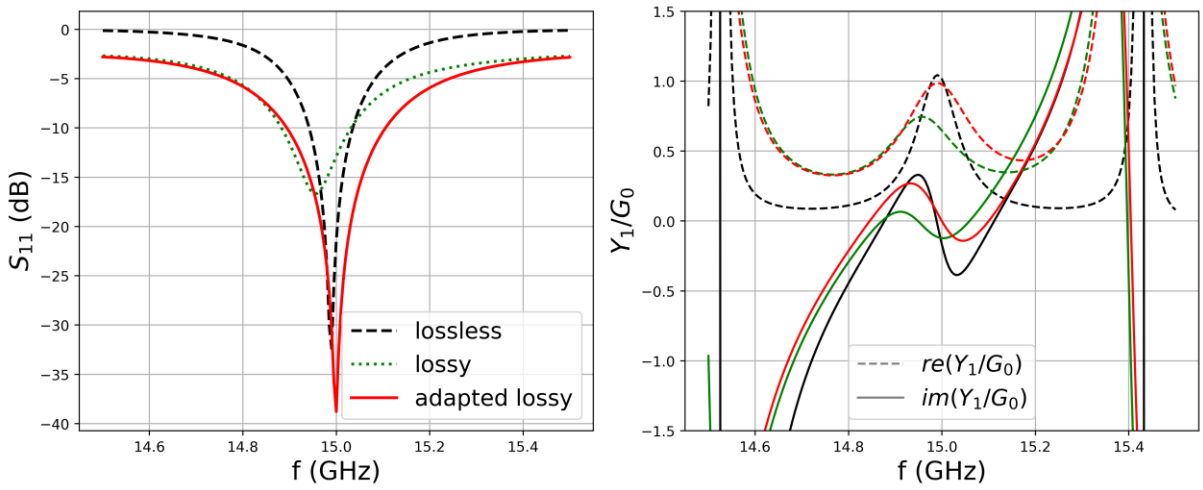

Figure 63 : Variations of the reflection coefficient for a 1×8 lossless, lossy and modified lossy design with coat of varnish

It can be observed in Figure 64 that the initial simulation shows excellent results. As presented in 3.3.5, the final matched slotted waveguide can be duplicated M times to obtain a M×N array without disturbing the matching of each line. An example of the final radiation pattern of the associated 8×8 array with the film of protection is given in Figure 64.

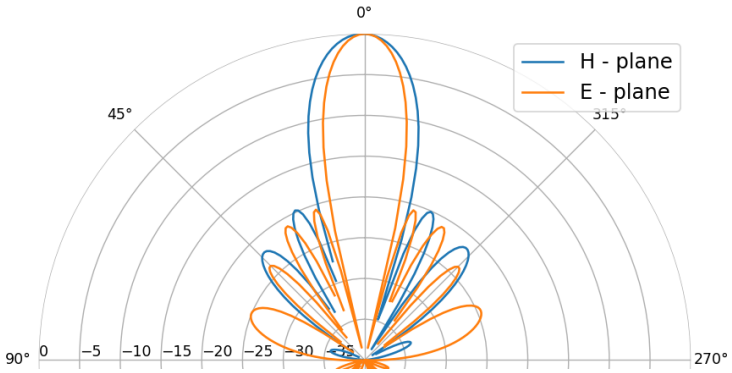

Figure 64 radiation pattern of an 8×8 slotted array coated with varnish

At this stage, an interesting point should be noted: the developed process quickly yields excellent simulation results, saving a significant amount of time through its theoretical simplicity and the associated algorithmic development, which remains at an accessible level. A classical theoretical approach would have required studying the two major articles by Elliott [31], [32], as well as the necessary adaptations of this theory for the presence of a protective film [33], [34]. The four aforementioned articles involve a high level of theoretical complexity, requiring several days of study before the corresponding code can be developed.

3.4.2 Application to the TE_{20} mode of propagation

- **Presentation of the problem**

For the TE_{20} mode of propagation, two slots can be placed within one half guided wavelength, because the transverse electric field has two half cutoff wavelength lobes across the waveguide width. It can be observed in Figure 65.

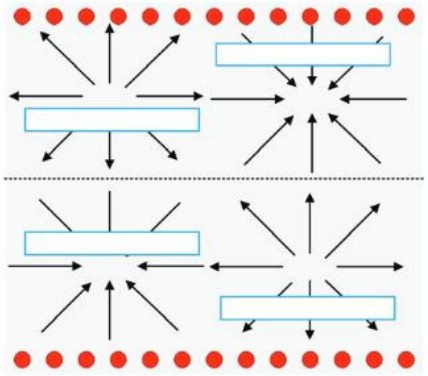

Figure 65 : From [50], the surface current distribution for TE_{20} mode and the four-slot configuration.

We can observe that slots are coupled by 2 on a same half guided wavelength section and alternatively both towards the global middle of the SIW, or the outward. It can be considered as 2 sublines in TE_{10} mode but with opposite sign of offset x for 2 consecutive lines.

In the literature, only few studies about RWG slotted array with TE_{20} mode of propagation exist. We can highlight the 3 articles [50],[51] and [52]. [50] and [51] both use SIW technology but with different thicknesses, respectively 0.5 mm and 1.58mm, while [52] is applied on a RWG 3D printed with an important thickness. Nonetheless, we can observe that in these 3 articles, the work is mainly focused on the transition from the feeding to the TE_{20} mode in the waveguide rather than the slot array itself. Indeed, all these networks have constant offset values and slot lengths, which is electromagnetically impossible when seeking to optimise frequency matching taking into account the mutual coupling and the weighting excitation for the radiation pattern.

In addition to their important work on TE_{20} mode excitation, their interest in using this propagation mode is supported by the idea that the feeding with slots of TE20 mode is less sensitive than the TE_{10}. Furthermore, in the case of the SIW slotted array (SIWSA), for a design with M waveguides of slots, TE_{20} mode allows to remove M/2 lines of vias. In addition to increased ease of manufacture, it is particularly interesting in the case of flexible SIW slotted array. Indeed, for a given copper-foiled dielectric, the via lines limit the flexibility of the prototype, particularly in the E-plane. Thus, a M×N design can be matched to the same frequency but with a better flexibility.

Nonetheless, to the author's knowledge, no technique specific to design an array considering mutual coupling (MC) in TE_{20} mode exists. Until now, the general approach was to take the simple approach of TE_{10}, ignoring MCs, and duplicating it by considering TE_{20} mode as two TE_{10} sublines. In our case of flexible SIW slotted array, taking the internal mutual coupling (MC_{int}) into account is essential for optimising the desired frequency matching and expected an amplitude distribution.

Then, the idea is to take again the last procedure of design of a 1×N waveguide (possibly duplicated M times) in a case of a strong internal mutual coupling (thin dielectric) by considering that the 1 slot elementary element is replaced by the 2 coupled slots of the TE_{20}. Some modifications must however be added.

- **Theoretical adaptation for TE_{20} modes**

For an array of 2×N slots in TE_{20} mode, we can adopt the numeration of Figure 66:

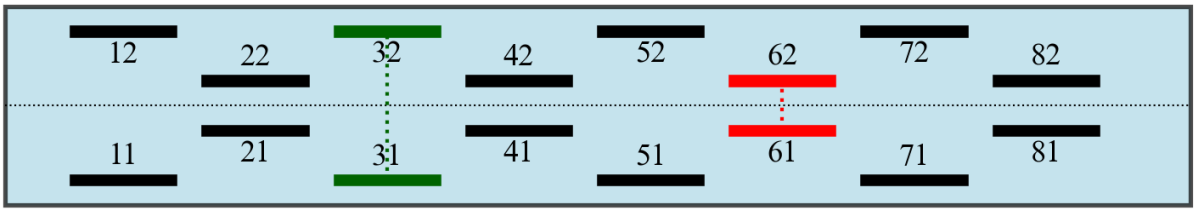

Figure 66 : Numeration of 2×N slot array in TE20 mode.

An important point that can be noted is that the odd couples have an 'external' position (green, 31 - 32) whereas the even ones have an 'internal' position (red, 61 -62). We can then anticipate that the electromagnetic behaviour of both is different due to their different gaps. Therefore, we need to reproduce the work to characterise the behaviour of 1 slot giving α and v_0 functions independently for both internal or external configuration cases. It results in 4 functions for single elements: α_{int}, α_{ext}, v_{0_int}, v_{0_ext}. Having 2 different functions for the individual slot's normalized voltage v_0 leads to 2 different mutual coupling p_{ab} functions. It is simply explained by the fact that contrary to the system (3.9), here the functions v_{10} and v_{20} are not the same, and then, the difference in the numerator in (3.9) leads to 2 different values depending on if the test procedure is done in the direction even-odd or odd-even. We call them p_{eo} and p_{oe} (for even and odd).

Hence, keeping the global numeration 1,2, …, N for the subsections 11 - 12, 21 - 22, …, N1 - N2, (3.13) can be rewritten:

$$\begin{pmatrix} v_1 \\ v_2 \\ v_3 \\ . \\ . \\ . \\ v_N \end{pmatrix} = \begin{pmatrix} 1 & -p_{oe12} & 0 & 0 & . & . & 0 \\ -p_{eo21} & 1 & -p_{oe23} & 0 & . & . & 0 \\ 0 & -p_{oe32} & 1 & -p_{oe34} & . & . & 0 \\ . & . & . & . & . & . & . \\ . & . & . & . & . & . & . \\ . & . & . & . & . & . & . \\ 0 & 0 & 0 & 0 & . & -p_{eoN(N-1)} & 1 \end{pmatrix}^{-1} \begin{pmatrix} v_{ext10} \\ v_{int20} \\ v_{ext30} \\ . \\ . \\ . \\ v_{intN0} \end{pmatrix} \quad (3.19)$$

leading to:

$$\begin{pmatrix} y_1 \\ y_2 \\ y_3 \\ . \\ . \\ . \\ y_N \end{pmatrix} = \begin{pmatrix} \alpha_{ext1} & . & . & . & . & . & . \\ . & \alpha_{int2} & . & . & . & . & . \\ . & . & \alpha_{ext3} & . & . & . & . \\ . & . & . & . & . & . & . \\ . & . & . & . & . & . & . \\ . & . & . & . & . & . & . \\ . & . & . & . & . & . & \alpha_{intN} \end{pmatrix} \begin{pmatrix} v_1 \\ v_2 \\ v_3 \\ . \\ . \\ . \\ v_N \end{pmatrix} \quad (3.20)$$

Furthermore, the HFSS designs used to obtain these functions are drawn as couple of slots:

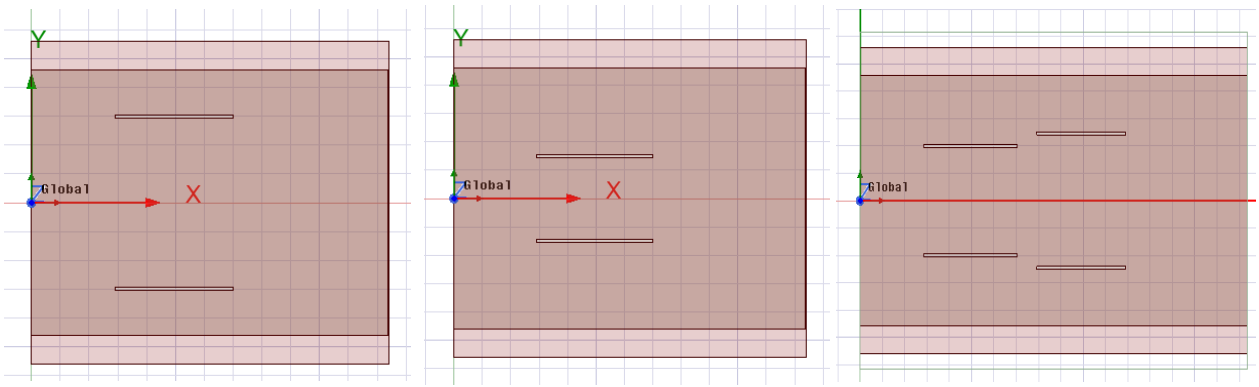

(a) (b) (c)

Figure 67 : Tested design for TE_{20} study with (a) individual external (b) configuration internal configuration and (c) mutual coupling study

The same process of simulations and calculus described in 3.3.1 is then applied.

- **Example of application**

For the following figures, the used dielectric is a RT/Duroid 5880 with a thickness of 254 µm, the frequency of work is f_0 =15 GHz and a cut-off frequency of the first mode TE_{10} at f_{c10} = 5.5 GHz giving a_{rwg} = 18.4mm. From the 3 designs, the values of (x, l) giving a matching between y = 0.5 +0j and 1+0j are found.

	x (mm)	l(mm)
2 slots - ext	0.2 – 0.36	4.1 – 4.23
2 slots - int	0.2 – 0.41	4.1 – 4.26
4 slots	0.1 – 0.3	3.91 – 4.03
1 slot – equivalent TE10	0.18 – 0.35	4.07 – 4.17

Table 4 : Matching range of couple (x, l) values for different slots configurations.

A very small difference between the couples in external and internal configurations can be observed. In the same way, a little difference with a single slot in the corresponding TE_{10} mode (half TE_{20} mode obtained with $a_{rwg}/2$) can be noted. Considering the thin dielectric of 254 µm, leading to a strong internal mutual coupling (MC_{int}), we can attribute this little shift more to the external mutual coupling (strong in the E-plane). Indeed, the consequence on the (x, l) matching considering an MC_{int} is supposed to decrease the (x, l) values from 1 slot to 2 slots. Here, contrarily, the value increases, a little bit like the impact of the external MC in 2.2.2, leading to a slow increase of the slot's length. Finally, as expected, adding 2 couples leads to the same kind of shift that for the previous study that is to say decreasing of l_{slot} and increasing of x for a same input normalized admittance y value. The area with a shift of 4.82% for l_{res} is chosen:

x = [0.1, 0.25] mm

l = [3.7,4.0] mm

It is then possible to obtain and compare the functions α and v_0 in external and internal configurations as shown in Figure 68 and Figure 69.

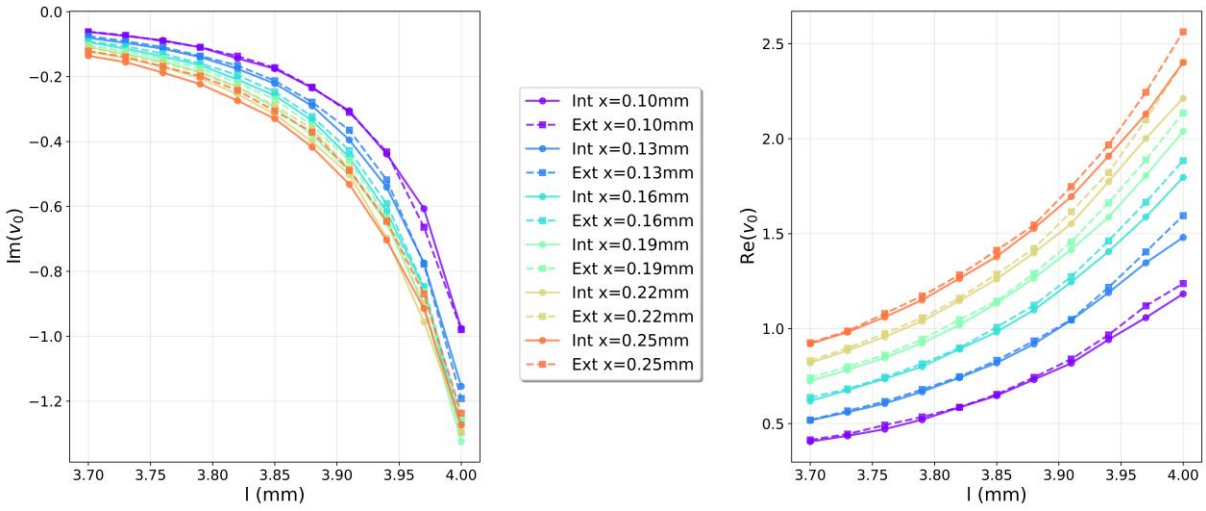

Figure 68 : Comparison of the (left) imaginary and (right) real parts of the v_0 function for both the internal and external configurations for the slot couples.

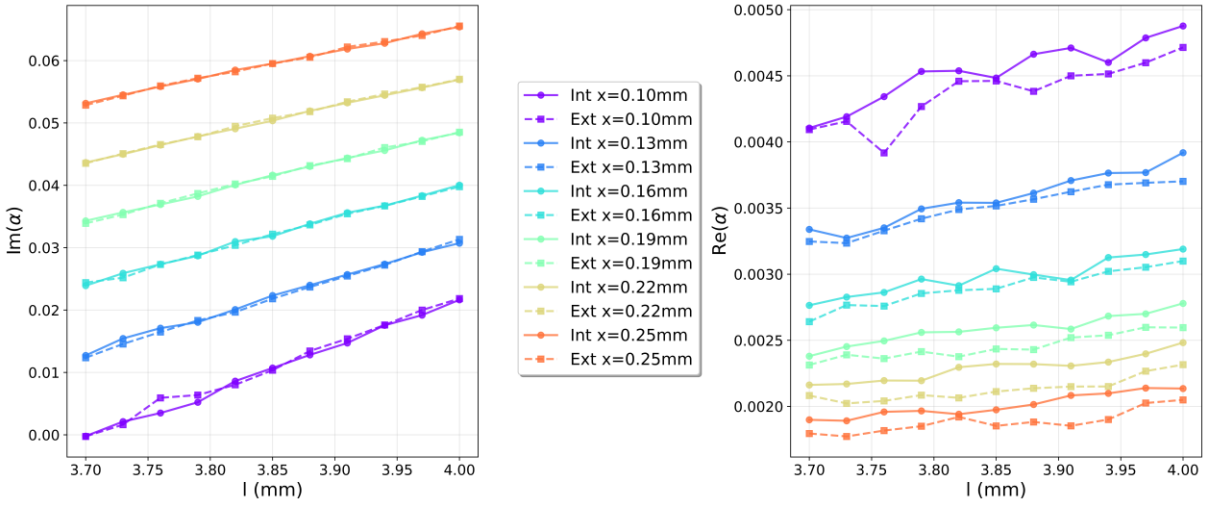

Figure 69 : Comparison of the (left) imaginary and (right) real parts of the α function for both the internal and external configurations for the slot couples.

Looking at the results, it can be noted that the difference of these 2 functions between external and internal configurations is very small. The most significant discrepancies appear in re(α) function, which is theoretically supposed to be null. This value is considered negligible compared to the imaginary part. The second more observable differences arise for re(v_0) function when $l_{slot} > 3.9$ mm. Nonetheless, anticipating that the final values of l_{slot} will be under 3.9 mm because of the 2 MC undergone by N-2 sections, the problem can be simplified by considering only 1 function for α and v_0, which simplifies the matrixial convergence problem, but, above all, the calculation and the use of only one mutual coupling function p_{ab}. This poor difference can be explained by the fact that, here, the maximum variation of distance between the 2 slots ($2\times x_{max}$) is less than 0.5/20 = 2.5% compared to the wavelength in the air and 0.5/18.4 = 2.7% of the waveguide width. This difference would be greater in the case of thicker waveguides because the offset values are greater (therefore more variations in distance) and the external mutual coupling (MC_{ext}) is more pronounced.

Finally, the classical procedure is applied to obtain α, v_0 and p_{ab} exactly like in 3.3 and applied on the matrix system to obtain an 8 sections line with a tapering of Chebyshev giving a side lobe level (SLL) at -20dB. The design can also be considered symmetrical in the H-plane (which geometrically is not exact because of the internal and external offsets). The following dimensions are obtained.

couple index	1	2	3	4
l(mm)	3.874	3.812	3.846	3.854
x(mm)	0.112	0.142	0.172	0.195

Table 5 : Values of the couples (x, l) for each section of the 2×8 SIWSA in TE20 obtained with python.

Once again, it can be observed that the offset x increases with the index and also that the longest slot is the first one (which undergoes the smallest mutual coupling). The first obtained results and the one after some corrections (10% on the offsets and 0.45% on the lengths) are given in Figure 70.

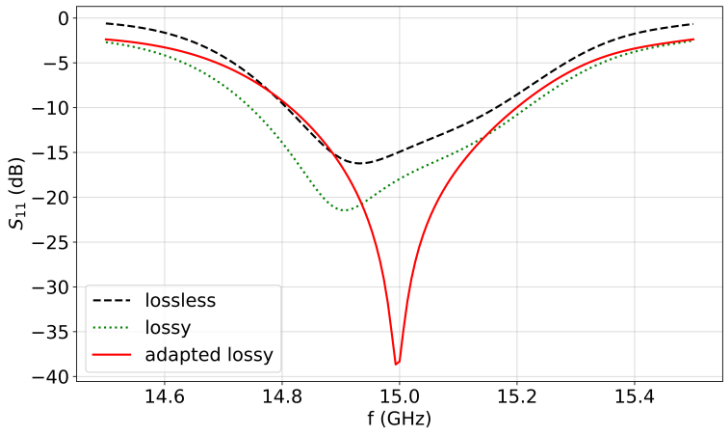

Figure 70 : Reflection coefficient of the TE20 mode for a 2×8 slotted waveguide lossless, lossy and lossy with corrections.

It can be observed that the first reflection coefficient of the TE_{20} is not very good, even for the lossless design but still placed at the desired frequency. It is then interesting to observe the input normalized admittance Y/G_0 of the mode as shown in Figure 71.

An interesting point is that even if the reflection coefficient of the lossless waveguide is not excellent, the expected Y/G_0 function behaviour is exactly at the wanted frequency. The error lies in the excessively high normalized conductance. Nonetheless, after some corrections on the slots' respective offset, an excellent reflection coefficient is obtained at the wanted frequency.

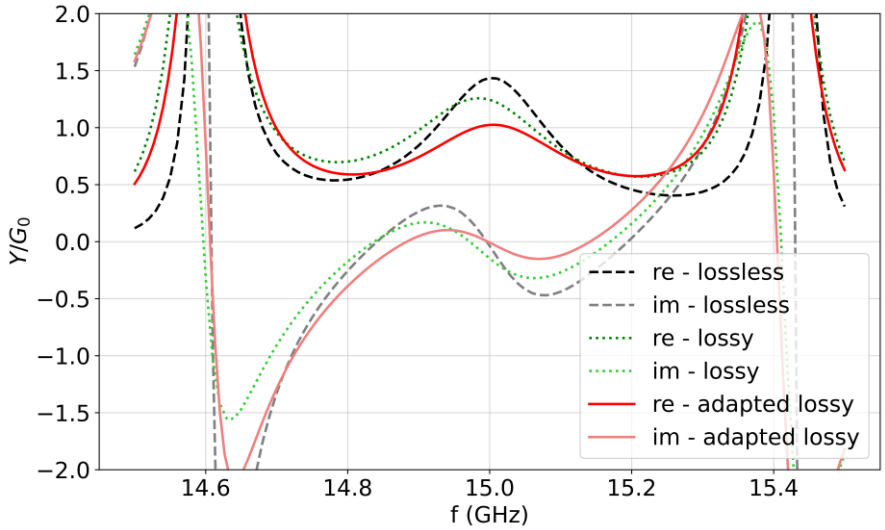

Figure 71 : Real and imaginary parts of the normalized admittance Y/G_0 of the TE20 mode for a 2×8 slotted waveguide, lossless, lossy and lossy with corrections.

As previously, the 2×8 waveguide is simply duplicated one time, given a 4×8 slotted array. The adaptation and radiation patterns are given in Figure 72.

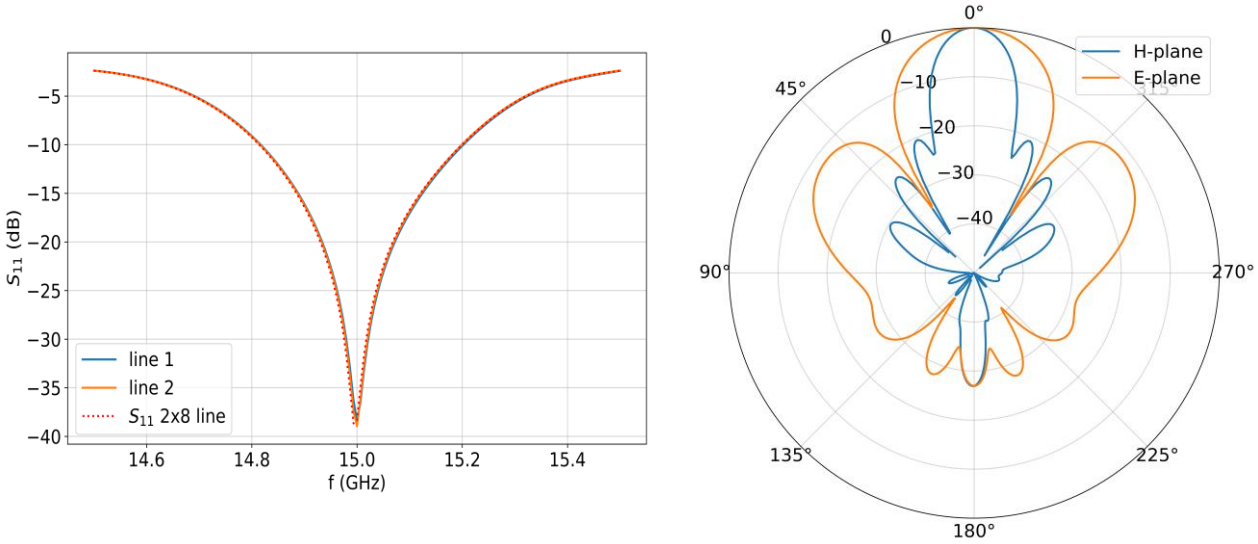

Figure 72 : Reflection coefficient of the 4×8 slotted array in TE20 mode and its associated normalized radiation pattern.

As expected, the variations in the reflection coefficient matching in frequency do not change thanks to the importance of the strong intern mutual coupling (MC_{int}). Looking at the obtained radiation pattern in H-plane, it can be observed that the side lobe level (SLL) doesn't respect the Chebyshev tapering for -20dB with a too much important decrease in level when approaching $\pm\pi/2$ (even if the sides lobes are supposed to decrease because of the magnetic dipole radiation pattern in H-plane). Nonetheless, it can be said that the use of this new method has been very useful to design a thin SIW slotted array in TE_{20} mode with the consideration of the mutual coupling. Something that had never been done before.

3.4.3 Consideration of the external mutual coupling

- **Presentation of the problem**

The previous presented method, for TE_{10} like TE_{20} modes, stays robust thanks to the monopole of the internal mutual coupling (MC_{int}). Nonetheless, the assumptions on which the matrix model and associated simulations were built are no more valuable when the thickness increases because of the decrease of the internal mutual coupling and the increase of the internal one. It would therefore be interesting to extend the method presented in this chapter to consider the external mutual coupling (MC_{ext}).

For the demonstration presented in this manuscript, an even and symmetrical M×N network will be considered, plus the external mutual coupling ((MC_{ext}) only with the 2 closest neighbours in E-plane (line to line). Therefore, for a given slot, the mutual coupling is considered with 4 slots, 2 in the H-plane (same waveguide) as previously plus 2 in the E-plane (line by line) as shown in Figure 73.

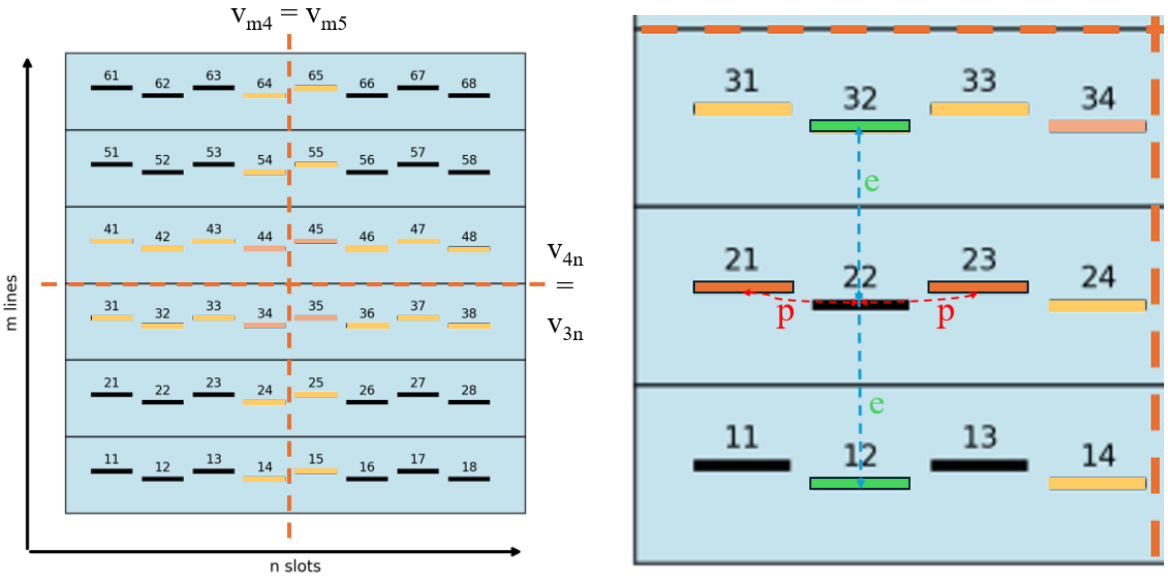

Figure 73 : (left) Geometrical representation of a symmetrical even M×N array and (right) coefficients of mutual coupling p and e in a subsection.

As it can be observed, thanks to the symmetry and considering the mutual coupling only with the four closest neighbours, the M×N array study is reduced to M/2×N/2 subsection studies with equal slot voltage $V_{N/2} = V_{N/2+1}$ for each waveguide and $V_{M/2} = V_{M/2+1}$ for the 2 middle waveguides. This last point corresponds to the orange slots in the figure (slots 21 and 23). Moreover, as presented in the subsection figure, the coefficient of mutual coupling slot to slot in the same waveguide is still named with the letter p, and the letter e corresponds to the one line by line, exclusively depending on the external mutual coupling (MC_{ext}).

The fundamental difficulty here is that the mode voltage V_{in_m} of each waveguide m can be different depending on its own matching and the wanted weighting excitation. Therefore, the full approach must stay in voltage and cannot be normalized from the beginning. The method presented in 3.2 and 3.3 must then be reviewed.

- **Theoretical adaptation for external mutual coupling**

For the following of the study, the following variables will be used:

- V_{mn} for the voltage in slot m.n
- V_{in_m} for the maximal voltage at belly of the guided wave in waveguide m
- v_{mn} for the normalized slot voltage in slot m.n by V_{in_m}
- V_{mn0} for the slot voltage without MC for the given V_{in_m}
- v_{mn0} for the normalized slot voltage without MC for the given V_{in_m}
- $p_{m.n1.n2}$ for MC_{int} between 2 slots n1 and n2 from the same waveguide m
- $e_{n.m1.m2}$ for MC_{ext} of same slot number n between waveguides m1 and m2

For a subsection M/2×N/2, the voltage slot system is defined as:

$$\begin{cases} V_{11} = V_{110} + p_{112}V_{12} + e_{112}V_{21} \\ V_{12} = V_{120} + p_{121}V_{11} + p_{123}V_{13} + e_{212}V_{22} \\ \vdots \\ V_{1\frac{N}{2}} = V_{1\frac{N}{2}0} + p_{1\frac{N}{2}\left(\frac{N}{2}-1\right)}V_{1\frac{N}{2}\left(\frac{N}{2}-1\right)} + p_{1\frac{N}{2}\left(\frac{N}{2}+1\right)}V_{1\frac{N}{2}\left(\frac{N}{2}+1\right)} + e_{\frac{N}{2}12}V_{2\frac{N}{2}} \\ V_{21} = V_{210} + p_{212}V_{22} + e_{121}V_{11} + e_{123}V_{31} \\ V_{22} = V_{220} + p_{222}V_{21} + p_{223}V_{23} + e_{221}V_{12} + e_{223}V_{32} \\ \vdots \\ V_{2\frac{N}{2}} = V_{2\frac{N}{2}0} + p_{2\frac{N}{2}\left(\frac{N}{2}-1\right)}V_{2\frac{N}{2}\left(\frac{N}{2}-1\right)} + p_{2\frac{N}{2}\left(\frac{N}{2}+1\right)}V_{2\frac{N}{2}\left(\frac{N}{2}+1\right)} + e_{\frac{N}{2}21}V_{1\frac{N}{2}} + e_{\frac{N}{2}23}V_{3\frac{N}{2}} \\ \vdots \\ V_{\frac{M}{2}1} = V_{\frac{M}{2}10} + p_{\frac{M}{2}12}V_{\frac{M}{2}2} + e_{1\frac{M}{2}\left(\frac{M}{2}-1\right)}V_{\left(\frac{M}{2}-1\right)1} + e_{1\frac{M}{2}\left(\frac{M}{2}+1\right)}V_{\left(\frac{M}{2}+1\right)1} \\ V_{\frac{M}{2}2} = V_{\frac{M}{2}20} + p_{\frac{M}{2}21}V_{\frac{M}{2}1} + p_{\frac{M}{2}23}V_{\frac{M}{2}3} + e_{2\frac{M}{2}\left(\frac{M}{2}-1\right)}V_{\left(\frac{M}{2}-1\right)2} + e_{2\frac{M}{2}\left(\frac{M}{2}+1\right)}V_{\left(\frac{M}{2}+1\right)2} \\ \vdots \\ V_{\frac{MN}{2\,2}} = V_{\frac{MN}{2\,2}0} + p_{\frac{MN}{2\,2}\left(\frac{N}{2}-1\right)}V_{\frac{M}{2}\left(\frac{N}{2}-1\right)} + p_{\frac{MN}{2\,2}\left(\frac{N}{2}+1\right)}V_{\frac{M}{2}\left(\frac{N}{2}+1\right)} + e_{\frac{NM}{2\,2}\left(\frac{M}{2}-1\right)}V_{\left(\frac{M}{2}-1\right)\frac{M}{2}} + e_{\frac{NM}{2\,2}\left(\frac{M}{2}+1\right)}V_{\left(\frac{M}{2}+1\right)\frac{M}{2}} \end{cases} \quad (3.21)$$

By considering:

$$\begin{cases} V_{\frac{M}{2}\mathrm{n}} = V_{\left(\frac{M}{2}+1\right)\mathrm{n}} \\ V_{m\frac{N}{2}} = V_{m\left(\frac{N}{2}+1\right)} \end{cases} \quad (3.22)$$

It can be written with the matrixial form :

$$V_0 = Q.V \Leftrightarrow V = Q^{-1}.V_0 \quad (3.23)$$

With V and V_0 the column matrices of the slots' voltage considering the mutual coupling MC and the own slot voltage (without MC) respectively. Q corresponds to the matrix of respectively internal and external mutual coupling coefficients e and p. Taking the 6×8 RWG slotted array given in Figure 73, the Q matrix of the subsection M/2×N/2 is defined as:

$$Q = \begin{pmatrix}
1 & -p_{112} & 0 & 0 & -e_{112} & 0 & 0 & 0 & 0 & 0 & 0 & 0 \\
-p_{121} & 1 & -p_{123} & 0 & 0 & -e_{212} & 0 & 0 & 0 & 0 & 0 & 0 \\
0 & -p_{132} & 1 & -p_{134} & 0 & 0 & -e_{312} & 0 & 0 & 0 & 0 & 0 \\
0 & 0 & -p_{143} & (1-p_{145}) & 0 & 0 & 0 & -e_{412} & 0 & 0 & 0 & 0 \\
-e_{121} & 0 & 0 & 0 & 1 & -p_{212} & 0 & 0 & -e_{123} & 0 & 0 & 0 \\
0 & -e_{221} & 0 & 0 & -p_{221} & 1 & -p_{223} & 0 & 0 & -e_{223} & 0 & 0 \\
0 & 0 & -e_{321} & 0 & 0 & -p_{232} & 1 & -p_{234} & 0 & 0 & -e_{323} & 0 \\
0 & 0 & 0 & -e_{421} & 0 & 0 & -p_{243} & (1-p_{245}) & 0 & 0 & 0 & -e_{423} \\
0 & 0 & 0 & 0 & -e_{132} & 0 & 0 & 0 & (1-e_{134}) & -p_{312} & 0 & 0 \\
0 & 0 & 0 & 0 & 0 & -e_{232} & 0 & 0 & -p_{321} & (1-e_{234}) & -p_{323} & 0 \\
0 & 0 & 0 & 0 & 0 & 0 & -e_{332} & 0 & 0 & -p_{332} & (1-e_{334}) & -p_{334} \\
0 & 0 & 0 & 0 & 0 & 0 & 0 & -e_{432} & 0 & 0 & -p_{343} & (1-e_{434}-p_{345})
\end{pmatrix} \quad (3.24)$$

Even if the building logic of the Q matrix doesn't initially appear, Figure 74 is useful to understand it. This Q square matrix is of size M/2×N/2 of M/2×M/2 subsections, each one of size N/2×N/2. The (m, m) subsections on the diagonal correspond to the internal MC, the (m, m±1) subsections correspond to the external MC and the last one (M/2, M/2) takes both into account because of the supposed symmetry in E and H planes.

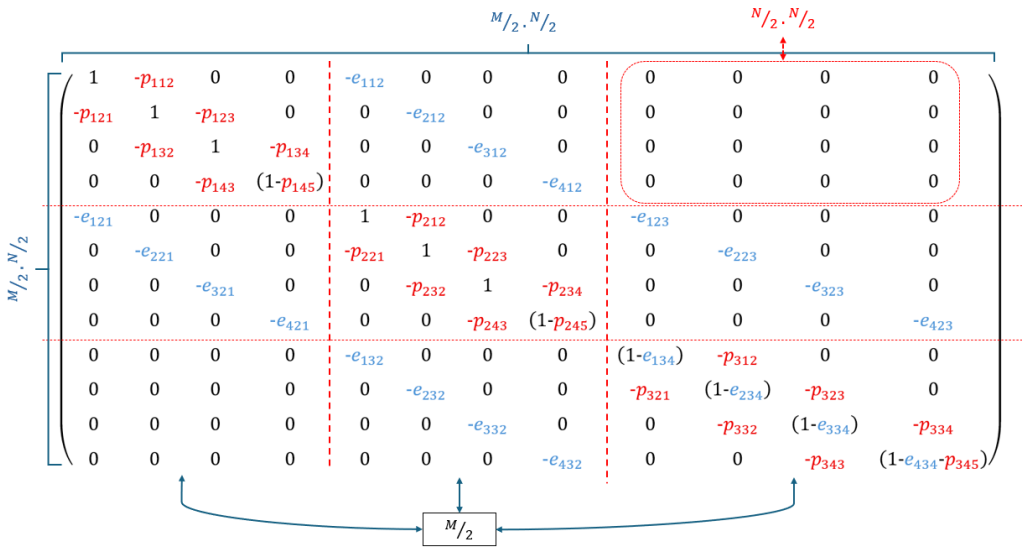

Figure 74 : diagram of the building of the Q matrix

From the matrix system $V = Q^{-1}.V_0$, two important points arise:

- How to obtain the V_{mn0} values?
- How to reduce this voltage-based matrix system to the normalized impedance matrix system?

To obtain the V_{mn0} values, the general approach remains the same that in 3.2.3 section: knowing that the ratio V_s/V_{in} remains constant, the own slot voltage for the given mode voltage is obtained with:

$$y_{mn0}(x,l) = \alpha(x,l).\frac{V_{mn0}(x,l)}{V_{in_m}} \Leftrightarrow V_{mn0}(x,l) = \frac{y_{mn0}(x,l)}{\alpha(x,l)}.V_{in_m} \quad (3.25)$$

$$V_{mn0}(\mathrm{x},\mathrm{l}) = v_{mn0}(x,l).V_{in_m} \tag{3.26}$$

Knowing already the normalized slot's voltage without mutual coupling v_0 functions, this last expression can be used from the simulation by also exporting V_{in_m} values and then calculating the value of V_{mn0} on the simulation in question. V_{in_m} can also be obtained theoretically by the following approach:

$$V_{in_m} = V_0^+ + V_0^- = V_0^+(1+\Gamma) \tag{3.27}$$

$$P = V^2/R = \left|V_0/\sqrt{2}\right|^2/R \Leftrightarrow |V_0| = \sqrt{2.P.R} \tag{3.28}$$

So

$$V_{in_m} = V_0^+(1+\Gamma) = (1+\Gamma_m)\sqrt{2.P_m.R} \tag{3.29}$$

P corresponds to the power of excitation assigned to the waveport m, and R is the constant resistance of the waveguide which can be obtained with the software by using the waveport impedance as Z_{pv} mode. This last formula is particularly useful to obtain the final V_{in_m} values which will be obtained for a matched design. Therefore, in the matrixial model presented in (3.23), the V_0 matrix can be written as:

$$V_0 = \begin{pmatrix} V_{110} \\ \vdots \\ V_{1\frac{N}{2}0} \\ \vdots \\ V_{\frac{M}{2}10} \\ \vdots \\ V_{\frac{MN}{2\,2}0} \end{pmatrix} = \begin{pmatrix} v_{110}V_{in_1} \\ \vdots \\ v_{1\frac{N}{2}0}V_{in_1} \\ \vdots \\ v_{\frac{M}{2}10}V_{in_{\frac{M}{2}}} \\ \vdots \\ v_{\frac{MN}{2\,2}0}V_{in_{\frac{M}{2}}} \end{pmatrix} \tag{3.30}$$

Concerning this matrix, a complex point here is that the value of V_{in_m} for each waveguide m giving the value of V_{mn0} depends on the adaptation of that waveguide itself (and therefore of all the pairs (x, l) of this waveguide).

Concerning the final full matrix system, it is necessary to pass from the column matrix V (in volt) to the normalized column matrix y and normalize in the process. To do so, the system can be written as:

$$\begin{pmatrix} y_{11} \\ \vdots \\ y_{1\frac{N}{2}0} \\ \vdots \\ y_{\frac{M}{2}10} \\ \vdots \\ y_{\frac{MN}{2\,2}0} \end{pmatrix} = \begin{pmatrix} \alpha_{11}/V_{in1} & \dots & 0 & \dots & 0 & \dots & 0 \\ \vdots & \ddots & \vdots & . & \vdots & . & \vdots \\ 0 & \dots & \alpha_{1\frac{N}{2}}/V_{in1} & \dots & 0 & \dots & 0 \\ \vdots & . & \vdots & \ddots & \vdots & . & \vdots \\ 0 & \dots & 0 & \dots & \alpha_{\frac{M}{2}1}/V_{in\frac{M}{2}} & \dots & 0 \\ \vdots & . & \vdots & . & \vdots & \ddots & \vdots \\ 0 & \dots & 0 & \dots & 0 & \dots & \alpha_{\frac{MN}{2\,2}}/V_{in\frac{M}{2}} \end{pmatrix} \begin{pmatrix} V_{11} \\ \vdots \\ V_{1\frac{N}{2}} \\ \vdots \\ V_{\frac{M}{2}1} \\ \vdots \\ V_{\frac{MN}{2\,2}} \end{pmatrix} \tag{3.31}$$

In (3.31), the diagonal matrix α from (3.14), allowing to do the relation between slot's normalized admittance y and its normalized slot voltage v, is adapted by integrating the inverse factor $1/V_{in_m}$ to normalise the values of V matrix allowing to return to the normalize mode. The final matrixial product can then be written as:

$$y = \alpha'.Q^{-1}.V_0 \tag{3.32}$$

α' corresponds here to the adaptation of the classical diagonal α matrix with the inverse factor $1/V_{in_m}$. Consequently, the definition of α introduced in (3.2) as a ratio of unitless slot's normalized admittance y and its normalized voltage v is now defined by $\alpha' = \alpha / V_{in_m}$ in V^{-1}.

As mentioned earlier, a significant difficulty in using this matrix network for the convergence algorithm to size the network is that the used value of V_{in_m} depends on the sum $\sum y_n$ value for each waveguide m (as previously but ignored thanks to the general normalization). This value, which appears in the square matrix α and the column matrix V_0, is supposed to change in time when modifying the values of each couple (x_{mn}, l_{mn}) for a given iteration. Consequently, the real value of each of the slot normalized admittance y_{mn} and then the mode voltage in the waveguide m V_{in_m} cannot be independently obtained. However, when we want to converge to a given specific adaptation (classically $\sum y_n = 1 + 0j$), the seeked value of the mode voltage V_{in_m} can be deduced from (3.29). The convergence algorithm can therefore be launched with these values set. The pairs (x, l) obtained are then what would theoretically validate these V_{in_m} values and therefore the adaptation of the network.

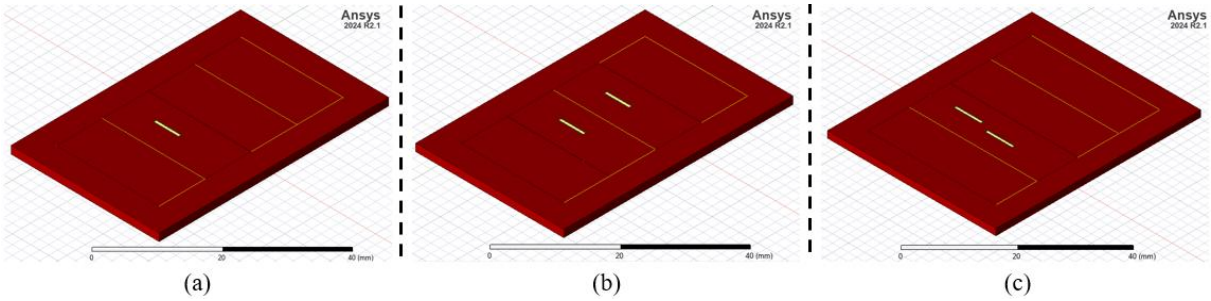

Figure 75 3 used designs to analyse the electromagnetic behaviour of (a) the individual slot, (b) the external (c) and the internal mutual coupling

A last point on this theoretical approach is the deduction of $p_{m.n1.n2}$ and $e_{n.m1.m2}$ functions. To do so, the 3 HFSS designs presented in Figure 75 are used. The designs (a) and (c) are independent of the waveguide number in a way that all is normalized by the same V_{in_m} value. The real new interesting point here is the second design (b) allowing to study the coefficient e defined as:

$$e_{n.m1.m2} = \frac{V_{m1.n.} - V_{m1.n.0}}{V_{m2.n.}} \tag{3.33}$$

In the second design (b) with the slot1 and the slot2, it is easier to numerically define it as:

$$e_{12} = \frac{V_1 - V_{10}}{V_2} = \frac{V_1 - v_{10}.V_{in_1}}{V_2} \tag{3.34}$$

Knowing already v_{10} values from the design (a), simulating the design (b) with some given couples (x_1, l_1) and (x_2, l_2) allows to export the values of V_1, V_2 V_{in_1} and V_{in_2} and numerically obtain e_{12} and e_{21}. Consequently, with the same kind of python script control of HFSS as described in 3.3, it is finally possible to obtain the function $e_{ab}(x_a, l_a, x_b, l_b)$.

An important and limiting point here is that for same couples (x_a, l_a) and (x_b, l_b), changing the weighting of the power excitation between the waveguides slowly change the value of e_{ab}. Consequently, in a case of tapering between the M waveguides, this exercise must be done M/2 times. Nonetheless, in the case of a classical weighting between M waveguides, the ratio of weighting waveguide to waveguide is relatively small, conducing to a poor relative change in the e_{ab} coefficient. Accepting this small error allows the simulation to be performed only once and saves a lot of time.

- **Example of application**

To illustrate this extension to the external mutual coupling consideration, a test is done with a 4×8 design at 15GHz with a Ro4003 dielectric of 1.574 mm thickness. A uniform distribution is applied between the waveguide and a tapering of Chebyshev for a desired SLL of -23 dB. The width of the rectangular waveguide is $a_{rwg} \approx 8$mm, the ratio b/a ≈ 19%. This RWG slotted array is then still impacted by the internal mutual coupling according to the Elliott's observations in [32] but the external mutual coupling is also important.

Following the procedure starts by finding the matching zone for each design, the one for 1 slot design (a), 2 parallel slots (b) and 2 slots in the same waveguide (c) are given in the Table 6:

	1 slot design	2 slots – MC_{ext} design	2 slots - MC_{int} design
x (mm)	[0.3 – 0.76]	[0.3 - 0.85]	[0.2 - 0.65]
l (mm)	[3.25 – 3.45]	[3.25 - 3.45]	[3.15 – 3.3]

Table 6 : Matching zone for the (x, l) couple for the 3 used designs with an external MC study.

Consequently, the selected zone of simulation is x = [0.15 – 0.6] mm and l = [3.0 – 3.25] mm. The first simulations are then done on the individual slot, allowing to obtain α and v_0 functions given in Figure 76 and Figure 77.

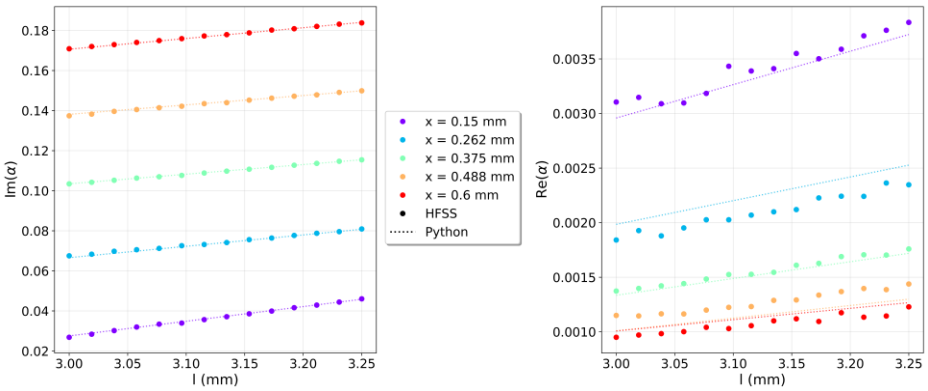

Figure 76 : Variation of α function depending on (x,l) values for the Ro4003 design and its numerical approximation.

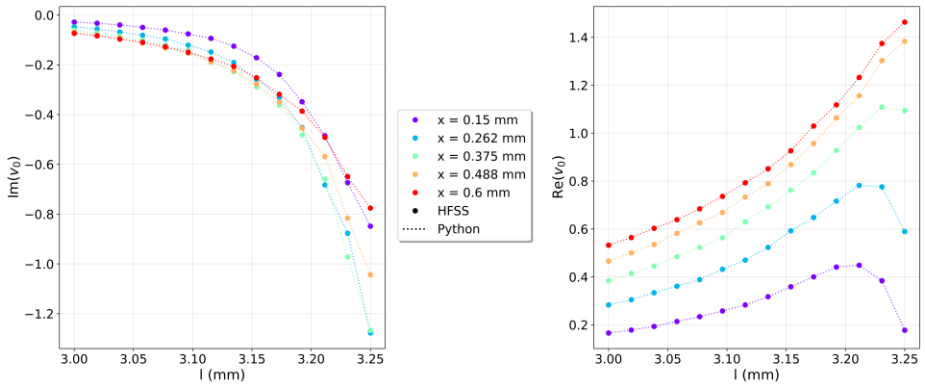

Figure 77 : Variation of v_0 function depending on (x,l) values for the Ro4003 design and its numerical approximation.

It can be observed that the α function continues to follow its affine function behaviour. Furthermore, thanks to the more important waveguide thickness and then the more important offset x values than for the 127 µm thickness design, the real part of α becomes really neglectable in front of the imaginary part allowing to neglect the little inaccuracy in the numerical approximation for high offsets.

On the other side, the v_0 function, corresponding to the normalized slot's voltage without mutual coupling, starts to follow the initial behaviour around the individual resonant slot length observed in Figure 50. The previous used analytical exponential approximation is no more valuable. A 2D interpolation method is then used. Even if the matching is excellent as observed in Figure 77, the disadvantages of numerical interpolation functions will be experienced during the convergence algorithm, namely heavier using functions and a limitation on use to the simulation range itself.

Next, the 2 functions p_{ab} and e_{ab} respectively representing the internal and external mutual coupling must be obtained. To do so, the automation procedure of simulation for a set of couple (x_b, l_b) as presented in 3.3.3 is applied. As shown in Figure 78 and Figure 79 at the same scales, the exponential approximation is not applicable either. The 2D interpolation is also used with the idea that the numerical object returned by the SciPy functions allowing to use the 2D interpolation is saved in a numerical dictionary with [x_2, l_2] key. Two final dictionaries are then respectively used in the functions p_{ab} and e_{ab} thus complicating the convergence methods.

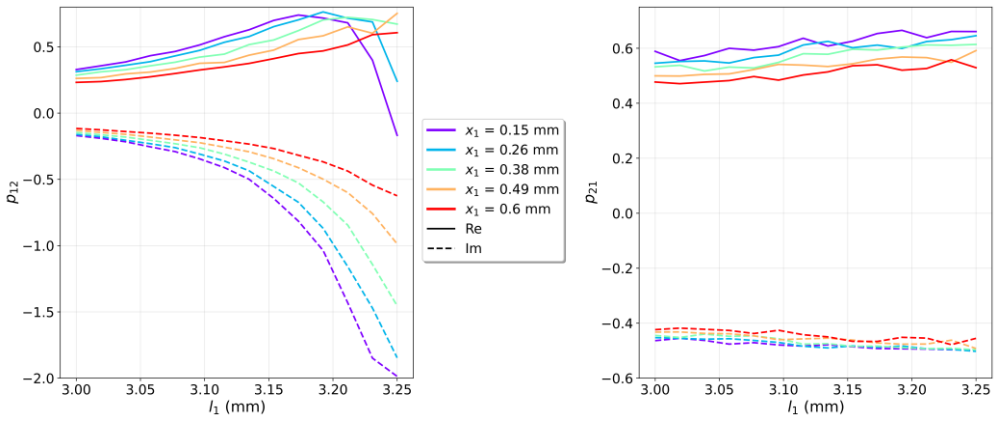

Figure 78 : Variations of the p_{12} and p_{21} coefficients depending on (x_1, l_1) for (x_2, l_2) fixed at (-0.3, 3.14) mm.

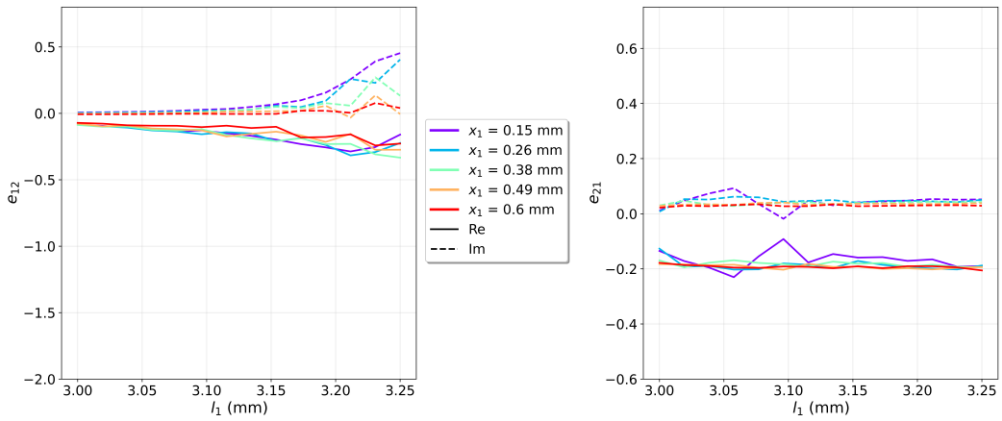

Figure 79 : Variations of the e_{12} and e_{21} coefficients depending on (x_1, l_1) for (x_2, l_2) fixed at (-0.3, 3.14) mm.

Different points can be observed:

- The p_{ab} coefficient of MC_{int} stays more important than the e_{ab} coefficient of MC_{ext}
- The values of the e_{ab} coefficient are more sensitive to statistical noise errors with their values are low
- The real and imaginary parts of p_{ab} and e_{ab} have opposite signs.
- As a reminder, p_{21} and e_{21} values, which are simpler to analyse and represent the electromagnetic effect a nearby slot would exert on the analysed slot when its (x, l) pair varies, with the pair of the studied slot remaining fixed. We can see here that the variations are more important for the coefficient p than for coefficient e and above all, the relative variations of p_{21} with of offset x_1 is far more important than for the thinnest design of 127 µm as viewed in Figure 52.

Once all the upstream numerical procedure is done, the matrix system can be used, and the convergence algorithm allows to obtain the (x, l) values of the quarter subsection for the wanted weighting in H-plane. The design is drawn, and the first matching test can be simulated as shown in Figure 80.

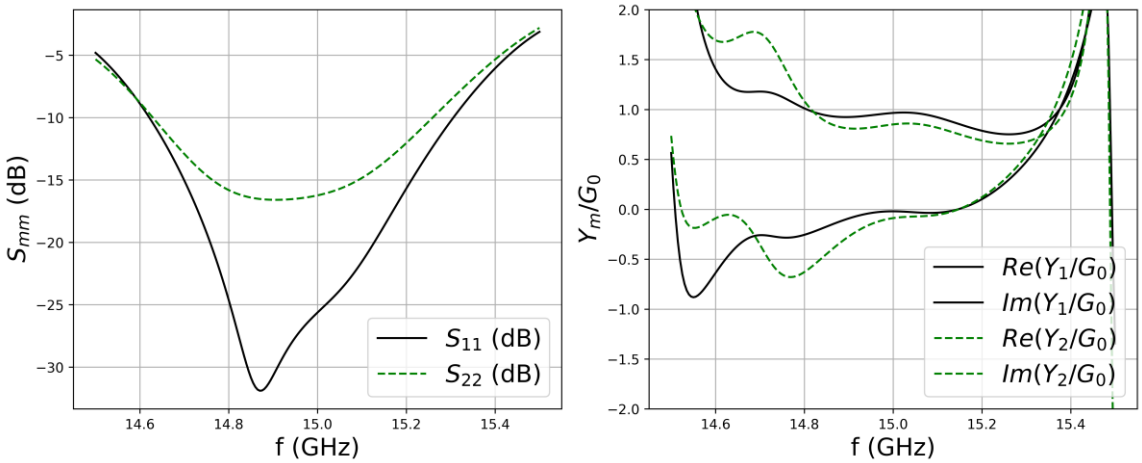

Figure 80 : Reflection coefficient and normalized admittance for the 2 first waveguides of the 4×8 Ro4003 design of 1.574 mm.

It can be observed that the reflection coefficient is not excellent, especially for the internal waveguide, but close to the expected frequency of matching. As previously, factors of correction are used and allow us to obtain the results given in Figure 81.

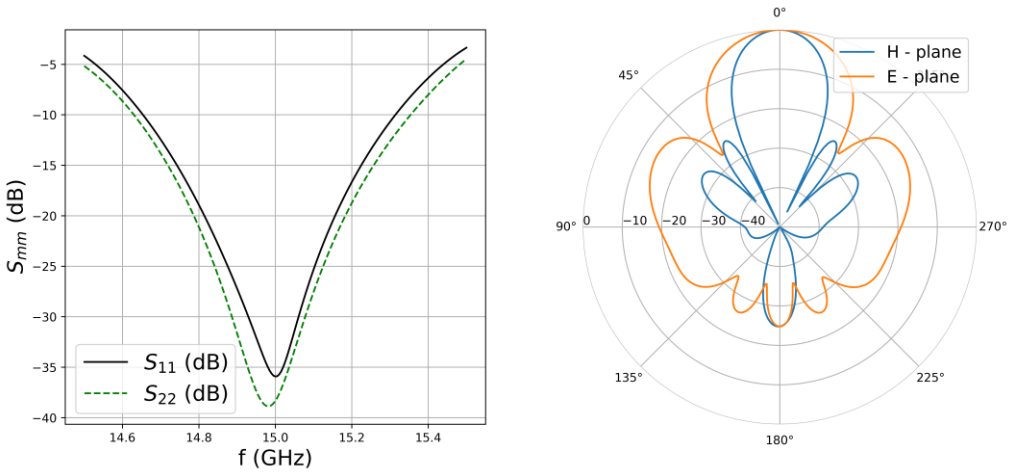

Figure 81 : Reflection coefficient for the 2 first waveguides of the corrected 4×8 Ro4003 design of 1.574 mm and its associated radiation pattern in log scale.

From the corrected reflection coefficient, it appears clearly that the thickness of the waveguide is an important factor to increase the bandwidth of the antenna.

The approach presented in this section highlights the difficulties involved in adapting the new method initially developed for SIW slotted array (SIWSA) with a very strong internal mutual coupling to SIWSA when an external mutual coupling also plays an important role that can no longer be ignored. The main difficulties that can be identified are:

- The expansion of the matrix system used in the convergence algorithm, and therefore the more apparent limits in computing power
- Longer simulation time due to a larger design and above all, the automation script for simulations and the calculations of external mutual coupling function e_{ab} in addition to the previous internal mutual coupling function p_{ab}
- The functions p_{ab} and e_{ab} take only into account the mutual coupling with the first neighbour slots in H and E plane respectively. A first improvement would be to do the same exercise with q_{ab} coefficient which would consider the MC_{ext} with slot at 45° from other waveguides. This would give us the coefficients for the eight antennas closest to the slot under study. However, this would further increase the time required for simulation and equation setting.

Nevertheless, this approach can remain particularly useful in cases where a protective film is added or even choke structures between the waveguides to try to limit a line to line mutual coupling. Furthermore, it could be used directly on RWG or SIW slotted array networks in cylindrical curvature, whose thickness would require considering the external mutual coupling. This last point corresponds to using a parallel solution from article [35] which adapts Elliott's theoretical method to cylindrical curvature.

3.5 Application of the method to realize a flexible slotted SIW

Although most of the results obtained with this novel method are simulated, a physical test was considered. The general design pattern stayed the same as that realized design in the previous chapter: a 4×8 slots array fed by a 1×4 divider on the opposite side of the slot array. The used dielectric is also RT/Duroid 5880 of 127 µm and the expected tapering for convergence is a Chebyshev weighting for -23dB SLL.

The same procedure and data that in 3.3 are used and the convergence algorithm returns the following (x, l) couples:

couple index	1	2	3	4
l(mm)	3.221	3.022	3.092	3.103
x(mm)	0.092	-0.109	1.517	-1.707

Table 7 : Deduced couple (x, l) values for the design of a 1×8 array at 15 GHz with Ro5880 of 127µm.

As previously, the 1×8 waveguides is drawn and tested in lossless configuration, lossy and matched lossy as shown in Figure 82.

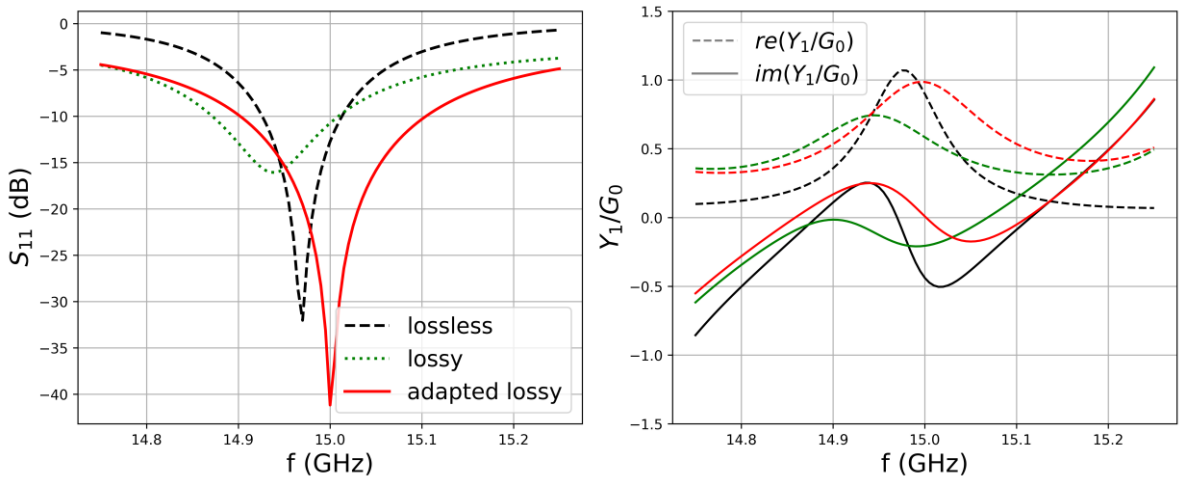

Figure 82 : Variations of the reflection coefficient and its associated normalized equivalent admittance for the 1×8 lossless, lossy and matched lossy designs.

The 1×8 waveguide matched for RT/Duroid 5880 and copper is then duplicated 3 times. In parallel, the 1×4 divider is drawn and adapted in HFSS. The adaptation and radiation pattern of the final numerical design are given in Figure 83.

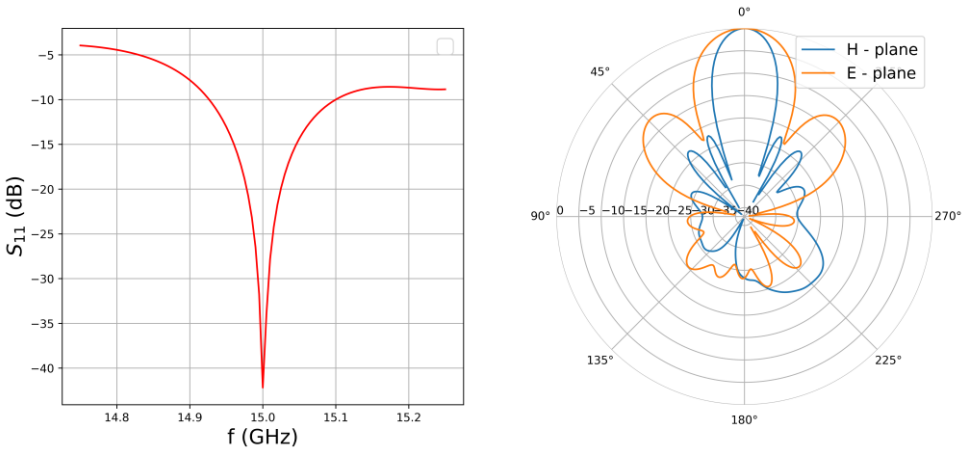

Figure 83 : Final results from HFSS of the reflection coefficient of the 4×8 slotted design and its associated normalized radiation pattern in log scale.

As it can be observed, the reflection coefficient is excellent but suffers from a poor bandwidth due to the thinness. The radiation pattern is close to the expected forward pattern but a dissymmetry in the backward direction is observed because the reflector plane suffers from the dissymmetry caused by the 1×4 ground feeding.

The gerber and dxf files are exported from the software and the design is realised in the Lab-STICC with the available technologies. Due to technical difficulties in implementation, the prototype is still under development.

3.6 Conclusion

This third chapter introduced a new novel method more conducive to the matching of very thin SIW slotted array. This has the advantage of being easily understandable with the application of the procedure and the development of the associated algorithm being relatively simple. The initial numerical results for network dimensioning have always yielded a frequency adaptation extremely close to the expected result and with better weighting control than the classic Elliott method often cited in the literature.

The general logic of this new approach was first presented together with the mathematical model used and the associated numerical tools. The algorithmic development was then introduced, including an indirect analysis of the functions involved and the construction of the convergence algorithm. Examples of design adaptation implemented in software were subsequently provided.

In addition to the classic design of an M×N network as with Elliott's procedure used in the second chapter, two excellent interests of this method were introduced. The first one is the possibility to add a protective film or varnish on the array without changing anything in the procedure. This point avoids complicating Elliott's procedure, which remains purely theoretical in this case as well. The second one is the possibility to decline this approach to the adaptation of array in TE_{20} mode, something for which there was currently no more effective method than simply designing the network in associated equivalent TE_{10} mode. This last point is particularly

useful with the aim of increasing flexibility for SIW slotted array by reducing the number of via rows.

This new method opens a lot of new possibilities of study. Some of them can directly be applied like the add of chokes or other motifs between the waveguide to reduce the external MC and also to work on the shape of the slots to try to change the radiation pattern or bandwidth. Another possibility, which would require more work, would be to fully adapt this model to the external mutual coupling. An initial attempt was made in this chapter by considering only the first two neighbouring slots in the E-plane (line to line).

Chapter 4 - Theoretical and Experimental Investigation of Curvature Effects on SIW Slotted Array Radiation Pattern

4.1 Introduction

In the context of conformal array, the study of the radiation pattern is one of the most studied subjects. As briefly described in 1.5, the subject is particularly complex because the classical notion of array factor (and all the associated theoretical work available in the literature) is no more applicable. This is due to the fact that unitary direction and possibly the polarisation are different for all elements. An excellent document to overview this problem is the chapter 10 from Johnsson and Persson Book [53] which details different synthesis techniques for designing the desired radiation pattern for conformal antenna arrays. Methods are presented for controlling main beam direction, sidelobe levels and polarization by controlling elements with their phase shift, their weighting excitation, their relative position on the conformal array and their oriented polarization. Analytical approach from the XXth century like the shape optimization, the method of Fourier or aperture projection method are presented. In the same way, a brief overview of all the algorithm methods for optimization are discussed, such as genetic or hybrid algorithms. Consequently, this exercise is a subject in its own right.

A main difficulty to directly link this topic to flexible SIW slotted array (SIWSA) is the difficulty to match weighting or phasing from a radiation pattern optimization algorithm to the real flexible SIW slotted array adapted on HFSS/CST : for a linear in phase array, a well validation of the initial desired weighting is difficult when correction factors are used to be well matched in frequency. Furthermore, create a phase shift between the slot (non-resonantly linear spaced longitudinal slots) means non constant element to element distance which makes adaptation considerably more difficult. Some articles on the literature on these topics are available like the one given in Table 1. Nonetheless, it can be observed that this work is always done for a given radius of curvature (mostly on a cylinder). It was therefore decided to follow another line of thinking: for a flexible SIW slotted array designed in a conventional manner (in-phase linear flat array), how can the electromagnetic impact of the array's curvature be anticipated for radii of the order of the wavelength? This study is particularly useful in the idea where a single flexible SIW slotted array would be mass produced and used in different cases where small radii of curvature are used (fixed on different masts, added on a coat or a helmet, weld or screwed onto vehicles like drones). In the idea of keeping the same global radiation pattern for all radii, a study on the different linear array parameters like the weighting or the slot-to-slot distance must be studied in the idea of limitations of HPBW or directivity variations.

On the other side, work on optimising the radiation pattern for given radius of curvature remains interesting. This topic already leads to a scientific library containing various types of complex algorithms or methods. It would be interesting to find a simpler approach that is quicker to implement and provides an acceptable initial approximation before optimisation using software in the case of in phase slot array.

Therefore, the different points treated in this chapter focus on the study of the radiation pattern of a cylindrically curved SIWSA in X and Ku bands for radii $R<10\lambda_0$. The first point will deal with the necessity to adapt the classical formula of bent radiation pattern for small radii because of the variations of radiation pattern of the slot antenna with important curvature. The second one will put into practice the developed theory with simulations and a set of

measurements realised with flexible SIWSA designs and compare it with theoretical approach. The curvature of the flexible SIWSA is always done on a cylinder, with bending in E plane as H plane, and in convex as in concave, leading to 4 possibilities of cylindrical curvature. Finally, in the idea of radiation pattern optimization for linear in phase SIWSA, a new method based on theory from combinatorics is presented.

4.2 Study of the radiation pattern formula of conformal array for curved slot with small radii of curvature

In this section, the integration of the radius variable R in the radiation pattern formula of 1 curved slot is first discussed. Then, integration of the first point in cylindrically conformed array's radiation pattern formula is addressed. Finally, in the idea of using the design for different possible small radii of curvature, a study is done on the impacts of linear arced array parameters such as the distance between slots, the weighting excitation or the unitary slot's directivity on the opening of the main beam with radii of curvature.

4.2.1 Study of 1 curved slot radiation pattern

The theoretical investigation of the radiation pattern of slot antennas on cylindrical waveguides was the subject of several complex scientific studies between the 1950s and the 1980s. Notable contributions include [54] or [55]. However, these works are characterized by a high level of electromagnetic and mathematical complexity. The empirical method proposed here, based on HFSS simulations, offers the advantage of straightforward implementation with a relatively simple coding framework. Moreover, it remains valid with or without the addition of a protective dielectric film, is applicable to different slot geometries, and inherently accounts for parameters such as slot width and conductor thickness, which are sometimes neglected in theoretical approaches to simplify the analytical derivations.

Thanks to an electromagnetic simulation software like HFSS, 1 curved slot can be drawn with different kind of curvature, in both E- and H-plane. It is then possible to obtain the radiation pattern of a slot for different radii of curvature and observe the global behaviour of this one depending on the radius R. From the simulations results, a method to obtain the numerical function approximating the radiation pattern $A(\theta,R)$ must be developed.

To observe the radiation characteristics from the software's simulations, 2 important results can be obtained: the directivity $D(\theta,\varphi)$ and the function $rETot(\theta,\varphi)$ which gives the magnitude in Volt of the total radiated electric field **E** in far-field multiplied by the radial distance **r**. This last one is particularly useful to obtain the amplitude of the voltage field independently of the distance. Knowing that, in far field, the E and H fields are directly proportional, its normalized value is then usable to obtain the normalized radiation pattern (in field) in E or H planes.

HFSS study

As explained before, HFSS is used to draw the slot for different planes of curvature as in Figure 84 where the slot is convexly curved but in H vs E planes. In the same way, Figure 85 presents a same slot curved in H plane but with convex vs concave curvature.

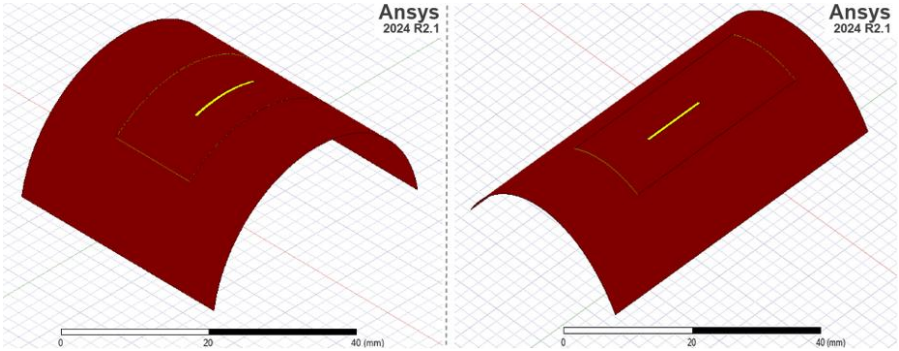

Figure 84 : 1 slot curved in H plane (left) and E plane (right) for radius of 2cm in cylindrical convex way.

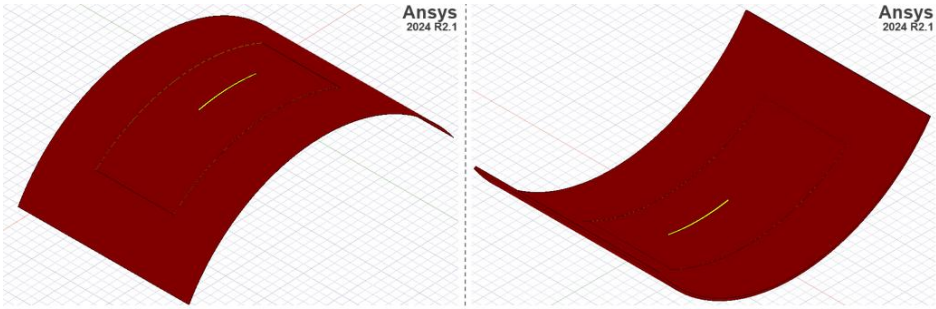

Figure 85 : 1 slot curved in convex (left) and concave (right) for radius of 4cm in H-plane.

Some difficulties may arise when designing these structures due to numerical errors stemming from software meshing and simulation constraints. Moreover, even when mesh and simulation convergence are achieved, results remain sensitive to initial parameters. The parameters selected for this study were those that yielded the best convergence and consistent results across different simulations. Consequently, the figures in this chapter may occasionally display results from different iterations that do not strictly follow the expected local behaviour. However, these results are retained to ensure consistency and comparability among the various designs.

The observation of the radiation pattern's variations with the radius of curvature $R<10\lambda_0$ is easiest in the H-plane curvature because of the radiation properties of the magnetic dipole. The gradient of variation is indeed more important that the one in E-plane. To avoid too much repetitive figures for a same global study of radiation pattern's opening with radius, the global study is done for curvature in H-plane and finally compared to the one in E-plane.

Taking for design reference the slot matched for SF280 dielectric at 15GHz, the directivity $D(\theta,\varphi)$ of the curved antenna for various R can be obtained in polar coordinate system as observed in Figure 86.

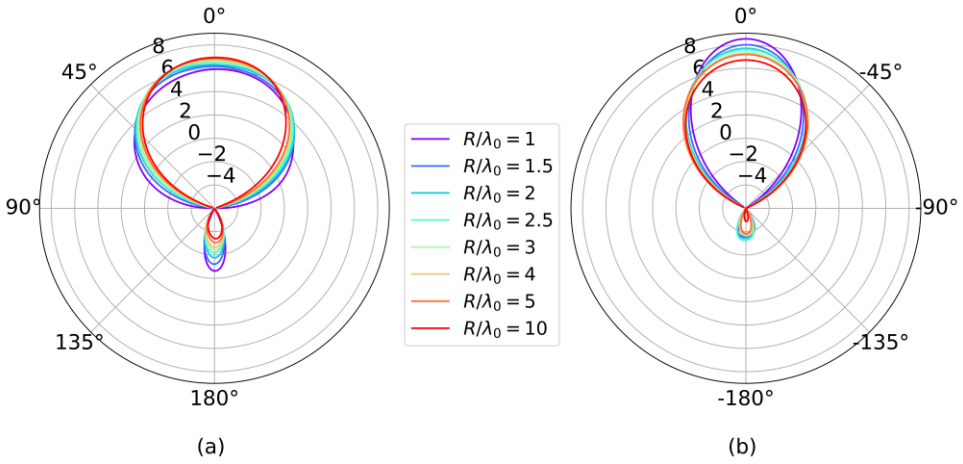

Figure 86 : Directivity in dB of a curved slot in H-plane for convex (a) and concave (b) curvature.

The superposed directivities being not extremely exploitable, 2 important curves are the variations of the maximal directivity D_{max} with radius and the variations of the half power beamwidth (HPBW) with radius (HPBW relative to the given radius).

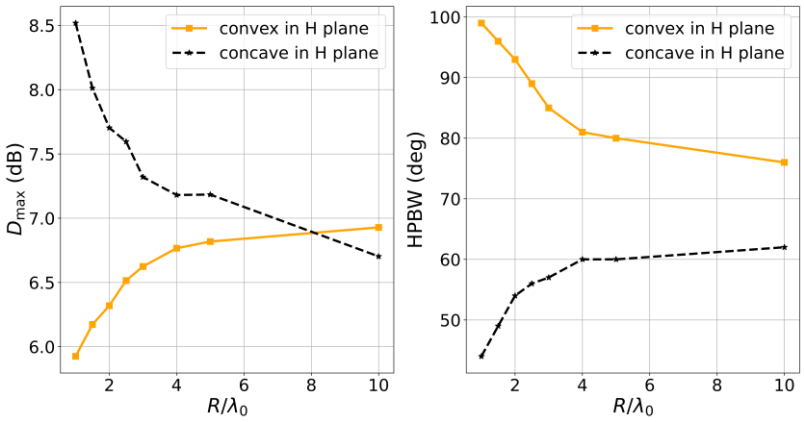

Figure 87 : Variations of the maximal directivity D_{max} and the associated half power beamwidth (HPBW) with radius in convex and concave curvature.

Figure 87 is particularly interesting to compare the opposite behaviour of $D_{max}(R)$ and HPBW(R) in a same plane of curvature for convex vs concave curvature. The main point is that a single curved slot loses its maximal directivity and open its main beam with decreasing radius of curvature R for convex curvature whereas the concave curved slot increases its directivity. The main reason for these variations is the curvature of the ground plane reflector itself. The edge effect of the ground plane hugs the main beam in concave curvature contrary to the convex curvature which deviate from the main beam. Concerning the geometry of the bent slot itself looking like an arc, the strongest radius with $R = \lambda_0$ leads to a difference in height (z points) between the middle of the arc and the edges of the arc smaller than 1% of the radius. Consequently, the only real cause of the variations of the radiation pattern for convex as concave curvature is the geometrical bend of the plane of reflection and not the bend of the slot itself.

These last simulation results illustrate well the need to consider the radius of curvature R as a variable. This can be numerically observed by comparing the HPBW for convex and concave curvatures, which show a gap of 60 deg. This requirement is particularly important for

H-plane curvature. Nonetheless, it can be observed in Figure 88 that the variations in the E-plane are far less significant.

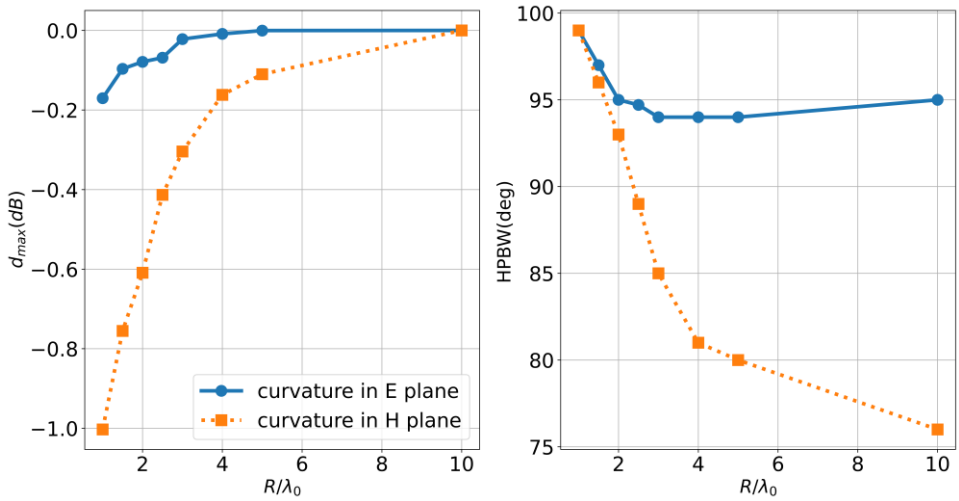

Figure 88 Variations of the normalized maximal directivity d_{max} and the associated half power beamwidth (HPBW) with radius in convex curvature in both E- and H-planes.

The gap values for the normalized directivity $d_{max}(R)$ in E-plane is less than 0.2dB and less than 5 degrees for HPBW(R). This is mainly explained by the fact that radiation pattern of the magnetic dipole in E-plane has a main beam already very large. The perturbation is then very small for the tested radii.

Now that the variation of the radiation pattern of a single slot with radius of curvature is well observed, a numerical approximation is needed to obtain the radiation pattern function for 1 slot $A_{1slot}(R, \theta)$.

Numerical approximation

When working on the radiation pattern, the mathematical approach is based on the electromagnetic fields (**E** or **H** fields) to apply the superposition theorem. From the software, it is not possible to directly obtain the fields **E** or **H**. Nonetheless, as explained before, the results from *rETot(θ,φ)* software function (in Volt) can be used and thanks to the excellent slot's linear polarization as described in the first chapter, the magnitude of the radiated **E** and **H** fields (independent of the distance) can be obtained with $\varphi = 0°$ and $\varphi = 90°$ respectively.

It is important to note that the aim of obtaining the radiation pattern function $A_0(R, \theta)$ of a single curved slot from a set of simulation for different radii R is done from the obtain results normalized by the flat slot (not normalized by the local maximum proper to each radius) in a way that final curved array takes for the reference the flat array for normalization. Then, we are looking for the function $e_{slot}(R, \theta)$ and $h_{slot}(R, \theta)$, respectively corresponding to the normalized radiating field in E- and H-plane, tending to 1 for $\theta=0$ and $R = \infty$. Once again, the demonstration is done in H-plane with a slot matched at 15GHz with SF280 dielectric. The aim is to approximate the normalized radiation pattern $h_{slot}(R, \theta)$ given in Figure 89.

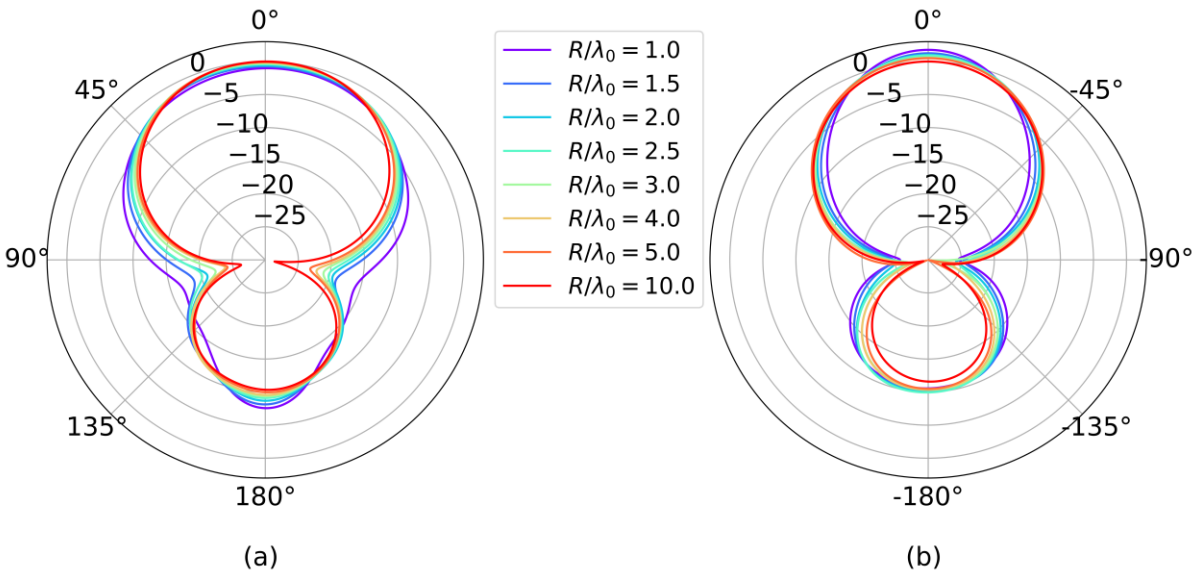

Figure 89 : Normalized field radiation pattern (dB) in H-plane for a SF280 slot curved convexly (a) and concavely (b).

the same global observation that in Figure 86 can be done for directivity: decrease the radius in concave leads to maximal normalized radiation pattern positive whereas the latter is negative in convex (in log scale).

To obtain a numerical function allowing to approach the values of $h_0(R, \theta)$, the simplest way is to use 2D interpolation function. Nonetheless, as previously highlighted, this approach can lead to significant discrepancies outside the simulated radius values. Furthermore, when used with a large number of iterations, as in an optimisation algorithm, the use of the numerical object created for the numerical function is more cumbersome than a simpler analytical approach. In the idea of obtaining an analytical function corresponding to the normalized slot radiation pattern $h_0(R, \theta)$ (in H-plane) valid outside the simulation range, the solution of even Fourier's series with coefficients depending on the radius was exploited. The used function is:

$$h_{slot}(R,\theta) = \frac{a_0(R)}{2} + \sum_n a_n(R).cos(n.\theta) \qquad (4.1)$$

Thanks to SciPy library, a recursive algorithm to obtained the a_n coefficients and smooth them depending on R in a way that final values of $a_n(R)$ follow a wanted function fitting the coefficients values of $a_n(R)$ is developed. The more the degree n of the Fourier's series is important, the more the numerical approximation is well matched. Nonetheless, increase the degree increases the size of the dictionary for coefficients of the chosen function for each $a_n(R)$ and then a more important time calculation for the final numerical function. It could be problematic for a use in convergence algorithm. As trade-off, it can be observed that a degree of 5 or 6 is enough sufficient for a good approximation.

Concerning the choice of the function to fit the independently found $a_n(R)$ points, a simple solution would be to use a quadratic function. The Figure 90 shows a good approximation.

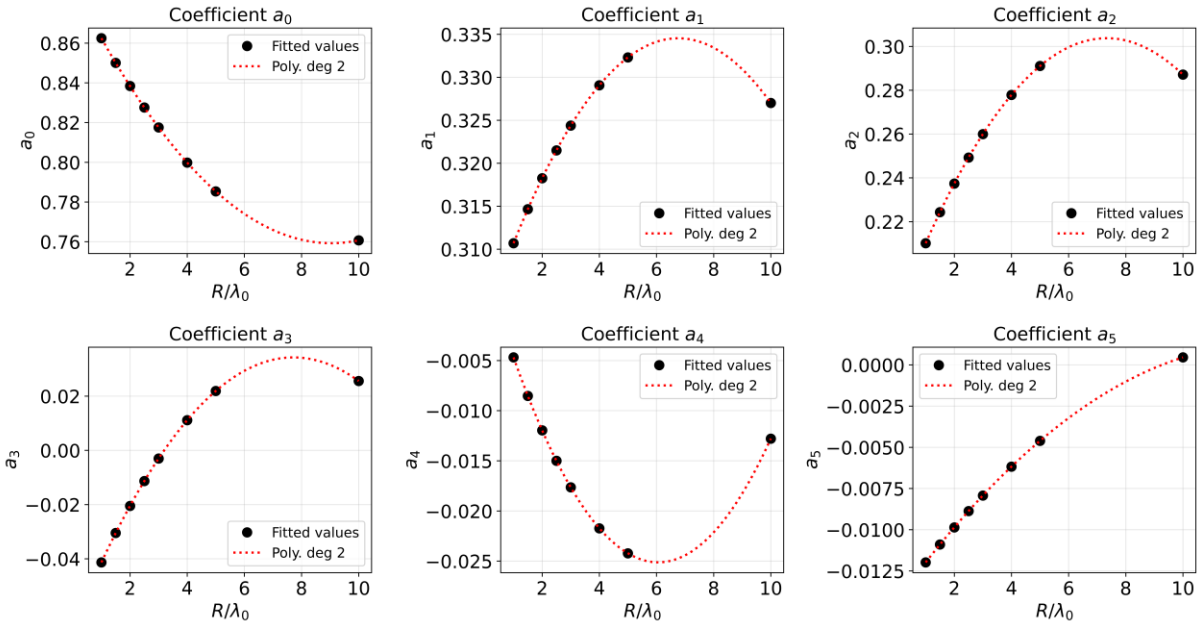

Figure 90 : Variations of the coefficients of the even Fourier's series depending on the radius and their quadratic approximations for the approximation of the normalized radiation pattern of 1 slot convexly curved in H plane.

Nevertheless, an important point must be highlighted: the limits values for R tending to 0 or +∞. From the Figure 89, it can anticipated that the radiation pattern will continue to open itself under $R/\lambda_0 < 1$ (even if R = 0 is not mechanically possible), and with the values of $R/\lambda_0 = 5$ and 10, it can be anticipated that the closure of the main lobe slowly increases until R = +∞ (meaning flat design). This mathematically means that the variations under $R/\lambda_0 < 1$ continue to follow the behaviour in this range of $1 < R/\lambda_0 < 5$ values, and above $R/\lambda_0 > 10$, the limit must tend in a constant with a slow linear coefficient of variations. In the above example in Figure 90, the quadratic approximation is a wrong solution because the limit in R = ∞ tends also in ∞. Therefore, the mathematical chosen approximation is the saturating exponential function:

$$a_n(R) = c_0 + c_1(1 - e^{-c_2 R}) \qquad (4.2)$$

Where c_0 is the y-intercept, c_1 impacts the variation of amplitude (saturation range) and c_2 impacts the saturation rate (convergence speed). For R tending to +∞, $a_n = c_0 + c_1$ (asymptote). To use this approach, a modification in the algorithm to find all the a_n coefficient must be down. Indeed, 2 conditions must be respected in parallel:

1) for a given radius R, a_n coefficients fit the associated simulated radiation pattern
2) For all the radii, all the values a_n follow the behaviour of a saturating exponential behaviour

A simple recursive algorithm is developed to respect these both conditions allowing to find the coefficients c_0, c_1 and c_2 for the n saturating exponential function fitting the $a_n(R)$ values. It can be noted that in the last quadratic approach, the second condition was not imposed. An example of this saturating exponential function approach is given in Figure 91 for convex curvature.

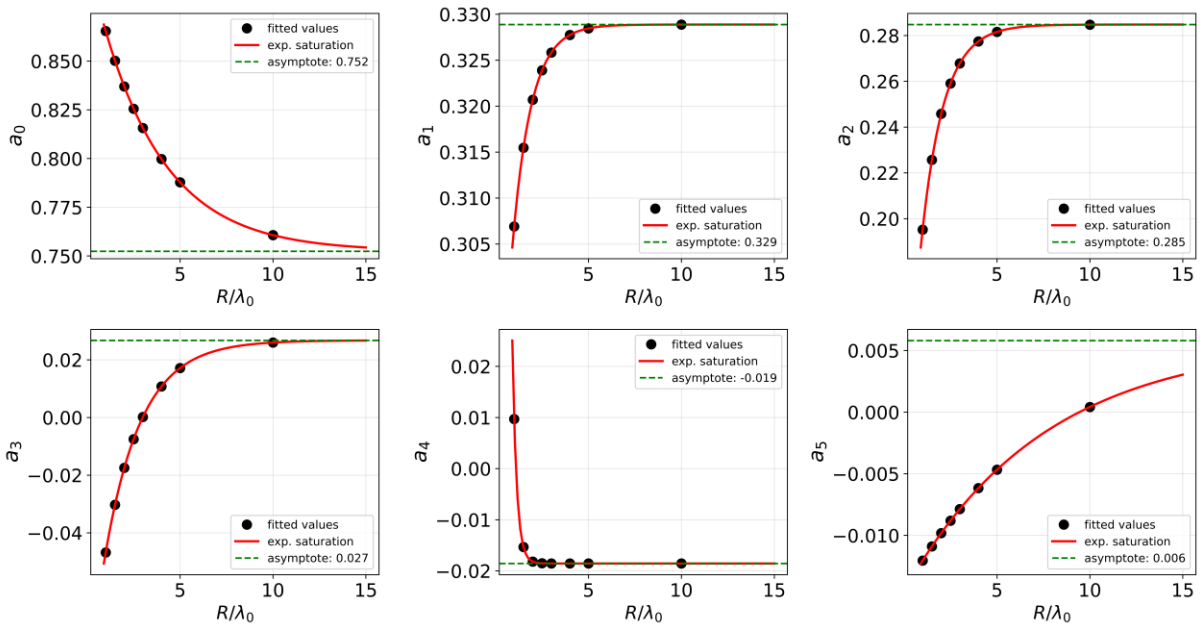

Figure 91 : Variations of the coefficients of the even Fourier's series depending on the radius and their saturating exponential function approximations for the normalized radiation pattern of 1 slot convexly curved in H plane.

In the figure, the constant asymptote is interesting by showing the limit value. The function (4.2) can be tested with the obtained coefficients suturing exponential functions.

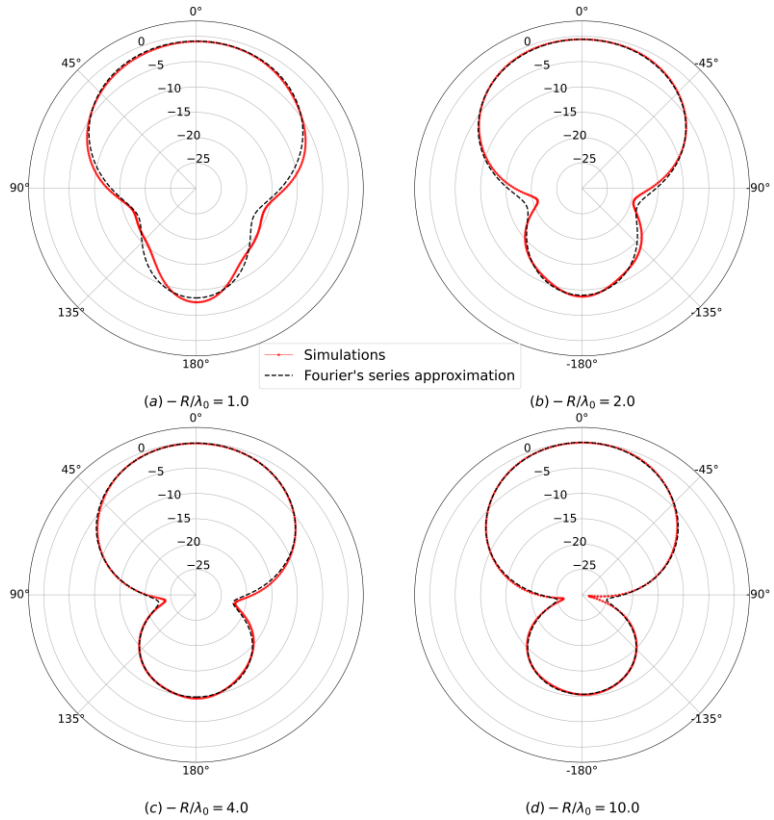

Figure 92 Comparison between simulated normalized radiation pattern of 1 slot convexly curved in H plane and its numerical approximation thanks to an even Fourier's series.

As presented in Figure 92, still with the slot matched at 15 GHz with SF280 dielectric, a well match between simulations and the Fourier coefficients method for $R/\lambda_0 = 1$, 2, 4 and 10 is observable. Best results can be found by using a bigger degree.

It can be concluded that this approach aiming to obtain a numerical function of radiation pattern $h_0(R, \theta)$ thanks to Fourier's cosine series with coefficients a_n function of the radius is possible for small radii as well as large ones with suturing exponential functions. As mentioned above, this also has the advantage of being valid outside the simulation area and faster for numerical calculation.

4.2.2 Adaptation of the general arced radiation pattern formula

As observed in 1.5.2, the ring array theory already exists and put into an equation with (1.23). Nonetheless, this expression doesn't take into account the variation of the elementary radiating element. This subsection therefore begin by theoretically incorporate the work from the previous section and link the new approach to variations according to R of standardised directivity to the standardised field radiation pattern. A direct comparison between theory and simulation is then illustrated for a curved 1×N network.

- **Theory**

As a reminder, the expression of the ring array radiation pattern formula is given in (1.23) with variables explained in 1.5.2 and relative to the geometrical Figure 10. Nonetheless, in the case of cylindrically curved SIW slotted array (SIWSA) as presented in Figure 93, with the reference coordinate system placed in the middle of the curved array, it is more logical to consider θ as the name of the angle variable when studying the far field radiation pattern, φ corresponds then to the plane of the studied field (φ = 0° in E-plane and φ = 90° in H-plane).

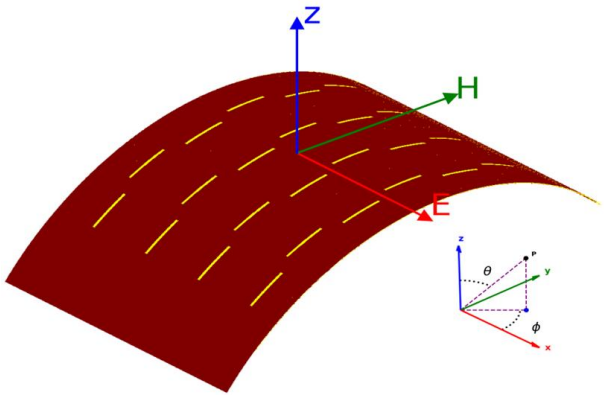

Figure 93 : Orientation of the coordinate system on a cylindrically curved SIWSA.

Furthermore, in the case of a cylindrical curvature, the problem can be first simplified with a 2D problem considering array in arc as outlined in Figure 94 for convex as concave curvature.

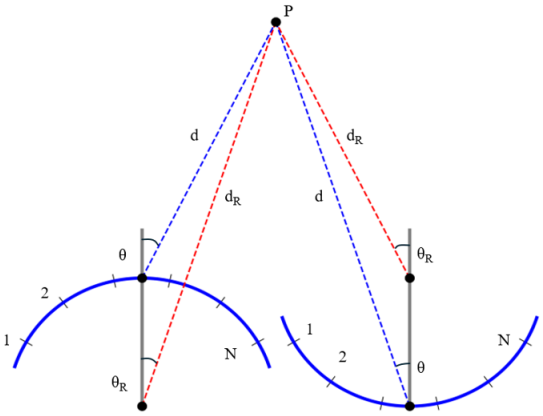

Figure 94 : Application of geometrical cosine theorem on 1×N arced array in convex and concave.

The problem of arc-curved radiating elements with radius on the order of the wavelength can be further simplified by the El-Kashi's theorem (law of cosines). As we can see in Figure 94, determination of the far-field behaviour at a point P from the middle of an array in convex or concave curvature can be approximated by taking for reference the centre of curvature. Therefore, with R of the order of the wavelength, one can consider $\theta \approx \theta_R$ and $d \approx d_R$ (d and $d_R \gg \lambda_0$), which simplify the problem. In the following study, centre of the curvature is taken as the reference for far-field analysis. The expression (1.23) can then be used for arced array and rewritten using more appropriate variable as presented in Figure 95.

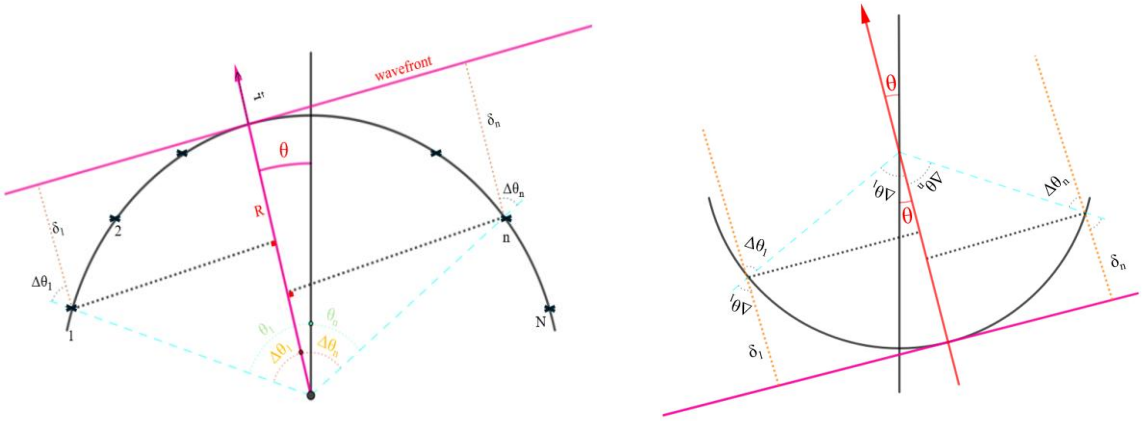

Figure 95 : Geometrical pattern of arced array in convex as in concave used for the demonstration.

The Geometrical configuration presented in Figure 95 for convex and concave curvatures shows that the demonstration presented for convex curvature is also valid for concave curvature by central symmetry. This point is particularly interesting because even if the curved individual slot has inverse behaviour looking at the radiation pattern, presented through the variation of the directivity $D_{max}(R)$ and the half power beamwidth HPBW(R) in Figure 86, the global 1×N network, whether convex or concave, must exhibit the same general radiation pattern variation depending on the radius. This can be anticipated geometrically by seeing that for the concave once the individual radiation from each slot passes through the focal point (centre of the circle) and after the radiation diverges in the same way as in convex.

For a given radius R, θ_n is the fixed angular position (positive or negative) of the nth radiating element measured from the reference (vertical black line in Figure 95). Considering M and N even, and a linear array of resonantly spaced longitudinal slots, θ_n can be defined by:

$$\theta_n = \pm(2k+1)\frac{\lambda_g}{4R} \tag{4.3}$$

$$\theta_n = \pm(2k+1)\frac{a_{siw}}{4R} \tag{4.4}$$

With k ϵ [0, M/2-1]. Equation (4.3) is used for curvature in the H-plane, where λ_g is the guided wavelength within the SIW, and equation (4.4) is used in the E-plane curvature, where a_{siw} is the width of the SIW line.

Wavefront is assumed to be perpendicular to the observation direction $\vec{r}$, expanding outward at an angle θ from the reference. Length δ_n (parallel to $\vec{r}$ direction) is the distance between a single radiating element n and the wavefront, and each radiating element has a different angle of field radiation to the wavefront. It can be defined as $\Delta\theta_n$, angle formed between the normal radiation direction of the nth element and $\vec{r}$, array wavefront propagation direction. $\Delta\theta_n$ can be expressed as:

$$\Delta\theta_n = \theta - \theta_n \tag{4.5}$$

$$\delta_n = R - R.cos(\Delta\theta_n) = R\big(1 - cos(\Delta\theta_n)\big) \tag{4.6}$$

and summation of fields, alike for isotropic circular arrays, allows to obtain:

$$\vec{H}(r,R,\theta) = \sum_n W_n \overrightarrow{H_n}(\mathrm{r},\Delta\theta_n)e^{jkR\left(1-cos(\Delta\theta_n)\right)} \tag{4.7}$$

$$\vec{E}(\mathrm{r},\mathrm{R},\theta) = \sum_n W_n'\overrightarrow{E_n}(\mathrm{r},\Delta\theta_n)e^{jkR\left(1-cos(\Delta\theta_n)\right)} \tag{4.8}$$

respectively in A/m and V/m, with k the wavenumber, r the distance from the source, and:

$$\mathrm{W_n} = \mathrm{w_n}e^{\mathrm{j}\beta_n} \tag{4.9}$$

where w_n represents the amplitude distribution and β_n is the phase of the nth element (null here because slots are in phase). $\overrightarrow{E_n}$ and $\overrightarrow{H_n}$ are the functions representing the radiated field of the unit element n^{th} in the plane of curvature.

As shown previously, radiation pattern of a single curved slot is closely related to the curvature radius R when R/λ_0 is lower than 10. Taking also R as variable in the individual radiation pattern function, (4.7) and (4.8) can be rewritten in normalized expression with:

$$e(\mathrm{R},\theta) = \sum_n w_n' e^{j\beta_n} e_n(R,\Delta\theta_n)e^{jk\delta_n} \tag{4.10}$$

$$h(\mathrm{R},\theta) = \sum_n w_n\, e^{j\beta_n} h_n(R,\Delta\theta_n)e^{jk\delta_n} \tag{4.11}$$

Which can be developed as:

$$h(\theta,R)=\sum_n w_n e^{j\beta_n}\left(\frac{a_0(R)}{2}+\sum_i a_i(R).cos(i\Delta\theta_n)\right)e^{jk\delta_n}$$
$$=\sum_n\sum_i w_n\, a_i'(R)\left(e^{j(k\delta_n+\beta_n+i\Delta\theta_n)}+e^{j(k\delta_n+\beta_n-i\Delta\theta_n)}\right) \quad (4.12)$$

with $a_i'(R)=a_i(R)/2$ for i > 0. This equation describes the radiation pattern of a curved array for the H-plane case (similar development can be made for E-plane case).

Finally, a relation between the theoretical normalized radiating field expression (4.12) and the antenna's normalized gain measured in anechoic chamber or simulated on the software must be found. To do so, we start by express the module of the time-averaged complex Poynting vector given by:

$$\left|\vec{S}\right|=\left|\frac{1}{2}Re\left(\vec{E}\times\overrightarrow{H^*}\right)\right| \xrightarrow[Far\ Field]{} \left|\vec{S}\right|=\frac{\eta_0}{2}\left|\vec{H}\right|^2.\vec{r}=\frac{1}{2\eta_0}\left|\vec{E}\right|^2.\vec{r} \quad (4.13)$$

with η_0 the wave impedance of a plane wave in free space. The module of the Poynting vector is linked to the radiation intensity by:

$$U=\left|\vec{S}\right|r^2 \xrightarrow[Far\ Field]{} \frac{\eta_0}{2}\left|\vec{H}\right|^2r^2=\frac{1}{2\eta_0}\left|\vec{E}\right|^2r^2 \quad (4.14)$$

Which can be rewritten with the function $rETot(\theta,\varphi)$ defined in the first section and used on electromagnetic simulations software:

$$U(\theta,\varphi) \xrightarrow[Far\ Field]{} \frac{rETot(\theta,\varphi)^2}{2\eta_0} \quad (4.15)$$

With r the distance. Then, by applying the definition of directivity:

$$D=\frac{U}{U_{\text{avg}}}=\frac{\left|\vec{E}\right|^2r^2/2\eta_0}{P_{\text{rad}}/4\pi} \quad (4.16)$$

$$D(\theta,\varphi)=\frac{|rETot(\theta,\varphi)|^2/2\eta_0}{P_{\text{rad}}/4\pi}=\alpha.|rETot(\theta,\varphi)|^2 \quad (4.17)$$

It is essential to note the linear relationship α between the directivity and the square of the field. Finally, by using the linear relation between the realized gain and directivity:

$$G(\theta,\varphi)=(1-|\Gamma|^2)e_{\text{cd}}D(\theta,\varphi)=(1-|\Gamma|^2)e_{\text{cd}}.\alpha.|rETot(\theta,\varphi)|^2 \quad (4.18)$$

with e_{cd} the efficiency which depends on the dielectric and conductor properties (product of $e_c e_d$). Γ is the reflection coefficient of the array, corresponding to the matching.

Assuming that the variations of the efficiency e_{cd} and the matching Γ are neglectable across the considered curvature radii, both the directivity and the gain are directly proportional

to the square of the radiated field amplitude, $|rE|^2$. After normalization, a direct comparison can be made between the square of the normalized radiation pattern and the normalized gain $g(R, \theta, \varphi_{cte})$. We then consider the following equivalences:

$$g(R, \theta, \varphi_{0°}) = e^2(R, \theta) \quad (4.19)$$

$$g(R, \theta, \varphi_{90°}) = h^2(R, \theta) \quad (4.20)$$

The electromagnetic derivation previously presented for a 1×N curved array can be extended to an M×N curved model : when considering an M×N slotted antenna array curved in the H-plane (or E-plane), the elementary radiating element is no longer a single slot but a sub-array (M×1 or 1x×N) aligned perpendicular to the plane of curvature. Consequently, the elementary radiation functions h_n (or e_n) are defined at the sub-array level, and the method presented in 4.2.1 is applied to this perpendicular subsection. Since these sub-arrays are oriented orthogonally to the curvature plane, their array factor theoretically does not affect the normalized radiation pattern in the plane of curvature, although minor discrepancies may arise in practice. Therefore, for improved accuracy, the method can be applied to each sub-array, or alternatively, single-slot radiation coefficients may be used with a slight loss in precision but significantly reduced computational cost.

Consequently, theoretical models for radiation pattern obtained in (4.12) can be directly compared to the normalized measured or simulated gain, equal to the normalize directivity, allowing for assessment of these models.

- **<u>Comparison with simulations</u>**

In order to verify the last developed method, a comparison is made between theoretical approach and the obtained simulation results with a 1×8 SIW slotted array matched at 15GHz on SF280 dielectric with curvature in the H-plane. The flat adapted design is taken as reference for the global normalization and curvatures are applied in convex as in concave as shown in Figure 96.

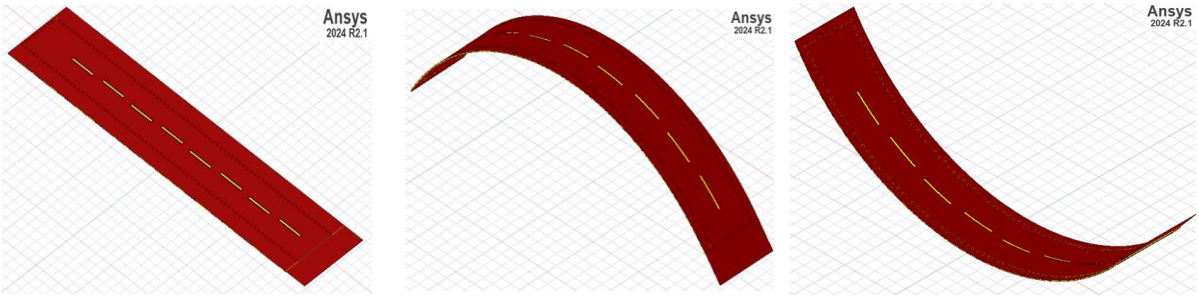

Figure 96 : Tested 1×8 designs in flat configuration and curved in H-plane in convex and in concave.

From the flat design, the reference values are obtained such as the maximal directivity D_{max} = 12.93 dB, associated quantity related to the field rE_{max} = 26.435 dBV, the half-power beamwidth HPBW = 20 deg, and the real field weight between the 8 slots. To do so, the HFSS 'field calculator' is used to obtain the power radiated by each slot (integration over the surface of each slot of the product of the normal vector and the Poynting vector), applying the square

root and normalizing by the sum. These latter values correspond to w_n variable in the theoretical formula.

A set of simulations was carried out for different radii of curvature going from $R/\lambda_0 = 0.75$ to 10 in convex curvature. Note that we cannot have the same small radii in concave like in convex otherwise the structure closes in on itself. The minimum radius chosen for the concave is $R/\lambda_0 = 1.5$ which gives a half circle structure. A direct comparison of the simulated results between convex and concave curvature can be obtained, as shown in Figure 97.

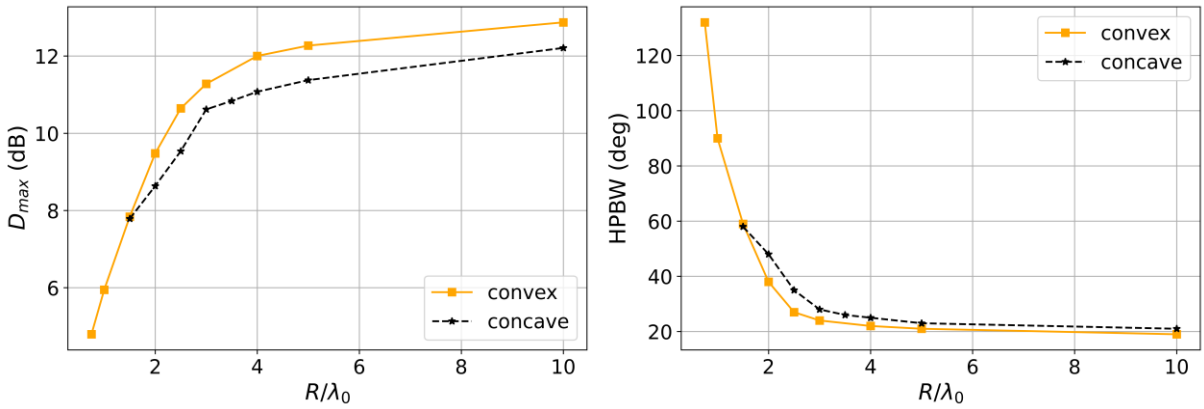

Figure 97 : Variations of the maximal directivity and HPBW depending on the ratio R/λ_0 for curvature in H plane in convex and concave.

The theoretical prediction of the same global behaviour of the decrease of the maximal directivity $D_{max}(R)$ and the opening of the half-power beamwidth HPBW(R) in convex as in concave can be validated, even though the radiation pattern of an individual slot exhibits inverse behaviour with curvature. Furthermore, a difference of approximately 0.8 dB between convex and concave curvatures can be observed for D_{max} values. One explanation is that concave curvature tends to increase mutual coupling between slots, contrary to convex curvature, leading to variations in the local radiation weighting of the array. Moreover, radiation from the convex network diverges directly, whereas radiation from the concave network first passes through a focal point before diverging. Electromagnetic phenomena specific to the near field, which are not captured by the geometric approach, may therefore occur.

Even though the common global behaviour is already observed, it is interesting to examine the normalized directivity as a function of the radius in a polar coordinate system, independently for convex and concave cases, as presented in Figure 98.

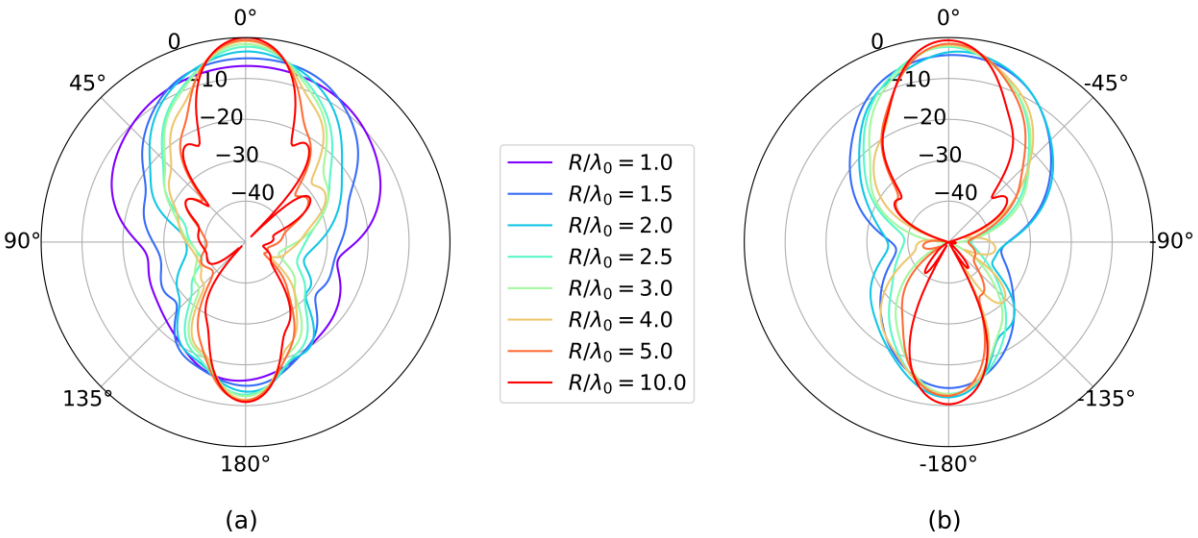

Figure 98 : Normalized directivity d(R, θ) in convex (a) and concave (b).

Then, based on the approach developed in Section 4.2.1, which allows the approximation of the normalized radiation pattern of a curved slot $h_{slot}(R, \theta)$, and on the theoretical developments in Section 4.2.2, it is possible to directly compare the variations of the normalized maximum directivity $d_{max}(R)$ and HPBW(R) for a 1×8 array curved in the H-plane, for both convex (Figure 99) and concave (Figure 100) configurations.

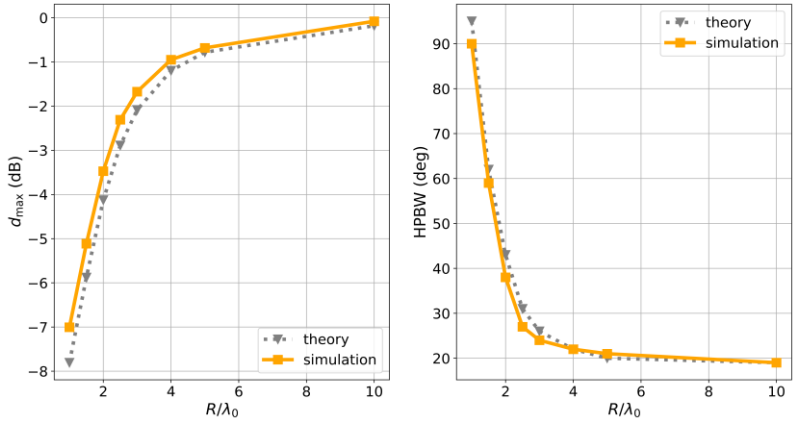

Figure 99 : Comparison between simulations and theoretical approach of the variation of the normalized maximal directivity d_{max} and HPBW depending on the radius for a 1×8 convexly curved SIWSA.

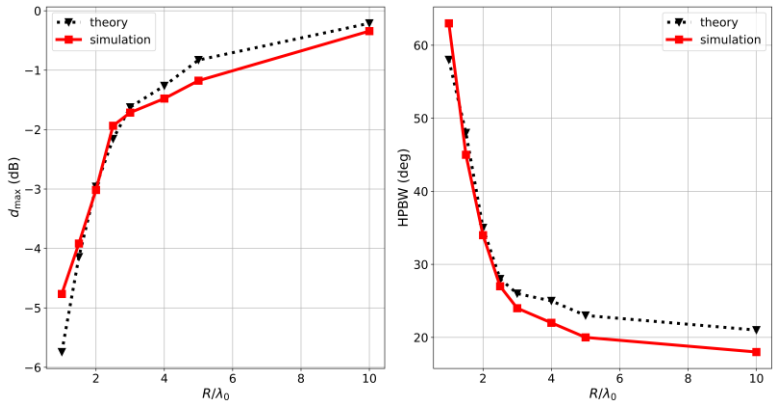

Figure 100 : Comparison between simulations and theoretical approach of the variation of the normalized maximal directivity d_{max} and HPBW depending on the radius for a 1×8 concavely curved SIWSA.

A good overall agreement is observed for both convex and concave configurations, although the results are better for the convex case. Similarly, the normalized radiation pattern can be examined for a given radius.

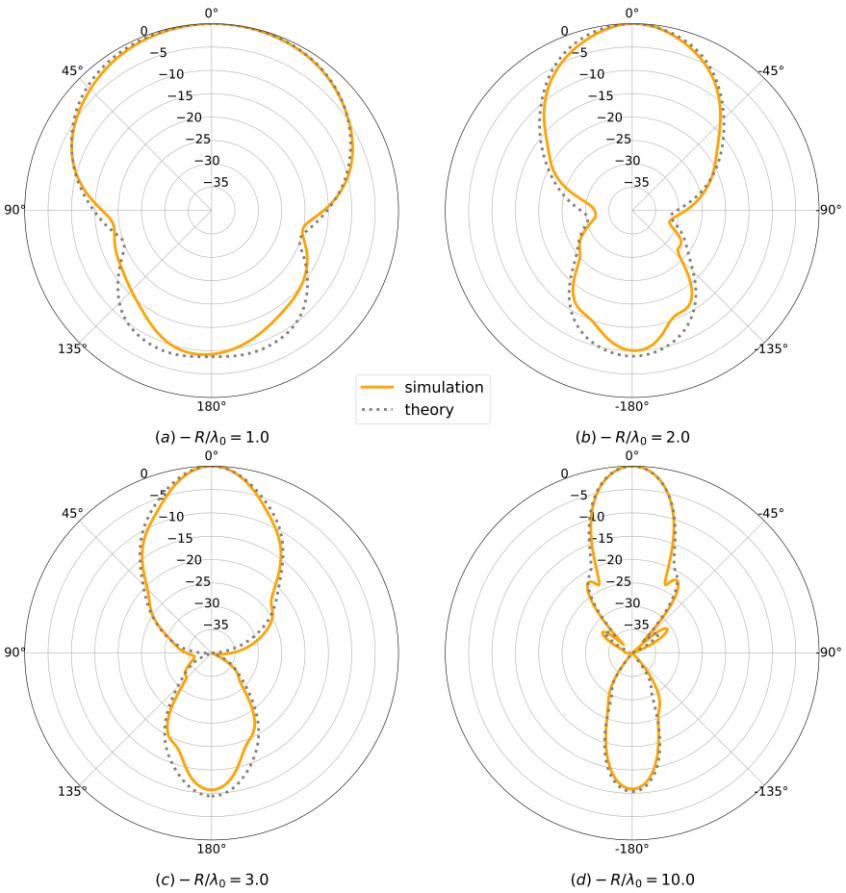

Figure 101 : Comparison between simulations and theoretical approach of the normalized radiation pattern for different radii of a 1×8 convexly curved SIWSA.

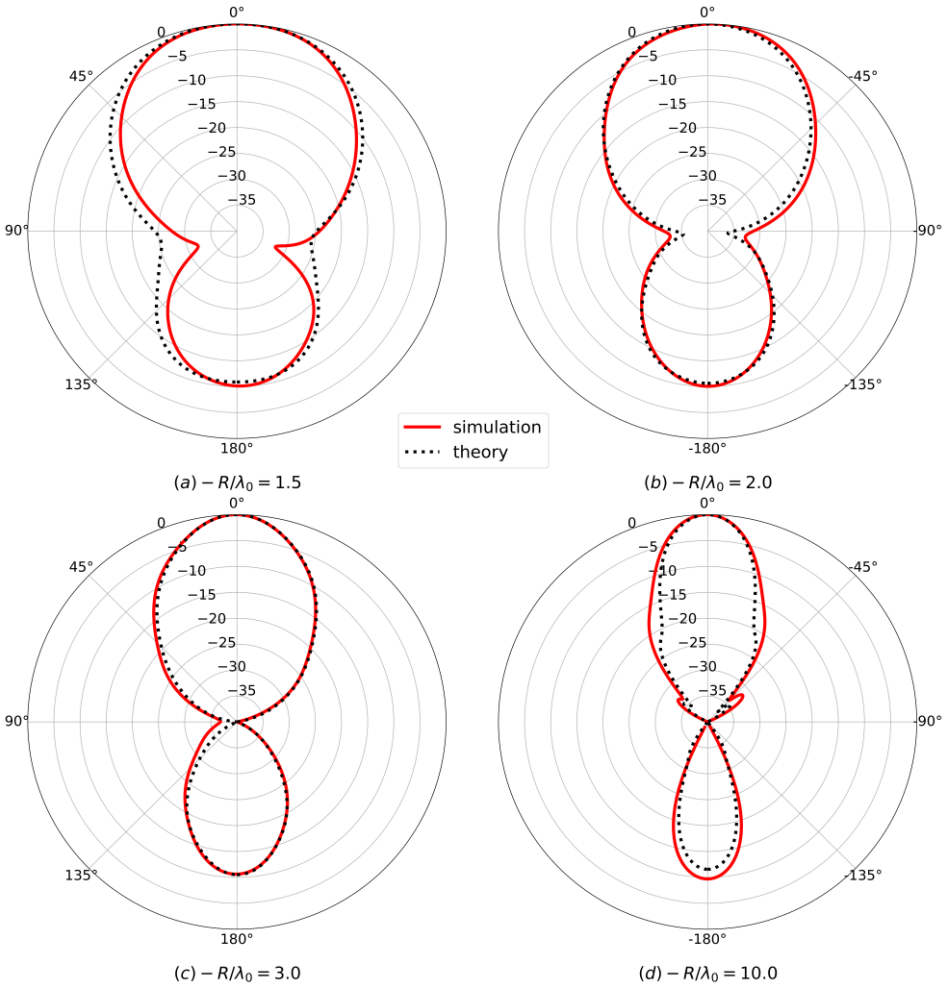

Figure 102 : Comparison between simulations and theoretical approach of the normalized radiation pattern for different radii of a 1×8 curved SIWSA in concave.

The agreement is better for convex curvature in the forward direction, whereas it is better for concave curvature in the backward direction. It can also be noted that the model begins to show its limitations for concave curvature in case (a), where the small radius R/λ_0 results in a half-circle configuration with slots 1 and N facing each other. More complex electromagnetic effects must therefore be considered.

Having described these models, the next section is devoted to studying the impact of curvature on the radiation patterns of SIW slotted antenna arrays.

4.2.3 Study of the impacts of linear arced array parameters on the opening of the main beam with radii of curvature

Curved slot antenna arrays involve many parameters, as shown in (4.12), such as the radius R, the observation angle θ, the amplitude distribution w_n and the individual normalized radiation pattern function h_1 or e_1. Other parameters include the distance between elements d_{e2e}, which is correlated to the angle of the slot n relative to the zenith θ_n and the distance from the slot to the wavefront δ_n. Some of these parameters cannot be isolated for a direct analytic analysis or are inherently linked to the physical implementation. For instance, the distance slot

to slot d_{e2e} for E-plane curvatures depends on the width of the waveguide a_{rwg}, making it a function of the chosen cut-off frequency f_{c10} and the dielectric permittivity ε_r. For H-plane curvatures, $d_{e2e} = \lambda_g/2$ with λ_g depending on f_0, f_{c10} and ε_r.

Although many parameters can be investigated, here the impact of three parameters is analysed through the directivity and half power beamwidth variations, namely distance between elements (d_{e2e}), amplitude weighting w_n and single element directivity d_0. Choosing to directly study the distance between elements d_{e2e2} allows for indirectly accounting for the combined impacts of variations in cut-off frequency f_{c10} and relative permittivity ε_r. These parameters are linked to the waveguide width in the E-plane and the guided wavelength in the H-plane.

All the directivities are normalized with respect to D_{max0}, directivity of a flat (infinite curving radius) 1×8 array with a distance between elements of $d_{e2e} = 0.4\lambda_0$ and an amplitude distribution with Chebyshev coefficients for a side lobe level (SLL) at -23 dB.

The first study focuses on the distance between slots, d_{e2e}, which is considered through $\Delta\theta_n$, θ_n and δ_n. It is made by varying the value of d_{e2e} in a range between $d_{e2e}/\lambda_0 = 0.3$ and 0.6, which are feasible values for SIW slotted arrays. Theoretical results are given in Figure 103.

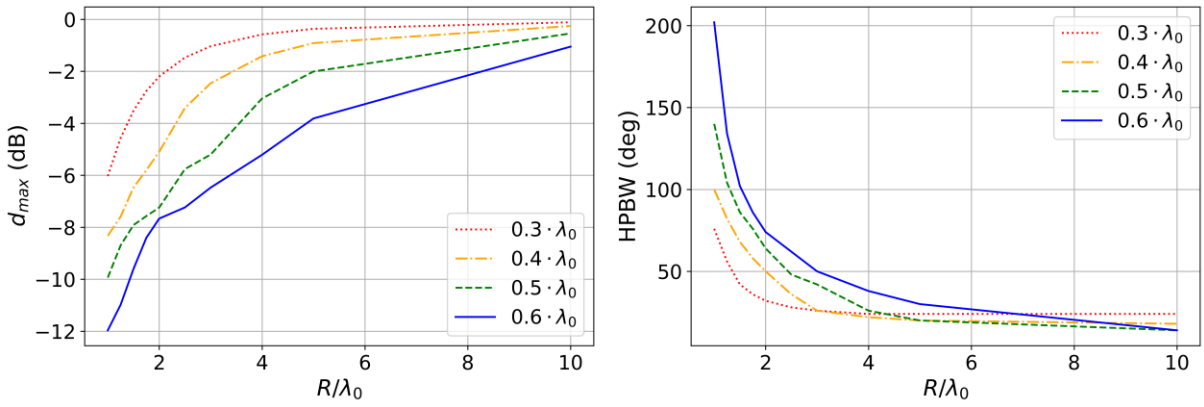

Figure 103 : Variations of the normalized maximal directivity and half-power beam width depending of the radius for different distances between the slots of a 1×8 array curved in H-plane.

It appears that the closer the radiating elements are to each other, the lower the opening of the radiation pattern is for almost all bending radii. This could be explained by the fact that shorter distances between elements decrease the angle θ_n for a given bending radius, putting slots closer to the zenith. An interesting point is the lack of linearity in the curves of $d_{max}(R)$ and HPBW(R) for the two most important distance parameters d_{e2e}. It is explained by the fact that for small radii, ripples appear in the global main beam, leading to jumps in the computed values of HPBW.

Second parameter to be studied is the amplitude distribution, which corresponds to w_n factors. Various distributions are investigated: uniform weighting and Chebyshev distribution of Side Lobes Levels (SLL) at -20dB, -23 dB and -26 dB as shown in Figure 104. Except for the weighting, all other parameters are the same those of the 1×8 SF280 array tuned for 15 GHz.

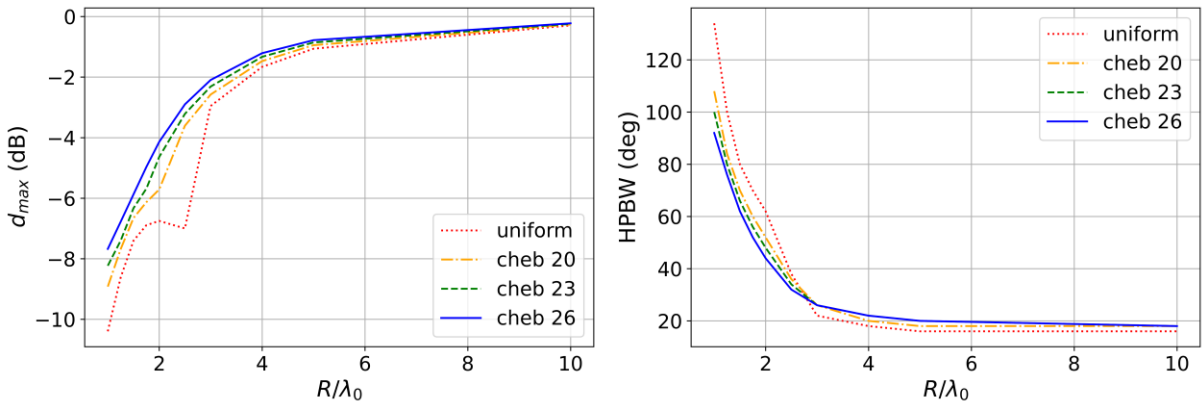

Figure 104 : Variations of the maximal normalized directivity and half-power beam width depending of the radius for different tapering excitation of a 1×8 array curved in H-plane.

It appears that the more the amplitude distribution concentrates the power toward the centre of the array, the lower the impact of curvature on the radiation pattern, which seems consistent as central elements are geometrically closest to the zenith direction and thus experience minimal angular deviation with curvature. Once again, we can observe the lack of linearity in the curve of maximal normalized directivity $d_{max}(R)$, especially for the uniform distribution. It is explained by the fact that for this distribution, the radiation pattern exhibits ripples in the main lobe with amplitudes larger than the value at $\theta = 0$, which explains the slight stagnation of $d_{max}(R)$, around $R/\lambda_0 = 2$. This value does not correspond here to the maximum at zenith, which is actually lower.

Finally, the impact of the directivity of the single slot element, related to the Fourier coefficients, a_i in eq. (4.1), on the array radiation pattern is studied. Three different radiation patterns were chosen for the single element: directive, moderately directive, and less directive with a HPBW respectively corresponding to values of 80, 90, and 100 degrees. Thie latter correspond to classical values for slot antenna on RWG.

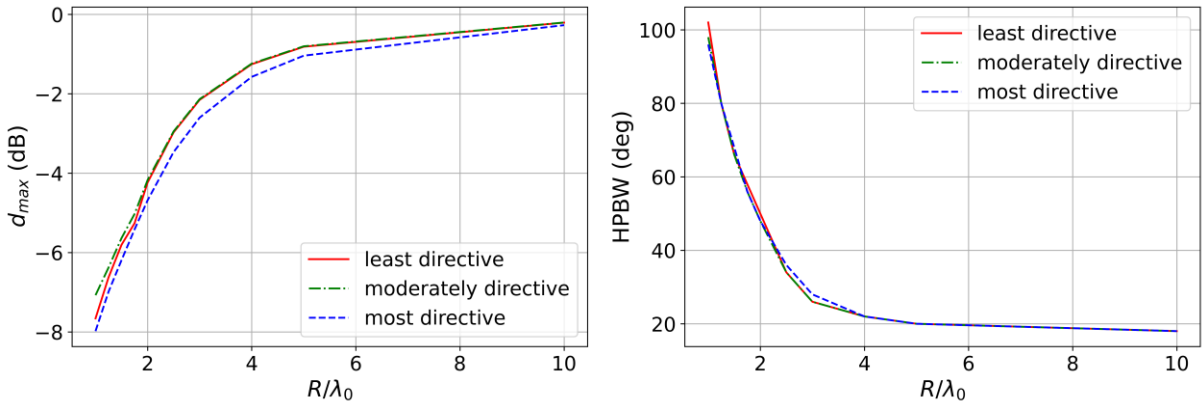

Figure 105 : Variations of the maximal normalized directivity and half-power beam width depending of the radius individual slot's directivity of a 1×8 array curved in H-plane.

As shown in Figure 105, the more directive individual radiating elements, the more the radiation pattern is affected. We can nonetheless observe than this parameter is far less important that the other ones tested previously.

By considering these three parameters in the classical range of values for a slot array, the maximal normalized directivity $d_{max}(R/\lambda_0)$ appears to be very much impacted by the distance between the elements. The amplitude distribution, within the studied ranges, has a relatively lower impact and finally the directivity of the single radiating element has the least impact. Consequently, if minimal impact on the gradient of variation of the radiation pattern is sought with the bending radius R/λ_0 between 1 and 10, a minimum distance between elements d_{e2e} as well as a significant difference in amplitude distribution should be chosen. However, one should be aware that choosing such parameters results in lower directivity for the flat array, according to planar array theory. Therefore, a trade-off must be made between the actual directivity of the array for small curvatures $R/\lambda_0 \approx 10$ and the acceptable variations in the radiation pattern for smaller radii.

4.3 Comparison of the last developed theoretical approach with the range of simulations and measurements on the flexible SIWSA designs

In the previous section, the theory of radiation patterns of SIW slotted array (SIWSA) with convex and concave cylindrical curvature for radii on the order of the wavelength was investigated and improved. The results were compared with those obtained using electromagnetic simulation software and yielded encouraging results. This work can then be put into practice with different designs created through the automation method presented in Chapter 2.

Hence, this subsection has 2 main objectives. The first one is to compare the measurements with each other by observing the variations of the normalized maximal gain $g_{max}(R)$ taking the flat design as a reference and half-power beamwidth HPBW(R). These are compared to the expected order of decreasing depending of the values of the distance slot to slot relative to the wavelength d_{e2e}/λ_0 for each design in both plane of curvature. The second objective is to assess the agreement between measurements, simulations, and the theoretical approach regarding the variations of the $g_{max}(R)$ and HPBW(R) curves. Before addressing these two points, a brief description of the measurement tools used, and the protocol applied is provided.

4.3.1 General protocol for the study

As observed in (4.19), the primary goal is to correlate the normalized theoretical field radiation pattern for various radii with the corresponding normalized measured gain radiation patterns. The objective is to validate this approach for all possible cylindrical curvatures, specifically for both E- and H-planes in convex and concave configurations. This analysis is conducted for radii on the order of the wavelength λ_0. The R/λ_0 ratios selected for the exercise are R/λ_0 = [1, 1.5, 2, 2.5, 3, 4] for convex curvatures and R/λ_0 = [2, 2.5, 3] for concave curvatures.

Since very small radii of curvature will be tested, the main flexible designs selected for this study are the two prototypes printed on SF280 dielectric for X and Ku bands, along with the RT/Duroid 5880 design adapted for 15 GHz. All three were initially designed using a Chebyshev tapering to achieve a side lobe level (SLL) of -23 dB. This combination of designs allows, on the one hand, for a comparison of the 4x8 array characteristics at two different frequencies using the same dielectric and, on the other hand, at the same target frequency using two different dielectrics. A photograph of these three designs is provided in Figure 106.

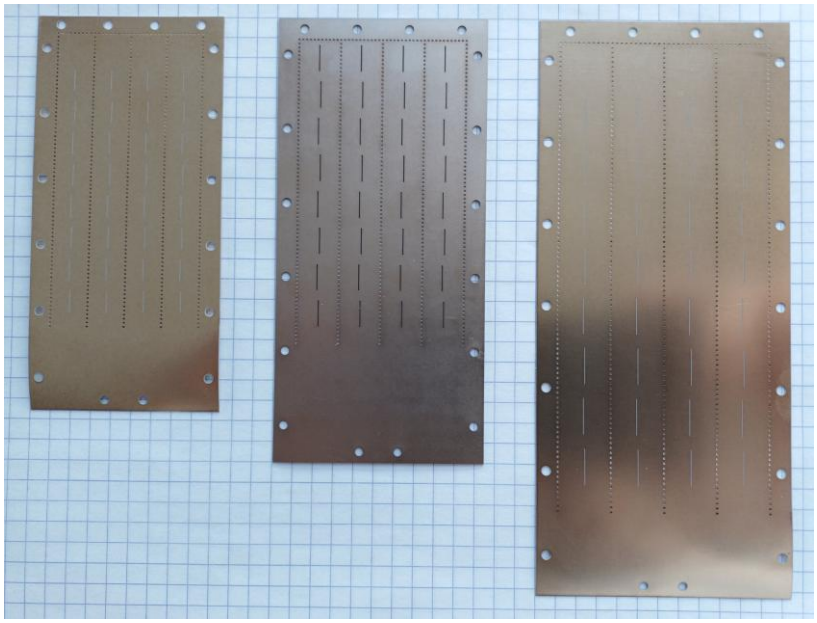

Figure 106 : Realized protypes of slotted SIW 4x8 array: SF280 at 15GHz, Ro5880 at 15GHz and SF280 at 10GHz from left to right on a squared grid of 0.5mm.

The frequency response of these three designs is first measured using a vector network analyser (VNA). The radiation pattern of the 4x8 array is then measured in the anechoic room of the IMT. As shown in Figure 107, the walls of the room absorb the radio waves to eliminate reflections, enabling a direct link between the directive radiating antenna (horn antenna in the photo) and antenna under test (AUT). The antenna under test is placed facing a measurement antenna, and its radiation pattern and performance are recorded in a controlled, reflection-free environment. Knowing the transmission frequency, the distance between the antennas, the transmitted power and horn's gain, as well as measured received power, the Friis' formula can be used to determine the gain of the antenna under test. Since this antenna is mounted on a rotating mast, measurements can be performed from $-\pi$ to $+\pi$ in a given plane. In this study, the radiation pattern is measured only in the E-plane and H-plane.

To hold the antenna under test in a given plane, and possibly with a specific curvature radius, custom 3D-printed resin pieces are used. Some of these are presented in Figure 108. The model of the transparent one is used for the measurements of the flat design in H-plane, the 2 black models are used for measurements in concave (left) and convex (right) for both the E- and H-planes. An example of the associated curvature is given in Figure 109.

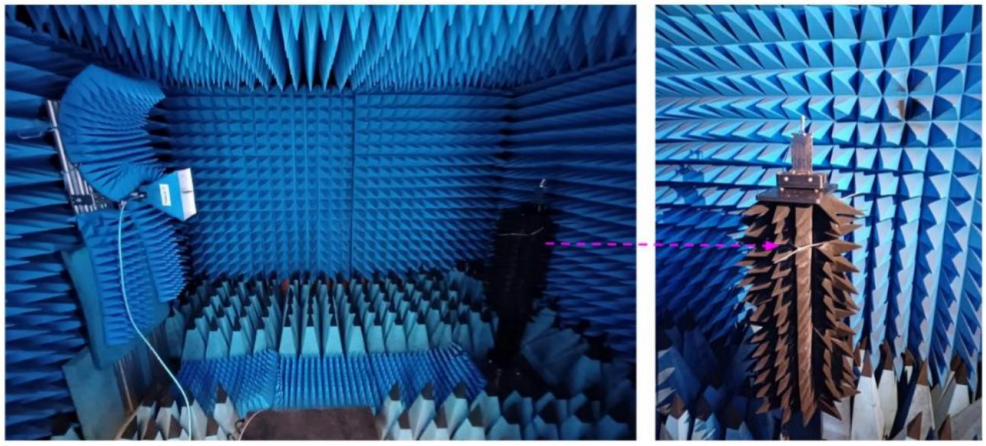

Figure 107 : Photo of the used anechoic chamber and the associated rotating mast.

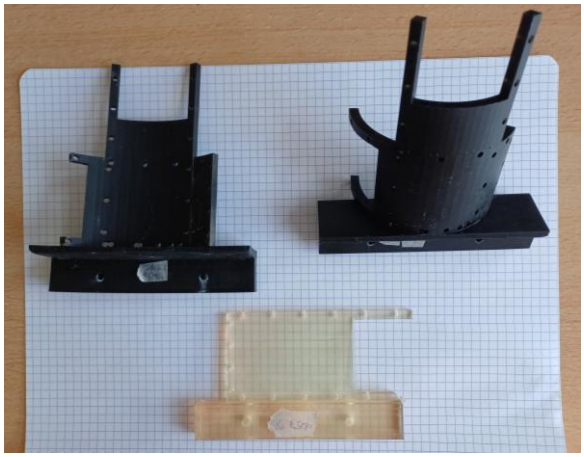

Figure 108 : Some of the 3D printed resin pieces used for measurements.

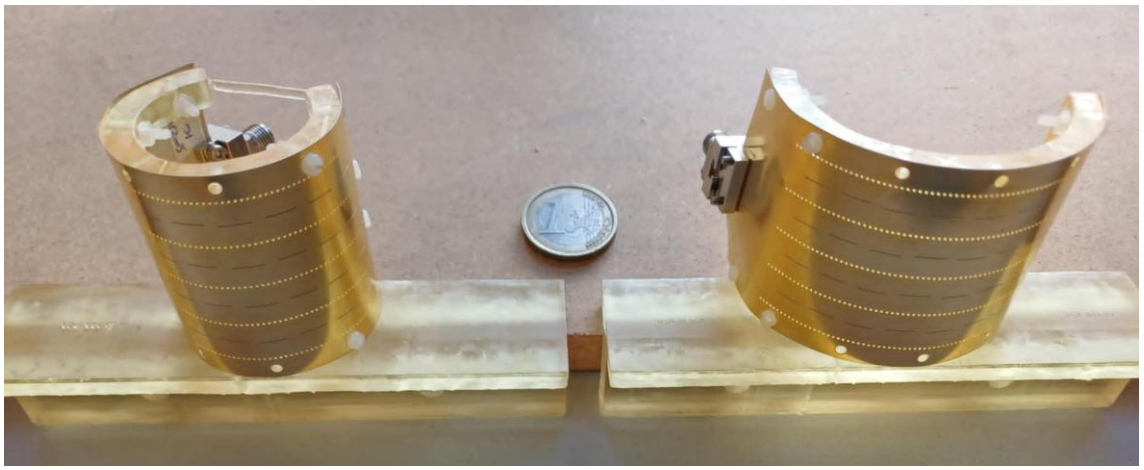

(a)

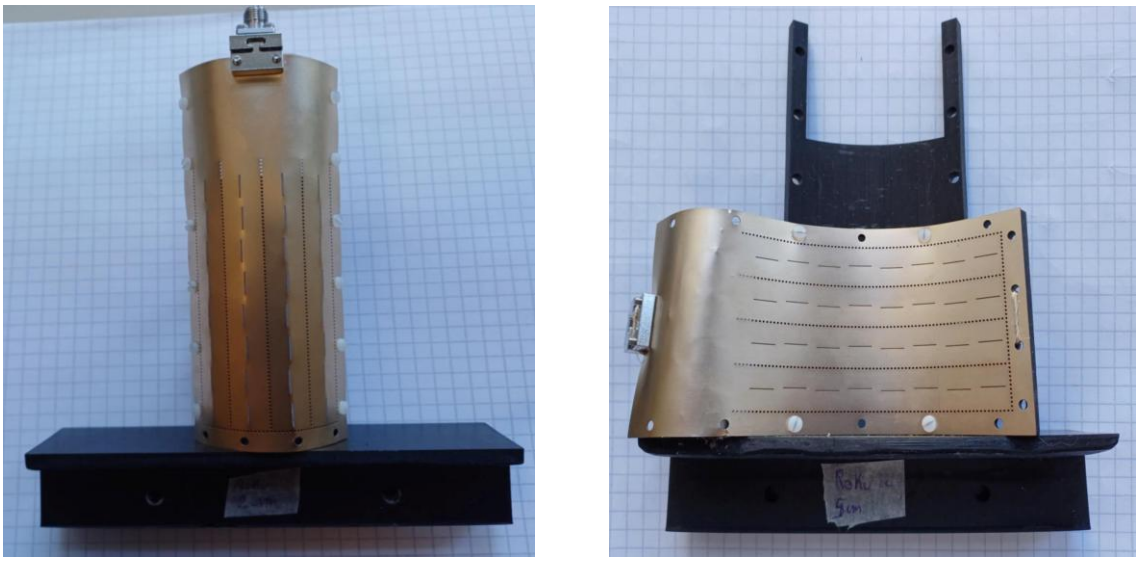

(b) (c)

Figure 109 : Example of fixed measured designs for convex curvatures in H-plane (a), E-plane (b) and concave curvature in H-plane (c).

In order to compare the measured results with the simulations and theoretical approach, a preliminary study was carried out on HFSS and Python, starting with an analysis of the individual behaviour of the slots specific to the three different designs. This allows the theoretical part developed in 4.2.1 to be used. At the same time, the three designs are also drawn and simulated for the same radii of curvature and the same convex/concave cylindrical curvatures in E- and H-planes. Given that the curved SIW slotted array (SIWSA) design is quite complex in software, a Python script was developed to easily draw all the curvature mentioned above and for different designs (M×N dimensions such as SIW characteristics). However, as the design of the 1×4 divider is highly complex from a trigonometric standpoint, it was decided not to model it and instead to feed the four lines independently. This significantly reduces the design time, although discrepancies between simulations and measurements are expected, particularly due to differences in the size and asymmetry of the ground plane.

Consequently, by combining the gain measurements of the curved designs, normalized by their respective gains in the flat configuration, the corresponding simulations, also normalized with respect to the flat case, and the theoretical approach implemented as a calculation algorithm, a comparison between these three approaches becomes possible.

4.3.2 Measurements of the matching of the 3 tested designs and their associated gain for different radii of curvature in each plane

- **Flat designs' characteristics**

Thanks to the VNA for the reflection coefficients measurement and the possibilities of measurement of the gain G of the antenna in a given plane φ with the anechoic chamber. The following data can then be remained:

	Ro5880_Ku	SF280_X	SF280_Ku
G(dBi)	13.88	10.21	12.55
$HPBW_E$ (deg)	22	27	26
$HPBW_H$ (deg)	16	19	19
f_0	14.97 GHz	9.76 GHz	14.71 GHz

Table 8 : Measured RF characteristics of the 3 tested designs.

It can be observed that the RT/Duroid 5880 design exhibits higher gain than the two SF280 designs, along with a narrower HPBW in both planes. These measured gain values are used as references for normalising the gains of the curved designs. Based on the measurements in anechoic chamber for different radii of curvature, the normalized radiation pattern for the 3 designs are presented in Figure 110, Figure 111 and Figure 112.

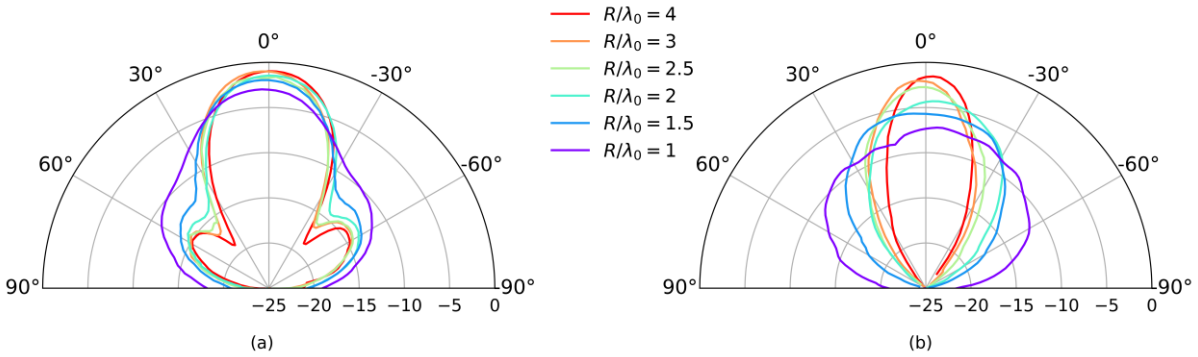

Figure 110 : Opening of the normalized radiation pattern in dB for different ratio R/λ_0 in E plane (a) and H plane (b) in convex for the SF280_X design.

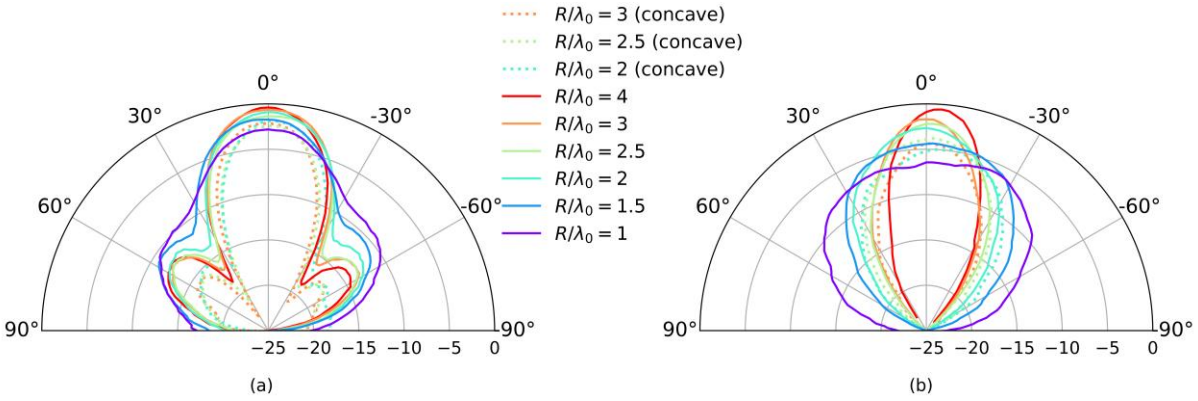

Figure 111 : Opening of the normalized radiation pattern in dB for different ratio R/λ_0 in E plane (a) and H plane (b) in convex and concave for the SF280_Ku design.

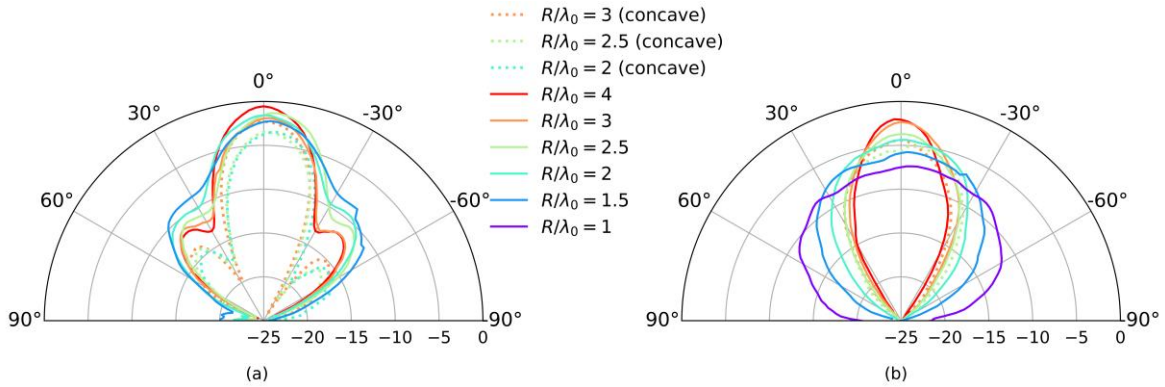

Figure 112 : Opening of the normalized radiation pattern in dB for different ratio R/λ_0 in E plane (a) and H plane (b) in convex and concave for the Ro5880_Ku design.

As expected, a decrease in the maximum normalized gain g_{max} and a widening of the main beam can be observed in both planes. The widening is much more pronounced in the H-plane than in the E-plane, resulting in an overall flattened beam in the H-plane, while the two side lobes are still visible for the smallest radius in the E-plane. It should be noted that for the $Ro5880_{Ku}$ design, measurements of the radiation patterns are missing in the E-plane for convex curvature with $R/\lambda_0 = 1$ and in the H-plane for concave curvature with $R/\lambda_0 = 1$ due to a mechanical failure of the prototype.

Nonetheless, the measurements in concave configurations were not very conclusive, particularly in E-plane. The first explanation is that the mechanical forces applied to achieve a concave curvature in the H-plane, combined with the deviation of the distribution network shown in Figure 109.c, distort the board and affect both matching and the local electromagnetic behaviour. The second explanation, specific to the poor normalized gain measured in the E-plane, is related to the structure of the 3D-printed resin fixture used for concave curvatures in both H- and E-planes. For measurements in the E-plane, this fixture introduces plastic surfaces in the forward direction (originally used to hold the board in the concave H-plane), which interfere with the radiation pattern measurements.

An important point expected here is the comparison of the values of the maximal normalized gain $g_{max}(R)$ and HPBW(R) for the 3 designs. But first, due to the shift in frequency adaptation of both SF280 designs, the distance between the elements relative to real wavelength d_{e2e}/λ_0 of adaptation must be recalculated:

	Ro5880_Ku	SF280_X	SF280_Ku
d_{e2e}/λ_0 (E-plane)	0.52	0.42	0.44
d_{e2e}/λ_0 (H-plane)	0.45	0.40	0.39

Table 9 : Distance between the radiating elements for the 3 designs relative to their wavelength of adaptation in both planes E and H.

Following the study presented in section 4.2.3 on the impact on the radiation pattern of the distance between the radiating elements relative to the wavelength d_{e2e}/λ_0 for a same tapering, it can be expected that, with curvature, the radiation pattern will widen more rapidly in E plane for $Ro5880_{Ku}$, then $SF280_{Ku}$ and finally $SF280_X$. In H-plane, the expected order is $Ro5880_{Ku}$, then $SF280_X$ and finally $SF280_{Ku}$. This theoretical expectation can be verified with the Figure 113 and Figure 114.

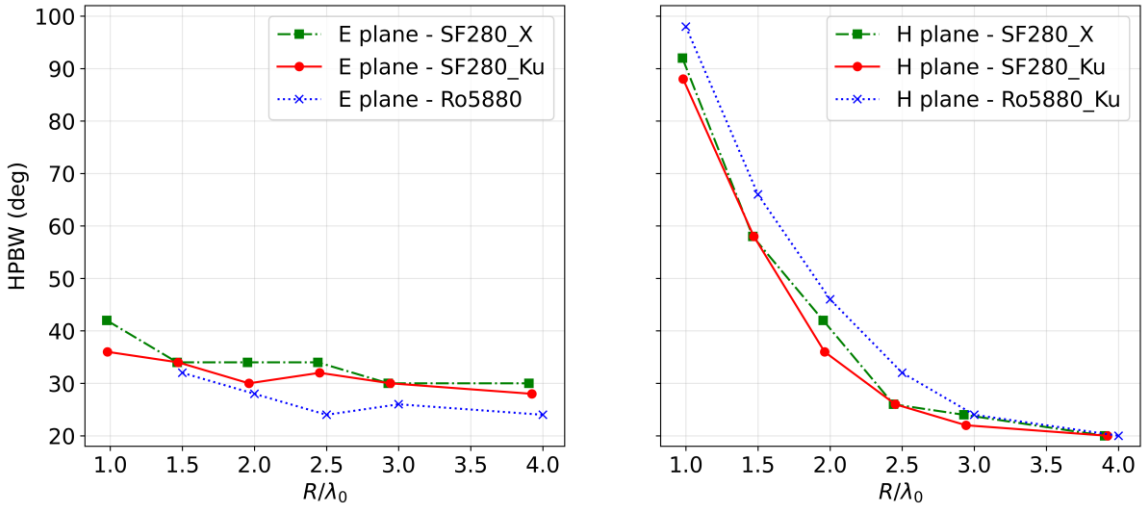

Figure 113 : Variations of the HPBW of the 3 designs for different radii of convex curvature in both planes.

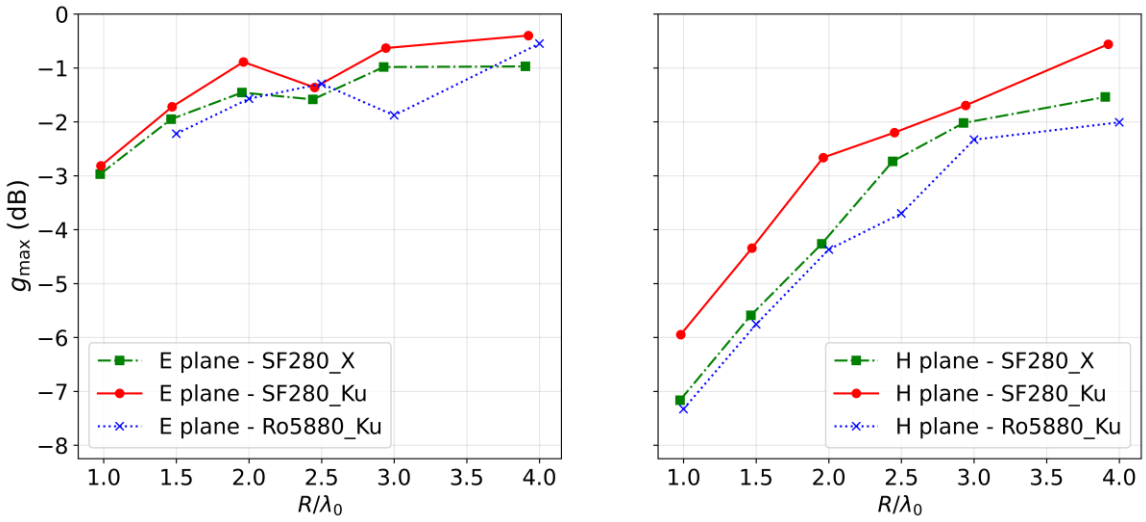

Figure 114 : Variations of the normalized maximal gain g_{max} of the 3 designs for different radii of convex curvature in both planes.

The expected order for the widening of the radiation pattern (increase of HPBW and decrease of g_{max} for small radii) is well observed for curvature in the H-plane. Since the measurements were carried out over approximately ten days, the comparison of the maximum normalized gain $g_{max}$is more sensitive to metrological uncertainties, particularly those arising from daily VNA calibrations across different frequency bands and other measurement-related issues. In contrast, the HPBW values are more reliable, as they reference the maximum gain of the measurement itself for a given R, rather than that of a different measurement of the flat-design antenna. The two SF280 designs, having very similar d_{e2e}/λ_0 and nearly identical tapering, also exhibit similar HPBW(R) values.

Nonetheless, the expected order for E-plane curvature is not observed. This may be due to the fact that the variation range is below 10° for all R/λ_0 values, making the measurements highly sensitive to uncertainties. Furthermore, when comparing these results with the HPBW in the H-plane, it can be inferred that the system is still in the region where R/λ_0 =1 marks the

onset of HPBW broadening. Reducing R/λ_0 below this value is unfortunately not feasible for mechanical reasons.

With the analysis of the measurements complete, a direct comparison between these results, the simulations, and the theoretical approach can now be performed.

4.3.3 Comparisons between the results from theoretical approach, simulations and measurements

With the measurements in the anechoic chamber completed, it is now possible to compare them with the simulation and theoretical results. The two comparison criteria remain the normalized maximum gain $g_{max}(R)$ and HPBW(R). It should be noted that, for a given design, the measurements are normalized using the associated flat design, while the simulation results are normalized using the simulated flat design. The theoretical approach is already normalized through the simulated variations of the normalized field as a function of θ and R.

This analysis was carried out for the three designs in the convex configuration for both planes, as shown in Figure 115, Figure 116, Figure 117. From these figures, it can be observed that the theoretical approach closely follows both the simulated results and the measurements obtained in the anechoic chamber. However, significant discrepancies are noted in the maximum normalized gain g_{max} for the $SF280_{Ku}$ design, as well as in the HPBW of the $Ro5880_{Ku}$ design, both occurring in the H-plane. In the first case, the discrepancies can primarily be attributed to metrological measurement errors. In the second case, they may also result from the limitations of the HPBW metric itself; the definition of the −3 dB beamwidth can lead to considerable variations when applied to flattened main beams. Finally, in both cases, asymmetry introduced by the feed plane is not accounted for in either the simulations or the measurements.

However, for the analysis of the radiation pattern of an arc-shaped array, where the individual element radiation pattern itself varies with the radius R, the approach based on even Fourier series remains a robust and computationally efficient method. It provides an effective means to approximate the radiation behaviour of a given array, including cases where the radius satisfies $R/\lambda_0 < 10$.

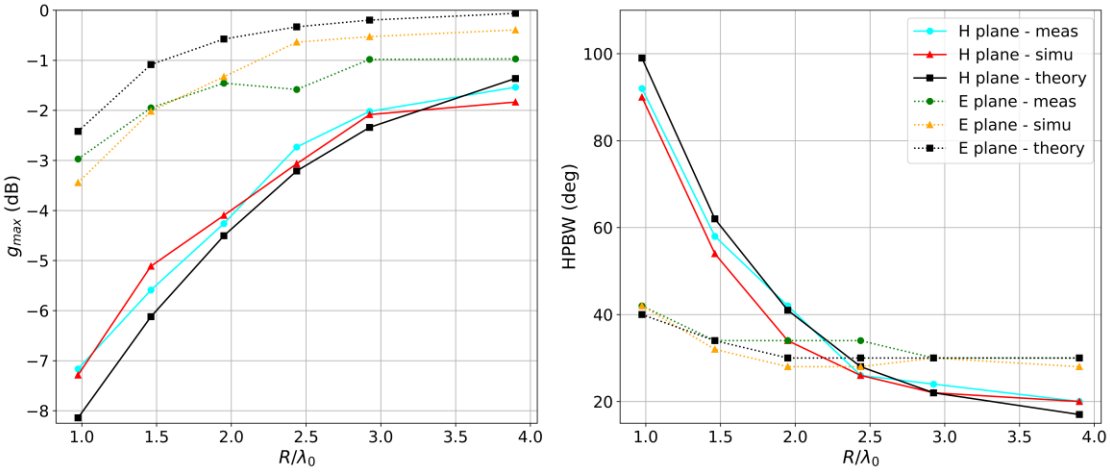

Figure 115 : Comparison of the normalized maximal gain g_{max} and associated HPBW for different ratios R/λ_0 between measures, simulations and theory for the SF280 design adapted in X band convexly curved in both planes E and H.

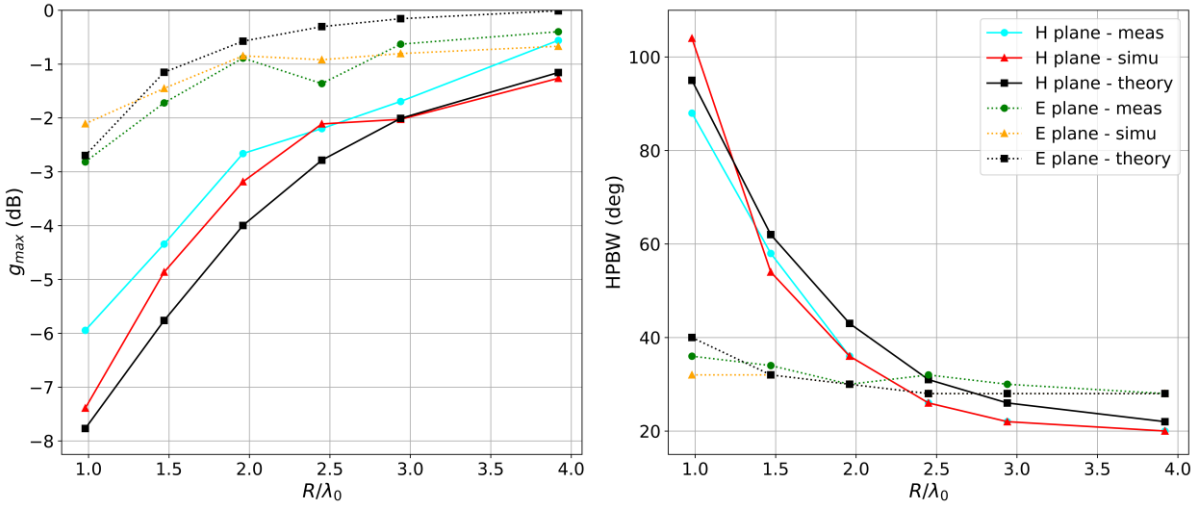

Figure 116 : Comparison of the normalized maximal gain g_{max} and associated HPBW for different ratios R/λ_0 between measures, simulations and theory for the SF280 design adapted in Ku band convexly curved in both planes E and H.

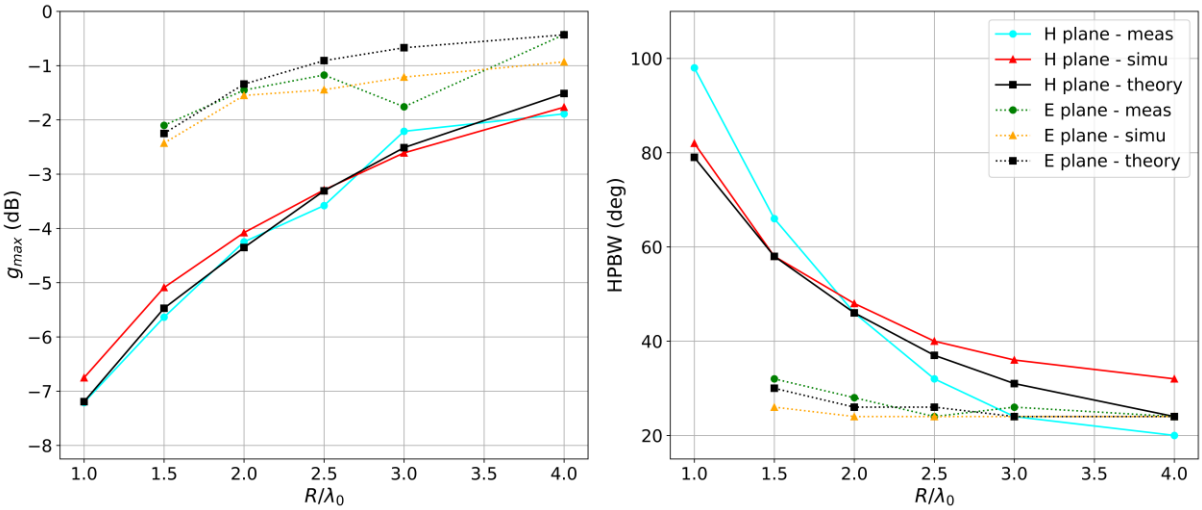

Figure 117 : Comparison of the normalized maximal gain g_{max} and associated HPBW for different ratios R/λ_0 between measures, simulations and theory for the Ro5880 design adapted in Ku band convexly curved in both planes E and H.

4.4 Optimisation of the radiation pattern of a curved in-phased slotted array with a given radius of curvature based on theory from combinatorics

In the literature on conformal arrays, radiation pattern optimization and beam-steering are widely studied theoretical subjects, as described in section 4.1. In the case of our flexible SIW slotted array (SIWSA), the internal mutual coupling is strong enough that adding further M lines does not disturb the matching of the array. Therefore, when radiation pattern conformation for a cylindrically curved SIW slotted array is required, it is far easier to achieve in the E-plane because the weighting and phase shifts between lines do not affect the matching. The challenge is then purely theoretical, involving complex algorithms to determine the necessary phase shifts and weightings to achieve the desired radiation pattern. In the H-plane, however, the problem is much more difficult. In addition to theoretical optimization, maintaining the required weightings and phase shifts between slots on the same waveguide while ensuring matching at a given frequency is a demanding task. In both cases, an in-depth study of the theory and associated algorithms is necessary.

Following the idea that the elements would remain in phase (whether between waveguides for E-plane curvature or between slots for H-plane curvature), there is no simple algorithm, to the author's knowledge, for determining the weightings required to achieve a desired radiation pattern at a given curvature. Indeed, as it can be observed in one of the refence book on the subject [5], which presents a set of numerical methods to optimize the radiation pattern's form, developing an algorithm that converges toward the expected result is a complex task. Furthermore, ambiguity arises when such an algorithm fails: it remains unclear whether the failure stems from an error in the development, the method, or the search conditions, or if a mathematical solution capable of producing the expected radiation pattern simply does not exist.

Consequently, since the number of in-phase elements per waveguide remains low for small radii R, a combinatorial method was developed. This approach consists of precalculating all possible weightings, testing each of them using vector calculus, and retaining the best solutions, provided they exist. This solution does not claim to match the complex algorithms already existing on this subject. Instead, it aims to provide a simple algorithmic approach that is quick to develop and relies on a straightforward theoretical framework, while still delivering perfectly acceptable results.

4.4.1 Mathematical approach

- **Mathematical theory**

Considering a 1×N element line, the normalized weighting is simply a distribution of 100% of the radiated field among the N elements. In most cases, the expected radiation pattern is symmetric and N is even, meaning that the analysis can be carried out using a half line of 1×N/2 sharing 50% of the weighting.

The classical weighting algorithm like the one given in [56] returns floating values for all elements corresponding to the real mathematical results. Nevertheless, comparing the weights between a small number of elements, changing or rounding the weight values below 10^{-2} leads to no significant variation in the global radiation pattern. Consequently, assuming that the weightings are all discrete to within 0.01, this is equivalent to writing:

$$w_1 + w_2 + w_3 + \cdots + w_{N/2} = 0.5 \tag{4.21}$$

with $w \in \left[0.01, \left(0.5 - 0.01\frac{N}{2}\right)\right]$. To obtain all the possible combinations of weighting, it is necessary to reason in integers and divide the result by 100, leading to:

$$w_1 + w_2 + w_3 + \cdots + w_{N/2} = 50 \tag{4.22}$$

with $w \in \left[1, \left(50 - \frac{N}{2}\right)\right]$. This problem corresponds in combinatorics to the 'stars and bars' method applied on strictly positive integers. This one stipulates that if:

$$x_1 + x_2 + x_3 + \cdots + x_k = n \tag{4.23}$$

with $x_i \geq 1$, the possible number of combinations allowing to obtain the last sum is given by:

$$\binom{n-1}{k-1} = \frac{(n-1)!}{(k-1)!\,(n-k)!} \tag{4.24}$$

with n = 50 and k = N/2. It can therefore be anticipated that the total number of possible configurations increases exponentially with the number of elements. As an order of magnitude, 8 slots lead to 18,424 possibilities, 10 slots to 211,876, and 12 slots to 1,906,884. These values highlight the limitations of this approach for small arrays. Nevertheless, some strategies can be used to reduce the number of possibilities. For example, imposing a minimum weighting percentage avoids combinations where an element is close to being switched off. Indeed, in the traditional approach, the unit weighting of a radiating element in small arrays is rarely as low as 1% or 2% (which would be equivalent to switching the element off), so these cases can be excluded. For instance, with 12 slots, imposing a minimum weighting of 3% instead of 1% reduces the number of possibilities from 1,906,884 to 10,660, which is a significant reduction.

A numerical function which returns an array containing all the possible combinations can be easily found on the internet or even generated by AI. It can then be used by giving as input the wanted sum (50), the number of elements (N/2), possibly the minimal threshold value (like 3%) and returns all possible combinations. When the return values are multiplied by a factor equal to 0.01, the values correspond to the tested normalized weighting of our 1×N array.

Until now, the mathematical approach has been presented with a sampling interval of 1% in order to easily visualise the problem. Nonetheless, if more precision is sought (meaning falling below one percent), the value of the sum can be increased and the sampling factor adapted in a way that the product of the sum and the factor stays always equal to 0.5. First tested levels of increased precision are the half percent and the quarter percent, respectively leading to the sum and factor product equal to 100×0.005 and 200×0.0025. On the other hand, the number of combinations increases exponentially. For example, with 8 slots, passing from one

percent (1%), half percent (0.5%) and quarter percent (0.25%) of precision leads to a number of possibilities of respectively 18,424, 156,849 and 1,293,699.

The general concept of using stars and bars combinations is presented here with the aim of testing all weighting possibilities and retaining the ones that meet a target radiation pattern for in-phase antenna. However, given the impact on the number of combinations when increasing the number of slots and the desired tapering precision, this tool must be used cautiously; otherwise, memory issues (RAM) may occur.

- **Algorithmic reasoning**

Since all possible combinations of normalized weights for a given number of slots and weighting precision (e.g., 1%, 0.5%, and 0.25%) are already known, the algorithm's general approach is to vectorially apply the theoretical formula for the curved array's radiation pattern, presented in (4.12), to all pre-calculated tapering combinations.

Since this analysis is performed for a fixed radius of curvature, the radiation pattern in the curved plane of a slot h_0 depends only on the θ variable which simplifies the problem. Consequently, equation (4.12) can be written as:

$$h(\theta, \mathrm{R}) = \sum_{n} w_n \, h_0(\Delta\theta_n) e^{jk\delta_n} \qquad (4.25)$$

where h_0 function is common to all slots. Furthermore, it can be observed that, except for the sought-after w_n values, all the other variables $h_0(\Delta\theta_n)$ and $\exp(jk\delta_n)$ which depend on the array characteristics, the radius and θ can be pre-calculated upstream. This calculation can be expressed in matrix form using a 'PreCalc' matrix of size (M×N), where each row M corresponds to a direction of observation (θ variable) and each column N corresponds to the N slot elements. Consequently, taking 'Weight' as a matrix of size (N×1), the final normalized field h = PreCalc @ Weight, where h is an (Mx1) vector corresponding to the normalized radiation pattern values for all θ.

This simple approach, corresponding to a vectorisation of the numerical calculations, allows for significant time savings. As a result, all the weighting combinations previously presented can be tested. The remaining distributions are those that meet the desired radiation pattern characteristics, such as a flat radiation pattern over a given angular range with a specified ripple tolerance. The approach presented here, although basic, has the advantage of being associated with an algorithm that is easy to implement and that tests all possible discrete combinations for a given sampling. It is therefore possible to determine whether the specifications are numerically feasible simply by adjusting the weighting of the in-phase slots.

4.4.2 Numerical test

The numerical study presented here highlights the procedure using the developed algorithm. The RF characteristics of the design under consideration, along with the specifications, are first introduced. The importance of the local radiation pattern of the slots is

then examined. Next, the theoretical results of the convergence algorithm are presented. Finally, the theoretical approach is compared with simulations performed using HFSS

- **Specifications**

For this exercise, the design is a 1×8 slotted array matched at 15 GHz with an RT/Duroid 5880 dielectric with a thickness of 254 µm. The radius of curvature R is 2 cm, leading to a structure in which slots 1 and 8 face opposite directions within 1 degree, as shown in Figure 118. The conductive surface has been deliberately extended at each end to avoid excessive edge effects.

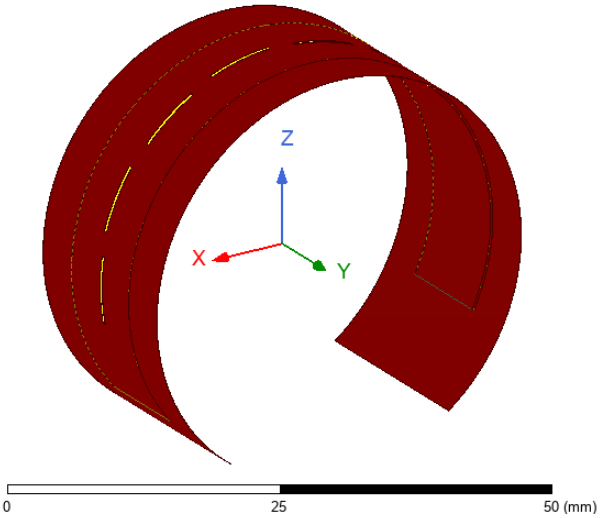

Figure 118 Design of the 1×8 curved slot array.

Concerning the target radiation pattern, a flat main beam over 180 degrees is expected, with a ripple tolerance of −2 dB within this angular range. The ripple value was arbitrarily chosen for this exercise and corresponds to a maximum field decrease of approximately 21% (37% in power).

- **Individual radiation pattern study**

Before using the algorithm to determine the weights required to meet the specifications, the numerical function approximating the radiation pattern of the slot h_0 must be obtained. Two levels of study can then be distinguished:

1) Assuming that all slots have the same radiation pattern. The reference case is simulated as a slot placed at the centre of the reflector plane
2) Considering the local radiation pattern of each slot on the curved reflector plane

The first approach is by far the simplest. It was used in previous works in this chapter for the sake of simplicity. Furthermore, since the elements studied at that time had a conventional weighting, with a distribution concentrated on the antennas located near the centre of the curved structure (i.e., the reflector plane), the resulting theoretical difference is very small. However, in the present case, the distribution gradient is less concentrated than in

previous work, and may even be more pronounced at the edges than at the centre. Therefore, optimizing the radiation pattern in this case study requires a more realistic approach. A comparison between the two approaches is shown in Figure 119.

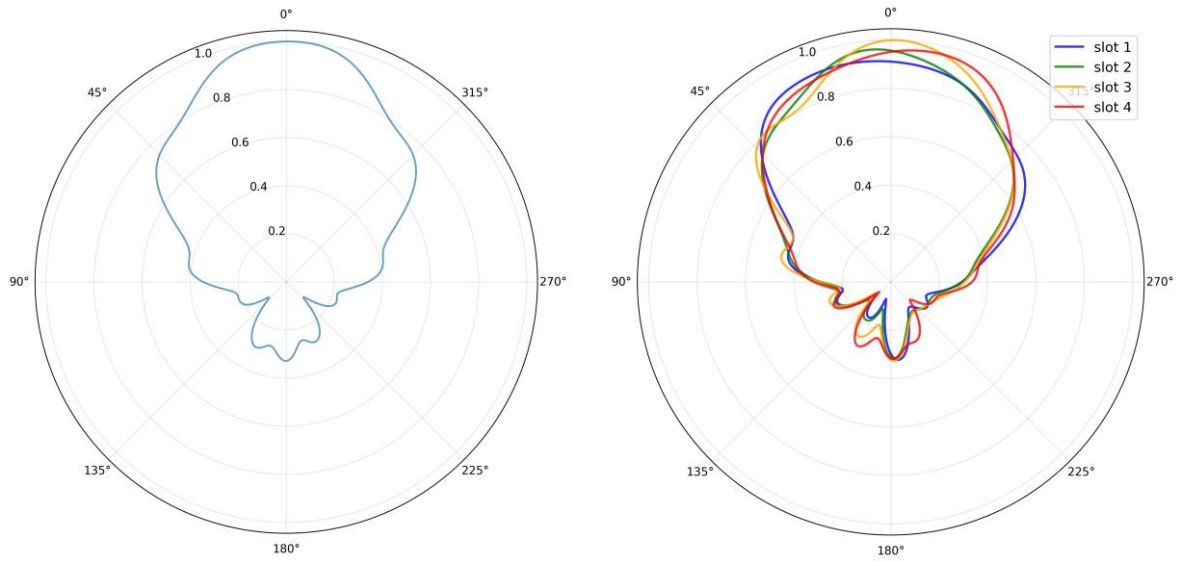

(a) (b)

Figure 119 Comparison of the normalized field radiation pattern for 1 slot placed on the centre of the curved reflector plane (a) and the one's in the locale position of half the slots of the design.

As observed, the radiation pattern of the slot located at the centre of the curved reflector plane is nearly symmetrical. In contrast, the four individual slots at their actual positions in the design all exhibit radiation patterns that are asymmetrical and distinct from one another.

- **Results of the developed algorithm**

Although the remainder of this study uses the radiation pattern specific to each slot, the element pattern is used to illustrate two important points. The first is a comparison of the weighting and results between the two approaches, which will be addressed later. The second concerns the impact of the chosen sampling on the resulting weights, as shown in Table 10.

Table 10 Obtained weighting and associated ripple for different sampling intervales.

sampling	number of combinations	number of solutions	max ripple in the beam	obtained coefficients for slots 1, 2, 3, 4
1.00 %	10.660	33	-1.12 dB	0.13 - 0.14 - 0.08 - 0.15
0.50 %	121.485	285	-1.05 dB	0.125 - 0.14 - 0.09 - 0.145
0.25 %	1.143.135	2250	-0.98 dB	0.125 - 0.1375 - 0.0925 - 0.145

A first observation is the difference in the weighting distribution compared to classical tapering. Indeed, slot 3 is the least excited. As expected, the number of combinations to be tested increases exponentially to achieve a 0.14 dB improvement in the internal ripple. A comparison of these three normalized radiation patterns is shown in Figure 120.

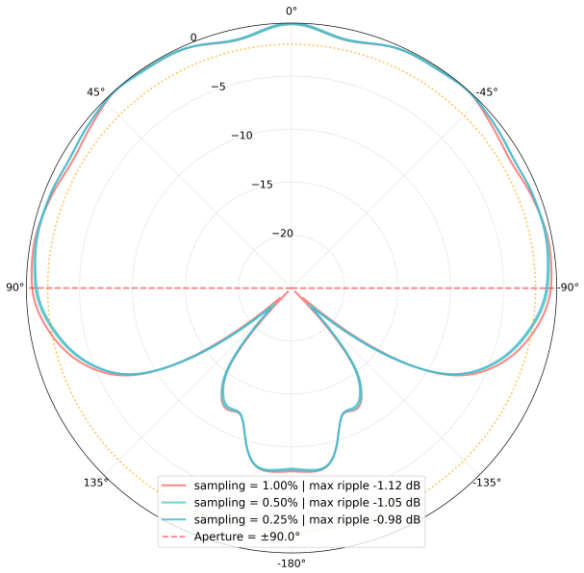

Figure 120 Comparison of the normalized radiation patterns from the weighting obtained for the 3 tested sampling intervals.

As it can be observed, the difference between the 3 normalized radiation patterns is very small. If the aim of this exercise is to obtain a general shape of the main lobe without necessarily seeking absolute performance, a weighting sampling step of 1% or 0.5% is perfectly adequate. Furthermore, in the case of flexible SIW slotted array, actually achieving the expected weighting to within one per cent is already very complex, so achieving accuracy below one per cent is not realistic in a typical project.

Concerning the results for the weighting with the second approach taking into account the individual slot's radiation pattern, the best theoretical obtained results with a sampling step of 0.5% for the expected specifications are given in Table 11.

Table 11 Obtained best weighting and associated ripples with consideration of local slot's radiation pattern.

best solutions	minimal normalized field	Max Ripple (dB)	Weighting
#1	0.8070	-1.86 dB	0.130 - 0.140 - 0.105 - 0.125
#2	0.8047	-1.89 dB	0.135 - 0.130 - 0.105 - 0.130
#3	0.8037	-1.90 dB	0.115 - 0.155 - 0.090 - 0.140
#4	0.8033	-1.90 dB	0.120 - 0.150 - 0.100 - 0.130
#5	0.8025	-1.91 dB	0.125 - 0.140 - 0.100 - 0.135

Different points can be observed. First, the obtained weightings lead to maximal ripple values very close between them, but with an offset of around -0.8 dB with the results of the first approach considering only 1 centred slot's radiation pattern. Secondly, the least excited slot is always the 3rd (and 6th), while the most excited is not always the 2nd (and 7th). Thirdly, while 285 solutions respected the specifications with the first approach, only 12 validate the specifications in this second approach. Finally, an interesting point which can be observed in Figure 121 is the fact that even if the weighting and the obtained maximal ripple values are close, the behaviour of the radiation patterns of the 5 best weightings presents differences.

Indeed, behaviour of the directivity depending on the angle θ is not the same with local maximal and minimal at different angles.

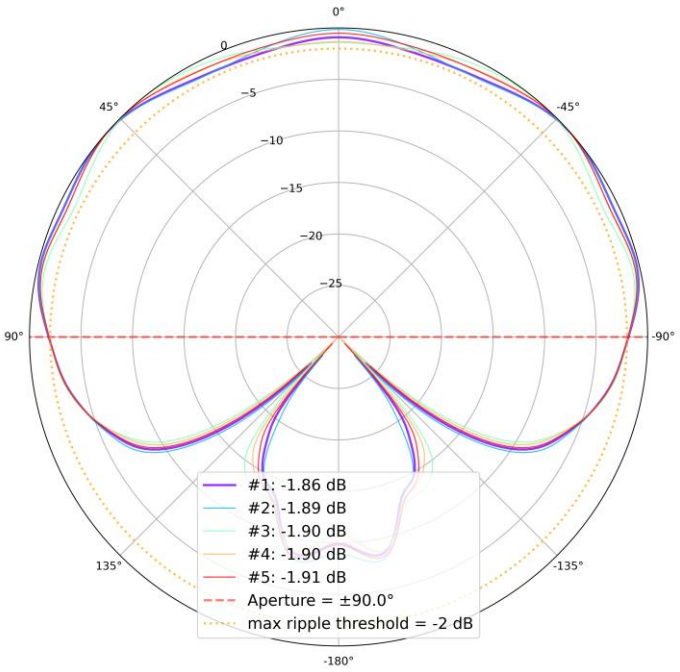

Figure 121 Comparison of the normalized radiation patterns for the 5 best the weighting.

- **Comparison with simulations**

To compare the theoretical approach with the simulation, the 1×8 design must first be scaled to match the target weights. Since simulation times for curved arrays are substantial, this process is first conducted on a flat array to determine the (x, l) pairs for each slot that best meet the matching requirements. These pairs are then applied as is to the curved array without further correction. The resulting weights are presented in Table 12.

Table 12 Comparison between theoretical expected weighting and the flat and curved HFSS designs.

expected weighting	0.1300, 0.1400, 0.1050, 0.1250
(HFSS) flat design's weighting	0.1286, 0.1410, 0.1054, 0.1248
(HFSS) curved design's weighting	0.1335, 0.1398, 0.1032, 0.1235

As observed, the maximum deviation from the expected value is 0.35%, which is below the initial sampling interval of 0.5%. This error is therefore considered acceptable, especially since optimising the dimensions to achieve greater weighting accuracy is physically unnecessary, as well as extremely time-consuming and complex.

Finally, Figure 122 presents a comparison between the normalized radiation pattern obtained from the HFSS simulation and the theoretical patterns derived from the two levels of study (using either a single slot radiation pattern as a reference or the local radiation patterns of the array elements).

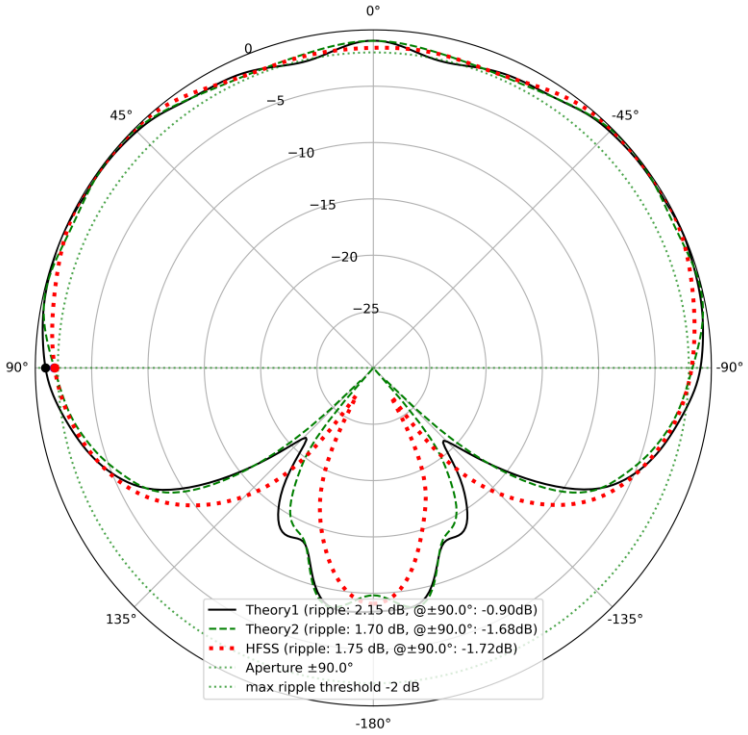

Figure 122 Normalized radiation pattern in log scale of the 1×8 curved simulated design and the 2 theoretical approaches.

The two theoretical approaches are applied using the floating weighting values obtained from HFSS. This explains the lower maximum ripple of 1.70 dB observed in Figure 122 for the second approach, compared to the initially expected -1.86 dB obtained with a 0.5% sampling step. This discrepancy highlights the benefit of decreasing the sampling step to gain an additional 0.1 or 0.2 dB, as previously noted in Table 10. Comparing the three curves, it can be observed that the second approach, which considers the local radiation patterns of all slots, yields results closer to the simulation than the first approach. The primary difference is most visible in the back-lobe radiation (backward radiation). Furthermore, the numerical values for the maximum ripple at 180° and the radiation levels at ±90° are more accurate with the second approach than with the first.

- **Conclusion**

The presented new method to easily obtain a discrete weighting of a curved array of in-phase elements allowing to reach a wider opening of the main beam with a tolerated ripple value inside shows very conclusive results. Indeed, from the radiation pattern of 1 slot centred on the design, or half of the slots on their own place, a combinatorial theorem enabling to obtain all the possible combinations of weighting for a given sampling interval, plus the vectorization of the calculations of the radiation pattern, enable to test quickly all the discrete combinations and retain the ones corresponding to the expectations.

Two points of general observation can be retained for this exercise. The first one is that a better accuracy between simulations and theory is obtained when the individual radiation pattern of all the slots is considered contrary to only one slot of reference. The second one is that the lower the sampling step, the better the obtained weighting coefficients allow to optimize the expected radiation pattern. Nonetheless, depending on the real application of the array of

in-phase elements designed to provide consistent directivity over a wide aperture angle, seeking accuracy to within a few hundredths of a dB may be unnecessary. Therefore, keeping the centred slot as reference for the radiation pattern is much more time-efficient and greatly simplifies algorithmic development. Furthermore, minimising the sampling step in order to gain a few hundredths of a dB leads to an extremely large number of solutions to be tested, which leads to weighting accuracy unrealistic in relation to the actual accuracy of the software adaptation. To achieve even greater optimization, the use of genetic algorithms or particle swarm optimization are required.

4.5 Conclusion

In this chapter, a work was done to study the radiation pattern of flexible SIW slotted array (SIWSA) for radii of the order of the wavelength.

The first aspect, which is essentially theoretical, highlights the need to consider variations in the radiation pattern of the unit element for small radii. This is approximated numerically with a cosine Fourier series whose coefficients depend on the radius. This work then makes it possible to adapt the classic function of the circular array radiation pattern to the case study of a flexible SIW slotted array with $R/\lambda_0 < 10$. The resulting function can then be used to assess the impact of certain factors other than the radius itself, such as the distance between the radiating elements or the weighting, on the rate at which the radiation pattern broadens as the radius decreases.

The second point presents the measurement protocol and work applied to different flexible SIW slotted arrays realized in an anechoic chamber. These measurements are compared with each other in order to validate the theoretical work on the impact of distance between elements relative to the wavelength on the broadening of the radiation pattern. Subsequently, the measurements specific to each design are compared with the simulations and the theoretical approach to validate the developed theory.

Finally, the last point attempts to simplify the algorithmic process for obtaining the weighting in a linear phased SIW slotted array tailored to a desired radiation pattern without passing through the development of a convergence algorithm. This approach consists in using the stars and bars theorem from combinatorics and testing all possible discrete combinations. Although the results may not match the performance achieved by more complex optimization algorithms such as genetic algorithms or PSO, this method offers a fast, straightforward and easy-to-implement alternative, providing satisfactory results with minimal development effort.

The work carried out in this chapter paves the way for two main extensions. The first would involve developing an algorithm to determine the inter-element spacing in the plane of curvature, as well as the necessary weighting, such that the planar radiation pattern meets specific requirements (e.g., maximum directivity, narrow HPBW) while limiting variations for small radii of curvature. It should be noted that this task can be performed by combining the theories developed in Sections 4.2 and 4.4. Conversely, one could imagine the reverse scenario where a highly directive flat array undergoes significant beam broadening in the case of a reconfigurable array, where the radius of curvature varies in real-time according to the required

HPBW (for either wide or directive coverage). The second extension would be to further develop the method presented in Section 4.4 for weighting optimization at a given radius, with the objective of incorporating phase shifts between the slots to allow for better control of the radiation pattern.

General conclusion and perspectives

This thesis work falls within the general context of using slotted arrays on flexible SIW for radii of curvature on the order of the wavelength. Among the major research axes on this subject, such as materials engineering or industrial processes, the focus was placed on antenna theory. The work has thus enabled improvement of the design procedure for these arrays where mutual coupling is very strong, as well as the study of the radiation pattern function of a curved array considering the variations in the unit element radiation with small curvature angles.

The first chapter introduces the electromagnetic quantities and parameters necessary for a concise presentation of array antenna theory. This foundation enables the discussion of conformal antennas and the associated theory. A brief survey of various slot antenna arrays based on Rectangular Waveguide (RWG) or Substrate Integrated Waveguide (SIW) is presented. The justification for employing a flexible array within the context of the significant curvature requirements is emphasized, along with a state-of-the-art examination of this technology.

The second chapter presents a direct improvement to the conventional theoretical approach for designing medium-sized slot arrays, explicitly accounting for mutual coupling. It begins with an analysis of the mathematical formulation governing individual slot's electromagnetic behaviour, followed by an automated Python–HFSS method for correcting array design parameters. These developments culminate in a full automated design algorithm, demonstrated through several prototypes operating in the X- and Ku-bands.

The third chapter presents a new matching procedure developed for slot antenna arrays on thin waveguides (thus enabling flexibility) specifically subject to strong mutual coupling. The theoretical approach and associated algorithmics of the procedure are described and validated through the adaptation of different designs on software. The slot design obtained with this new approach provides slightly improved simulation results compared to Elliott's approach. The procedure is then applied to other case studies, such as the addition of a protective film and the adaptation to the mode, both of which have shown promising results, or the inclusion of external mutual coupling, which still requires further improvement.

The fourth and final chapter focuses on analysing radiation pattern variations in the flexible slot array for curvature radii on the order of the wavelength. The first line of investigation concerns adapting circular-array theory to account for radiation pattern variations with radius, acknowledging that the individual slot pattern changes for small radii. This theoretical development is then compared and validated with a set of simulations and measurements performed on prototypes with curvatures $R/\lambda_0<10$. This study addresses a relatively unexplored area regarding flexible slotted arrays. The second line of investigation focuses on developing an algorithmic method to determine the weighting required to achieve the desired radiation pattern for a curved in-phase slotted array. Although more limited in scope than the approaches found in the literature, the method presented here prioritises simplicity and rapid development over absolute performance, while still delivering acceptable results.

The two major research axes pursued during this thesis work have enabled, on one hand, the development of a new matching method for flexible slot arrays more suitable to the subject than classical literature on slot arrays, and on the other hand, a novel mathematical approach to obtain the radiation pattern function of a slot array curved over small radii. The first axis provides improved design capabilities for these arrays in this study case, with significant features such as accounting for a protective film on the array. The second axis enables a mathematical investigation of the curved array radiation pattern with radius R as a variable, thus allowing anticipation and study of the radiation pattern broadening rate at small radii according to various array parameters.

The work presented here opens new avenues and perspectives. Regarding the second chapter, the algorithmic method for total automation of slot array design could integrate a form of AI to accelerate convergence based on data from previous developed designs. For the third chapter, it would be valuable to enhance the developed tool to precisely correct the expected weighting in the software, for instance using a genetic algorithm. Moreover, given the narrow bandwidth of these thin waveguides, investigating slot shapes would be worthwhile and would remain fully compatible with the developed protocol. For the final chapter, it would be interesting to develop an algorithm to obtain the inter-element spacing values in the curvature plane as well as the necessary weighting, such that the flat radiation pattern meets certain requirements (maximum gain, narrow HPBW) while variations in the radiation pattern for small radii of curvature remain within a given range.

References

[1] R. C. Johnson, *Antenna Engineering Handbook*, 3rd edition. New York: McGraw-Hill, Inc., 1993.

[2] C. A. Balanis, *Antenna Theory: Analysis and Design*, 4th edition. John Wiley & Sons, Inc.

[3] R. J. Mailloux, *Phased Array Antenna Handbook*, 2nd ed. Artech House, 2005.

[4] "IEEE Standard Definitions of Terms for Antennas," *IEEE Std 145-1993*, pp. 1–32, Jul. 1993, doi: 10.1109/IEEESTD.1993.119664.

[5] L. Josefsson and P. Persson, *Conformal Array Antenna Theory and Design*, 1st ed. Wiley, 2006. doi: 10.1002/047178012X.

[6] Hopkins, M. A.; Tuss, J. M.; Lockyer, A. J.; Alt, K.; Kinslow, R.; Kudva, J. N., "Smart Skin Conformal Load-bearing Antenna and Other Smart Structures Developments," *Proceedings of American Institute of Aeronautics and Astronautics (AIAA), Structures, Structural Dynamics and Materials Conference*, pp. 521–530, 1997.

[7] S. Agarwal, D. Masotti, S. Nikolaou, and A. Costanzo, "Conformal Design of a High-Performance Antenna for Energy-Autonomous UWB Communication," *Sensors*, vol. 21, no. 17, 2021, doi: 10.3390/s21175939.

[8] S. Subramani and R. Subramaniam, "An eight-element conformal MIMO antenna for 5G-enabled Internet of Medical Things (IoMT) communications," *Int. J. Microw. Wirel. Technol.*, vol. 17, no. 4, pp. 710–720, May 2025, doi: 10.1017/S1759078725000558.

[9] R. J. Mailloux, "conformal and low-profile arrays," in *Antenna Engineering Handbook*, 3rd edition., New York: McGraw-Hill, Inc., 1993, p. 21.1-21.24.

[10] W. Kummer, "Preface to special issue on conformal antennas," *IEEE Trans. Antennas Propag.*, vol. 22, no. 1, pp. 1–3, Jan. 1974, doi: 10.1109/TAP.1974.1140744.

[11] H. M. El Misilmani, M. Al-Husseini, and K. Y. Kabalan, "Design procedure for planar slotted waveguide antenna arrays with controllable sidelobe level ratio for high power microwave applications," *Eng. Rep.*, vol. 2, no. 10, 2020, doi: 10.1002/eng2.12255.

[12] J. S. Meiguni, S. K. Haddad, and A. Hosseinbeig, "Longitudinal slotted waveguide array feed networks," *Int. J. Microw. Wirel. Technol.*, vol. 10, no. 4, pp. 512–517, May 2018, doi: 10.1017/S1759078718000259.

[13] D. M. Pozar, "transmission lines and waveguides," in *microwave engineering*, 1st ed., Addison-Wesley Publishing Company, 1990.

[14] M. Bozzi, A. Georgiadis, and K. Wu, "Review of substrate-integrated waveguide circuits and antennas," *IET Microw. Antennas Propag.*, vol. 5, no. 8, pp. 909–920, 2011, doi: 10.1049/iet-map.2010.0463.

[15] D. Deslandes and K. Wu, “Accurate modeling, wave mechanisms, and design considerations of a substrate integrated waveguide,” *IEEE Trans. Microw. Theory Tech.*, vol. 54, no. 6, pp. 2516–2526, Jun. 2006, doi: 10.1109/TMTT.2006.875807.

[16] Y. Cassivi, L. Perregrini, P. Arcioni, M. Bressan, K. Wu, and G. Conciauro, “Dispersion characteristics of substrate integrated rectangular waveguide,” *IEEE Microw. Wirel. Compon. Lett.*, vol. 12, no. 9, pp. 333–335, Sep. 2002, doi: 10.1109/LMWC.2002.803188.

[17] Feng Xu and K. Wu, “Guided-wave and leakage characteristics of substrate integrated waveguide,” *IEEE Trans. Microw. Theory Tech.*, vol. 53, no. 1, pp. 66–73, Jan. 2005, doi: 10.1109/TMTT.2004.839303.

[18] F.T. Ladani, S. Jam, and R. Safian, “Comment on Analytical Equivalence Between Substrate-Integrated Waveguide and Rectangular Waveguide,” *IET Microw. Antennas Propag.*, vol. 7, no. 1, pp. 24–25, 2013, doi: 10.1049.

[19] J.-F. Liang, H.-C. Chang, and K. A. Zaki, “Coaxial probe modeling in waveguides and cavities,” *IEEE Trans. Microw. Theory Tech.*, vol. 40, no. 12, pp. 2172–2180, Dec. 1992, doi: 10.1109/22.179878.

[20] D. Deslandes, “Design equations for tapered microstrip-to-substrate integrated waveguide transitions,” in *2010 IEEE MTT-s international microwave symposium*, IEEE, 2010, pp. 704–707. Accessed: Aug. 28, 2025. [Online]. Available: https://ieeexplore.ieee.org/abstract/document/5517884/

[21] H. G. Booker, “Slot aerials and their relation to complementary wire aerials (Babinet’s principle),” *J. Inst. Electr. Eng. - Part IIIA Radiolocation*, vol. 93, no. 4, pp. 620–626, 1946, doi: 10.1049/ji-3a-1.1946.0150.

[22] A. Dorne and D. Lazarus, “slot antennas,” in *Very High-Frequency Techniques*, McGraw-Hill Book Company., vol. 1, 1947, pp. 171–191.

[23] Balanis, “aperture antenna,” in *Antenna Theory, analysis and design*, 4th ed., Wiley, 2016, pp. 639–718.

[24] R. S. Elliott, “The Design of Waveguide-Fed Slot Arrays,” in *Antenna Handbook: Theory, Applications, and Design*, Y. T. Lo and S. W. Lee, Eds., Boston, MA: Springer US, 1988, pp. 805–842. doi: 10.1007/978-1-4615-6459-1_12.

[25] A. F. Stevenson, “Theory of slots in rectangular wave-guides,” *J. Appl. Phys.*, vol. 19, no. 1, pp. 24–38, 1948.

[26] R. J. Stegen, “Longitudinal shunt slot characteristics,” 1951. Accessed: Aug. 28, 2025. [Online]. Available: https://apps.dtic.mil/sti/html/tr/ADA800305/

[27] R. J. Stegen, “Slot radiators and arrays at X-band,” *Trans. IRE Prof. Group Antennas Propag.*, vol. 1, no. 1, pp. 62–84, Feb. 1952, doi: 10.1109/TPGAP.1952.6366355.

[28] A. Oliner, “The impedance properties of narrow radiating slots in the broad face of rectangular waveguide: Part I–Theory,” *IRE Trans. Antennas Propag.*, vol. 5, no. 1, pp. 4–11, Jan. 1957, doi: 10.1109/TAP.1957.1144488.

[29] T. Vu Khac and C. Carson, “Impedance properties of a longitudinal slot antenna in the broad face of a rectangular waveguide,” *IEEE Trans. Antennas Propag.*, vol. 21, no. 5, pp. 708–710, Sep. 1973, doi: 10.1109/TAP.1973.1140563.

[30] R. Elliott and L. Kurtz, “The design of small slot arrays,” *IEEE Trans. Antennas Propag.*, vol. 26, no. 2, pp. 214–219, Mar. 1978, doi: 10.1109/TAP.1978.1141814.

[31] R. Elliott, “An improved design procedure for small arrays of shunt slots,” *IEEE Trans. Antennas Propag.*, vol. 31, no. 1, pp. 48–53, Jan. 1983, doi: 10.1109/TAP.1983.1143002.

[32] R. Elliott and W. O’Loughlin, “The design of slot arrays including internal mutual coupling,” *IEEE Trans. Antennas Propag.*, vol. 34, no. 9, pp. 1149–1154, Sep. 1986, doi: 10.1109/TAP.1986.1143947.

[33] G. A. Casula and G. Montisci, “Design of Dielectric-Covered Planar Arrays of Longitudinal Slots,” *IEEE Antennas Wirel. Propag. Lett.*, vol. 8, 2009, doi: 10.1109/LAWP.2009.2021963.

[34] Z. Jin, G. Montisci, G. Mazzarella, M. Li, H. Yang, and G. A. Casula, “Effect of a Multilayer Dielectric Cover on the Behavior of Waveguide Longitudinal Slots,” *IEEE Antennas Wirel. Propag. Lett.*, vol. 11, 2012, doi: 10.1109/LAWP.2012.2222335.

[35] Hu Yang *et al.*, “Design Equations for Cylindrically Conformal Arrays of Longitudinal Slots,” *IEEE Trans. Antennas Propag.*, vol. 64, no. 1, pp. 80–88, Jan. 2016, doi: 10.1109/TAP.2015.2496965.

[36] G. P. Le Sage, “3D Printed Waveguide Slot Array Antennas,” *IEEE Access*, vol. 4, pp. 1258–1265, 2016, doi: 10.1109/ACCESS.2016.2544278.

[37] S. G. Kirtania *et al.*, “Flexible Antennas: A Review,” *Micromachines*, vol. 11, no. 9, Sep. 2020, doi: 10.3390/mi11090847.

[38] M. U. Ali Khan, R. Raad, F. Tubbal, P. I. Theoharis, S. Liu, and J. Foroughi, “Bending Analysis of Polymer-Based Flexible Antennas for Wearable, General IoT Applications: A Review,” *Polymers*, vol. 13, no. 3, Jan. 2021, doi: 10.3390/polym13030357.

[39] D. M. John, S. Vincent, S. Pathan, P. Kumar, and T. Ali, “Flexible Antennas for a Sub-6 GHz 5G Band: A Comprehensive Review,” *Sensors*, vol. 22, no. 19, Oct. 2022, doi: 10.3390/s22197615.

[40] S. Cheng, H. Yousef, and H. Kratz, “79 GHz Slot Antennas Based on Substrate Integrated Waveguides (SIW) in a Flexible Printed Circuit Board,” *IEEE Trans. Antennas Propag.*, vol. 57, no. 1, pp. 64–71, Jan. 2009, doi: 10.1109/TAP.2008.2009708.

[41] H. Yousef, Shi Cheng, and H. Kratz, “Substrate Integrated Waveguides (SIWs) in a Flexible Printed Circuit Board for Millimeter-Wave Applications,” *J. Microelectromechanical Syst.*, vol. 18, no. 1, pp. 154–162, Feb. 2009, doi: 10.1109/JMEMS.2008.2009799.

[42] Y. F. Wu and Y. J. Cheng, “Conical Conformal Shaped-Beam Substrate-Integrated Waveguide Slot Array Antenna With Conical-to-Cylindrical Transition,” *IEEE Trans. Antennas Propag.*, vol. 65, no. 8, Aug. 2017, doi: 10.1109/TAP.2017.2716404.

[43] K. K. Fan and Z.-C. Hao, “Cylindrical conformal array antenna with tilted H-plane Fan-shaped beam for millimeter-wave application,” *Microw. Opt. Technol. Lett.*, vol. 58, no. 7, pp. 1666–1671, Jul. 2016, doi: 10.1002/mop.29879.

[44] Y. J. Cheng, H. Xu, D. Ma, J. Wu, L. Wang, and Y. Fan, “Millimeter-wave shaped-beam substrate integrated conformal array antenna,” *IEEE Trans. Antennas Propag.*, vol. 61, no. 9, pp. 4558–4566, 2013.

[45] O. Bayraktar and O. A. Civi, “Circumferential traveling wave slot array on cylindrical substrate integrated waveguide (CSIW),” *IEEE Trans. Antennas Propag.*, vol. 62, no. 7, pp. 3557–3566, 2014.

[46] Y. Ma, X. Shi, J. Wang, Y. Zhang, F. Sun, and F. Wu, “Millimeter-wave conformal directional leaky-wave antenna based on substrate-integrated waveguide,” *Electronics*, vol. 12, no. 14, p. 3111, 2023.

[47] Robert S. Elliott, “the design of feeding structures for antenna elements array,” in *Antenna Theory and Design*, Wiley-IEEE Press, 2003, pp. 351–426.

[48] SHENGYI TECHNOLOGY CO, “datasheet - SF280.” [Online]. Available: https://www.syst.com.cn/

[49] Rogers Corportation, “datasheet - RO4000 series,” 2022. [Online]. Available: https://www.rogerscorp.com/

[50] Rogers Corporation, “datasheet - RT/duroid 5870/5880,” 2022. [Online]. Available: https://www.rogerscorp.com/

[51] Z. Wang and Y. Dong, “Travelling-Wave SIW Transmission Line Using TE20 Mode for Millimeter-Wave Antenna Application,” in *2020 IEEE/MTT-S International Microwave Symposium (IMS)*, Aug. 2020, pp. 169–172. doi: 10.1109/IMS30576.2020.9223890.

[52] J. Xu, Z. N. Chen, X. Qing, and W. Hong, “A Single-layer SIW Slot Array Antenna with TE20 Mode”.

[53] Y. Chairi *et al.*, “Design of a Slotted Waveguide Antenna Based on TE20 Mode in Ku-Band Suitable for Direct Metal Laser Sintering,” *Electronics*, vol. 11, no. 13, Jul. 2022, doi: 10.3390/electronics11132079.

[54] Josefsson and Persson, “conformal array pattern synthesis,” in *Conformal Array Antenna Theory and Design*, Wiley., 2006.

[55] P. H. Pathak and R. G. Kouyoumjian, “An analysis of the radiation from apertures in curved surfaces by the geometrical theory of diffraction,” *Proc. IEEE*, vol. 62, no. 11, pp. 1438–1447, Nov. 1974, doi: 10.1109/PROC.1974.9650.

[56] C. Balanis and L. Peters, “Radiation from TE10mode slots on circular and elliptical cylinders,” *IEEE Trans. Antennas Propag.*, vol. 18, no. 3, pp. 400–403, May 1970, doi: 10.1109/TAP.1970.1139709.

[57] Balanis, “Arrays: Linear, Planar, and Circular,” in *Antenna Theory, analysis and design*, 4th ed., Hoboken, NJ, USA: Wiley, 2016, pp. 285–384.

COLLEGES SCIENCES
BRETAGNE POUR L'INGENIEUR
LOIRE ET LE NUMERIQUE

IMT Atlantique
Bretagne-Pays de la Loire
École Mines-Télécom

Titre : Etude de réseau d'antennes conforme sur substrat flexible : diagramme de rayonnement et techniques d'adaptation

Mots clés : antenne conforme, antenne flexible, SIW à fentes, couplages mutuels

Résumé : L'utilisation de réseaux d'antennes à fentes sur substrate integrated waveguide (SIW) flexible est étudiée depuis plus de 20 ans. Cette technologie permet d'utiliser certaines méthodes de fabrication de réseaux planaires, qui peuvent être conformés sur une surface donnée.
Les travaux présentés dans cette thèse portent sur la théorie de ces réseaux conformes dans les bandes de fréquences X et Ku. Un premier axe d'étude concerne l'adaptation en fréquence de ces réseaux à fentes, particulièrement complexe en raison de la faible épaisseur des guides d'ondes flexibles.
Ensuite, une autre approche, consiste à simuler puis à mettre en équation les couplages mutuels entre antennes à fentes. Le second axe d'étude porte sur la mise en équation de l'ouverture du diagramme de rayonnement pour des rayons de courbure de l'ordre de la longueur d'onde. Cela permet d'analyser l'influence des caractéristiques du réseau sur l'élargissement du lobe principal en considérant le rayon de courbure comme un paramètre et également de fournir des outils de conception.

Title : Flexible conformal antenna array: study of the radiation pattern and matching techniques

Keywords : conformal antenna, flexible antenna, slotted SIW, mutual coupling

Abstract : The use of slot antenna arrays based on flexible Substrate Integrated Waveguide (SIW) technology has been a subject of research for over two decades. This technology enables the implementation of planar array fabrication methods, which can be conformed to specific surfaces.
The research presented in this thesis focuses on the theory of conformal arrays operating within the X and Ku frequency bands. The first research axis addresses the frequency matching of these slot arrays, which is particularly challenging due to the small thickness of flexible waveguides.
The methodology initially involves leveraging existing theory and developing automated design algorithms for use with electromagnetic simulation software. Subsequently, an alternative approach is presented, involving the simulation and analytical modeling of mutual coupling between slot antennas. The second research axis focuses on formulating the radiation pattern for curvature radii on the order of the wavelength. This allows for an analysis of how array characteristics influence main lobe broadening, treating the radius of curvature as a design parameter, while also providing practical design tools.